Fundamental Investigation
of Particle-Layer Rearrangement Events
in Ceramic Wall-Flow Filters

Resolved Particle Simulations with Lattice Boltzmann Methods

Zur Erlangung des akademischen Grades eines

DOKTORS DER INGENIEURWISSENSCHAFTEN (DR.-ING.)

von der KIT-Fakultät für
Chemieingenieurwesen und Verfahrenstechnik
des Karlsruher Instituts für Technologie (KIT)
genehmigte

DISSERTATION

von
M. Sc. Nicolas Hafen
aus Bad Honnef

Tag der mündlichen Prüfung: 07. Februar 2024

Referent: PD Dr. rer. nat. Mathias J. Krause
Korreferent: Prof. Dr.-Ing. habil. Achim Dittler

Zusammenfassung

Wandstromfilter werden bei der Abgasnachbehandlung von Verbrennungs-
motoren eingesetzt, wo sie zur Entfernung von emittierten Partikeln verwen-
det werden. Solche Filter bestehen aus gegenläufig angeordneten Ein- und
Auslasskanälen, die durch poröse Substratwände getrennt sind. Beim Durch-
strömen des Filters wird das eintretende Abgas gezwungen, diese Wände zu
passieren, während ein Großteil der Partikeln abgeschieden wird. Auf diese
Weise bildet der eingetragene Feststoff auf dem Filtersubstrat eine durchläs-
sige Partikelschicht. Mit der Zeit nimmt deren Dicke, und damit der Druck-
verlust, über den Filter zu, sodass eine Regeneration des Filters erforderlich
wird. Während eines solchen Regenerationsvorgangs kann die geschlossene
Schicht in einzelne Schichtfragmente aufbrechen, die sich potenziell inner-
halb einzelner Filterkanäle umlagern. Dies kann schließlich zur Bildung be-
stimmter Ablagerungsmuster führen, die den Druckverlust eines Filters, seine
Asche-Speicherkapazität und den Gesamtabscheidegrad beeinflussen. Der Um-
lagerungsprozess wird durch die Wechselwirkung von hydrodynamischen und
adhäsiven Kräften bestimmt, die nur durch die Berücksichtigung der Ober-
flächen einzelner Schichtfragmente genau modelliert werden können. Trotz
der bekannten Bedeutung für den Filtrationsprozess lässt sich die Ausbildung
bestimmter Ablagerungsmuster noch nicht eindeutig auf bestimmte Einfluss-
faktoren zurückführen. Weiterhin fehlen geeignete Berechnungsmodelle, die
eine Quantifizierung der entsprechenden Faktoren ermöglichen. Die vorliegen-
de Arbeit verfolgt daher den Ansatz einer grundlegenden Untersuchung von
Umlagerungsvorgängen in keramischen Wandstromfiltern mittels oberflächen-
aufgelöster Partikelsimulationen mit Lattice-Boltzmann-Methoden (LBM). Das
Hauptziel ist dabei die Bestimmung der Sensitivität und die Quantifizierung der
Auswirkungen von ingenieurtechnischen Einflussfaktoren auf den transienten

Umlagerungsprozess in Wandstromfiltern.

Eine vielseitige und leicht erweiterbare Implementierung der Lattice-Boltzmann-Methode wird durch die Open-Source-Software OPENLB bereitgestellt. Diese wird daher in der vorliegenden Arbeit verwendet und entsprechend erweitert. Auf diese Weise wird die Erhaltung der entwickelten Methodik in einer öffentlich zugänglichen Ressource gewährleistet, die eine vollständige Reproduzierbarkeit der erzielten Ergebnisse ermöglicht. Die Entwicklung und Anwendung eines geeigneten Simulationsmodells erfolgt in vier aufeinanderfolgenden Schritten, die auf vier separaten Arbeiten beruhen.

Der erste Schritt ist der Modellentwicklung gewidmet, indem ein Simulationsansatz bereitgestellt wird, der in der Lage ist, die zeitabhängige Entwicklung des gasförmigen Strömungsfeldes innerhalb eines Wandstromfilters während seiner Regeneration abzubilden. Seine Gültigkeit und Anwendbarkeit wird durch die Durchführung von Gitterkonvergenzstudien und den Vergleich mit einer Referenzlösung bewertet. Eine stationäre fragmentierte Partikelschicht wird im Hinblick auf die räumliche Verteilung der wirkenden hydrodynamischen Kräfte und den Einfluss von Fragmentclustern an verschiedenen Kanalpositionen untersucht. Anschließend werden einige erste instationäre Simulationen der Ablösung von Partikelschicht-Fragmenten in einem Regime kleiner Gasgeschwindigkeiten durchgeführt und die Auswirkungen verschiedener Schichteigenschaften untersucht.

Ein zweiter Schritt soll nähere Einblicke in das Verhalten einzelner Schichtfragmente während der Filterregeneration geben. In diesem Zusammenhang wird die zeitliche Entwicklung der hydrodynamischen Kräfte, die auf die Oberfläche eines Fragments wirken, für unterschiedliche Fragmentdichten und Ablösepositionen detailliert untersucht. Relevante Schlüsselgrößen, wie die Aufprallgeschwindigkeit am Kanalende und die Stoppdistanz, werden definiert, bestimmt und im Hinblick auf Vorhersagen über die resultierenden Ablagerungsmuster interpretiert. Zunächst wird eine physikalisch sinnvolle Substratpermeabilität durch einander entsprechende experimentelle und numerische Druckverluststudien ermittelt. Anschließend wird das zeitliche Verhalten einzelner Schichtfragmente mit unterschiedlichen Dichten unter Berücksichtigung aller wirkenden Kräfte detailliert untersucht. Der pneumatische Transport der Fragmente durch den Kanal wird dann für verschiedene Startpositionen, Substratpermeabilitäten, Einströmgeschwindigkeiten und mittlere Feststoffdichten der eingetragenen Partikeln untersucht. Schließlich werden die allgemeinen Bewegungsmerkmale hinsichtlich ihrer qualitativen Übereinstimmung mit experimentellen Beobachtungen bewertet.

In einem dritten Schritt wird der entwickelte LBM-Ansatz auf einen erweiterten Geschwindigkeitsbereich angewandt, der einen möglichst großen Teil des physikalisch relevanten Bereichs abdeckt und mittlere Kanal-Einströmgeschwindigkeiten von bis zu 80 m/s umfasst. Nach einer Anpassung der Randbedingungen werden drei verschiedene Szenarien untersucht, indem nur die partikelfreie Strömung, ein einzelnes Schichtfragment, das an einer der Substratwände haftet, und eine fragmentierte Partikelschicht betrachtet werden. Zunächst wird eine umfassende Quantifizierung der Stabilität und Genauigkeit sowohl der partikelfreien als auch der partikelbehafteten Strömungen unter Berücksichtigung statischer, Schichtfragmente durchgeführt. Anschließend werden die lokalen Auswirkungen einer fragmentierten Partikelschicht für verschiedene stationäre Situationen entlang des Kanals untersucht. Um Vorhersagen über die Ablösewahrscheinlichkeit einzelner Schichtfragmente und deren gegenseitige Beeinflussung ableiten zu können, wird zusätzlich die räumliche Verteilung der hydrodynamischen Kräfte ausgewertet.

Ein letzter Schritt ist speziell der Untersuchung des Prozesses der Stopfenbildung gewidmet, indem zusätzlich das dynamische Verhalten der Schichtfragmente nach der Schichtfragmentierung betrachtet wird. Dies umfasst die Ablösung und den Transport der Fragmente entlang des Kanals sowie die anschließende Stopfen-Bildung. Um den Kontakt der Fragmente während ihres Transports genau zu berücksichtigen, wird das Modell um eine zuvor entwickelte diskrete Kontaktmethode erweitert. Mit dem aktualisierten Modell wird der Einfluss der Topologie der Fragmentschicht, der Eigenschaften der Fragmente und der Betriebsbedingungen bewertet und relevante Schlüsselgrößen werden bestimmt.

Die mit diesen vier Schritten erzielten Ergebnisse stellen eine umfassende Quantifizierung der Auswirkungen relevanter Einflussfaktoren auf verschiedene Aspekte des transienten Umlagerungsprozesses in Wandstromfiltern dar. Damit leistet die vorliegende Arbeit einen wichtigen Beitrag zu den noch bestehenden Forschungslücken in diesem Bereich. Darüber hinaus beschreibt sie potenzielle Möglichkeiten für Modifikationen des Filtrationsprozesses, die zu einer Optimierung von Motorleistung, Kraftstoffverbrauch und Lebensdauer von Wandstromfiltern führen können.

Abstract

Wall-flow filters are applied in the exhaust treatment of internal combustion engines, where they are used for the removal of emitted particulate matter (PM). Such filters consist of oppositely arranged inlet and outlet channels separated by porous substrate walls. When traversing the filter, the entering exhaust gas is forced to pass through those walls while being stripped from the majority of the contained particles. This way, the introduced solid material forms a permeable deposition layer on the filter substrate with continuously increasing thickness. Over time, the pressure drop over the filter increases, respectively, leading to the necessity of the filter's regeneration. During such a regeneration process, the coherent layer can break up into individual layer fragments, which potentially rearrange inside single filter channels. This can, eventually, lead to the formation of specific deposition patterns, which affect a filter's pressure drop, its ash storage capacity and the overall separation efficiency. The rearrangement process is governed by the interaction of hydrodynamic and adhesive forces, which can only be accurately modelled by taking the surfaces of individual layer fragments into account. Despite its well-known significance on the filtration process, the formation of specific deposition patterns can still not consistently be attributed to particular influence factors and appropriate calculation models that enable a quantification of respective factors do not exist. This present work, therefore, approaches a fundamental investigation of particle-layer rearrangement events in ceramic wall-flow filters by means of surface resolved particle simulations with lattice Boltzmann methods (LBM). The main goal is the determination of the sensitivity and the quantification of the impact of engineering-related influence factors on the transient rearrangement process in wall-flow filters.

A versatile and easily extendable implementation of the LBM is provided by

the open source software OPENLB. It is therefore used and extended accordingly in the present work. This way, the conservation of the developed methodology is ensured in a publicly available resource that enables full reproducibility of the obtained results. The development and application of an appropriate simulation model is considered in four consecutive solution steps, which are based on four separate works.

The first step is dedicated to the model development by providing a simulation approach, which is capable of capturing the time dependent development of the gaseous flow field inside a wall-flow filter during its regeneration. Its validity and applicability is then assessed by conducting grid convergence studies and comparing it to a reference solution. A static fragmented particle layer is examined regarding the spatial distribution of the acting hydrodynamic forces and the impact of fragment clusters at different channel positions. Afterwards, some first transient simulations of fragment detachment are conducted in a low velocity regime and the impact of assorted layer properties is examined.

A second step is intended to provide closer insights into the behaviour of individual particle layer fragments during the filter regeneration. In this context, the temporal evolution of the hydrodynamic forces acting on a fragment's surface are examined in detail for different fragment densities and detachment positions. Relevant key quantities, such as the impact velocity at the channel's back wall and the stopping distance, are defined, determined and interpreted with respect to predictions regarding the resulting deposition patterns. At first, a physically sensible substrate permeability is determined by performing aligned experimental and numerical pressure drop studies. Afterwards, the transient behaviour of single particle layer fragments with different densities are examined in detail with respect to all acting forces. The fragment's pneumatic transport through the channel is then investigated for different starting positions, substrate permeabilities, inflow velocities and average densities of the introduced PM. Eventually, the general movement characteristics are assessed with respect to their qualitative accordance with experimental observations.

In a third step, the developed LBM approach is applied to an extended velocity range that covers as much as possible of the physically relevant domain, which includes averaged channel inflow velocities of up to $80\,\mathrm{m/s}$. After an adaption of the boundary conditions, three different scenarios are investigated, by considering the particle-free flow only, a single layer fragment attached to one of the substrate walls and a fragmented particle layer. At first, a comprehensive quantification of the stability and accuracy of both particle-free and particle-including flows, considering static, impermeable deposition-layer fragments,

is conducted. Afterwards, the local effects of a fragmented particle layer are investigated for different static situations along the channel. In order to derive predictions on the detachment likelihood of individual layer fragments and their mutual influence, the spatial distribution of hydrodynamic forces is evaluated additionally.

A final step is specifically dedicated to the investigation of the process of plug formation, by additionally considering the fragments' dynamic behaviour following the layer fragmentation. This includes the detachment and transport of the fragments along the channel, as well as the subsequent formation of a channel-plug. In order to accurately account for fragment contact during their transport, the model is extended by a previously developed discrete contact method. With the updated model, the influence of the fragmented layer topology, the fragment properties and the operating conditions is evaluated and relevant key quantities are determined.

The results attained with those four steps represent a comprehensive quantification of the impact of relevant influence factors on various aspects of the transient rearrangement process in wall-flow filters. In that way, the present work represents a significant contribution to the persisting research gaps in this field. It additionally, provides potential opportunities for modifications of the filtration process, which could lead to an optimization of engine performance, fuel consumption and service life of wall-flow filters.

Contents

1
Introduction

1.1 Emission Legislation

Internal combustion engines (ICEs) are widely used in passenger and commercial vehicles both on-road and off-road or as non-road mobile machinery (NRMM). During operation, they emit particulate matter (PM) as a result of complex combustion processes [28] throughout various fuel types. Those include diesel fuel, gasoline, liquefied petroleum gas (LPG) and compressed natural gas (CNG) [29]. Accompanied by ozone, nitrogen dioxide, sulfur dioxide and carbon monoxide, PM (including both $PM_{2.5}$ and PM_{10}) is classified as *classical air pollutant* by the World Health Organization (WHO) [30]. According to a systematic review commissioned by the WHO, there is clear evidence that PM is associated with increased mortality from all causes, cardiovascular disease, respiratory disease and lung cancer [31]. Those results are substantiated by numerous toxicological and epidemiological studies over the last decade [32–35].

In order to counteract air pollution by vehicle emissions, respective standards have been developed and implemented worldwide. Those include quantitative limits on the permissible amount of specific air pollutants that may be released from differing sources over predefined timeframes as well as testing procedures and driving cycles [36]. One of the three most prominent standards is the *Euro* emission standard according to EU Regulation No 715/2007 [37], adopted or adapted by other countries such as the UK [38], Russia [39] and Argentina [40]. The two prominent others are the *Tier* standard [41] of the

United States Environmental Protection Agency (EPA), adopted by Canada [42], and the *China* regulation [43] of the Chinese State Environmental Protection Administration (SEPA). India [44] and Australia [45], additionally, implemented some own regulations.

While quantitative limits, implementation details and degree of complexity vary significantly throughout the world, all standards have been subject to continuous tightening over the last century since the introduction of the first air quality standards by the Los Angeles Air Pollution Control District in 1955 [46]. In the exemplary case of the type approval of light vehicles according to the *Euro* emission standard, the allowed amount of PM from diesel exhaust was continuously decreased from 140 mg/km at *Euro 1* in 1992 to 4.5 mg/km at *Euro 5b* in 2011 [37]. The additional consideration of the particle number (PN) was then added with *Euro 5b* for Diesel engines and *Euro 6b* (2014) for direct injecting gasoline engines. After the implementation of a PN limit in real driving emissions (RDE) tests on the road with the *Euro 6d-Temp* in 2017, the mandated conformity was tightened with *Euro 6d* in 2020. It will eventually be tightened even further with the *Euro 7* in 2025 [47] in order to meet stricter air quality standards proposed by the European Commission in 2022 [48]. Both EPA and European standards additionally regulate emissions from NRMM [49] and an extension to other fuel types is suggested [29].

1.2 Wall-Flow Filters

Compliance with present and future emission legislation, respectively, mandates the usage of sophisticated exhaust after-treatment systems, which have been developed in mutual dependency with the emission standards development [46, 50]. Respective means range from in-cylinder technologies, such as homogeneous charge compression ignition (HCCI) [51], reactivity controlled compression ignition (RCCI) [52] and thermal barrier coating (TBC) [53] over alternative fuels [54, 55] and additives [56] to particle filters. Fulfillment of the increasingly stringent emission regulations can, however, not be achieved without the latter [57]. Due to their efficient separation of particles in a wide size range starting from a few nanometers [58] at comparably small pressure drops and their high thermal and mechanical resistance [59], wall-flow filters represent the centerpiece for the separation of PM in modern after-treatment systems of ICEs. Depending on the fuel type, they are often denoted respectively as diesel particulate filters (DPF) with diesel engines [58, 60] and gasoline particulate

1 cm
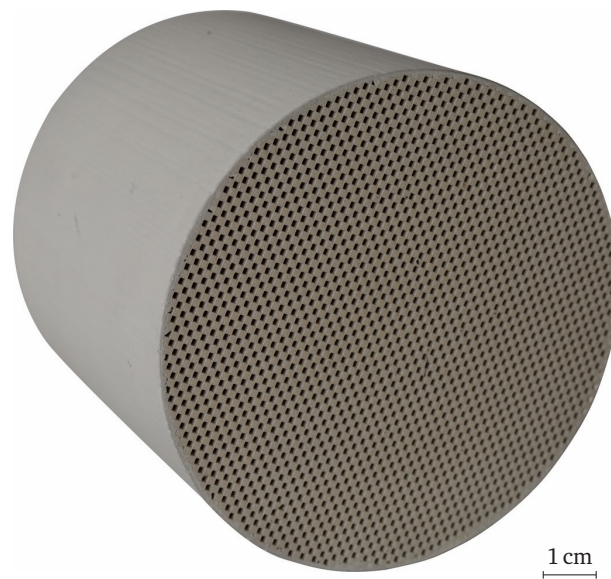
Figure 1.1: *Wall-flow filter with circular cross-section made from cordierite.*

filters (GPF) with spark-ignited gasoline engines [61, 62].

1.2.1 Characteristics and Working Principle

Commercial wall-flow filters are made of porous ceramics, such as cordierite [63, 64], silicon carbide [65, 66] or aluminum titanate [67, 68], and are produced by an extrusion process from ceramic suspensions with subsequent firing [69–71] in various shapes. While square and triangular shaped cross-sections enable those structures to be used as single elements in a split-type filter to reduce crack probability [65], monoliths with round and oval-shaped cross-sections are used directly. This way, a ceramic structure with hundreds of parallel channels is created. Afterwards, the alternate channel openings on one side are closed with an impermeable ceramic plug that is fired in place [66], which results in a checkerboard look [71]. The remaining channels are closed on the other side. An example of the resulting monolith with alternatively closed inflow and outflow channels is shown in Figure 1.1. Due to this specific design of such a wall-flow filter, a large filtration area can be achieved with respect to the actual filter cross-section as nearly the whole channel-length can be used. The entering gas is then filtered as it flows through the walls between adjacent channels [70]. For an exemplary pair of inflow and outflow channels, the process is outlined in
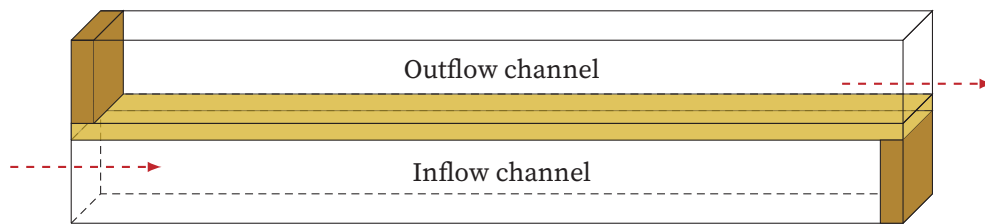
Figure 1.2: *Sketch of inflow/outflow channel pair. Dark yellow structures represent porous filter substrate, brown structures solid walls. Red arrows indicate inlet and outlet region.*

Figure 1.2.

1.2.2 Filtration Process

The exhaust gas enters a wall-flow filter through the open flow area comprised of all inlet channels, which accounts for less than half of the filter's cross-sectional area [65, 72, 73]. Inside the filter, it is guided along those channels with a continuously increasing fraction being forced to penetrate the separating porous walls instead. Here, the contained particles are separated with efficiencies of up to 99 % [74]. After the wall penetration, the filtered gas enters the neighbouring channels with a corresponding continuously increasing flux over the channel length and eventually exits the filter [75].

Engine generated PM consists of reactive soot and small amounts of ash, which mainly originates from inorganic lubricant oil additives and to a small extent from engine abrasion, fuel additives and other minor sources [58, 76]. Those solid exhaust components initially get trapped inside the porous walls of a clean filter, before starting to exclusively deposit on the walls' surfaces [73]. With continuing loading, this leads to the formation of a porous particle layer, which covers most of the filter surface and leads to a significant increase in flow resistance and a corresponding increase in the filter's pressure drop [77]. In order to retain the filtration capability, a wall-flow filter, therefore, has to be regenerated continuously or in reoccurring intervals [78, 79].

1.2.3 Regeneration

A passive regeneration strategy denotes a continuous NO_2 based soot reaction with temperatures around 200 °C to 500 °C, while an active one consists of reoccurring O_2 based soot oxidation intervals at temperatures around 550 °C [58].

(a) *Continuous layer*   **(b)** *Plug*
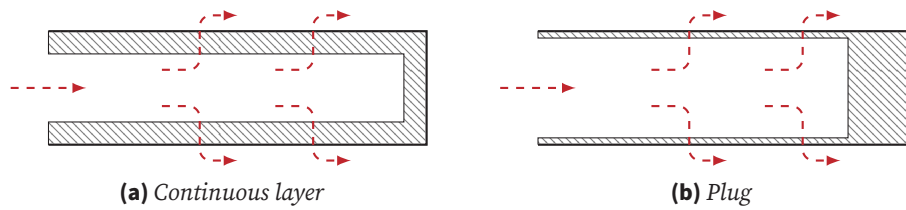
Figure 1.3: *Sketch of boundary deposition patterns in inflow channel. Red arrows indicate path of entering gas. Hatched region represents particle layer.*

Such a regeneration successfully removes nearly all soot constituents [59]. The non-combustible ash, however, remains in the filter and accumulates over the filter's operation time [80]. This leads to a gradually increasing ash load and ever-changing conditions, the continuously introduced PM is subjected to. Additionally, small ash precursors embedded in a surrounding soot matrix can reposition slightly during soot removal [77]. Cohesive forces can then lead to their accumulation over the long term, which enables the formation of larger ash agglomerates. As a result, the particle layer becomes increasingly inhomogeneous, which at some point can cause it to break up into individual layer fragments during the regeneration process [9, 81].

1.2.4 Rearrangement and Deposition Layer Formation

The presence of single particle layer fragments potentially enables rearrangement events inside an inflow channel. Once the hydrodynamic surface force on such a fragment is large enough to allow adhesive forces to be overcome, the fragment can detach from the filter surface and be re-suspended into the gaseous flow. During ongoing regeneration, those forces may change, as, due to the reduction of its soot content, a fragment experiences continuous shrinking and a decrease of the contact area shared with the porous wall [9, 81].

Those dynamics eventually lead to the formation of specific deposition patterns inside the channels, which can be found in wall-flow filters that have been opened and examined after long-term operation. While those patterns have been reported in many different forms [50, 60, 82–84], the two boundary cases shown in Figure 1.3 have been identified by most authors: A *continuous layer* is characterized by an equal height around the whole channel confinement. It features significantly increased axial fluid velocities with respect to the average velocity entering the channel due to the reduced cross-section available for the flow. A *plug* formation, in turn, is associated with a thinner particle layer

covering the substrate's surface and a great reduction in the accessible channel length, effectively reducing the available filtration area. The exact nature of the resulting pattern has a significant impact on the filter's separation efficiency and its overall pressure drop. This, in turn, determines the necessary regeneration frequency, the engine operational performance, the fuel consumption and the chance of filter failure [58]. Scientific research regarding the separation of PM in wall-flow filters with specific focus on deposition pattern formation, therefore, allows for environmental and economical advances as well as an improvement in sustainability.

1.3 Research Gaps and Open Questions

The broad field of PM separation with wall-flow filters has been subject of a myriad of scientific works over the past decades. Fortunately, those works include comprehensive literature reviews with a focus on different specific aspects. A detailed examination of contributions relevant for the present work until 2022 has been conducted in Hafen et al. [1] and can be found in Chapter 2. An update at the time of writing this thesis is provided by the following three works published in 2023: A review focussing on filter regeneration mechanism of modern internal combustion engines and methods of reducing PM emissions can be found in Zhang et al. [85]. Luo et al. [86] compiled a review of works focussing on the effect of regeneration methods and ash deposition on DPF performance. With a specific focus on computational fluid dynamics (CFD), Zhang et al. [87] provide a review of numerical simulation works. In all three review endeavours, however, no dedicated work on the topic of deposition pattern formation and rearrangement events is mentioned, rendering the compiled state-of-the-art in Hafen et al. [1] the most recent one in this field.

Based on this, it can confidently be statet that the formation process of specific deposition patterns is still not fully understood, despite its well-known significance on the filtration process. Its sensitivity to relevant influence factors related to the filter geometry, the operating conditions and the composition of fuel and lube oil has not been analysed in detail yet and has, at most, been subject to speculations. Additionally, formulated tendencies, attributing the formation of specific patterns to e. g. the regeneration strategy only [82], a set of required mechanisms [50, 83] or the layer's soot to ash ratio [84] partially contradict each other. A fundamental question, eventually, remains:

Which influence factors do affect the deposition pattern formation to what extent and how can those be influenced in such a way that environmental and economical improvements can be achieved?

The respective research gap spans over the following influence factors, which represent operating conditions, the filter geometry and material properties as well as some intermediate conditions:

Operating conditions   As one of the most important quantities of the operating conditions [75, 88, 89], the *average inflow velocity* potentially affects all processes inside a channel. Next to its impact on the overall flow conditions, it is responsible for the nature and magnitude of hydrodynamic forces and is therefore of profound interest in all studies. Additionally, it directly reflects the engine's exhaust flow rate [90] and, thus, represents a particularly tangible process quantity.

Filter geometry   While the pressure drop of a duct or pipe with impenetrable walls linearly depends on the *channel length* [91], the situation is very different for a wall-flow filter channel. As the momentum loss, responsible for the pressure drop, primarily results from the penetration of the porous walls, rather than the wall friction [90], any change in the wall penetrating velocity, has a large impact. For a given flow rate and channel cross-section, this velocity, directly depends on the available filter surface area and eventually on the channel length. The cross-section, in turn, depends on the *channel-diameter*, which affects the filter's overall ash storage capability [92].

Material properties   If one is not particularly interested in the investigation of microscopic phenomena inside the porous substrate itself [93, 94], the *wall permeability* is the most relevant non-geometric filter quantity of a clean filter channel [75, 90]. When considering a significant PM coverage of the filter walls, the *layer fragment permeability* becomes relevant additionally, as the flow is penetrating those fragments as well. After the detachment of individual fragments, their pneumatic transport along the channel is affected by the continuously decreasing axial gas velocity. The fragment's inertia, directly depending on the *PM density* [95], respectively defines their capability to following those varying flow conditions. Also connected to the fragment transport is their behaviour during fragment–wall and fragment–fragment contact. This behaviour is defined by

their *contact properties* [96]. The initial *adhesive forces* that keep individual fragments attached to the filter surface are a result of complex physical phenomena on the microscale [97]. In order to reduce the complexity, in this work, those are simply considered a joined property characterizing a specific pair of PM and substrate material.

Intermediate conditions   As the full process, covering layer fragmentation, fragment detachment, fragment transport and deposition pattern formation, is characterized by many interdependencies, some assorted intermediate influence factors can provide additional insights. A few of those factors are represented by the particle layer topology after fragmentation due to the soot oxidization [81]. It can be described by the remaining *layer height*, the *fragment dimensions* and the orientation and amount of individual fragments in form of the *layer structure*. For the isolated investigation of a single fragment's behaviour, its relative *detachment position* can be of specific interest [9] as well.

The persisting absence of clear relations between those factors and the deposition pattern formation can be attributed to some derived research gaps: Local gas velocities severely affect acting forces, individual fragment dynamics and local pressure drop contributions in the porous walls. Nonetheless, the development of three-dimensional locally resolved velocity and pressure profiles have not been investigated during ongoing regeneration. As a result, no information can be found on the temporal evolution of hydrodynamic forces that act on individual layer fragments. While the transport of such fragments has been subject of only a few studies [81], no general quantities have been formulated, which would allow a standardized comparison across different studies and solution approaches, such as experiments and simulations. The transient formation process of a channel plug as an accumulation of individual layer fragments has not been studied at all. Eventually, across all studies reviewed in Hafen et al. [1], it is noticeable that only a few approaches take advances of previously developed models and methods into account. Most studies, however, rather rely on setting everything up from scratch. An accessible way of preserving developed methodology apart from plain publications is therefore considered a final research gap.

1.4 Research Aims Addressed in This Thesis

In order to answer the questions formulated above in consideration of the laid out influence factors, a *fundamental investigation of particle-layer rearrangement events in ceramic wall-flow filters* is conducted in the present work. In this light, the work's main aim is formulated as follows:

> *The primary goal of this work is the determination of the sensitivity and the quantification of the impact of engineering-related influence factors on the transient rearrangement process in wall-flow filters.*

This rearrangement process includes the break-up and fragmentation of a coherent particle layer, the dynamic behaviour of separated layer fragments and the potential formation of a channel-plug. The latter represents a porous, unordered packing, resulting from the accumulation of particle layer fragments, which can occupy a significant amount of the available channel volume [83, 84, 98, 99]. In this context, some sub-goals can be formulated, which need to be realized as a requirement for achieving the primary goal:

1. Obtainment of a wall-flow model that allows the envisaged investigations

2. Quantification of the model's validity and applicability

3. Determination of the time dependent development of the three-dimensional flow field during the filter's regeneration process

4. Determination of the temporal evolution of the hydrodynamic forces acting on the fragments' surfaces

5. Identification of universal key quantities that accurately depict the dynamic behaviour of single fragments

6. Forecast of detachment occurrence and the favoured detachment location of individual fragments and fragment clusters

7. Quantification of a channel plug's impact

8. Provision of qualitative but descriptive visualizations of both flow and fragments

9. Conservation of the developed methodology in a publicly available resource that enables full reproducibility of the obtained results

Each one of those is associated with one of the three contribution components *Modelling and Methodology*, *Validation and Assessment of Applicability* as well as *Application and Investigation*.

1.5 General Solution Approach

In order to achieve the formulated research aims and close the presented research gaps, investigations in a single representative wall-flow filter channel have to be conducted. This represents a challenge, as a single channel's embedding within a filter impedes any access without causing a modification of the flow conditions. The sample preparation itself represents another challenge, as precise machining of ceramic material is particularly delicate [100, 101]. While filter dimensions can extend over several centimetres, the width of a single channel is typically less than 2 mm. The size of deposited particles and their agglomerates ranges from less than 1 μm over two orders of magnitude up to 500 μm. The resulting large scale disparity is challenging as well.

The non-invasive nature of a CFD approach makes it prone for the investigation of the processes of interest in a single wall-flow channel. It additionally enables simply extendable parametrization and full reproducibility, reducing the number of individual studies necessary to ensure a representative database. The difficulty of providing a sufficient PM load necessary for representative investigations of the rearrangement process, which has led to its own field of study on accelerated ash loading methods [61, 73], can be circumvented with a CFD approach as well. In order to achieve the presented goals, however, such a solution approach needs to meet the following basic requirements:

1. Allow the interdependent consideration of confined fluid flow, flow through porous media and the dynamics of particle layer fragments

2. Enable both multi-fragment and isolated single-fragment evaluations

3. Be capable of dealing with a large parameter window

4. Ensure an appropriate consideration of multiple length scales

5. Provide geometrical flexibility (e. g. for the comparison with experiments and the adaption of the computational load)

6. Be integrated into a publicly available open-source software, which provides the right to study, modify, and distribute the software free of charge to anyone for any purpose [102]

While the geometrical flexibility might pose a difficult requirement for experimental studies, the first five requirements are not CFD specific and should, for the most part, be valid for experimental approaches equally.

Based on those requirements and the challenges described above, the lattice Boltzmann method (LBM) represents a favourable choice as it efficiently handles large computational domains with complex geometries on modern multi-core processor architectures [103–105]. Its mesoscopic character [106] additionally enables the efficient consideration of broad scale diversities. The recent rise of general purpose computation on graphics processing unit (GPGPU) [107] represents another advantage of LBM over other CFD approaches, as it provides excellent vectorization and parallelization capabilities due to the algorithm's decomposition (cf. Section 2.2.1) into an exclusively local collision step and a separate streaming step [106].

The investigation of the rearrangement of individual particle layer fragments requires the accurate evaluation of hydrodynamic forces acting on the surfaces of non-spherically shaped particles. This can only be achieved by means of surface-resolved particle simulations [103] for which the LBM is especially suitable due to its generally equidistant mesh character. With it, computationally expensive interpolations necessary in alternative approaches, such as the immersed boundary method (IBM) [106], can be circumvented effectively. The present work, therefore, approaches a *fundamental investigation of particle-layer rearrangement events in ceramic wall-flow filters* by means of *resolved particle simulations with lattice Boltzmann methods*. As the open source software OPENLB [5, 27] provides a versatile and easily extendable implementation of the LBM while meeting the final requirement, it is used in the present work. In order to ensure full reproducibility of the obtained results, all application cases used in this work can be found in Section A of the appendix.

1.6 Thesis Outline and Concrete Steps

The development and application of an appropriate simulation model have been considered in four consecutive solution steps, while adhering to the requirements listed in Section 1.5. Those steps are dedicated by four separate works [1–4], which are presented in a particular chapter each. Every step covers the three distinct contribution components *Modelling and Methodology*, *Validation and Assessment of Applicability* as well as *Application and Investigation*. With increased confidence in the model's validity and applicability in the more

advanced steps, the contribution's focus is shifted towards applying the developed model and conducting the actual investigations. The overview of the four solution steps is shown in Figure 1.4. Relevant topics covered in the respective

| **Step 1**
Model development | **Step 2**
Single fragment investigation | **Step 3**
Model velocity scaling | **Step 4**
Plug formation investigation |

Small velocities (up to $2.0\,\mathrm{m/s}$) ←——————→ Elevated velocities (up to $60.0\,\mathrm{m/s}$) ——————→

Chapter 2 based on Hafen et al. [1]	**Chapter 3** based on Hafen et al. [2]	**Chapter 4** based on Hafen et al. [3]	**Chapter 5** based on Hafen et al. [4]
Channel Model	Transport parameters	Stabilization	Fragment contact
Linear porosity error	Physical permeability	Stability domain	Average plug density
Grid convergence	Fragment movement	Grid convergence	Transient effects
Fluid field reference	Single surface forces	Single surface forces	Layer topology
Layer characteristics	Detachment mechanics	3D force distribution	Material properties
Fragment detachment	Transport behaviour	Detachment likelyhood	Operating conditions

▫ Modelling and Methodology   ▫ Validation and Assessment   ▫ Application and Investigation

Figure 1.4: *Overview of consecutive solution steps. Indication of small and elevated velocity consideration. Covered topics shaded according to contribution component.*

contribution components are laid out as well. Those are elaborated on in the following:

Step 1 – Model development   In a first step, an LBM approach is developed, which is capable of capturing the time dependent development of the gaseous flow field inside a wall-flow filter during its regeneration. This includes the definition of an application setup with appropriate operating and boundary conditions. For this, a channel model is developed which represents a single filter channel embedded into fractions of neighbouring inflow and outflow channels (termed *four-channel* setup). The developed model is presented in Chapter 2 based on Hafen et al. [1]. Its validity and applicability is then assessed, considering various aspects: At first, the choice of using a simplified porous media model for the flow through the porous walls is examined. This is done

by evaluating the error from neglecting the non-linear Forchheimer pressure drop contribution [108] in the considered parameter range (cf. Section 2.3.1). Afterwards, the gas flow in the single channel is retrieved and the model's order of accuracy in the particle-free case is examined by conducting grid convergence studies (cf. Section 2.3.2). Additionally, the flow field is compared to a reference solution retrieved by a semi-analytic 1D model according to Konstandopoulos and Johnson [75] (cf. Section 2.3.3). A static fragmented layer consisting of individual permeable fragments is then added on each of the four surrounding permeable channel walls. The layer is examined regarding the spatial distribution of the acting hydrodynamic forces and the impact of fragment clusters at different channel positions (cf. Section 2.3.4).

After ensuring the model's capability of consistently capturing the general characteristics of the particle-free flow, the model is extended by including a surface resolved particle approach for the simulation of the detachment and movement of individual particle layer fragments. With this, some first transient simulations of fragment detachment are conducted in a low velocity regime and the impact of assorted layer properties is examined.

Step 2 – Single fragment investigation In a second step, the behaviour of individual particle layer fragments during the filter regeneration is investigated in detail, with a focus on their detachment as well as their acceleration and deceleration during transport. This includes a detailed examination of the temporal evolution of the hydrodynamic forces acting on a fragment's surface, the fragment's position and its velocity for different fragment densities and detachment positions. In this context, relevant key quantities such as the wall impact velocity and the stopping distance are determined and interpreted with respect to predictions regarding the resulting deposition patterns. Those are presented in Chapter 3, which is based on Hafen et al. [2].

In this context, a *two-channel setup* is introduced as a second channel model. While the four-channel setup, developed in the previous step, is intended to resemble a single channel with a realistic embedding into the surrounding ones, the two-channel setup is designed to represent the experimental setup used by Thieringer et al. [9, 109]. This setup includes all simplifications necessary to account for the real-world design limitations, such as optical access, resulting from the experimental measurement procedure. While both setups feature an inlet channel with a square cross-section, they differ in their embedding in the surrounding channels, the respective boundary conditions and slightly in their

dimensions.

Prior to considering the actual movement of particle layer fragments, the particle-free flow is examined in detail in both setups: At first, the two-channel setup is used to retrieve a physically sensible substrate permeability by performing aligned experimental and numerical pressure drop studies (cf. Section 3.4.1). Afterwards, the influence of permeability and channel length on the pressure and velocity distribution in the inflow channel of the four-channel setup is analysed (cf. Section 3.4.2). On this basis, the transient behaviour of single particle layer fragments with different densities is examined: First, the transient particle movement of a single representative simulation run is analysed and relevant key parameters, utilizable for a standardized comparison of different simulation and experiment runs, are derived (cf. Section 3.5.1). Those include the peak velocity, the impact velocity and the stopping distance according to Hinds [110]. In order to assess the likelihood of a detachment from the channel surface, the hydrodynamic forces in tangential and normal flow direction are analysed (cf. Section 3.5.2). The detachment from the substrate's surface is then examined in detail with respect to all acting forces. Eventually, the fragment's pneumatic transport through the channel is investigated for different starting positions, substrate permeabilities, inflow velocities and PM densities (cf. Section 3.5.3). The experimental observations from Thieringer et al. [9] are then used to assess the qualitative accordance with the general movement characteristics (cf. Section 3.5.4).

Step 3 – Model velocity scaling   While the previous steps prove the applicability of the simulation approach in the low velocity regime, the considered inflow velocities of up to $\bar{u}_{in} = 2.0\,\text{m/s}$ only cover a small portion of the real world ranges that include velocities up to $\bar{u}_{in} = 80\,\text{m/s}$ [83]. The focus of the model scaling in Chapter 4, based on Hafen et al. [3], is therefore to apply the developed LBM approach to an extended velocity range that covers as much as possible of the physically relevant domain.

In order to provide the necessary stabilization in the upper velocity range, the boundary conditions are adapted initially. Afterwards, three different scenarios are investigated, by considering the particle-free flow only, a single layer fragment attached to one of the substrate walls and a fragmented particle layer. With those, a comprehensive quantification of the stability and accuracy of both particle-free and particle-including flows, considering static, impermeable deposition-layer fragments, is conducted. Additionally, the hydrodynamic

surface forces are determined and the local detachment likelihood of individual layer fragments is deduced for different parameter setups. First, the particle-free flow in a clean channel is examined in order to define the parameter domain that represents a necessary stability criterion for the wall-flow model under study (cf. Section 4.4.1). In a second scenario, featuring a single layer fragment, the parameter domain is re-evaluated and the individual components of the hydrodynamic force acting on the fragment's surface are examined separately (cf. Section 4.4.2). In the third scenario, assuming the fragmented particle layer, its local effects on the fluid field and the acting forces are investigated for different static situations along the channel (cf. Section 4.4.3). The spatial distribution of hydrodynamic forces is evaluated additionally in order to derive predictions on the detachment likelihood of individual layer fragments and their mutual influence, similarly to the low-velocity counterpart in Chapter 2.

Step 4 – Plug formation investigation   The last step additionally considers the fragments' dynamic behaviour following the layer fragmentation. This step is presented in Chapter 5, which is based on Hafen et al. [4]. It includes the investigation of the detachment and transport of the fragments along the channel, as well as the subsequent formation of a channel-plug. This can only be achieved by considering the interaction of moving fragments with each other, of moving fragments with a static fragment accumulation and of fragments with the substrate walls. The resolved particle methodology, developed and utilized in the previous steps, is therefore extended by a thoroughly validated discrete method to treat particle–particle and particle–wall interactions [96] and is applied to dynamic rearrangement events in wall-flow filters.

With this, the influence of the fragmented layer topology, the PM properties and the operating conditions on the described process is evaluated and relevant key quantities are determined. The latter include the final pressure drop, as well as the size and the mean density of resulting channel-plugs. The sensitivities of those factors are then evaluated and their impact on the rearrangement process is quantified. Contrary to the previous chapters, in which the simulations' stability, accuracy and validity were accessed with convergence studies, literature findings and experimental results, this chapter rather focusses on the derivation of quantitative statements (cf. Figure 1.4). Nonetheless, the average plug density is compared to literature findings.

At first, the complete transient rearrangement process is evaluated in detail, considering a constant base configuration of the relevant influence factors

(cf. Section 5.4.1). Afterwards, the impact of influence factors that lead to a change in the fragmented layer topology on both the initial flow condition and the rearrangement process are laid out (cf. Section 5.4.2). Eventually, material properties and operating condition that do not alter the initial fragmented layer topology are investigated (cf. Section 5.4.3).

With those four steps, a large variety of different studies over a wide range of inflow velocities are conducted, with each one contributing to the achievement of the primary goal and its sub-goals formulated above (cf. Section 1.4). In the following four chapters (Chapters 2, 3, 4 and 5), the individual steps are described in detail, while revising relevant motivational aspects, describing mathematical modelling as well as numerical methods and elaborating on the design of the conducted studies. At the end of each chapter, intermediate results are presented in form of a dedicated conclusion. Eventually, in Chapter 6 the cumulated outcome is summarized and concluded with respect to the formulated research gaps (cf. Section 1.3).

2

Development of a Channel Model

2.1 Introduction

2.1.1 Motivation

Wall-flow filters are widely applied for the removal of particulate matter (PM) from the exhaust emitted from internal combustion engines for more than a decade [58]. The emitted PM is made up of individual particles with a size in the range of 10^{-9} m to 10^{-7} m [58], which pose potential health risks [32, 35] and therefore have been regulated by law across the world. Despite geographical and national differences, those emission laws have been tightened continuously and are expected to be further globally intensified. This includes limits for the emitted PM mass and, following the European Union, the solid particle number (PN) emission. In order to still be able to meet those regulations, wall-flow filters are used as diesel particulate filters (DPF) in the aftertreatment system of diesel engines in on-road and off-road vehicles and appliances or as gasoline particulate filters (GPF) in spark-ignited gasoline engines [61]. Due to

the described developments, the demand of wall-flow filters is expected to grow [58].

A wall-flow filter retains up to 99 % of the introduced solid PM, which consists of reactive soot and small amounts of ash. Next to engine abrasion, fuel additives and other minor sources, the ash mainly originates from inorganic lubricant oil additives. During its operation, a filter continuously fills up forming porous PM layers on the surface of the filter channels. This results in an increase of flow resistance, which leads to the necessity of removing the soot deposits by passive or active regeneration. While the prior denotes a catalytic soot reaction with temperatures around 200 °C to 500 °C, active regeneration consists of a soot oxidation at temperatures around 550 °C [58]. As non-combustible ash is not removed during regeneration, it remains in the filter and accumulates over the long-term operation while accompanying the periodically introduced soot in the PM layer formation. Due to cohesive forces, small ash precursors are drawn together and can form larger agglomerates, which introduce local inhomogeneities in the deposition layer composition. During soot oxidation, those can eventually cause the layer to break up into individual fragments, which shrink inward towards their respective centre [81]. Rearrangement events can then be caused by the detachment of such fragments from the filter surface during the filter's regeneration.

With increasing vehicle mileage, this results in specific non-regeneratable ash deposition patterns that significantly impact the filter's separation efficiency and its pressure drop. This can eventually lead to higher regeneration frequencies, reduced engine operational performance, higher fuel consumption and an increased chance of filter failure [58]. The formation of a specific ash deposition pattern, however, depends on numerous influencing factors related to the filter geometry, the operating conditions and the composition of fuel and lube oil. Thus, a thorough analysis of the individual influence factors and detailed insights into the rearrangement process itself allow for both economical and environmental improvements.

Due to its adaptability, its versatile parametrization, and its inherent reproducibility a computational fluid dynamics (CFD) approach for surface resolved particles represents a beneficial solution to the investigation of the fluid flow and the movement of complex submerged structures. The present work is therefore intended to both provide a solid foundation for the simulation of the fluid flow inside a single wall-flow filter channel and present an approach to the simulation of the detachment and movement of individual porous PM layer fragments.

2.1.2 State of the Art

From the large number of scientific works related to the filtration process in wall-flow filters, a selection of works focussing on four distinct fields is presented in the following. The first one covers relevant findings on the deposition pattern formation and the second one describes general numeric approaches to wall-flow filter modelling. As in the present work, the lattice Boltzmann method (LBM) is used, the third and fourth field discuss respective research regarding the flow through porous media and the simulation of surface resolved particles with the LBM. The prior is used to recover the flow through the porous filter walls. The latter is necessary to describe the behaviour of the detachment and movement of PM layer fragments.

An initial classification of two borderline cases of deposition patterns was done by Ishizawa et al. [82] by identifying an ash accumulation in the rear channel section denoted as end-channel plugs and a uniform accumulation from inlet to outlet denoted as wall layer. They directly connected an active regeneration strategy to end-channel plugs and the passive one to a thick wall layer with minor plugs. Dittler [50, 83], however, described the formation of end-channel plugs independent of the regeneration conditions and described layer breakup, re-entrainment and axial transport of ash as main factors leading to specific deposition patterns. A third distinct borderline type was added, when Wang and Kamp [84] described the effects of mid-channel ash plugs. Later, Kamp et al. [60] investigated their formation with X-ray imaging and concluded that a specific ratio of soot to ash during filter regeneration might be the root cause of the mid-channel phenomenon. However, the authors also stated that it is most likely connected to a combination of several reasons. A detailed review of works directly related to ash deposition patterns until 2012 can be found in the work of Dittler [83]. For a more recent review, the reader is referred to the comprehensive summary of experimental works focussing on filter ash by Wang et al. [58].

A first numerical approach to wall-flow filter modelling was done by Bissett [78], who described a set of non-linear partial differential equations based on the conservation of mass, momentum and energy. Based on these, Konstandopoulos and Johnson [75] developed a 1D perimeter averaged model, which describes the velocity and pressure profiles in the axial direction of a monolith cell and the pressure drop across its porous walls. A 2D computational model to describe the flow in a wall-flow trap for both steady state loading and the transient behaviour of the flow and filtration process was later described by Opris and Johnson

[111]. Konstandopoulos et al. [112], however, found that it overestimates the total pressure drop. They then compared the previously developed 1D model both with simple 3D CFD simulations and experimental data and reported them to agree well with each other. Later, Konstandopoulos [88] extended the 1D model by accounting for additional pressure drop contributions caused by inlet and outlet friction as well as contraction and expansion losses. Due to its extensive study over many years and the validation with experimental data, this 1D perimeter averaged model is used in the present work to evaluate the plausibility of the simulation results. A detailed review of wall-flow simulation approaches covering different dimensions, single and multi channel models as well a pore scale simulations in the filter walls can be found in the work of Yang et al. [113].

When interested in describing the flow field in a wall-flow filter in detail, the porous channel walls have to inevitably be considered. With sufficient accuracy for many applications, the fluid flow through a permeable porous medium can be described by Darcy's law. Brinkman [114] then modified Darcy's equation with the goal of obtaining consistent boundary conditions. Based on this modification, Spaid and Phelan [115] presented a first LBM description of fluid flow in a heterogeneous porous medium. Here, the method of Shan and Chen [116] was used to introduce a dissipative forcing. Although it was found to be a simple and computationally efficient method to numerically approximate fluid flow described by the Brinkman equation, the model was criticized by Martys [117] for employing a forcing model, which was previously shown to produce considerable errors in the pressure tensor [118]. Martys [117] improved the method accordingly by introducing a linear body force term. Some further limitations of the Spaid-Phelan (SP) model were pointed out by Guo and Zhao [108]. In comparison to the Navier-Stokes equations (NSE) the Brinkman equation does not include a non-linear inertial term, which renders it suitable for low speed flows only. The absence of a convective term in the SP model was criticized as well, as the development of the flow field can not accurately be described. Guo et Zhao therefore generalized the model with different modifications including the consideration of the medium's porosity as the actual void volume fraction as well as external body forces and exchanging the forcing method of Shan et Chen by their own [119].

The accurate evaluation of hydrodynamic forces acting on individual submerged and non-spherically shaped particles can only be achieved by surface resolved particle simulations [103]. While the assumption of spherical shapes may lead to acceptable results for sub-micron sized particles, the PM layer

fragments under consideration range up to multiple microns leading to the necessity of considering their surfaces. Due to its generally equidistant mesh character, the LBM is especially suitable for such simulations and has proven to handle those efficiently [103].

For surface resolved particle simulations in the LBM, different fluid-solid interface approaches can be found in literature. Those can be classified into three main groups being partially saturated methods (PSM), moving boundary methods (MBM) and immersed boundary methods (IBM) as well as numerous sub-variants of those [103]. As both the previously described porosity models and PSM are based on a local partial cell saturation, the choice of PSM provides the possibility of sharing many modelling and implementation aspects. For that reason, MBM and IBM are not considered in the present work, however, a thorough comparison of PSM and MBM focussing on Galilean invariance can be found in a recent study of Haussmann et al. [6].

The initial version of PSM was described by Noble and Torczynski [120], in which a local particle volume fraction approximation is defined at each grid node. Independent of this original formulation and its following advances, Krause et al. [121] proposed the homogenized lattice Boltzmann method (HLBM) as an alternative fluid-solid interface approach by extending the SP model by a moving porous medium approach in two dimensions. Later on, it was extended to three dimensions [95] applying it to the simulation of limestone particles based on geometry data generated from computer tomography scans. Due to the similar basic mechanism, Haussmann et al. [6] eventually generalized the original definition of PSM to all fluid-solid interface approaches in the LBM, which consider a partial cell saturation including the HLBM. Its dynamic porous media character, however, makes the HLBM to the best knowledge of the authors the only method available which is suitable for the actual simulation of moving porous PM layer fragments with the LBM. The literature overview additionally reveals that in this context no work can be found which both provides a consistent calculation of the fluid field by accounting for the porous walls, while employing transient resolved particle simulations at the same time.

The goal of this work is to present an LBM approach for the simulation of PM structure detachment which is capable of capturing the time dependent development of the flow field during the filter's regeneration process. The work further aims at presenting a numerical model of a single wall-flow filter channel and demonstrating its validity by conducting grid convergence studies and a comparison with a reference solution for the particle-free flow. In this context, a final objective is to present a holistic LBM approach, which is capable of both

simulating the movement of resolved particles and the flow through porous media.

In the following, the numerical methods and modelling approaches are presented in Section 2.2. Their application to a wall-flow filter and studies regarding its validity are then described and evaluated in Section 2.3. In Section 2.4, the respective results are summarized and further studies planned in following works are laid out.

2.2 Mathematical Modelling and Numerical Methods

The present section is intended to provide the theoretical basis for the mathematical modelling and the utilized numerical methods. This includes a description of the LBM (cf. Section 2.2.1), an approach to porous media modelling (cf. Section 2.2.2) and the extension to surface resolved moving porous media with the HLBM (cf. Section 2.2.3). The section concludes with a description of the quantification of errors and convergence (cf. Section 2.2.4) used in this work.

2.2.1 Lattice Boltzmann Method

In order to simulate the dynamic behaviour of PM structure detachment from the surface of wall-flow filter channels, both fluid flow and particle movement have to be considered. In this work the macroscopic fluid flow is simulated using the LBM as a mesoscopic approach recovering the incompressible NSE. Discretizing the fluid domain by a voxel mesh with spacing δx that consists of sets of discrete velocity distribution functions f_i and corresponding lattice velocities c_i, the flow can be solved numerically with the LBM at every position x in time t. Depending on the physics of interest resulting in the necessity of providing derivatives with specific orders, those sets can be chosen accordingly. The present work utilizes a set of $q = 19$ discrete velocities c_i covering three dimensions and thus being denominated as *D3Q19* descriptor set (Figure 2.1). The force free lattice Boltzmann equation (LBE) describes the evolution of the distribution functions f_i over discrete time steps δt due to collisions on a microscopic scale modelled with a mesoscopic collision operator Ω_i. Assuming $\delta x = \delta t = 1$ at lattice scale, the LBE reads

$$f_i(x + c_i, t + 1) = f_i(x, t) + \Omega_i(x, t). \tag{2.1}$$

The simplest way to model the collision for Navier-Stokes simulations is to use the Bhatnagar-Gross-Krook (BGK) collision operator [122] assuming an isotropic
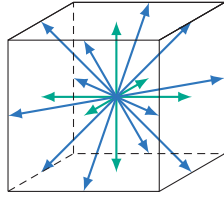
$$c_i = \begin{cases} (0,0,0) & \text{for } i = 0 \\ (\pm 1, 0, 0), (0, \pm 1, 0), (0, 0, \pm 1) & \text{for } i = 1, \dots, 6 \\ (\pm 1, \pm 1, 0), (\pm 1, 0, \pm 1), (0, \pm 1, \pm 1) & \text{for } i = 7, \dots, 19 \end{cases}$$

Figure 2.1: *D3Q19 descriptor set with q discrete velocities c_i.*

linear relaxation of the individual distribution functions towards their equilibria $f_i^{(eq)}$ with the relaxation time τ

$$\Omega_i(\boldsymbol{x}, t) = -\frac{1}{\tau} \left(f_i(\boldsymbol{x}, t) - f_i^{(eq)}(\boldsymbol{x}, t) \right). \tag{2.2}$$

Derived from the continuous Boltzmann equation [123], the equilibrium distribution function can be described as

$$f_i^{(eq)}(\boldsymbol{u}, \rho) = w_i \rho \left[1 + \left(\frac{\boldsymbol{c}_i \cdot \boldsymbol{u}}{c_s^2} + \frac{(\boldsymbol{c}_i \cdot \boldsymbol{u})^2}{2c_s^4} + \frac{\boldsymbol{u}^2}{2c_s^2} \right) \right], \tag{2.3}$$

with ρ and $\boldsymbol{u}$ being the macroscopic density and velocity at lattice scale, w_i the lattice weights accompanying the discrete velocities $\boldsymbol{c}_i$ and the lattice speed of sound c_s, which for the *D3Q19* velocity set has a value of $c_s = \frac{1}{\sqrt{3}}$ [106]. The relation to macroscopic fluid flow quantities such as the kinematic viscosity ν, the density ρ and velocity $\boldsymbol{u}$ can be established by

$$\nu = c_s^2 \left(\tau - \frac{1}{2} \right) \tag{2.4}$$

in the incompressible limit and moments of the discrete distribution functions. The zeroth and first order moments yield the macroscopic density and velocity according to

$$\rho = \sum_{i=0}^{q-1} f_i \qquad \text{and} \qquad \rho \boldsymbol{u} = \sum_{i=0}^{q-1} \boldsymbol{c}_i f_i. \tag{2.5}$$

Assuming the applicability of the isothermal equation of state, the density ρ can be related to the lattice pressure p via

$$p = c_s^2 \rho. \tag{2.6}$$

A key property of the LBE in (2.1) is the fact that it can be decomposed into a purely local collision step and a subsequent streaming step making it suitable for highly parallel computations [106]. Therefore, the LBM within the framework of the open source software OpenLB [5] is used throughout this work.

2.2.2 Porous Media Modelling

As this work does not aim at investigating phenomena inside the filter walls itself, their inner structure is not resolved. Instead, the momentum loss experienced by a fluid passing through a porous medium with a unidirectional velocity u is modelled according to Darcy's law [114]

$$\nabla p = -\frac{\nu}{K}\rho u \tag{2.7}$$

by imposing an additional body force. Within the SP model, this linear force contribution due to the reduced medium's permeability K is assumed as

$$F(\boldsymbol{x},t) = -\frac{\nu}{K}\rho\boldsymbol{u}(\boldsymbol{x},t). \tag{2.8}$$

When interested in accounting for non-linear pressure drop contributions as well, the body force description in (2.8) can be extended by including the Forchheimer term according to Guo and Zhao [108]

$$F(\boldsymbol{x},t) = -\frac{\varepsilon\,\nu}{K}\rho\boldsymbol{u}(\boldsymbol{x},t) - \frac{\varepsilon}{\sqrt{K}}\frac{1.75}{\sqrt{150\varepsilon^3}}|\boldsymbol{u}(\boldsymbol{x},t)|\boldsymbol{u}(\boldsymbol{x},t). \tag{2.9}$$

By introducing the actual medium's porosity ε, (2.9) represents the force contributions according to Ergun's equation [124]. With the geometric and operational parameters used in this work, however, the error resulting from neglecting the non-linear inertial term is shown to be smaller than 0.5% (cf. Section 2.3). Therefore, due to its simplicity and the comparably small computational effort, the SP model is adopted here. As this model is based on the forcing method by Shan and Chen [116], the imposed force F is included by simply scaling the macroscopic fluid velocity $\boldsymbol{u}$ resulting in an effective velocity

$$\boldsymbol{u}^{eff}(\boldsymbol{x},t) = \boldsymbol{u}(\boldsymbol{x},t) + \frac{\tau}{\rho}F(\boldsymbol{x},t) = \frac{1}{\rho}\sum_{i=0}^{q-1}c_i f_i(\boldsymbol{x},t) + \frac{\tau}{\rho}F(\boldsymbol{x},t), \tag{2.10}$$

which then enters the equilibrium distribution function. Inserting (2.8), results in a simple velocity scaling at porous sites

$$\boldsymbol{u}^{eff}(\boldsymbol{x},t) = \boldsymbol{u}(\boldsymbol{x},t)\left(1 - \tau\frac{\nu}{K}\right). \tag{2.11}$$

With the introduction of a *confined permeability* d, (2.11) can be expressed as

$$\boldsymbol{u}^{eff}(\boldsymbol{x},t) = d\boldsymbol{u}(\boldsymbol{x},t) \qquad \text{with} \qquad d = 1 - \tau\frac{\nu}{K}. \tag{2.12}$$

As this formulation in principle allows a sign change in the velocity scaling, which does not represent any physical behaviour, it features a minimum resolvable permeability K_{min} specific to the numerical setup. This results into the confined permeability being restricted to $d \in [0, 1]$ as

$$\lim_{K \to \infty} d(K) = 1, \tag{2.13}$$

$$d(K_{min}) = 0 \quad \text{with} \quad K_{min} = \tau \nu. \tag{2.14}$$

2.2.3 Surface Resolved Particle Simulations

PSM [120] can be used to account for the effect of submerged solid structures by using a local weighting factor $B(\mathbf{x}, t) \in [0, 1]$ differentiating between liquid and solid contributions at a single node. This weighting factor can be related to a partial cell saturation $d(\mathbf{x}, t) \in [0, 1]$ defined over the entire simulation domain, which is $d = 1$ at cells occupied by fluid and $d = 0$ at those inside solid locations. A smooth transition layer of size ϵ is used to prevent fluctuations and numerical errors as it avoids abrupt changes from solid to fluid nodes. An exemplary formulation for a spherically shaped particle k with radius R and the centre of mass $\mathbf{X}_k$ can then be written as

$$d(\mathbf{x}, t) = \begin{cases} 1 & \text{for} \quad \|\mathbf{x} - \mathbf{X}_k(t)\|_2 \leq R - \frac{\epsilon}{2}, \\ \cos^2\left(\frac{\pi}{2\epsilon}(\|\mathbf{x} - \mathbf{X}_k(t)\|_2)\right) & \text{for} \quad R - \frac{\epsilon}{2} < \|\mathbf{x} - \mathbf{X}_k(t)\|_2 < R + \frac{\epsilon}{2}, \\ 0 & \text{for} \quad \|\mathbf{x} - \mathbf{X}_k(t)\|_2 \geq R + \frac{\epsilon}{2}. \end{cases} \tag{2.15}$$

In the specific case of HLBM, the partial cell saturation directly represents the local *confined permeability* according to (2.12). Therefore, permeable particles can simply be accounted for by allowing $d > 0$ at solid sites (cf. Figure 2.2). Based on results of Trunk et al. [95], the size of the smooth transition layer ϵ is set to equal the respective grid spacing for every particle-laden study in this work.

For the relation of the local weighting factor B and the partial cell saturation d, different variants can be found in the literature [103]

$$\textbf{B1:} \quad B(\mathbf{x}, t) = d(\mathbf{x}, t), \tag{2.16}$$

$$\textbf{B2:} \quad B(\mathbf{x}, t) = \frac{d(\mathbf{x}, t)\left(\tau - \frac{1}{2}\right)}{(1 - d(\mathbf{x}, t)) + \left(\tau - \frac{1}{2}\right)}. \tag{2.17}$$

Here, the sufficient stability condition $\tau > 0.5$ for the BGK collision operator [106] has to be met for **B2** in order to avoid a division by zero. When interested
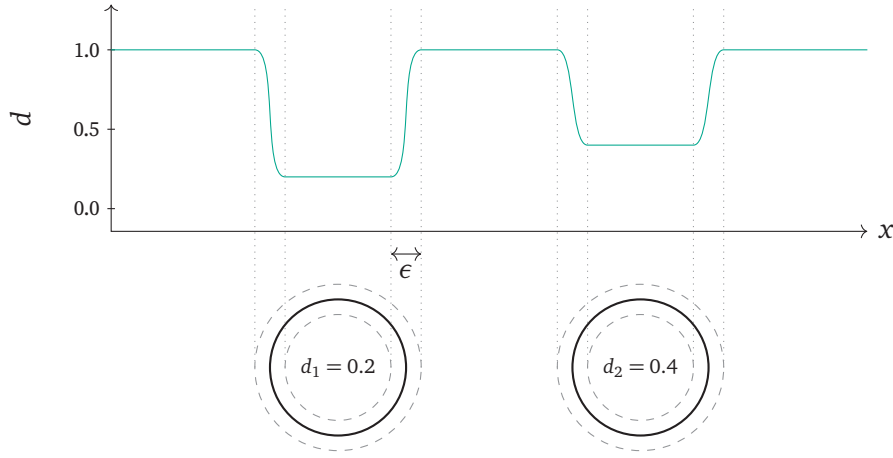
Figure 2.2: *Continuous description of $d(\boldsymbol{x}, t)$ along an axis x passing through the centre of two spherical particles with confined permeabilities d_1 and d_2 including a smooth transition layer with size ϵ.*

in recovering the SP model at permeable solid sites, however, a **B1** formulation has to be utilized. In the HLBM, the weighting factor is then used to calculate an effective velocity

$$\boldsymbol{u}^{eff}(\boldsymbol{x}, t) = B(\boldsymbol{x}, t)\boldsymbol{u}(\boldsymbol{x}, t) + (1 - B(\boldsymbol{x}, t))\boldsymbol{u}^{S}(\boldsymbol{x}, t) \qquad (2.18)$$

as a weighted average of fluid $\boldsymbol{u}$ and solid velocities $\boldsymbol{u}^{S}$ instead of fluid and solid collision operators as in conventional PSM [6]. The moving porous media character of HLBM becomes apparent when it simply reduces to the SP model for non-moving objects ($\boldsymbol{u}^{S} = 0$) and (2.18) essentially becomes (2.12).

The velocity scaling in (2.18) provides the possibility of using different forcing methods [106]. Due to the described criticism regarding the method by Shan and Chen [116], the one proposed by Kupershtokh et al. [125] is adopted here. Assuming this method, the scaled velocity then enters a modified LBE

$$f_i(\boldsymbol{x} + \boldsymbol{c}_i, t + 1) = f_i(\boldsymbol{x}, t) + \Omega_i(\boldsymbol{x}, t) + S_i(\boldsymbol{x}, t) \qquad (2.19)$$

in form of an additional source term

$$S_i(\boldsymbol{x}, t) = f_i^{\text{eq}}\big(\rho(\boldsymbol{x}, t), \boldsymbol{u}^{eff}(\boldsymbol{x}, t)\big) - f_i^{\text{eq}}\big(\rho(\boldsymbol{x}, t), \boldsymbol{u}(\boldsymbol{x}, t)\big). \qquad (2.20)$$

In order to retrieve the opposing force contribution acting on the particles themselves, the momentum exchange approach by Wen et al. [126] ensuring

Galilean invariance is used independently of (2.20). For every node x_b in the smooth boundary transition area of a single particle k, its force contribution

$$F_k(x_b, t) = \sum_{i=0}^{q-1} \left[(c_i - u^S(t)) f_i(\hat{x}_b, t+1) - (c_{\bar{i}} - u^S(t)) f_{\bar{i}}(x_b, t+1) \right] \quad (2.21)$$

is calculated by accounting for the differences between the discrete velocities c_i and the particle's solid velocity u^S. Here, $\hat{x}_b$ denotes the next node in the direction of i and $\bar{i}$ the opposite direction of it. By summing up the contributions over all nodes in this boundary transition region, the force and torque acting on the particle's centre of mass X_k can be calculated with

$$F_k(t) = \sum_{x_b} F_k(x_b, t) \quad \text{and} \quad T_k(t) = \sum_{x_b} (x_b - X_k(t)) F_k(x_b, t). \quad (2.22)$$

With those, the translational and rotational movement of the individual particles can be simulated by using simple discrete element method (DEM) algorithms. In the present work, the ones included in the HLBM framework are used, which can be found in Trunk et al. [95]. This, in particular, includes the velocity Verlet algorithm [127, 128], which is executed every LBM time step

2.2.4 Quantification of Errors and Convergence

Numerical instabilities resulting from initial large gradients in steady-state setups can often be avoided by ramping-up the inflow velocity by a discretization specific start-up time until convergence is reached. The respective criterion is given as the standard deviation σ of a flow quantity χ being smaller than a predefined residuum r multiplied by the average $\bar{\chi}$ over the last T time steps

$$\sigma(\chi) = \sqrt{\frac{1}{T+1} \sum_{t=1}^{T} (\chi_t - \bar{\chi})^2} < r\bar{\chi}. \quad (2.23)$$

In order to ensure convergence for both velocity and pressure field, the kinetic energy and the lattice density averaged by the total cell number M

$$\chi_t(u) = \frac{1}{M} \sum_{m=1}^{M} \left(\frac{1}{2} \|u\|^2 \right)_m \quad \text{and} \quad \chi_t(\rho) = \frac{1}{M} \sum_{m=1}^{M} \rho_m \quad (2.24)$$

are considered right after being calculated via the moments according to (2.5). For the evaluation of grid convergence, the error err_{L^2} based on the L^2 norm is
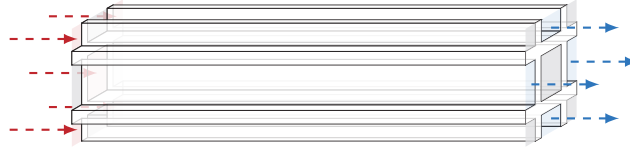
Figure 2.3: *Model of a wall-flow filter channel with porous walls and fractions of surrounding channels. Inflow (red) on the **left**, outflow (blue) on the **right**.*

used as an error criterion for the quantity χ at a given resolution N

$$err_{L^2}(\chi) = \sqrt{\frac{\sum_{m=1}^{M} \left(\chi_m^{\text{ref}} - \chi_m\right)^2}{\sum_{m=1}^{M} \left(\chi_m^{\text{ref}}\right)^2}}. \tag{2.25}$$

The experimental order of convergence (EOC) for two different resolutions N and N' is defined as

$$EOC_{N',N} := \frac{\ln(err_{L^2,N'}/err_{L^2,N})}{\ln(N'/N)}. \tag{2.26}$$

2.3 Application to a Wall-Flow Filter

In this section, the previously described methods and modelling approaches are applied to a wall-flow filter. First, the application setup including operation and boundary conditions is presented and a particle-free flow field is simulated (cf. Section 2.3.1). A grid convergence study is then performed for the particle-free flow (cf. Section 2.3.2) followed by the comparison of the simulation results with a semi-analytic 1D model (cf. Section 2.3.3). Afterwards, a static deposition layer consisting of individual PM fragments is considered (cf. Section 2.3.4) and the hydrodynamic force distribution as well as the influence of fragment clusters are examined. Finally, the results from a transient simulation of PM fragment detachment including the examination of the impact of assorted layer properties are presented (cf. Section 2.3.5).

2.3.1 Simulation of the Particle-Free Flow Field

The application setup represents a single wall-flow channel embedded into fractions of neighbouring inflow and outflow channels (Figure 2.3). Dirichlet boundary conditions are applied in form of a prescribed uniform velocity at the inlet and a constant pressure at the outlet. Due to commonly used wide-angled
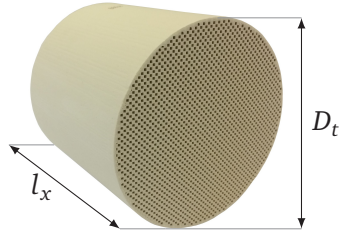
- channel width $l_y = 1.6\,\text{mm}$
- channel length $l_x = 120\,\text{mm}$
- wall thickness $l_w = 0.4\,\text{mm}$
- trap diameter $D_t = 125\,\text{mm}$
- structure (cpsi/mil): 200/8

Figure 2.4: *Picture of a common wall-flow filter trap with the respective geometric quantities used for the simulation setup. Structure given by cell number in cells per square inch (cpsi) and cell size in 10^{-3} inch (mil).*

planar diffusors fitted upstream of the actual filter [129], a uniform plug profile is reasoned to represent the realistic case closer than a developed channel or duct profile. Periodic boundary conditions are applied on either side orthogonally facing the main flow direction. In this way, it is ensured that aside from wall effects along the filter canning all relevant features of the particle-free flow in a wall-flow filter can be accounted for. Each channel is confined by a no-slip wall condition either in the front or in the back depending on its purpose as inflow or outflow channel. The fluid flow is solved by a BGK-LBM scheme with regularized local boundary conditions [130] at Dirichlet boundaries and a bounce-back condition [131] at no-slip boundaries. The porous filter material is modelled via the SP model.

Geometric quantities (Figure 2.4) are chosen to resemble common wall-flow trap dimensions. Channel inflow velocities can vary a lot during filter operation, while the permeability of the porous walls directly depends on the substrate's material and its inner structure. In the following, a fixed average inflow velocity of $\bar{u}_{in} = 2.0\,\text{m/s}$ and a permeability of $K = 1.5 \times 10^{-10}\,\text{m}^2$ are assumed. Both values represent the somewhat lower end of real world ranges that include velocities up to $\bar{u}_{in} = 80\,\text{m/s}$ [83] and permeabilities as small as $K = 0.9 \times 10^{-14}\,\text{m}^2$ for cordierite filters [132]. As in this work temperature effects are neglected, for now a kinematic viscosity of $\nu = 158.2 \times 10^{-7}\,\text{m}^2/\text{s}$ and a mass density of $\rho = 1.168\,\text{kg/m}^3$ at ambient conditions are assumed for the gaseous fluid flow. The described choice of parameters and simplifications represents a numerically favourable setup that is adopted here to primarily allow for the evaluation of the proposed method. This setup is, however, intended to be subject to a comprehensive extension in future studies.

With (2.27), separate Reynolds numbers for the flow in the open channel
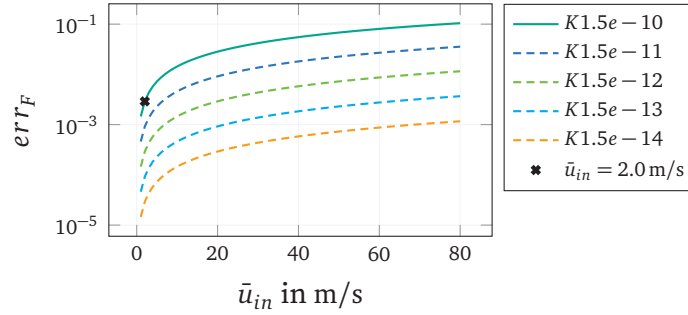
Figure 2.5: *Error err_F resulting from neglecting the non-linear Forchheimer pressure drop contribution in (2.8) by relating both terms in (2.9) for different Permeabilities. The average inflow velocity $\bar{u}_{in}$ used in this work is marked in black.*

area Re and the porous walls Re_w can be calculated as

$$\mathrm{Re} = \frac{\bar{u}_{in} l_y}{\nu} \qquad \text{and} \qquad \mathrm{Re}_w = \frac{\bar{u}_w l_y}{\nu} \qquad \text{with} \qquad \bar{u}_w = \frac{l_y}{4 l_x} \bar{u}_{in}. \qquad (2.27)$$

The average wall penetrating velocity $\bar{u}_w$ results from relating the inlet cross-section with the projected wall area. With the described quantities, this results in $\mathrm{Re} = 202.3$ and $\mathrm{Re}_w = 0.674$ with $\bar{u}_w = 6.67 \times 10^{-3}\,\mathrm{m/s}$.

In order to test the applicability of the SP model for the geometric and operational quantities used in this work, the effect of neglecting non-linear force contributions in (2.8) is evaluated. For that, (2.9) is split into its linear Darcy F_a and its non-linear Forchheimer term F_b. The resulting error err_F from ignoring the latter can be described by

$$err_F = \frac{F_b(\bar{u}_w)}{F_a(\bar{u}_w) + F_b(\bar{u}_w)} \qquad (2.28)$$

and related to the average inflow velocity $\bar{u}_{in}$ with (2.27). Assuming a common substrate porosity of around $\varepsilon = 0.4$ [133], the error's dependency on possible average inflow velocities $\bar{u}_{in}$ is shown in Figure 2.5. For the permeability and inflow velocity used in this work, this yields an error of $err_F = 2.9 \times 10^{-3}$ serving as a justification for the use of the SP model. When assuming the same permeability, it can be observed that for higher velocities the non-linear contribution can not be neglected any more and (2.9) has to be used. However, when considering lower permeabilities, a small error can be guaranteed even with velocities at the upper velocity range.

With the geometric properties in Figure 2.4, a single channel features a length-to-width ratio of $r_c = 75$. For a reasonable resolution of the channel
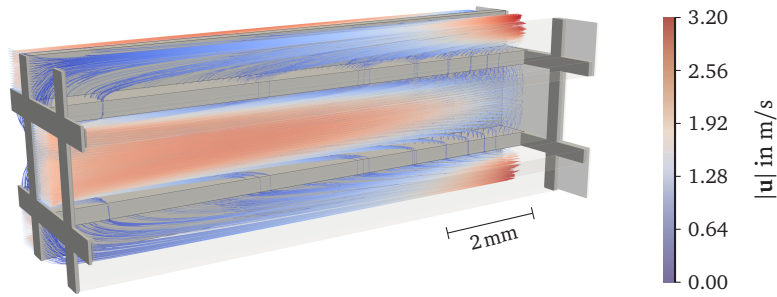
Figure 2.6: *Particle free flow in a single wall-flow channel with a scaling factor of $s_l = 0.1$ and a resolution of $N = 32$. Gray structures represent filter substrate. Streamlines exhibit local flow direction. Colour scale indicates local velocity magnitude.*

width, this results in a large number of cells for an equidistant grid and respectively in a high computational effort. That can lead to calculation times of multiple days for a single transient simulation. Provided a sufficiently large distance to the inflow and outflow boundaries, the local flow conditions in the channel mid do not differ significantly from an approximately linear behaviour [112]. Therefore, when not exactly interested in the actual pressure level, it is reasoned that assorted local effects and the sensitivity of specific parameters can be recovered on a channel geometry with a reduced length $l_{x,scaled}$. For that reason, only the comparison with the semi-analytical 1D model (cf. Section 2.3.3) is done considering a full length channel geometry. As a scaling factor of $s_l = l_{x,scaled}/l_x = 0.1$ still leads to a relatively large length-to-width ratio of $r_c = 7.5$, a respective geometry is used for the remaining studies in order to reduce the computational effort.

The application geometry including the simulation results of the flow field for a resolution of $N = 32$ cells per channel diameter is shown in Figure 2.6. A transition from the uniformly assumed inflow profile to a parabolic one can be observed. As the wall's friction is not specifically modelled (e.g. by a no-slip condition), the parabolically shaped profile solely results from the momentum loss in the porous walls. Due to the flow through the porous walls, the average flow velocity gradually decreases over the channel length in the inflow channels and increases in the outflow channels. Despite exhibiting higher maximum values due to the non-uniformity of the resulting flow profile, the average magnitude of the outlet velocity yields $\bar{u}_{out} = 2.009 \, \text{m/s}$ leading to a

global flux conservation error of $err_{Tot} = 4.5 \times 10^{-3}$ with

$$err_{Tot}(\bar{u}) = \frac{\bar{u}_{out} - \bar{u}_{in}}{\bar{u}_{in}}. \qquad (2.29)$$

Considering the fact that the LBM is not inherently based on momentum and mass conservation, this represents a satisfactory result for the selected resolution of $N = 32$. For a resolution of $N = 128$ used in the following section, this leads to an error of $err_{Tot} = 4.5 \times 10^{-5}$.

2.3.2 Grid Convergence

In order to quantify the setup's dependency on the spatial discretization, the grid convergence is evaluated for the particle-free case with resolutions of $N = 16, 32, 64$ and 128 assuming diffusive scaling ($\tau = $ const.). Here, a lattice relaxation time of $\tau = 0.51$ is used leading to a space-time relation of $c = \frac{\Delta t}{\Delta x^2} = 210.7\,\text{s/m}^2$. In order to differentiate between the inflow channel domain C_{in} and the outflow channel domain C_{out}, the model's centre inflow channel and one of the four outflow channels were selected as representatives. Due to its two-sided symmetry in the particle-free case, the flow quantities of interest do mainly vary along the main flow direction x. By averaging those quantities on discrete two-dimensional planes oriented normal to the main flow, a one-dimensional flow profile $\bar{\chi}(x)$ can be calculated for each quantity. This is done for the velocity component in x-direction $\bar{u}_x$ and the pressure $\bar{p}$ in both domains. The resulting profiles normalized by the average inflow velocity $\bar{u}_{in}$ and the maximum obtained pressure p_{max} are then plotted along the main flow direction x normalized with the channel's length $l_{x,scaled}$ in Figure 2.7.

The velocity $\bar{u}_x$ in the inflow channel domain C_{in} decreases from the imposed one at the inlet $\bar{u}_{in}$ (at $x/l_{x,scaled} = 0$) to zero at the channel end ($x/l_{x,scaled} = 1$). The initially nearly constant slope gradually decreases towards the channel end as well. The outflow channel domain C_{out} exhibits a flow profile with a mirrored, opposite behaviour. It can be seen that the effect of the channel's resolution is very small with respect to the covered velocity range. The pressure profiles $\bar{p}(x)$ in turn differ between both channels, as their contributions add up to the total pressure drop, which is experienced at the inflow channel's inlet. While the outflow channel exhibits a continuously decreasing pressure with a decreasing slope towards the end, the inflow pressure can be seen to eventually increase. This shows that the momentum transfer through the porous walls reaches its minimum close to the channel mid
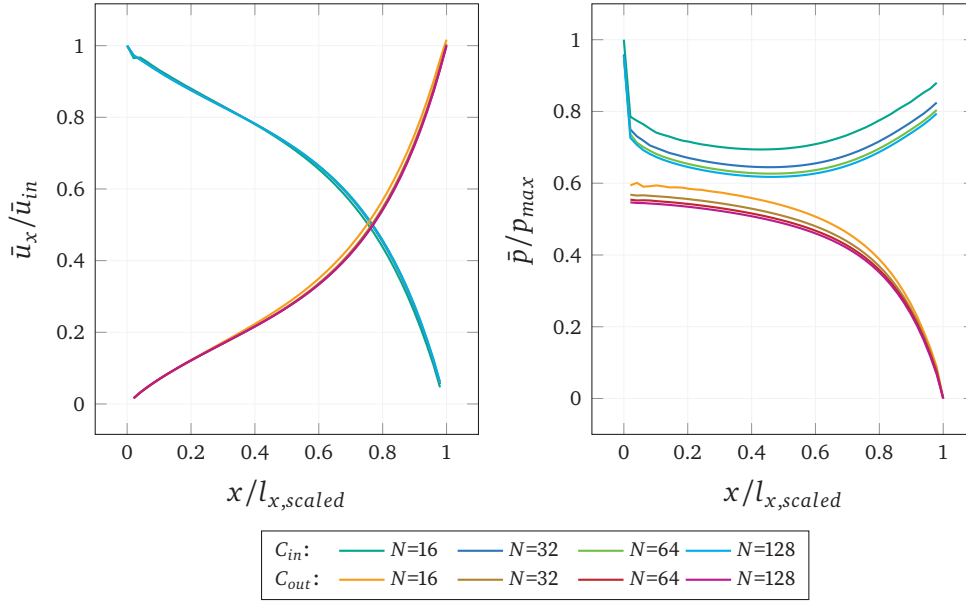
Figure 2.7: *Normalized velocity profiles $\bar{u}_x(x)/\bar{u}_{in}$ and pressure profiles $\bar{p}(x)/p_{max}$ in inlet channel domain C_{in} and outlet channel domain C_{out} for resolutions of $N = 16$, 32, 64 and 128.*

and increases both towards the front and the end. This observation agrees well with literature findings [112]. Compared to the velocity profiles, the pressure profiles exhibit a higher dependency to the channel's resolution.

The resulting values are then used to calculate the $err_{L^2}(\chi)$ according to (2.25), while the highest resolution is used as the reference solution χ^{ref}. Figure 2.8 shows the logarithmically scaled errors of the velocity $err_{L^2}(\bar{u}_x)$ and pressure profiles $err_{L^2}(\bar{p})$ for resolutions of 16,32 and 64 with 128 being the respective reference. The quadratic and linear EOC are included as visual guidelines. The corresponding EOC are calculated additionally and listed in Table 2.1. Table 2.1 describes the $EOC_{N,2N}$ for doubling the respective resolutions and the resulting average one. It can be seen that both pressure and velocity exhibit super-linear convergence with the velocity being close to a quadratic one. For all quantities, the $EOC_{32,64}$ yields better results than the $EOC_{16,32}$. In contrast to the inflow channel domain C_{in}, the outflow channel domain C_{out} exhibits inferior grid convergence both for the absolute velocity error and the pressure EOC. The LBM is a numerical scheme approximating the NSE with second-order accuracy in space and time assuming a constant lattice relaxation time [106].
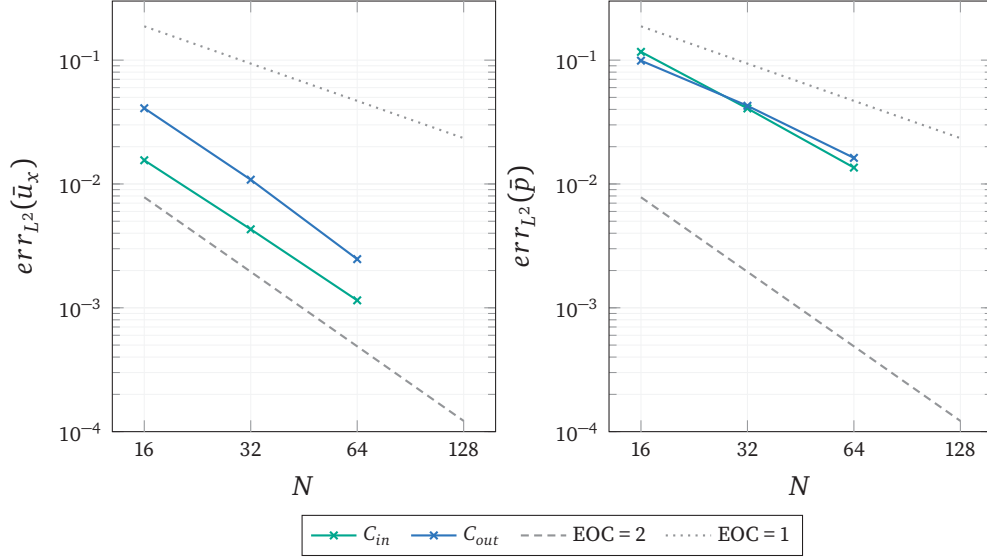
Figure 2.8: *Error $err_{L^2}(\bar{u}_x)$ and $err_{L^2}(\bar{p})$ according to (2.25) of averaged velocity and pressure profiles in inlet channel domain C_{in} and outlet channel domain C_{out}.*

Table 2.1: *Experimental order of convergence (EOC) between different resolution pairs obtained by the error err_{L^2} for velocity profiles $\bar{u}_x(x)$ and pressure profiles $\bar{p}(x)$ in inlet channel C_{in} and outlet channel C_{out}.*

	$\bar{u}_x(x)$		$\bar{p}(x)$	
	C_{in}	C_{out}	C_{in}	C_{out}
$EOC_{16,32}$	1.85	1.92	1.52	1.21
$EOC_{32,64}$	1.91	2.13	1.59	1.40
$\overline{EOC}$	1.88	2.02	1.55	1.30
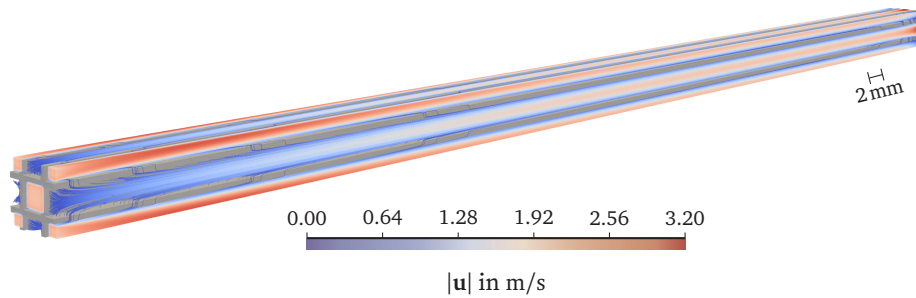
Figure 2.9: *Particle free flow in a single wall-flow channel of full length ($s_l = 1.0$) and a resolution of $N = 32$. Gray structures represent filter substrate. Streamlines exhibit local flow direction. Colour scale indicates local velocity magnitude.*

Thus, the resulting EOC in Table 2.1 exhibit excellent grid convergence for the velocity $\bar{u}_x$ and an acceptable one for the pressure $\bar{p}$.

2.3.3 Comparison of Simulations With Semi-analytic 1D Model

The semi-analytical 1D wall-flow model described by Konstandopoulos and Johnson [75] provides a simple and computationally efficient alternative to numerical calculations and has been validated thoroughly. Though Konstandopoulos et al. [112] presented a simple 3D model as well, their 1D version provides a much greater adaptability over a wide parameter range. Therefore it is compared to simulations of the symmetric particle-free flow in a full length ($s_l = 1.0$) wall-flow channel geometry as shown in Figure 2.9.

The resulting velocity and pressure profiles for both inlet and outlet channel as well as the 1D reference are shown in Figure 2.10. It can be observed that reference solution and retrieved data agree well with each other. The simulation over-predicts the pressure drop with a constant pressure difference, which is small compared to the total pressure drop between inlet and outlet. Although the flow profile can develop over the course of the channel, it is assumed as being uniform at the channel inlet, which at this location does not necessarily represent a realistic behaviour [129]. The high initial pressure value in the inlet channel can therefore be reasoned to be an artefact resulting from artificially high velocity gradients at the inlet edges and corners.
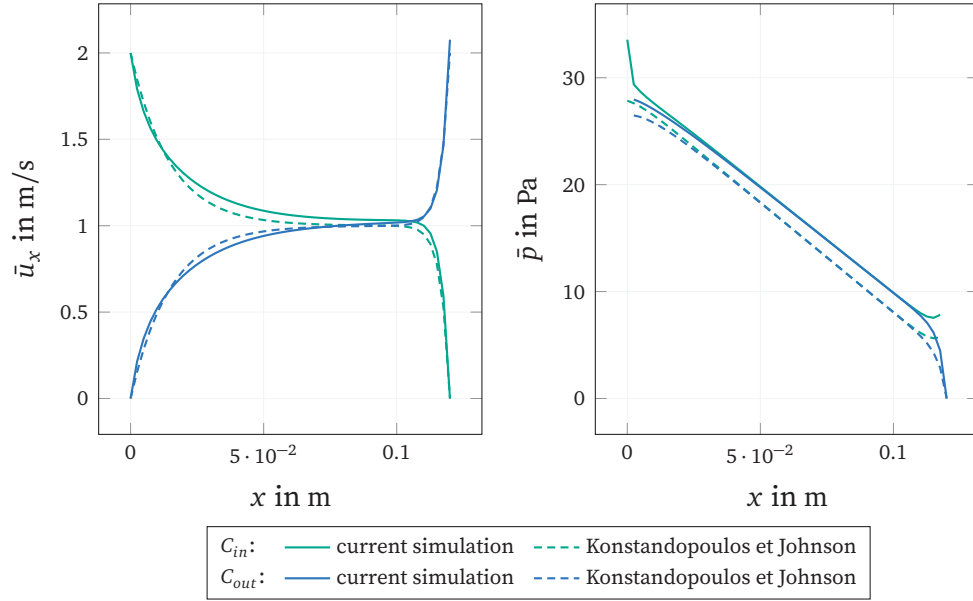
Figure 2.10: *Velocity profiles $\bar{u}_x(x)$ and pressure profiles $\bar{p}(x)$ in inlet channel domain C_{in} and outlet channel domain C_{out} compared to their reference solutions from Konstandopoulos and Johnson [75].*

2.3.4 Particulate Matter Layer Characteristics

After ensuring the model's basic capability in retrieving the fluid flow, the previously described moving porous media approach HLBM is used to investigate the influence of PM deposition inside the channel. Images corresponding to the transition from a continuous deposition layer to individual PM layer fragments due to the oxidization of the majority of its soot content [81] reveal numerous influence factors. Those include their size, form, surface topology, permeability and spatial distribution. In order to focus on single factors at a time, the layer fragments are modelled as a field of identical cubic discs with an edge ratio of $2 \times 2 \times 1$ and smooth edges covering the porous walls inside an inflow channel. While some factors are subject to variations in the remainder of this work, an initial set of parameters is determined by intending a visual resemblance to the literature findings. By choosing a factor of $f_p = 0.08$ relating the base length of the PM fragments l_p to the channel width l_y, a uniform field of 3×20 fragments with dimensions of $256\,\mu m \times 256\,\mu m \times 128\,\mu m$ is assumed. The respective flow field is shown in Figure 2.11. It shows the uniform distribution of cubic discs representing the individual PM layer fragments and the flow field after having
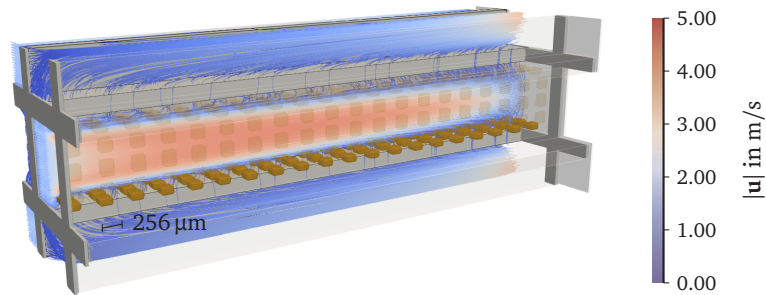
Figure 2.11: *Flow field with fragmented PM layer (brown) in a single wall-flow channel with a scaling factor of $s_l = 0.1$ and a resolution of $N = 32$. Gray structures represent filter substrate. Streamlines exhibit local flow direction. Colour scale indicates local velocity magnitude.*

reached velocity and pressure convergence according to (2.23). Due to the reduced cross-section available for the fluid flow, the core flow exposes greater velocity magnitudes with respect to the particle-free case in Figure 2.6. It can additionally be observed that the streamlines engage in steep turns at the back wall indicating a small area in which the flow direction is reversed close to the channel walls. In the following, the bottom layer emphasized in Figure 2.11 is examined more closely.

2.3.4.1 Hydrodynamic Force Distribution

The detachment process and the resuspension into the flow of individual PM layer fragments are governed by the interaction of hydrodynamic and adhesive forces [58]. The prior ones are therefore evaluated for each fragment along the channel length for the right, centre and left row of the fragment field. Their respective tangential and normal components regarding the wall's surface are displayed in Figure 2.12. While both directions expose a distinct profile covering high values at the inflow and slightly negative ones at the outflow, the tangential forces are much greater than the ones in normal direction. The latter stay, in fact, below zero over most of the channel length, while the negative contributions at the channel end in both directions can be attributed to the flow reversal observable in Figure 2.11. The elevated fluid velocity in the channel's centre leads to higher force values in the centre row. With those observations, the detachment behaviour during regeneration can already be predicted by expecting PM fragments in the centre of the channel's front section to detach
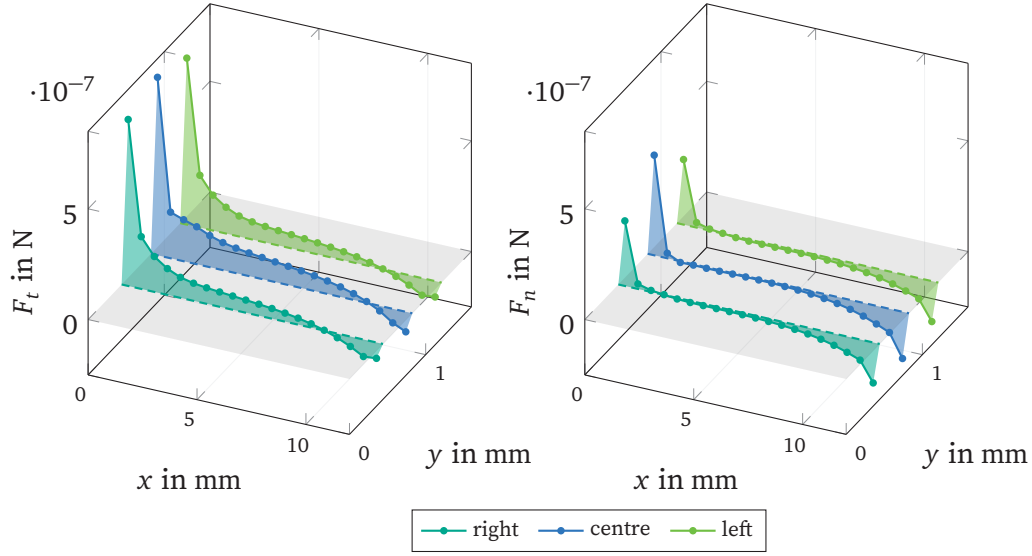
Figure 2.12: *Hydrodynamic forces in single fragmented PM layer over the channel length. Differentiation between right, centre and left row. Gray plane at zero crossing.*

first due to tangential forces.

2.3.4.2 Influence of Particulate Matter Fragment Clusters

From findings of mid-channel or end-channel plugs [60], it can be suggested that once rearrangement effects start at a specific location, the detachment process is self-reinforcing as the exposition of neighbouring layer fragments to the fluid flow increases. In order to test this hypothesis, clusters of PM fragments only covering the four walls along 20% of the channel length at different positions are investigated in separate simulations each as well. A sketch of the considered regions **A,B,C,D** and **E** and an exemplary cluster at region **B** is shown in Figure 2.13.

In order to evaluate the influence on the fluid flow, the velocity and pressure profiles normalized by the average inflow velocity $\bar{u}_{in}$ and the maximum obtained pressure p_{max} are shown in Figure 2.14. The respective profiles for both the particle-free case (cf. Figure 2.7) and a full coverage of PM fragments are included as a reference. The considered cluster's locations are indicated by shaded areas coloured according to their respective profile. By arguing with respect to the full deposition, it can be seen that a cluster in **A** results in an axial
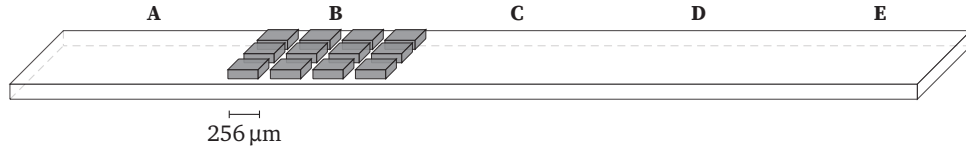
Figure 2.13: *Sketch of single filter wall with considered regions for fragment clusters. Exemplary cluster in red at region **B**.*
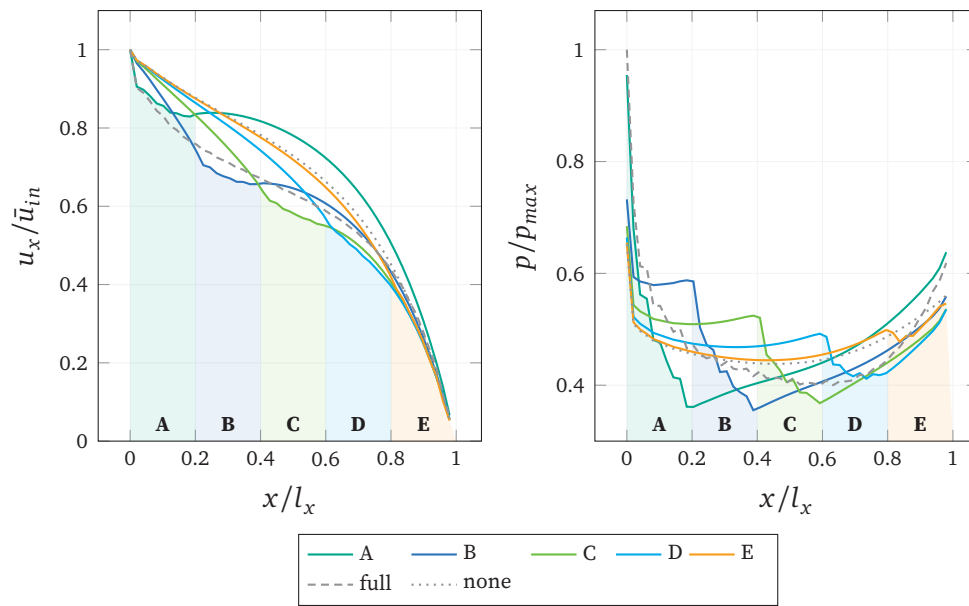
Figure 2.14: *Normalized velocity profiles $\bar{u}_x(x)/\bar{u}_{in}$ and pressure profiles $\bar{p}(x)/p_{max}$ in inlet channel domain C_{in} for separate simulations with different fragment cluster locations. Particle free case and full coverage as reference. Shaded areas indicate cluster locations.*
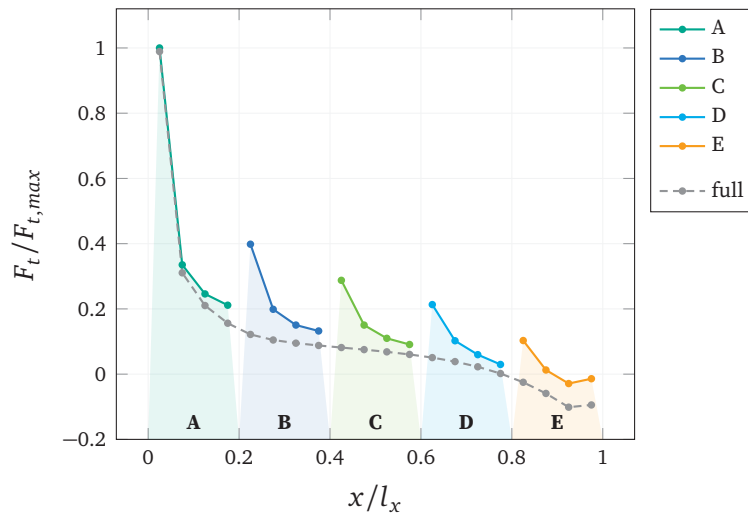
Figure 2.15: *Normalized tangential force $F_t/F_{t,max}$ for separate simulations with different fragment cluster locations. Full coverage as reference. Shaded areas indicate cluster locations.*

fluid velocity which is higher over the whole channel length. Most of the fluid, therefore, has to pass through the walls in the rear section. When considering clusters in **B** and **C**, a slight increase in the fluid velocity before and right after it can be observed. Both clusters in **D** and **E**, in turn, lead to a significant increase in the front section. The pressure can be observed to decrease right behind a cluster in every case due to the sudden expansion in the cross-section available for the fluid flow. As only 20% of the wall surface are covered, the total pressure drop is always smaller with respect to the full deposition. This effect is less distinct for the front most regions indicating that clusters in the rear sections are favourable when solely intending to reduce the total pressure drop.

Additionally, the centre line (cf. Figure 2.12) of the tangential forces is evaluated for each simulation and displayed in Figure 2.15. It can be seen that the forces in tangential direction acting on the individual PM fragments are indeed higher when considering fragment clusters **B**, **C**, **D** and **E** rather than the full deposition. While the first row in a cluster experiences the largest increase due to its exposed position, the following ones exhibit elevated values as well indicating the self-reinforcing effect during rearrangement events.

2.3.5 Simulation of PM Detachment

In the following, a general approach to the simulation of detachment and movement of PM layer fragments in a wall-flow filter channel is presented. This section aims at applying the previously described moving porous media approach HLBM and interpreting the respective results in an engineering context. Due to a lack of comparable data on the complex particle behaviour under study, this section does, however, not aim at performing a rigorous validation at this point. In order to investigate the transient behaviour of the detachment process during filter regeneration, the movement of the individual fragments is considered using DEM transport equations included in the framework of HLBM [95]. For now, the treatment of solid-solid interactions is simply modelled by relying on the momentum transfer via the surrounding fluid inherent to HLBM [7, 95] without the addition of an explicit collision model. In order to completely avoid any wall penetration, particle movement is additionally being restricted to the domain of the inlet channel.

Another restriction is introduced in form of a simplified adhesion force model that prohibits motion as long as adhesive forces exceed the hydrodynamic ones. For that, an artificial adhesive force contribution is introduced and initially set to a large value to keep the layer fragments attached to the porous walls. This way, an adhesive force can simply be treated as a detachment force threshold, which can be separated into normal and tangential direction. Once the regeneration process starts, the adhesive forces are set to decrease linearly over time representing the adhesion reduction due to the oxidization of reactive components in the deposition layer. Even though such a linear approach is far from close to a realistic and in part complex oxidization process, it provides a simple method to evaluate a transient process of detachment, resuspension and transport solely induced by hydrodynamic forces.

In Figure 2.16, four snapshots from the time series of the transient detachment process in a particle laden periodic channel are shown. For that, time $t = 0.00\,\mathrm{s}$ (**T1**), $t = 0.05\,\mathrm{s}$ (**T2**), $t = 0.10\,\mathrm{s}$ (**T3**) and $t = 0.15\,\mathrm{s}$ (**T4**) were examined. **T1** exhibits the fragmented PM layer and the respective fluid field at convergence. **T2** shows a later point in time, where the detachment process is in progress. The first layer fragments overc ome their adhesion force due to their exposition to the relatively high hydrodynamic forces close to the channel inlet resulting from the high local velocities (cf. Figure 2.12). They are then detaching one after another, resuspend into the core flow and move towards the channel's end. While Figure 2.12 suggests no significant lift-off due to mostly negative hydrody-
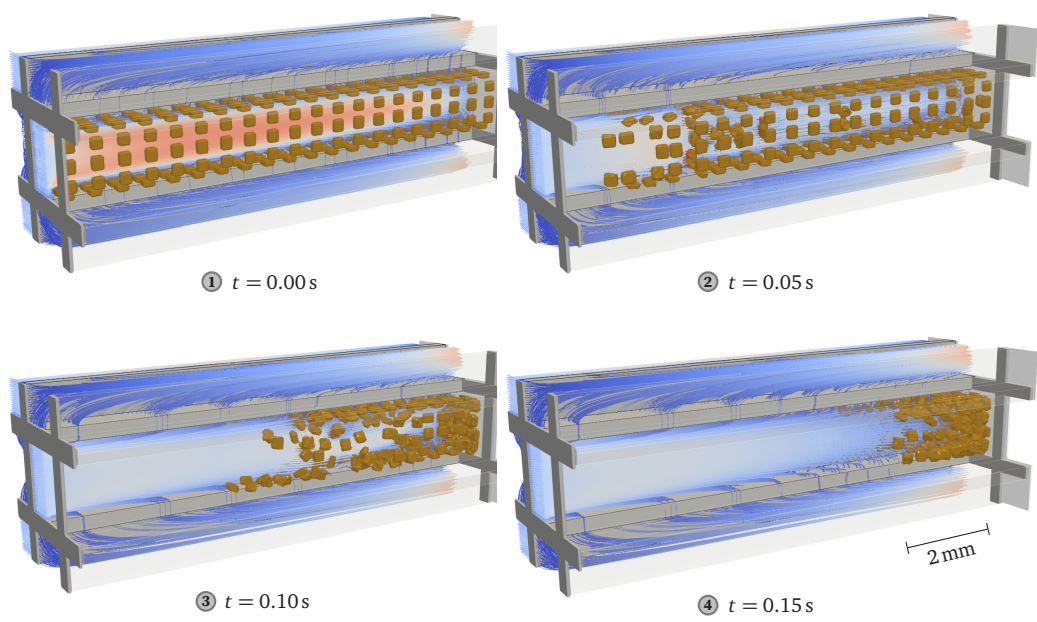
Figure 2.16: *Particle detachment in a single wall-flow channel with a scaling factor of $s_l = 0.1$ and a resolution of $N = 32$ at different times.*
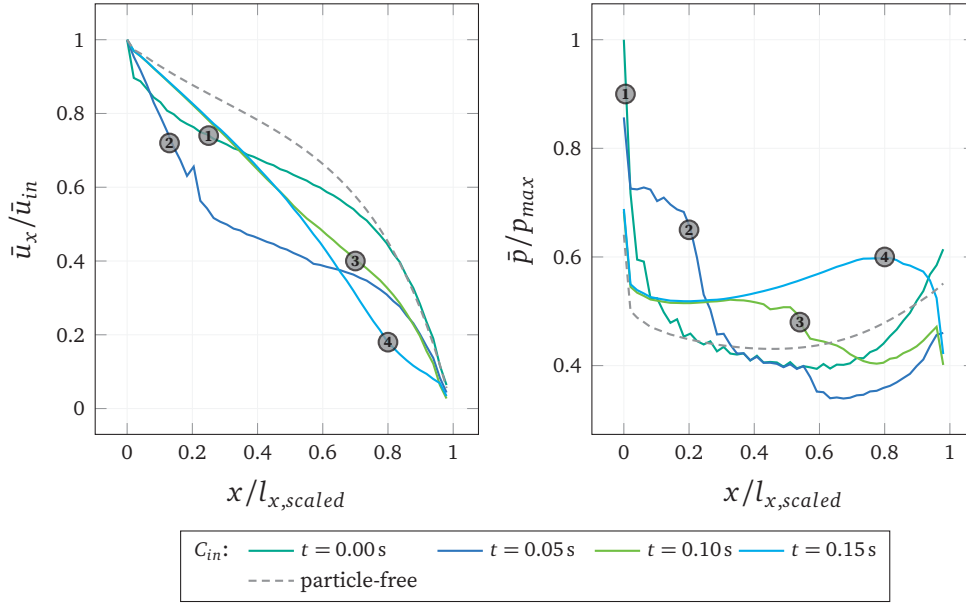
Figure 2.17: *Normalized velocity profiles $\bar{u}_x(x)/\bar{u}_{in}$ and pressure profiles $\bar{p}(x)/p_{max}$ in inlet channel domain C_{in} for different times as well as the particle-free reference from Figure 2.7.*

namic forces in normal direction, a majority of the fragments move along the channel with a significant distance from the wall's surface. Due to comparably large tangential forces, however, the fragments engage in a rotational movement quickly after detachment enabling the fluid to attack their bottom face and cause an upward motion. While out of scope at this point, a detailed study on relevant mechanics regarding the detachment process of single fragments will be the subject of a future publication. At **T3**, all particles have detached and start forming an initially highly porous particle packing. A compaction of this packing can then be observed in **T4** with a significant freeing-up of filter surface area.

The corresponding velocity and pressure profiles in the inlet channel are shown in Figure 2.17 for all four points in time and the particle-free case from Figure 2.7 as a reference. It can be seen that the rearrangement has a significant impact on both quantities. During the initial detachment (**T2**), the axial velocity drops in the channel's front part due to the blocked passage. This leads to a strong increase in the local pressure resulting from the greater amount of fluid having to pass through the permeable wall. Due to less wall throughput in the
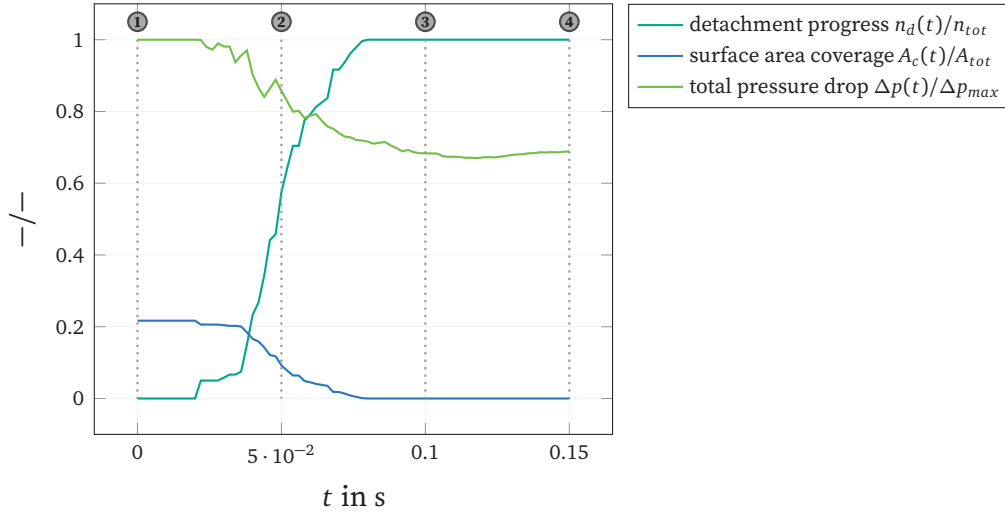
Figure 2.18: *Ratio of detached fragments to their total number $n_d(t)/n_{tot}$, coverage of filtration surface area $A_c(t)/A_{tot}$ and normalized total pressure drop $\Delta p(t)/\Delta p_{max}$ during transient detachment process.*

back of the filter, the local pressure decreases in that section. When all particles have detached at **T3**, the local axial flow velocity in the channel front approaches the one for the particle-free case due to the increase of free surface area on the porous walls. This results in less concentrated wall throughput and the local pressure can be observed to even out in the channel's front half. During the compaction of the resulting particle packing (**T4**), the local quantities in the front part nearly stay the same. However, by not being able to completely pass through the compacted particle packing in the filter's rear end any more, the fluid is abruptly redirected towards the porous walls. The axial velocity therefore experiences a decrease right in front of the packing, while the redirection and the higher wall throughput lead to an increase in the local pressure.

In addition to the evaluation of the local values of pressure and axial velocity, some essential global quantities are examined as well. Those include the ratio of the number of detached PM fragments n_d to their total number n_{tot}, the ratio of the filter surface area covered by the PM fragments A_c to the total filtration area A_{tot} and the total pressure drop for both inlet and outlet channel Δp normalized by its maximum value Δp_{max}. Their time dependent behaviour during the detachment process is shown in Figure 2.18.

The first fragments start to detach around $t = 0.025\,\text{s}$ with the last one

$$l_p = 48\,\mu m \qquad\qquad n_{l,x} = 10 \qquad\qquad K_p = 4.25 \times 10^{-7}\,m^2$$
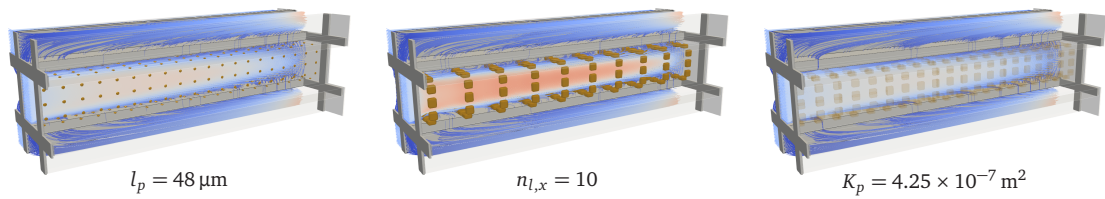
Figure 2.19: *Flow field with fragmented PM layer (brown) in a single wall-flow channel for different edge cases of considered layer properties. Here, fragment base size l_p, fraction number in x direction $n_{l,x}$ and particle permeability K_p indicated by transparency of fragments.*

overcoming its adhesive force at around $t = 0.075\,s$. Due to the uniformly sized PM fragments, the surface area coverage with an initial value of $A_c/A_{tot} = 0.217$ behaves directly proportional to the detachment ratio. It can further be observed that this coverage dictates the resulting overall pressure drop. It is worth noting that the compaction starting between **T3** and **T4** does not have a great impact on the total pressure drop, as most of the fluid passes through the filter wall before the respective section. As shown in the pressure drop distribution (cf. Figure 2.17), it does, however, have a significant influence on the local flow condition in the lower half of the channel. This can, presumably, have a great effect on the subsequent loading phase despite the negligible impact on the overall pressure drop.

2.3.5.1 Influence of PM Layer Properties

The fixed set of parameters considered above includes a fragment base length of $l_p = 128\,\mu m$, a number of fragments in x direction of $n_{l,x} = 20$ and impermeable particles with the minimum permeability of $K_p = 4.25 \times 10^{-12}\,m^2$ according to (2.14). Those quantities are varied by considering values up to $l_p = 48\,\mu m$, $n_{l,x} = 10$ and $K_p = 4.25 \times 10^{-7}\,m^2$. Figure 2.19 shows the respective fluid fields obtained at convergence for the described edge cases considered here. It can be seen that the fluid field with the minimum fragment size l_p approaches the one obtained in the particle-free case. A reduction of the number of fragments along the channel length $n_{l,x}$, however, does not change the visual representation significantly, since the relevant reduction of the available cross-section is already caused by the front most particle row. When considering a large particle permeability K_p with a confined permeability close to $d_p = 1.0$, the impact on the fluid's
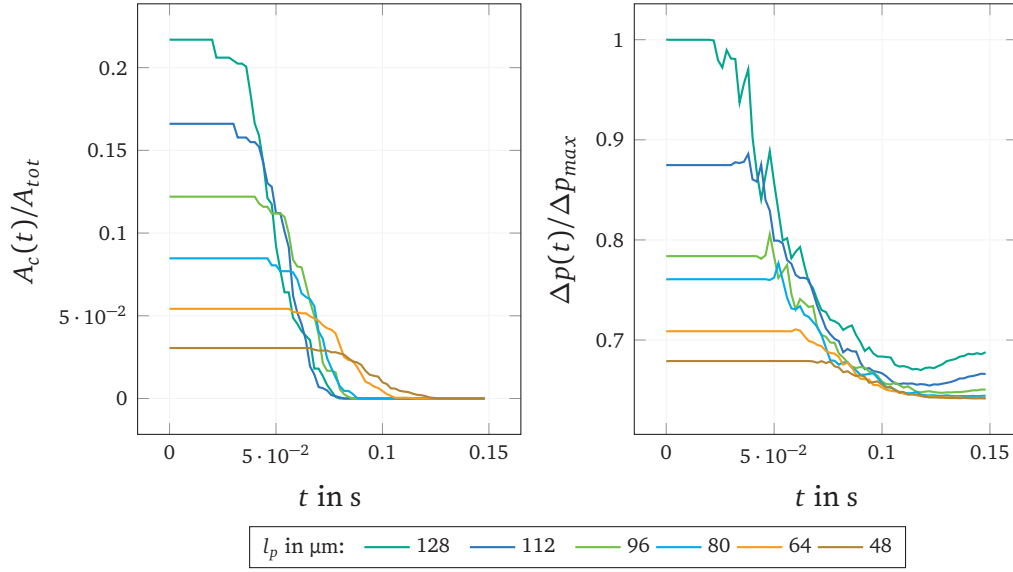
Figure 2.20: *Coverage of filtration surface area $A_c(t)/A_{tot}$ and normalized total pressure drop $\Delta p(t)/\Delta p_{max}$ during transient detachment process for different PM fragment base lengths l_p.*

momentum becomes negligible and the fluid field approaches the one resulting from the particle-free case as well.

The temporal evolution of the area coverage $A_c(t)/A_{tot}$ and the normalized total pressure drop $\Delta p(t)/\Delta p_{max}$ is shown in Figure 2.20 for different particle sizes. Assuming a constant edge ratio of the fragments, the base length l_p directly determines the size of the contact area, which is reflected in the initial coverage. Due to the reduced surface area of smaller fragments, the resulting hydrodynamic forces are smaller as well leading to a delayed detachment over the course of the simplified reaction process. As the pressure drop depends on the free surface area of the porous walls, its initial value decreases along with decreasing base lengths.

A variation of the number of fragments over the channel length in a PM layer leads to the results shown in Figure 2.21. Contrary to a variation in particle size, the initial coverage linearly follows the fragment number and the following coverage reduction proceeds with similar slopes for all numbers. While the pressure drop directly reflects this behaviour, it can be seen that a reduction to half of the fragment numbers only leads to a comparably small reduction
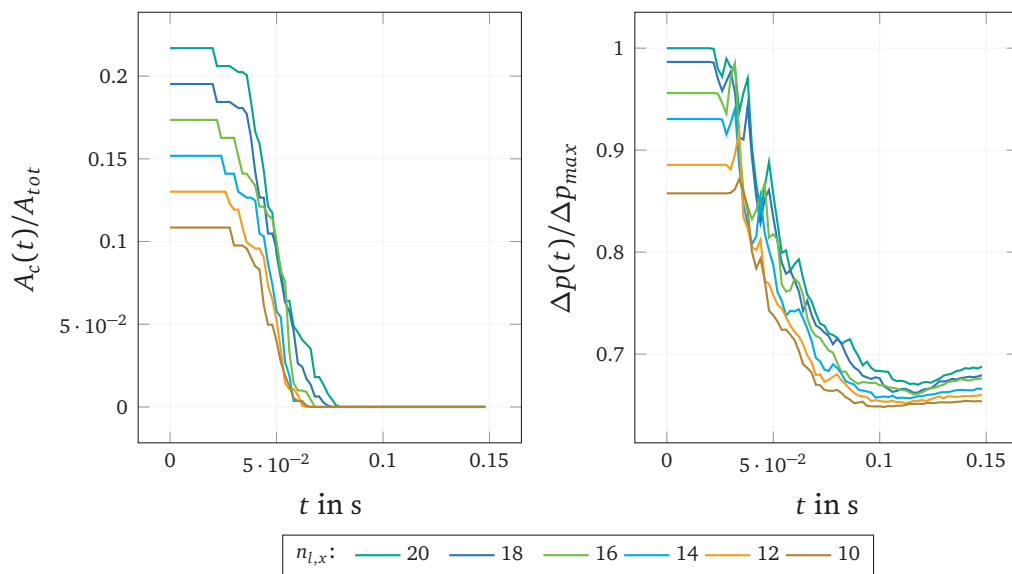
Figure 2.21: *Coverage of filtration surface area $A_c(t)/A_{tot}$ and normalized total pressure drop $\Delta p(t)/\Delta p_{max}$ during transient detachment process for different numbers of PM fragments in x direction $n_{l,x}$.*

Table 2.2: *Relation between confined permeability d_p and physical permeability K_p with minimum permeability of $K_{min} = 4.25 \times 10^{-12}\,\mathrm{m}^2$ according to (2.14).*

d_p	0.0	0.9	0.99	0.999	0.9999	0.99999	1.0
K_p in m^2	4.25×10^{-12}	4.25×10^{-11}	4.25×10^{-10}	4.25×10^{-9}	4.25×10^{-8}	4.25×10^{-7}	∞

of the initial pressure drop. This becomes apparent when comparing it to the pressure drop after complete detachment at around $t = 0.1\,\mathrm{s}$. In accordance with Figure 2.19, it shows that a PM deposition with significant size in the channel front has a dominating impact on the overall fluid field, which is then less sensitive to the remaining layer structure in the rear part.

The values considered for the permeability variation are listed in Table 2.2 accompanied by the respective confined permeabilities d_p according to (2.12). While a permeability of $K_p = 4.25 \times 10^{-12}\,\mathrm{m}^2$ represents the minimum resolvable value for the numeric setup considered in this work, a greater one leads to a smaller momentum contribution of submersed solid structures according to (2.18). This results in both decreased fluid resistance at particle sites and a smaller momentum exchange on the surface of the resolved particles under study. Figure 2.22 displays the results from considering different permeabilities of the fragments themselves. It can be seen that the decreased hydrodynamic forces resulting from the reduced momentum exchange lead to a delayed detachment similarly to Figure 2.20. When increasing the permeability even more, the obtainable force contributions close to the inflection point between positive and negative values observed in Figure 2.12 become very small. Detachment events can then only appear stepwise when assuming the simplified adhesion force reduction methodology used in this work. The pressure drop decreases accordingly when reducing the fluid resistance due to larger permeabilities. For the largest values considered ($K_p = 4.25 \times 10^{-8}\,\mathrm{m}^2$ and $K_p = 4.25 \times 10^{-7}\,\mathrm{m}^2$), the temporal change with respect to the initial pressure drop eventually becomes negligible.

2.4 Conclusion

The present work demonstrates the applicability of surface resolved particle simulations on the investigation of particulate matter structure detachment from the surface of wall-flow filters using lattice Boltzmann methods. At first, the gas flow in a single wall-flow filter was retrieved and the model's order of
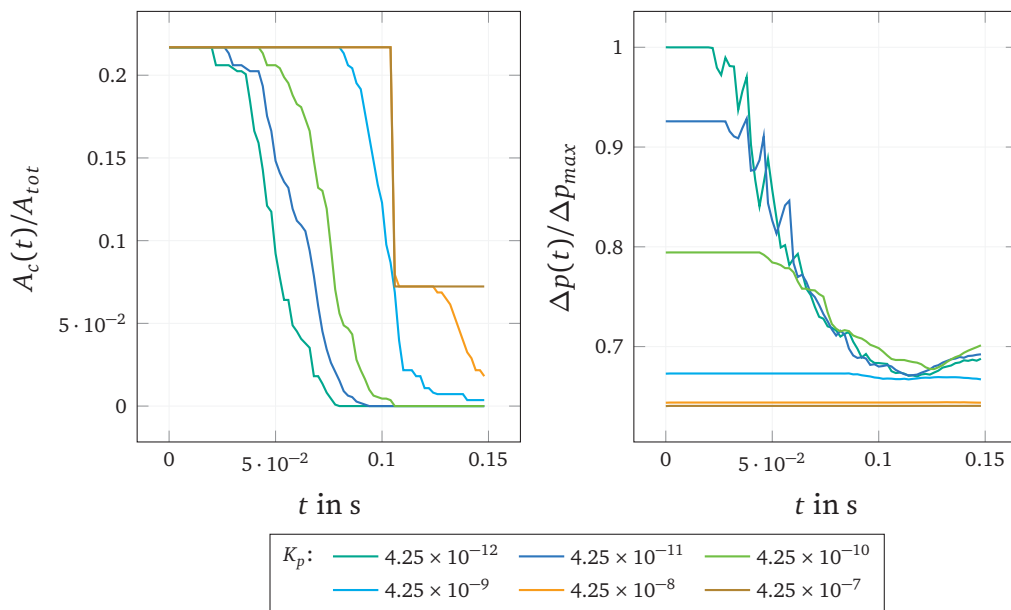
Figure 2.22: *Coverage of filtration surface area $A_c(t)/A_{tot}$ and normalized total pressure drop $\Delta p(t)/\Delta p_{max}$ during transient detachment process for different PM fragment permeabilities K_p.*

accuracy in the particle-free case was examined. Additionally, the flow field was compared to a reference solution. The model could be shown to exhibit super-linear grid convergence and good agreement with a reference solution, which has previously been validated thoroughly by experimental data [112]. The characteristics of a fragmented layer were then examined regarding the spatial distribution of the acting hydrodynamic forces and a clustering of PM fragments. This revealed clusters in the channel rear as favourable regarding a pressure drop optimization and indicated a self-reinforcing effect during rearrangement events. Due to those properties, the model is demonstrated to be capable of both consistently capturing the general flow characteristics of the particle-free flow and to serve as a stable foundation for the investigation of the respective particle laden flow. Furthermore, a general and easily extendable approach for the simulation of the detachment and movement of individual PM layer fragments was presented. Despite the described simplifications, this approach could be shown to enable the simulation of a transient detachment and transport process of surface resolved structures governed by hydrodynamic forces. This demonstrates the versatility of the entire LBM approach, which can be employed both for the simulation of the movement of resolved particles and the flow through porous media while being based on the same numerical method. With it, the direct relation between single influence factors, such as inflow velocity or adhesive behaviour, and the formation of a specific ash deposition pattern can be studied in detail and lead to the desired insights into the rearrangement process itself. The present work, therefore, represents a promising approach to further detailed investigations leading to the envisaged optimizations in engine performance, fuel consumption and failure probability in wall-flow filters.

Continuing from this work, the simplified adhesion force model will be extended by a more complex one capable of taking detailed reaction kinetics into account. Further efforts will be spent on the evaluation of different porosity models in order to extend the range of resolvable permeability values. In this context, the permeability influence of the PM layer fragments itself will be subject to more detailed investigations as well.

3

Investigation of Single Fragment Dynamics

3.1 Introduction

Wall-flow filters are used for the exhaust treatment of combustion engines employed in cars, heavy-duty vehicles and off-road applications. Despite recent endeavours towards electric drive systems, combustion engines will still represent a significant share in the years to come [58]. The particulate matter (PM) emitted by those engines poses potential health risks [32, 134], so current emission laws place strict limitations on them. As those by now include both PM and particle number (PN) limits, compliance cannot be achieved without the use of wall-flow filters.

Inside such a filter, the gas flow is separated into oppositely arranged inlet and outlet channels and forced through the porous wall separating them. The introduced PM mostly consist of combustible soot and small amounts of inorganic non-combustible ash. During operation, the filter's PM loading increases and a continuous layer forms on the surfaces of the walls. With increasing layer thickness, the pressure drop increases significantly [81, 82, 135] degrading engine

performance and fuel efficiency. A regeneration phase applied continuously or periodically is used to remove this layer by oxidizing its reactive components. The non-combustible ash, however, remains in the channel and accumulates over long term operation. Here, it forms larger ash agglomerates, which in turn affects the deposition layer composition.

Due to those inhomogeneities, a periodic regeneration strategy can lead to a break-up of the continuous layer into individual particle structures of soot ash agglomerates [81]. This potentially enables the resulting structures to detach from the filter surface and be transported by the gaseous flow. Such rearrangement events lead to specific deposition patterns of particle structures in the filter channels. The nature and topology of those patterns affect the filter regarding the local flow field, its pressure drop contribution, its loading capacity and the separation efficiency.

Several works can be found attributing different causes and influence factors to individual patterns. Those include a sole distinction between a periodic and continuous regeneration strategy [82], a formulation of required mechanisms [50, 83] and the layer's soot to ash ratio [84]. As those positions, however, do partially contradict each other, a universal and consistent formulation does not exist. In order to derive clear predictions on the formation of specific deposition patterns, the behaviour of individual particulate structures needs to be examined. The investigation of their detachment, acceleration and deceleration, is therefore subject of the present work.

For that, both an experimental and a numerical approach are considered. The prior is used for the examination of the pressure drop characteristics in a previously developed model filter channel and two exemplary detachment scenarios of agglomerates at constant flow velocity. The numerical approach, however, represents the focus of the present work by employing the lattice Boltzmann method (LBM) as an computational fluid dynamics (CFD) approach for surface resolved particle structures submersed in a gaseous fluid flow.

Many scientific works covering different aspects of the filtration process in wall-flow filters, have been published over the past decades. A selection of works focussing on distinct fields relevant for the present studies can be found in a previous work [1]. The review addresses relevant findings on the deposition pattern formation, general numeric approaches to wall-flow filter modelling and covers LBM related research regarding flow through porous media as well as surface resolved particle simulations. It additionally refers to a comprehensive summary of experimental works focussing on filter ash by Wang et al. [58] and a detailed review of wall-flow simulation approaches

by Yang et al. [113]. In a recent study, Trunk et al. [7] present an improved version of the homogenized lattice Boltzmann method (HLBM), which is used as the surface resolved particle approach in the previous work [1]. Here, the three-dimensional case of a sedimenting sphere at different Reynolds numbers, the pinch effect discovered by Segré and Silberberg [136, 137] and the process of a swarm sedimentation were examined and compared with literature data. The work additionally includes a comparison of the different momentum exchange and force methods.

The literature review reveals that no work can be found that investigates the transient behaviour of individual particulate structures inside a wall-flow filter channel. Regarding the numerical approach, no work is known which both provides a consistent calculation of the fluid field in such a filter, while simultaneously considering the transient behaviour of surface resolved particle structures.

This work therefore investigates detachment, acceleration and deceleration of particle structures during filter regeneration with 3D surface resolved simulations using an LBM. This includes a detailed examination of the temporal evolution of the hydrodynamic forces acting on a particle's surface, the particle's position and its velocity for different particle densities and detachment positions. The aim of this work is the determination of relevant key quantities such as impact velocity and stopping distance as well as their interpretation with respect to predictions regarding the nature of resulting deposition patterns.

The remainder of this work is organized as follows: First, the modelling approach and the numerical methods are introduced in Section 3.2 followed by a description of the simulation case setups in Section 3.3. An investigation of the particle-free flow field is then performed in Section 3.4. Section 3.5 presents the results from examining the detachment and transport behaviour of individual particle structures and a qualitative comparison with experimentally determined results. All findings are eventually summarized and concluded in Section 3.6.

3.2 Modelling Approach and Numerical Methods

In the following, the theoretical foundation for the simulation approach used in this work is presented. It briefly covers relevant aspects of the LBM, the modelling of flow through the porous walls and surface resolved particle simulations. Furthermore, the particle mobility and stopping distance are introduced.

3.2.1 Lattice Boltzmann Method

The envisaged investigations in this work require the retrieval of the fluid velocity $u(x, t)$ and the fluid pressure $p(x, t)$ at a three-dimensional position x in time t. The evolution of both quantities can be described by the incompressible Navier-Stokes equations (NSE), which in turn can be recovered using the LBM. The Boltzmann equation provides a mesoscopic description of the dynamics of a gas, which directly result from molecular collisions on a microscopic scale. While it considers a distribution function f rather than individual molecules, it can be shown to lead to solutions of the equations of fluid dynamics on a macroscopic scale [106].

In order to use this relation in a numerical approach, the fluid domain is discretized by a uniformly spaced voxel mesh with spacing δx. Within each node of the resulting lattice at position x and time t, the velocity space is discretized as well. This leads to a set of discrete-velocity distribution functions f_i associated with corresponding discrete velocities c_i. The size of those sets can be chosen according to the physics under study and the employed modelling approaches. A *D3Q19* set of $q = 19$ discrete velocities representing a common choice for three-dimensional simulations is used in this work.

Assuming the absence of additional forces, the lattice Boltzmann equation (LBE) then yields the discrete-velocity distribution function f_i after a discrete time step δt at a neighbouring node. The mesoscopic contribution of molecular collisions on the microscale is modelled by a collision operator, Ω_i for which manifold variants can be found in literature [122, 138, 139]. By providing some characteristic quantities inherent to the physics under study, all lattice related quantities can be described in dimensionless lattice units [106]. When additionally adopting the commonly used choice of $\delta x = \delta t = 1$, the LBE reads

$$f_i(x + c_i, t + 1) = f_i(x, t) + \Omega_i(x, t). \tag{3.1}$$

Analogously to a previous work [1], a Bhatnagar-Gross-Krook (BGK) collision operator [122] with a lattice relaxation time of $\tau = 0.51$

$$\Omega_i(x, t) = -\frac{1}{\tau} \left(f_i(x, t) - f_i^{(eq)}(x, t) \right) \tag{3.2}$$

is used in this work. It represents the relaxation of the discrete distribution function f_i towards its equilibrium $f_i^{(eq)}$ at a single fluid node

$$f_i^{(eq)}(u, \rho) = w_i \rho \left[1 + \left(\frac{c_i \cdot u}{c_s^2} + \frac{(c_i \cdot u)^2}{2c_s^4} + \frac{u^2}{2c_s^2} \right) \right]. \tag{3.3}$$

As the weights w_i for each discrete lattice velocity $\boldsymbol{c}_i$ and the lattice speed of sound c_s are inherent to the chosen velocity set [106], it only depends on the local macroscopic fluid quantities density ρ and velocity $\boldsymbol{u}$. Those can, in turn, be retrieved via the zeroth and first order moments of the discrete distribution function

$$\rho = \sum_{i=0}^{q-1} f_i \qquad \text{and} \qquad \rho\boldsymbol{u} = \sum_{i=0}^{q-1} \boldsymbol{c}_i f_i. \tag{3.4}$$

For a *D3Q19* set, the lattice speed of sound is $c_s = 1/\sqrt{3}$ [106]. By means of the Chapman-Enskog analysis [140], the macroscopic kinematic viscosity can be shown to depend on the relaxation time as

$$\nu = c_s^2 \left(\tau - \frac{1}{2} \right). \tag{3.5}$$

Eventually, the lattice speed of sound c_s can be used to relate the density ρ and pressure p at lattice scale via the isothermal equation of state

$$p = c_s^2 \rho. \tag{3.6}$$

In summary, (3.4), (3.5) and (3.6) provide the link between relevant macroscopic fluid quantities and the mesoscopic LBM approach, which can then be used as an alternative to conventional fluid methods as e.g. the finite volume method (FVM).

As only the left-hand side of the LBE in (3.1) includes neighbouring information, the algorithm can be split into a purely local collision and a subsequent streaming step. While the prior accounts for all collision related calculations, the latter solely propagates the respective distribution functions to the neighbouring nodes. The open source software OpenLB [5] makes use of this LBM inherent property by providing an efficient parallelization strategy and is therefore used throughout the present work.

3.2.2 Porous Media Modelling

A fluid's loss of momentum resulting from passing through a porous medium can be accounted for by means of an effective velocity [115]. As both relaxation time τ, kinematic fluid viscosity ν and the medium's permeability K stay constant throughout a simulation, they can be expressed in form of a *confined permeability* $d \in [0, 1]$ [1]. The permeability's influence on this simple velocity scaling can then be described as

$$\boldsymbol{u}^{eff}(\boldsymbol{x}, t) = d\boldsymbol{u}(\boldsymbol{x}, t) \qquad \text{with} \qquad d = 1 - \tau \frac{\nu}{K}. \tag{3.7}$$

while the non-negativity of all respective quantities guaranties an upper limit of $d = 1$, a minimum permeability K_{min} has to be introduced in order to avoid $d < 0$ and a subsequent reversal of the flow direction.

$$\lim_{K \to \infty} d(K) = 1, \tag{3.8}$$

$$d(K_{min}) = 0 \qquad \text{with} \qquad K_{min} = \tau v. \tag{3.9}$$

3.2.3 Surface Resolved Particle Simulations

In this work, a particle's influence on the fluid flow is modelled with the HLBM [7, 95, 121], which represents a specific form of the partially saturated method (PSM) [120]. The latter are generally characterized by employing a local weighting factor $B(\boldsymbol{x}, t) \in [0, 1]$ as a *cell saturation* differentiating between sole liquid ($B = 1$), sole solid ($B = 0$) and mixed ($0 < B < 1$) contributions at every node with position $\boldsymbol{x}$. A smooth transition layer of width ϵ is used symmetrically at the boundary of a single particle with index k, which can be described by its centre of mass $X_k(t)$ and a given point $\boldsymbol{x}$ on an outward facing normal of the surface

$$B(\boldsymbol{x}, t) = \cos^2 \left(\frac{\pi}{2\epsilon} (\|X_k(t) - \boldsymbol{x}\|_2) \right). \tag{3.10}$$

A detailed description of the particle's shape representation providing the respective normal can be found in Trunk et al. [7]. While in conventional PSM the factor is used to determine a weighted average of fluid and solid collision operators, in HLBM it is directly linked to the confined permeability d in (3.7). This leads to a weighted average of the fluid velocity $\boldsymbol{u}$ and the solid particle velocity $\boldsymbol{u}^S$

$$\boldsymbol{u}^{eff}(\boldsymbol{x}, t) = B(\boldsymbol{x}, t)\boldsymbol{u}(\boldsymbol{x}, t) + (1 - B(\boldsymbol{x}, t))\boldsymbol{u}^S(\boldsymbol{x}, t). \tag{3.11}$$

The opposing force contribution of the fluid on a particle is retrieved by a momentum exchange approach for boundary nodes at $\boldsymbol{x}_b$ originally proposed by Wen et al. [126] but extended for smooth interfaces by Trunk et al. [95]. The resulting force $\boldsymbol{F}_k$ and torque $\boldsymbol{T}_k$ acting on a particle's centre of mass X_k can then be retrieved by simply summing those contributions over all boundary nodes $\boldsymbol{x}_b$ via

$$\boldsymbol{F}_k(t) = \sum_{\boldsymbol{x}_b} \boldsymbol{F}_k(\boldsymbol{x}_b, t) \quad \text{and} \quad \boldsymbol{T}_k(t) = \sum_{\boldsymbol{x}_b} (\boldsymbol{x}_b - X_k(t))\boldsymbol{F}_k(\boldsymbol{x}_b, t). \tag{3.12}$$

The calculation of the resulting force induced particle movement is done by employing simple discrete element method (DEM) formulations as described in Trunk et al. [95].

3.2.4 Particle Mobility and Stopping Distance

The DEM provides the position and the velocity of individual particles at every discrete time step. For multiple similar movement patterns, however, some key parameters can be sufficient to describe relevant transport characteristics. The particle mobility μ_p and the particle relaxation time τ_p represent such parameters which are common in an engineering context [110]. The prior is a measure of the relative ease of following a steady motion, the latter describes the time required for a particle's movement to adapt to new flow conditions. It can be expressed as the product of a particle's mobility μ_p and its mass m_p

$$\tau_p = m_p \mu_p. \tag{3.13}$$

The maximum distance a particle with initial velocity $u_{p,init}$ can travel in still air after the sudden absence of external forces can be described by the stopping distance

$$\Delta l_s = u_{p,init} \tau_p. \tag{3.14}$$

Comparing this parameter to any chosen length Δl, it determines whether that length will be surpassed under the described conditions. With the relative particle velocity u_{rel}, the mobility is commonly defined through the reciprocal of the drag force F_D of a reference sphere with diameter d_p in creeping flow [110]

$$\mu_p = \frac{u_{rel}}{F_D} = \frac{1}{3\pi \nu \rho d_p}. \tag{3.15}$$

In the present work, the stopping distance Δl_s is used to determine, whether the moving particle structures will reach the channel end, once having reached their peak velocity assuming $u_{p,init} = u_{p,x,max}$. It can then be compared against the remaining distance to the wall at maximum velocity $\Delta l_{w,max}$. The fluid velocity in main flow direction decreases continuously over the channel length, so, contrary to the assumption of still air, the flow field exhibits additional pneumatic conveying. As this, however, can only increase the stopping distance, the assumption of still air holds as a borderline criterion.

3.3 Numerical Setups

In the present work, two simulation setups, both representing a single wall-flow filter channel, are used. The first one (*four-channel* setup) is supposed to resemble a realistic channel in a real world filter application. This setup
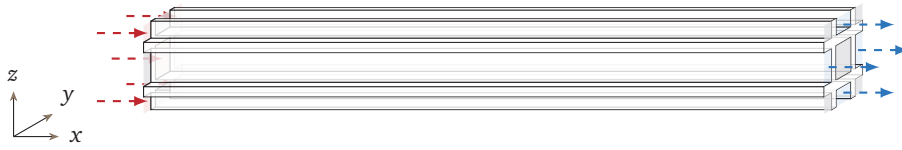
Figure 3.1: *Four-channel setup of one central inflow (red) channel with surround-ing inflow and outflow (blue) channels separated by porous walls. Gray no-slip walls. Sketch is scaled for improved visual clarity.*

is also used for all particle related studies in this work. The second one (*two-channel* setup) is constructed in order to align as closely as possible with a model filter channel from an experimental setup. This includes all simplifications necessary to resemble the construction limitations inherent to the experimental measurement procedure.

While both setups feature an inlet channel with a square cross-section, they differ in the embedding into the surrounding channels, the respective bound-ary conditions, and their scale. Independent of the setup, Dirichlet boundary conditions are applied at the channel inlets in form of a prescribed velocity and channel outlets with a constant pressure. The channel end caps on both sides are accounted for by imposing a no-slip condition. As a BGK-LBM is used to solve the fluid flow equations, no-slip walls are accounted for by a simple bounce-back condition [131] and regularized local boundary conditions [130] at inlet and outlet. The Spaid-Phelan (SP) model [115] is used to model the flow inside the porous walls. For both setups, the fluid flow is assumed to feature ambient conditions as those are present at the experimental setup as well.

3.3.1 Four-Channel Setup

The *four-channel* setup features a centre inflow channel accompanied by four additional quarter-sized inlet channels and four half-sized outflow channels resulting in a total volume of four full channels. All channels are spatially separated by a porous structure. In order to serve as a representation of a real wall-flow filter comprised of hundreds of individual channels, periodic boundary conditions are applied at the four outermost sides surrounding the complete model. In real-world applications, a wall-flow filter is preceded by a relatively large void space inside the filter canning. A non-developed uniform flow profile is therefore assumed at the inflow. The geometric quantities are laid out in Table 3.1.
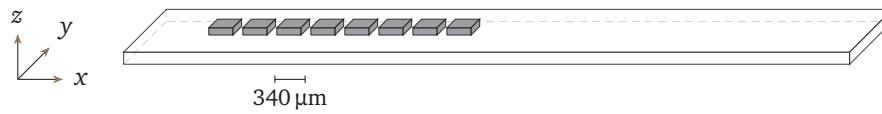
Figure 3.2: *Locations of representative particle structures placed flush on one filter wall at different positions. Dimensions of filter wall are scaled for improved visual clarity.*
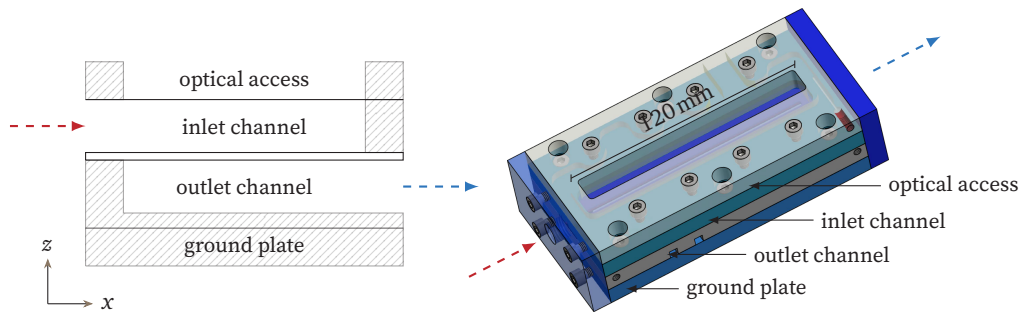
Figure 3.3: *Sketch (**left**) and 3D model (**right**) of stacked layer design used in the experimental setup. Sketch is scaled for improved visual clarity. Arrows indicate inflow (red) and outflow direction (blue).*

Next to the examination of the flow profile along the main flow direction x, this setup is used for the investigation of the transient behaviour of particle structures. For that, a representative particle structure is placed on one of the four filter walls at different locations according to Figure 3.2. The structure is represented by a cubical disk with an edge ratio of $2 \times 2 \times 1$ and a base size of 170 µm associated with its z dimension. Due to its square cross-section, its size will be referred to in form of a 2D quantity in the remainder of this work. The base size results from choosing 10% of the channel width plus half the grid spacing at minimal resolution to the walls on both sides each. As the size of those detaching structures is observed to range between 100 µm and 800 µm in the experiments, a particle structure of 340 µm $\times$ 170 µm fits these findings and is therefore used in this work.

3.3.2 Two-Channel Setup

The *two-channel* setup directly reflects characteristics and restrictions of the model filter channel in Figure 3.3 used for the experimental studies. It consists of a bolted stack of four separate functional layers made of stainless steel plates. In that way, it provides quick and flexible assembly (for e.g. gravimetric analysis)
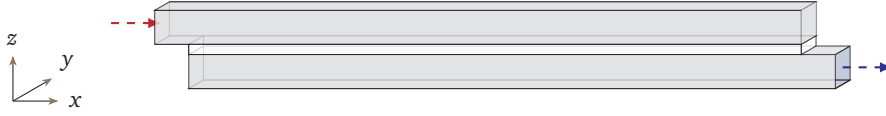
Figure 3.4: *Two-channel setup of one inflow (red) channel and one outflow (blue) channel separated by a porous wall. Both containing an inlet/outlet section of* 5 mm. *Gray no-slip walls. Sketch is scaled for improved visual clarity.*

yet introducing some limitations on the sealing design. Both inlet and outlet channel are integrated into one of the plates each, while the filter medium separating those channels is clamped in between. This construction results in a short inlet and outlet section, in which the fluid cannot already pass through the porous wall. In order to enable the observation of particle structure behaviour, a quartz glass plate is embedded into the top most layer serving as the upper confinement of the inlet channel. This allows the channel over its entire length of 120 mm to be observed with a high-speed camera operating at 500 frames per second (FPS). Heating cords can additionally be installed in two of the layers providing the option of initiating a thermal regeneration of the channel. The specific experimental procedure relevant in the context of this work is described in Section 3.5.4. A more detailed description of the experimental setup and relevant parameters can be found in Thieringer et al. [9].

The requirement of the optical access from at least one direction in the experiment impedes attempts towards a consistent simulation setup regarding the channel embedding. Instead, a single inflow channel and a single outflow channel separated by a porous wall between them are considered here. Due to the short inlet and outlet sections and a preceding pipe supplying the gaseous flow, a Poiseuille-shaped velocity profile [106] is assumed at the inflow. Here, the inflow velocity $\bar{u}_{in}$ is referring to its average. Boundary conditions for the simulation setup were chosen equivalently to the *four-channel* setup while confining the outermost walls with a no-slip condition rather than periodic boundaries.

3.3.3 Discretization

The models' spatial resolution is defined by the number of cells per channel width N assumed for its discretization. Due to the LBM's equidistant grid character, however, only specific resolutions can be considered for each setup in order to guarantee a constant ratio of channel width to wall thickness for the discretized model. Those resolutions can be derived as multiples of the minimum

Table 3.1: *Comparison of channel width l_y, channel length l_x, wall thickness l_w, length of the channel offset l_o caused by the inlet/outlet zone and the minimal channel width resolution of N_{min} for both setups.*

	Four-channel	Two-channel
l_y in mm	1.6	3.0
l_x in mm	120	120
l_w in mm	0.4	0.5
l_o in mm	0.0	10.0
N_{min}	16	30

resolution N_{min} in Table 3.1.

As in three-dimensional LBM simulations the resolution severely impacts the overall computational demand, a resolution close to its respective minimum represents a favourable choice. However, by adopting the SP porosity model [115], a restriction is placed on lowering the resolution by means of the minimum resolvable permeability K_{min} from (3.9). Another restriction on the resolution's lower limit stems from the maximum lattice velocity u_{max} inherent to a diffusively scaled LBM [106], which depends on the inflow velocity $\bar{u}_{in}$ under consideration. In order to a-priori estimate the computational demand, the resolution's dependency on the minimal resolvable permeability and the resulting total number of cells NOC are evaluated and shown in Figure 3.5 for the respective setups. It becomes evident that the intention of resolving smaller permeabilities quickly leads to the necessity of increasing the resolution significantly. With the same resolution, the *four-channel* setup allows for smaller permeabilities than the *two-channel* setup, while the resulting number of cells NOC is much greater. This value can be used to evaluate the feasibility of the simulation, as it could be observed that the computational demand becomes too large when approaching NOC $= 10^9$ with the available resources.

3.3.4 Simulation Run Execution

In each simulation run, the fluid velocity at the inflow is initially ramped-up by a discretization specific start-up time in order to avoid numerical instabilities from initial large gradients. After having reached the actual specified inflow velocity, both pressure and velocity convergence of the whole fluid field are evaluated in reoccurring steps to ensure no left-over effects of the artificial start-up process. Analogously to Hafen et al. [1], the convergence of a flow quantity χ
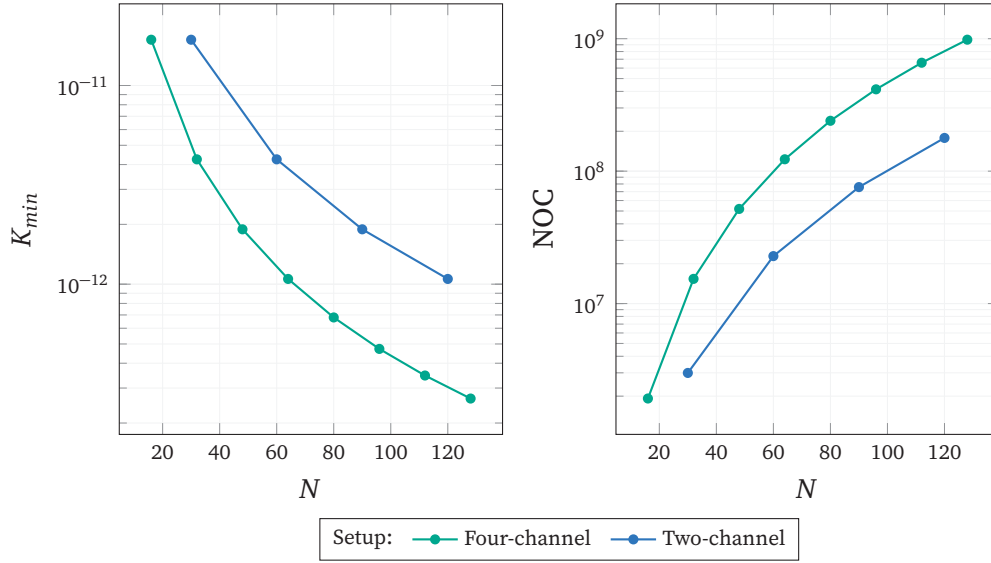
Figure 3.5: *Dependency of minimum resolvable permeability K_{min} in m^2 (**left**) and total number of cells NOC (**right**) on resolution N for both setups.*

is determined by evaluating whether the standard deviation σ of the quantity becomes smaller than a predefined residuum r multiplied by the average $\bar{\chi}$ over the last T time steps

$$\sigma(\chi) = \sqrt{\frac{1}{T+1} \sum_{t=1}^{T} (\chi_t - \bar{\chi})^2} < r\bar{\chi}. \tag{3.16}$$

In this context, the kinetic energy and the lattice density averaged by the total cell number M

$$\chi_t(\boldsymbol{u}) = \frac{1}{M} \sum_{m=1}^{M} \left(\frac{1}{2} \|\boldsymbol{u}\|^2 \right)_m \qquad \text{and} \qquad \chi_t(\rho) = \frac{1}{M} \sum_{m=1}^{M} \rho_m \tag{3.17}$$

are considered right after being calculated via the moments according to (3.4). Simulation runs including particle movement are conducted by first simulating the fluid field around a static particle structure placed at the respective position. When convergence is reached at $t = 0\,\text{s}$, the particle is released from its static state and movement is considered.

3.4 Investigation of the Particle-Free Fluid Flow Field

Prior to considering the actual movement of particulate structures, the particle-free flow is examined in detail. First, the *two-channel* setup is used to retrieve a physically sensible substrate permeability by performing aligned experimental and numerical pressure drop studies. Afterwards, the influence of permeability and channel length on the pressure and velocity distribution in the inflow channel of the *four-channel* setup is analysed. All simulations are run until reaching a convergence criterion for both average kinetic energy and average lattice density. The respective residuals of $r_{\bar{u}} = 10^{-7}$ and $r_\rho = 10^{-6}$ are derived from a single simulation run, which was selected as a representative one.

3.4.1 Retrieval of Substrate Permeability via Two-Channel Setup

While the substrate's permeability represents a given material property in the experimental setup, it has to be provided as an input parameter in the simulation runs. Assuming the same overall pressure-flux relation due to the aligned boundary conditions in both approaches, a comparison between them enables the retrieval of the substrate permeability. In order to ensure a physically sensible value, the pressure drop between inlet and outlet is measured in the experimental setup for different flow rates. All measurements are then repeated three times to provide a representative experimental data basis.

The simulation setup is used analogously to determine the respective pressure drop for different flow rates while varying the substrate's permeability. Initially, values commonly reported in literature [132] are used. In order to ensure numerical stability for inflow velocities up to $\bar{u}_{in} = 14.0\,\text{m/s}$, a relatively high resolution of $N = 90$ corresponding to a total number of cells of $\text{NOC} = 7.6 \times 10^7$ is chosen. The resulting flow for an inflow velocity of $\bar{u}_{in} = 1.0\,\text{m/s}$ assuming a permeability of $K = 4.3 \times 10^{-12}\,\text{m}^2$ is shown in Figure 3.6. By comparing the resulting pressure drop between experiment and simulation, the prescribed permeability is adapted until achieving a satisfactory accordance taking the standard deviation of the experimental results into account. The pressure drop for each flow rate including the standard deviation for the experimental measurements are displayed in Figure 3.7 for both approaches. It can be observed that a permeability of $K = 4.3 \times 10^{-12}\,\text{m}^2$ agrees well with the experimentally determined relation between inflow velocity and pressure drop. When using the SP model [115], this value is therefore assumed to ensure a correct material property representation of substrates commonly used in wall-flow filters.
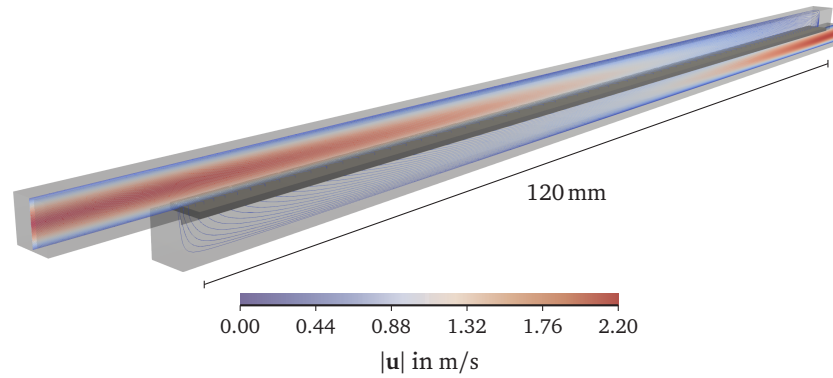
Figure 3.6: *Particle free flow inside two-channel setup with an inflow velocity of $\bar{u}_{in} = 1.0\,\text{m/s}$, a permeability of $K = 4.3 \times 10^{-12}\,\text{m}^2$ and a resolution of $N = 90$. Dark gray structures represent filter substrate. Streamlines exhibit local flow direction. Colour scale indicates local velocity magnitude.*
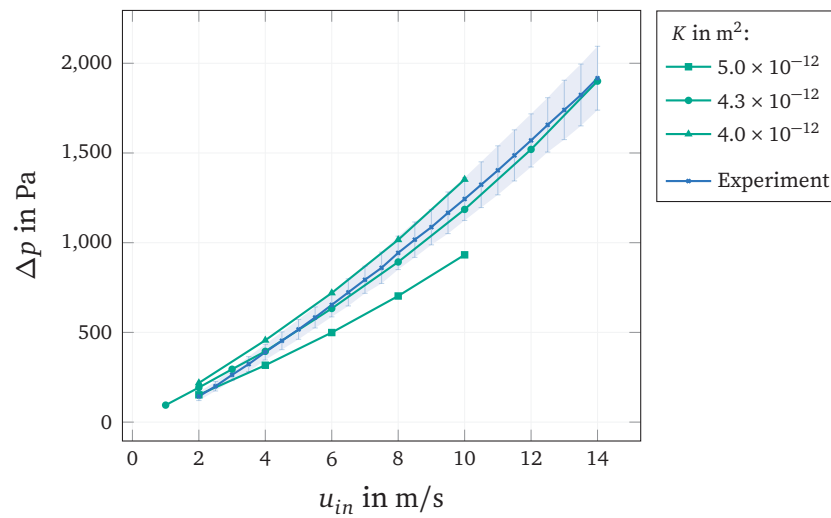
Figure 3.7: *Dependency of pressure drop Δp on inflow velocity $\bar{u}_{in}$ in two-channel setup for simulations with different permeabilities K and experiment. Shaded area indicates standard deviation of experimental results.*
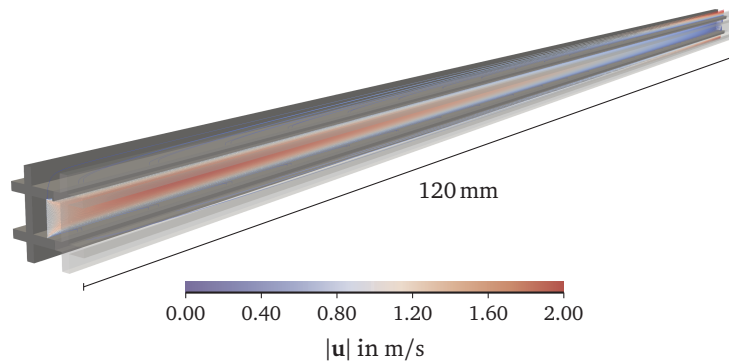
Figure 3.8: *Particle free flow inside four-channel setup with an inflow velocity of $\bar{u}_{in} = 1.0\,\text{m/s}$, a permeability of $K = 4.3 \times 10^{-12}\,\text{m}^2$ and a resolution of $N = 96$. Dark gray structures represent filter substrate. Colour scale indicates local velocity magnitude.*

3.4.2 Four-Channel Setup

As the following investigations of particle movements are conducted in the *four-channel* setup, the analysis of the resulting flow field is performed in more detail in order to examine the conditions the particulate structures are exposed to. Albeit assuming the previously determined value of $K = 4.3 \times 10^{-12}\,\text{m}^2$ for most studies, multiple simulations are performed with different substrate permeabilities in order to investigate its influence. The resulting flow field for an inflow velocity of $\bar{u}_{in} = 1.0\,\text{m/s}$ and a permeability of $K = 4.3 \times 10^{-12}\,\text{m}^2$ is shown in Figure 3.8. Here, a resolution of $N = 96$ is chosen initially to provide a good agreement with the *two-channel* setup. In order to reduce the computational demand, however, a resolution of $N = 48$ is used for the following studies, as it still provides a sufficient minimal permeability of $K_{min} = 1.89 \times 10^{-12}\,\text{m}^2$ according to Figure 3.5.

The acceleration or deceleration of a gas-borne particulate structure is characterized by the relative velocity between the structure and the surrounding gaseous flow. Therefore, the velocity in main flow direction and its evolution along the channel length is the single most important dynamic influence factor in a non-reactive flow. Figure 3.9 shows the respective velocity and the pressure averaged at fifty discrete locations over the inflow channel's cross-section chosen independently of the lattice discretization. As the last position in the inflow channel ($x = 120\,\text{mm}$) and the first one in the outflow channel ($x = 0\,\text{mm}$) is located inside the solid wall, no fluid information can be retrieved here. It
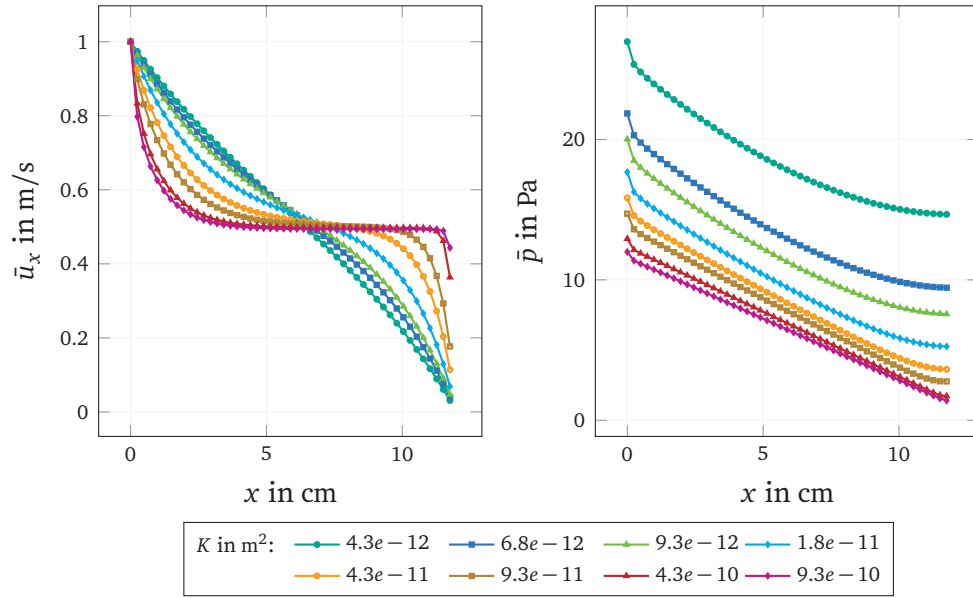
Figure 3.9: *Velocity profiles $\bar{u}_x(x)$ and pressure profiles $\bar{p}(x)$ in full length inlet channel domain for an inflow velocity of $\bar{u}_{in} = 1.0\,\text{m/s}$ and different substrate permeabilities.*

can be seen, that the substrate permeability has a significant impact on the nature of the velocity distribution over the channel length: Inside the inlet channel, the velocity always covers the range of $\bar{u}_{in}$ at the inlet to zero inside the backside wall. Due to the discrete sampling, however, the velocity at the last fluid covered position differs from zero depending on the intensity of the flow being directed to the outlet in the outflow channel. This becomes apparent for very low permeabilities, where the flow can pass the inlet channel nearly uninterrupted before abruptly reaching the back wall. The velocity course approaches a linear descent when reducing the permeability. While the channel mid is nearly unaffected, such a reduction leads to increased velocities at the channel front, which in turn increases the likelihood of the detachment of particulate structures. The opposite generally applies to the channel back while the deceleration of those structures also depends on their current momentum. The pressure evolution in the inlet channel is both characterized by a distinct profile and an absolute pressure drop owing to the porous wall between the channels. For higher permeabilities, the latter reduces to zero and the profile exhibits a linear slope as the porous walls mostly serve the purpose of a momentum sink rather than guiding the fluid flow. It can generally be observed, that the
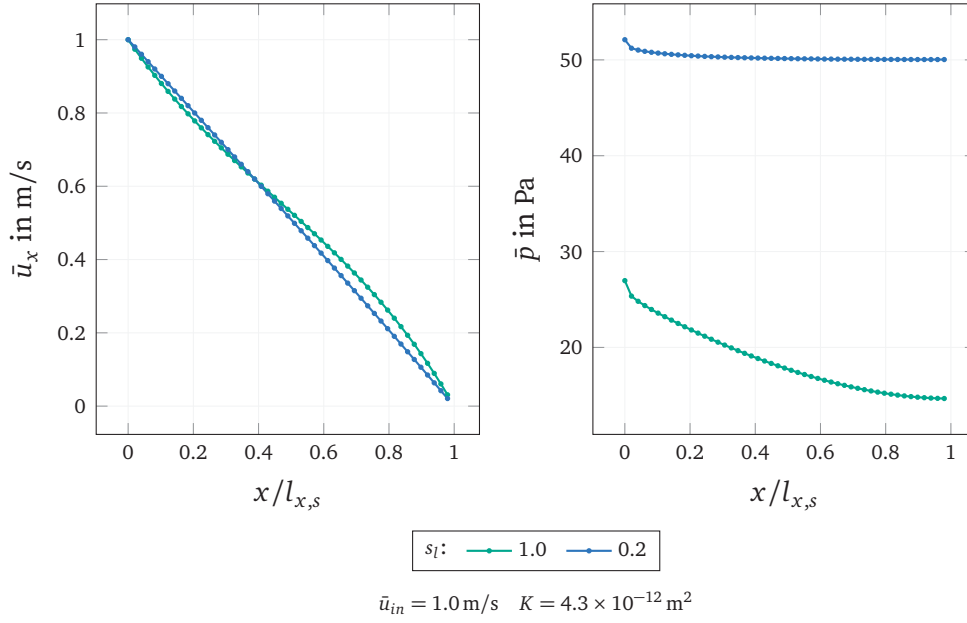
Figure 3.10: *Velocity profiles $\bar{u}_x(x)$ and pressure profiles $\bar{p}(x)$ in inlet channel domain with a permeability of $K = 4.3 \times 10^{-12}\,\mathrm{m^2}$ for different scaling factors s_l.*

permeability has a great impact on both quantities. Therefore, the permeability of $K = 4.3 \times 10^{-12}\,\mathrm{m^2}$ derived by the *two-channel* setup will be assumed for the following particle related studies in order to ensure a realistic environment.

A resolution of $N = 48$ cells per channel diameter leads to models of nearly $NOC = 52 \times 10^6$ computational cells for the *four-channel* setup. Compared to the retrieval of a converged particle-free fluid field, however, the examination of particle-laden flows requires additional computations per time step, the simulation of longer physical time spans and more simulations runs in order to allow for the envisaged parameter variations. By reducing the channel length, a great reduction in computational demand can be achieved, while ensuring the same resolution and similar flow characteristics for a permeability of $K = 4.3 \times 10^{-12}\,\mathrm{m^2}$. With the introduction of a scaling factor s_l, a scaled length can be described by

$$l_{x,s} = s_l l_x. \tag{3.18}$$

The velocity and pressure distribution for both the full channel length ($s_l = 1.0$) and a fifth of it ($s_l = 0.2$) are shown in Figure 3.10. The pressure profile shows significant differences, especially considering its absolute value due to the reduction of the total filtration area. Resulting from the conservation of mass,

the average wall penetrating velocity

$$\bar{u}_w = \frac{l_y}{4l_{x,s}}\bar{u}_{in}$$
(3.19)

can directly be related to the inlet velocity $\bar{u}_{in}$ and the channel's dimensions. A scaling factor of $s_l = 0.2$ does, therefore, lead to a much higher pressure drop owing to the increased wall penetrating velocity. Contrary, the velocity profile of the scaled channel exhibits a similar profile to the one of the full-length version while featuring an even more linear form. Thus, it is reasoned that a realistic particle behaviour can be retrieved within a scaled channel geometry with comparably small substrate permeabilities without any loss of generality. A scaling factor of $s_l = 0.2$ is therefore used for all particle related studies described in the following.

3.5 Investigation of Particle Movement

Rearrangement events during filter regeneration can cause a transition from a homogeneous deposition layer to an accumulation of particulate matter residing between the channel's mid [84] and its end [50, 83]. Their nature and occurrence is determined by three sub-mechanisms: After exposing individual layer fractions to the flow by breaking up the continuous layer, those structures need to be re-entrained into the flow and transported by pneumatic conveying [83]. While layer break-up is not the subject of the present work, both detachment of individual layer fractions and their transport are examined. First, the transient particle movement of a single representative simulation run is analysed and relevant key parameters are derived. Then, the detachment from the substrate's surface at different positions $x_{p,0}$ is examined by means of the acting forces. Eventually, the transport of individual particulate structures is analysed for different starting positions $x_{p,0}$, substrate permeabilities K, inflow velocities $\bar{u}_{in}$ and particle densities ρ_p. In order to improve the reader's orientation in the individual studies, constant parameters not included in the respective parameter variations are listed below each plot.

3.5.1 Examination of Transport Characteristics

According to the description in Section 3.3.4, the particle's movement is considered once pressure and velocity convergence have been determined. Figure 3.11 provides a visualization of the particle structure's transport starting from a
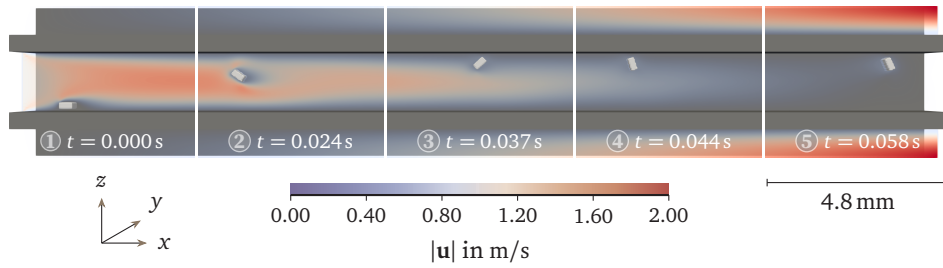
Figure 3.11: *Time series of detachment and transport of a particle structure inside four-channel setup. Inflow velocity of $\bar{u}_{in} = 1.0\,\text{m/s}$ and scaling factor of $s_l = 0.2$.*

position close to the inlet for five selected points in time **T1, T2, T3, T4** and **T5**. Initially, the particulate structure resides on the wall's surface enclosed tightly by the passing fluid. After release, it detaches and entrains into the flow while accelerating quickly. This entrainment is accompanied by a slow but steady upward motion towards the channel's upper wall. Due to its irregular shape and the resulting varying flow conditions it tumbles during its traversal through the channel. Right before hitting the back wall, it can be observed to decelerate while accelerating the nearby fluid in an otherwise nearly still surrounding due to its momentum inherited from the previous acceleration.

The evolution of the particle velocity u_p and the hydrodynamic force F are shown in Figure 3.12 separated into their x and z components. The particulate structure's velocity increases immediately after release. The velocity in z-direction exhibits an initial increase but drops to zero quickly after approaching the upper channel wall. The x-component, however, exposes of a distinct pattern of velocity increase, peak $u_{p,x,max}$ at t_{max} and decrease before impacting the back wall at t_{imp} with velocity $u_{p,imp}$. This behaviour is caused by the hydrodynamic forces acting on the structure's surface. It can be seen that the acceleration and deceleration phase can clearly be identified from the force in x-direction, which changes its sign by crossing the zero line at t_{max}. The force in z-direction is much smaller and features a less distinct behaviour while fluctuating around zero. The initial values $F_{x,0}$ and $F_{z,0}$ characterize the structure's ability to detach from the filter surface. It can be observed that the initial force in x-direction is much higher than in z-direction.
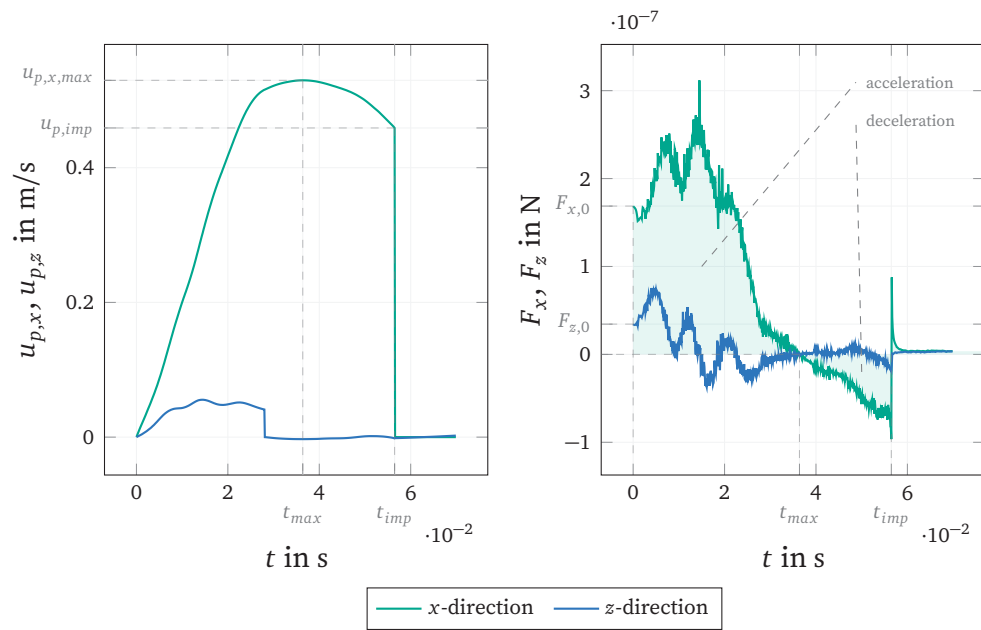
Figure 3.12: *Transient behaviour of particle velocity $\mathbf{u}_p$ and surface force $\mathbf{F}$ in x and z direction. Starting position of $x_{p,0}/l_{x,s} = 0.05$, particle density of $\rho_p = 500\,\text{kg/m}^2$.*

3.5.2 Detachment

The detachment of particulate structures inside a wall-flow filter channel is determined by the relation between adhesive and hydrodynamic forces acting on the particle's surfaces. A single detachment event can be caused by either increasing the hydrodynamic forces or reducing the adhesive ones. The prior results from an increased flow rate or a greater exposition of the structure's surface. The latter can, on the one hand, be caused by a reduction of connecting soot matter due to its reaction during filter regeneration. On the other hand, it can be caused by a continuous exposition to hydrodynamic forces being on the verge of overcoming the respective adhesive contributions over a certain period of time. When considering multiple detachment events, another possibility is an increase of the surface force due to the direct momentum transfer of a colliding second structure.

Due to those manifold mechanisms, the present work does not aim at assessing the occurrence of detachment events at this point. It rather provides insights into the borderline adhesive forces that need to be overcome for given flow conditions. In order to provide a close-up of the detachment process at **T1** in the time series shown in Figure 3.11, four successive sub time steps **T1a**, **T1b**, **T1c** and **T1d** are selected and displayed in Figure 3.13. Before release, the particulate structure rests flush on the filter wall at **T1a**. The passing flow circumvents the obstacle while slowing down right behind it. The detachment in **T1b** starts with a lift-off of the front surface and a following tilting around its y-axis. When fully erected in **T1c**, the structure exposes a large surface area opposing the main flow direction and reaches further into the core flow of higher velocities. This results into an increase in the hydrodynamic force eventually causing the structure to separate from the surface in **T1d** and re-suspend into the gaseous flow.

In order to investigate the influence of the relative channel location, the transient behaviour resulting from a release at different starting positions $x_{p,0}$ is examined. The course of the force's x and z-component is shown in Figure 3.14 for five exemplary positions. The development of the force F_x directly reflects the observed behaviour described above: Right after release, the force increases due to the enlargement of the affected surface area reaching its maximum in **T1c**. The subsequent tumbling results in an oscillation followed by a steep decrease due to a reduction of the relative particle velocity. For positions closer to the channel end, the absolute value decreases and the distinct pattern gradually evens out. Nonetheless, every position features a clear traversal from a positive
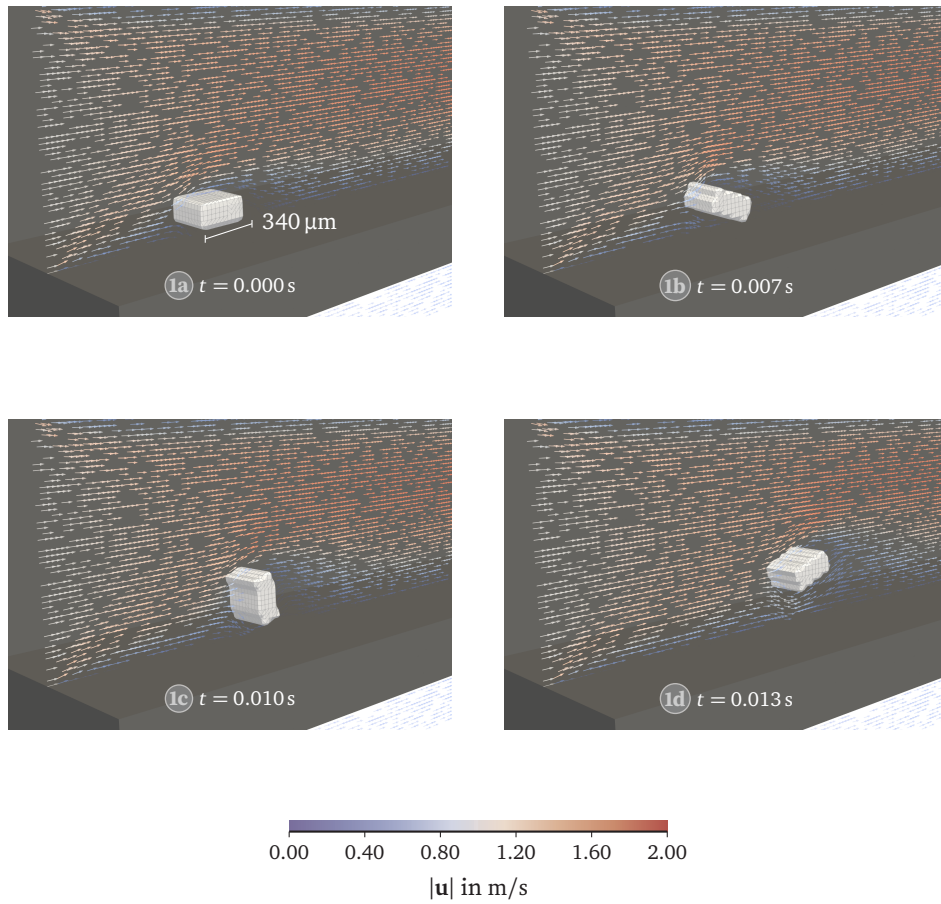
Figure 3.13: *Close-up of detachment process of particle structure from porous filter wall. Inflow velocity of $\bar{u}_{in} = 1.0\,\text{m/s}$. Arrows indicate direction and magnitude of local flow velocity.*
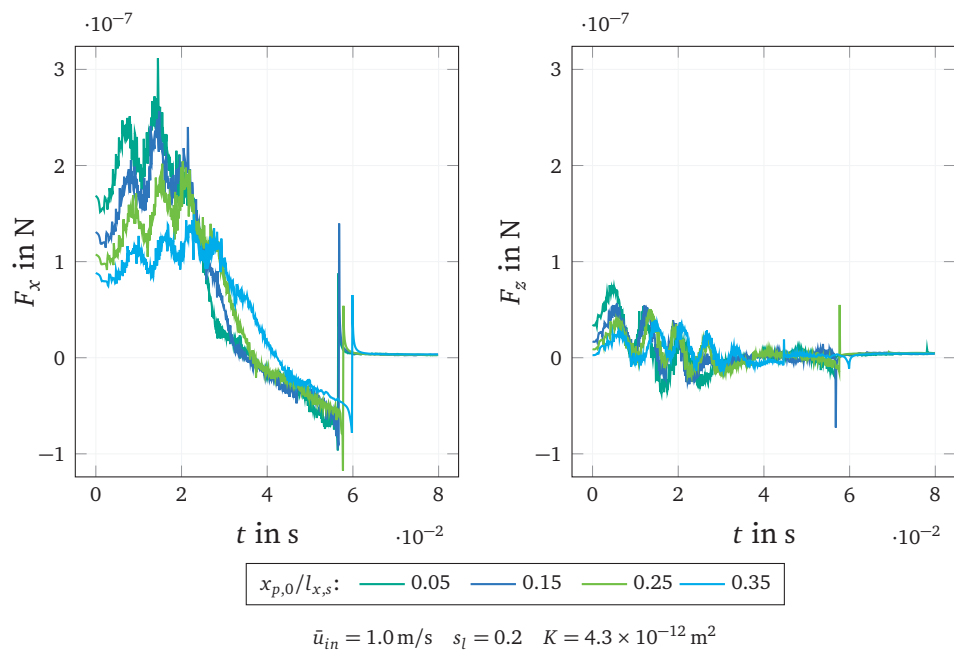
Figure 3.14: *Transient development of surface force* ***F*** *in x and z direction for different starting positions* $x_{p,0}$. *Particle density of* $\rho_p = 500\,\text{kg/m}^3$.

$\cdot 10^{-7}$
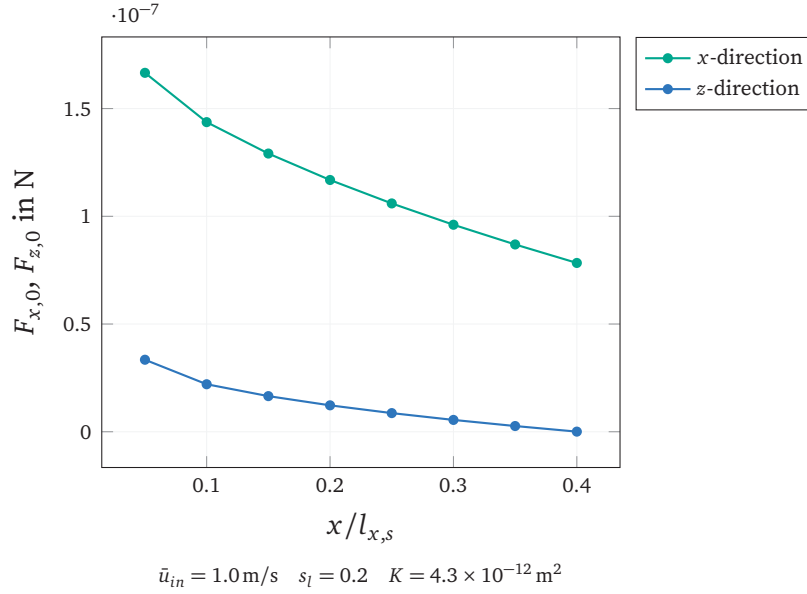
Figure 3.15: *Dependency of initial force value F_0 in x and z direction on the starting position $x_{p,0}$.*

to negative force before hitting the back wall. The force in z-direction is affected by the starting position similarly as the amplitude of the fluctuating behaviour gradually decreases.

The detachment itself is mainly affected by the force at time $t = 0\,\text{s}$. The dependency of those initial values on the starting position is shown in Figure 3.15. It becomes evident that the force in x-direction exceeds the one in z-direction by at least a factor of four in every case, while both decrease towards the channel end. As described via (3.12), those values stem from summing the force contributions at all boundary nodes and applying those to the particle's centre of mass. As the bottom surface is not accessible for the fluid, the individual contributions can act only on the particle's sides and its top surface. This uneven distribution results in a large torque around the y-axis leading to the immediate tilt of the particle in **T1b**. It can therefore be reasoned that a detachment of particle structures with similar form will most likely be caused by a rotational movement due to the x-directed force contributions rather than the significantly smaller lift force in z-direction.
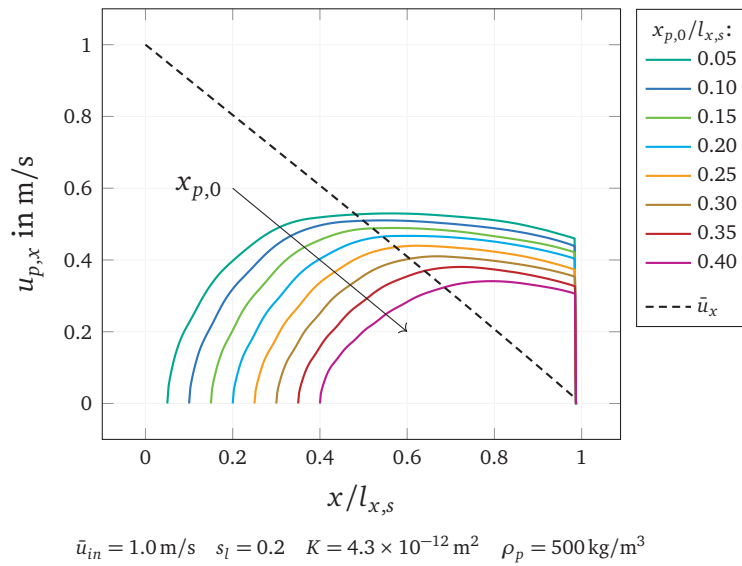
Figure 3.16: *Particle velocity in x direction $u_{p,x}$ for different starting positions $x_{p,0}$ at density of $\rho_p = 500\,\text{kg/m}^3$. Velocity profile $\bar{u}_x(x)$ of particle-free case as reference.*

3.5.3 Transport

In order to evaluate a particle's behaviour while traversing along the channel, its current relative position in the channel x_p is mapped to the absolute channel position x at the respective time t. Figure 3.16 shows the dependency of the particle's velocity in x-direction on the current channel position for different starting positions $x_{p,0}$. The x-component of the position dependent fluid velocity $\bar{u}_x$ for the particle free flow is added as well. Independent of the starting position, the velocity can analogously to Figure 3.12 be seen to increase initially, but decrease towards the channel end. For starting positions approaching the channel's rear, however, both maximum velocity $u_{p,x,max}$ and impact velocity $u_{p,imp}$ become smaller. This behaviour can directly be attributed to the relative velocity between the position dependent fluid velocity $\bar{u}_x$ and the particle velocity $u_{p,x}$, which can be derived directly from Figure 3.16. Big differences in both velocities lead to large accelerations or decelerations depending on their sign. Independent of the starting position, all particles are impacting the back wall with a velocity differing significantly from zero.

In Figure 3.10 a negligible dependency of the scaling factor s_l on the fluid velocity profile was shown for a permeability of $K = 4.3 \times 10^{-12}\,\text{m}^2$. The respective relations for higher permeabilities and their impact on the particle
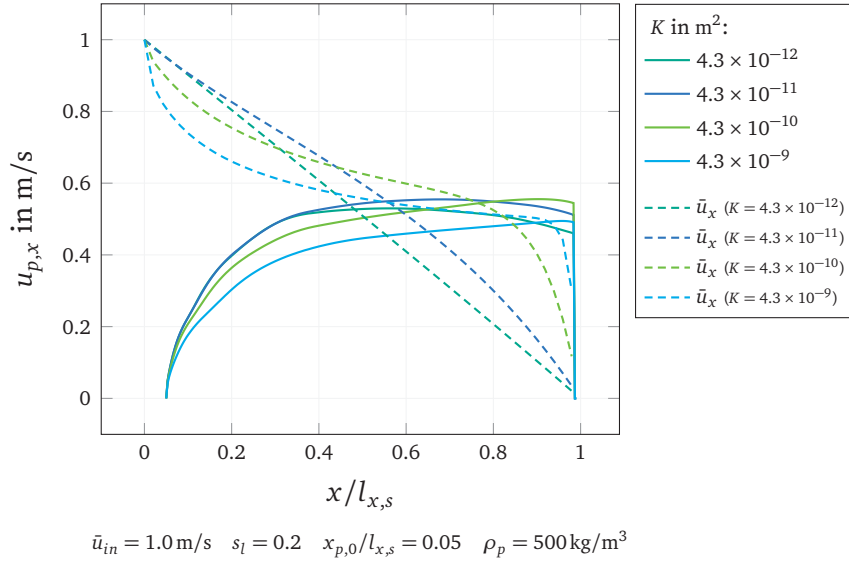
Figure 3.17: *Particle velocity in x direction $u_{p,x}$ for different substrate permeabilities K with starting position $x_{p,0}/l_{x,s} = 0.05$. Respective velocity profiles $\bar{u}_x(x)$ of particle-free cases as reference.*

structures' dynamic behaviour are displayed in Figure 3.17. The profiles of $\bar{u}_x$ for a scaling of $s_l = 0.2$ share the same general behaviour with the full length version displayed in Figure 3.9, however expose a smaller sensitivity to an increase of the substrate permeability. For higher permeabilities, the flow velocity decreases in the channel's front section and leads to smaller acceleration of a detached particle structure. Its impact velocity, however, additionally depends on the onset of deceleration enabling particle structures to potentially approach the wall with a greater velocity despite its initially smaller acceleration (e.g. for $K = 4.3 \times 10^{-9}\,\text{m}^2$). This shows that the permeability affects the structure's trajectories in a non-trivial manner and should therefore be chosen as close to a realistic value as possible. The following studies, therefore, exclusively consider a substrate permeability of $K = 4.3 \times 10^{-12}\,\text{m}^2$.

The overall magnitude of the linearly decreasing axial flow velocity is determined by the inflow velocity $\bar{u}_{in}$ which, in turn, directly dictates the profile of the axial particle velocity $u_{p,x}$. The extent of this influence is shown for two exemplary starting positions $x_{p,0}/l_{x,s} = 0.05$ and $x_{p,0}/l_{x,s} = 0.4$ in Figure 3.18. Next to the expected differences in the trajectory's magnitude, a shift of the maximum velocity $u_{p,x,max}$ towards the channel's rear can be observed for greater
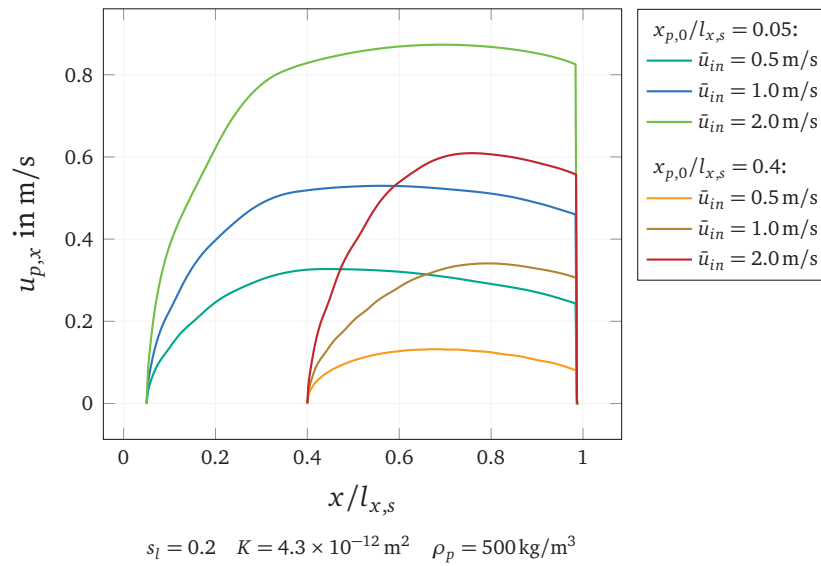
Figure 3.18: *Particle velocity in x direction $u_{p,x}$ for different inflow velocities $\bar{u}_{in}$ with exemplary starting position $x_{p,0}/l_{x,s} = 0.05$ and $x_{p,0}/l_{x,s} = 0.4$.*

inflow velocities. This exposes a longer acceleration time, leaving less remaining distance for the deceleration of the particle structure. This effect combined with the greater magnitude leads to increased impact velocities $u_{p,imp}$ at the channel end.

The dependency on the particle density ρ is shown in Figure 3.19 for the same starting positions. It can be observed that the particle structure density directly defines the intensity of acceleration and deceleration due to the relative velocity. While lower densities clearly lead to higher peak velocities, such a dependency does not hold for the impact velocity. A particle with a density of $\rho_p = 100.0\,\text{kg/m}^3$ is able to quickly adapt to the surrounding fluid conditions. Despite its high peak velocity, it features a steep velocity decrease in the channel back eventually resulting in a comparably small impact velocity.

In order to evaluate the impact of the particle density for different starting positions, the peak velocity $u_{p,x,max}$ and the impact velocity $u_{p,imp}$ are retrieved for multiple simulations and displayed in Figure 3.20. The same tendencies as discussed previously can be observed: The peak velocity decreases both with higher densities and advancing starting positions. The impact velocity, generally decreases towards the channel end, but exhibits a less predictable behaviour for smaller densities. Studying said parameter enables predictions

$\bar{u}_{in} = 1.0\,\text{m/s} \quad s_l = 0.2 \quad K = 4.3 \times 10^{-12}\,\text{m}^2$
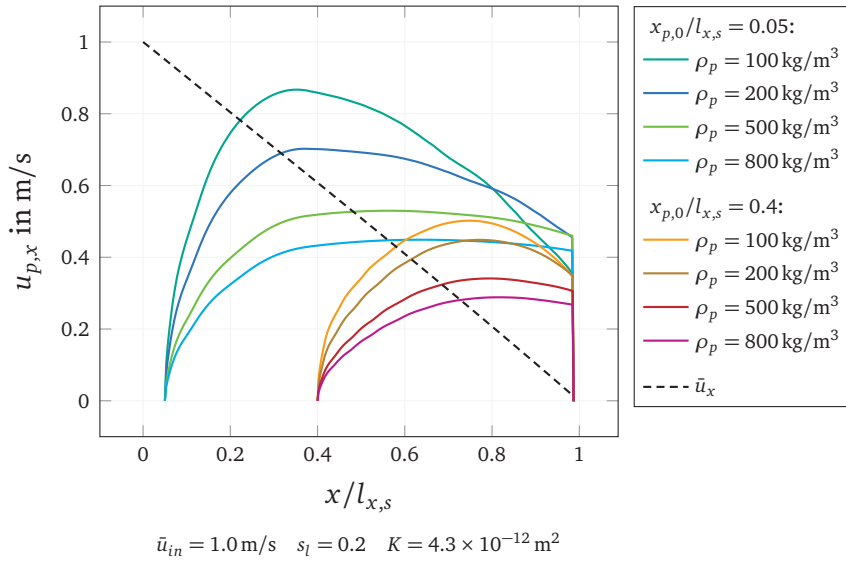
Figure 3.19: *Particle velocity in x direction $u_{p,x}$ for different densities with exemplary starting position $x_{p,0}/l_{x,s} = 0.05$ and $x_{p,0}/l_{x,s} = 0.4$. Velocity profile $\bar{u}_x(x)$ of particle-free case as reference.*

$\bar{u}_{in} = 1.0\,\text{m/s} \quad s_l = 0.2 \quad K = 4.3 \times 10^{-12}\,\text{m}^2$
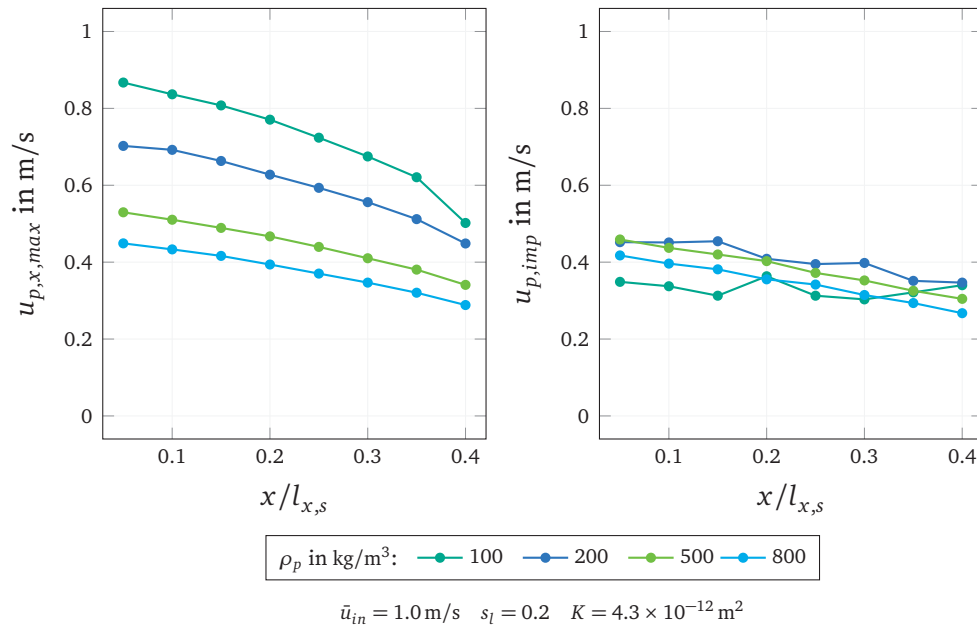
Figure 3.20: *Dependency of peak velocity $u_{p,x,max}$ and impact velocity $u_{p,imp}$ on the starting position $x_{p,0}$ for different particle densities ρ_p.*
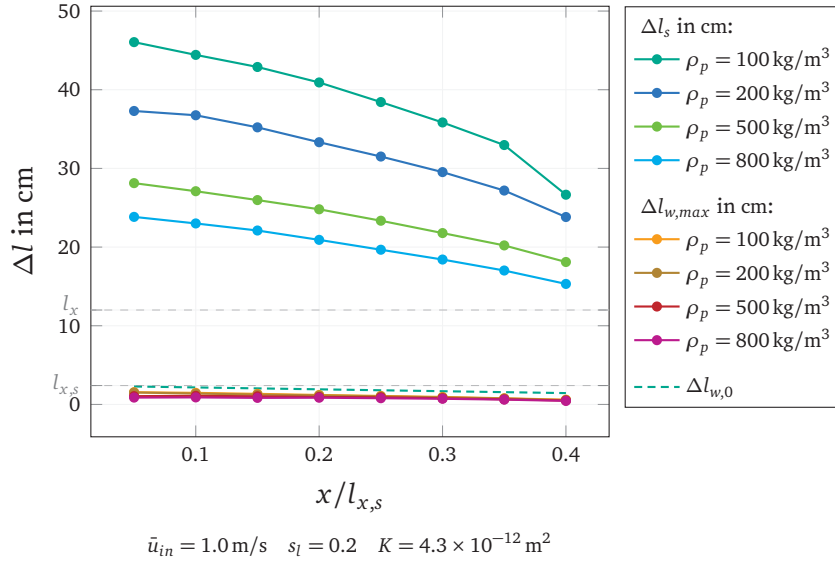
Figure 3.21: *Dependency of stopping distance Δl_s and distance to wall in x direction at maximum velocity $\Delta l_{w,max}$ on starting position $x_{p,0}$ for different particle densities ρ_p. Distance to wall in x direction at starting position $\Delta l_{w,0}$ as reference. Guidelines at l_x and $l_{x,s}$ indicate full and scaled channel length.*

for the packing density of accumulations at the channel end. It can, therefore, be assumed that particle structures detaching in the channel's front section are more likely to cause dense packings due to their elevated impact velocity.

Eventually the stopping distance Δl_s as introduced in Section 3.2.4 is evaluated for different starting positions and particle densities. The distance to the back wall from the respective position of the maximum velocity $\Delta l_{w,max}$ is calculated as well. The resulting values are shown in Figure 3.21. Due to the constant mobility of $\mu_p = 33.78 \times 10^6$ s/kg, the stopping distance exhibits the same characteristics as the peak velocity in Figure 3.20: It can be observed that the stopping distance exceeds the remaining distance to the back wall significantly in every case. By means of this engineering motivated parameter it can directly be deduced that within the range of the investigated parameters a particle is very likely to always hit the back wall once detached. While the described studies were exclusively performed on a scaled channel geometry with length $l_{x,s}$, Figure 3.21 reveals that the stopping distance even exceeds the unscaled total channel length l_x. This eventually proves the applicability of the scaling methodology, as it reduces computation times while being capable of

leading to statements which are generalizable to the full length setup as well.

3.5.4 Comparison With Experimental Results

The plausibility of the presented results is assessed by comparing them to some exemplary ones retrieved from the experimental setup (cf. Section 3.3.2). Prior to the detachment experiments, a continuous particle layer is prepared from soot particles and glass spheres serving as ash replacement. The loaded channel is subsequently utilized to investigate the detachment and transport behaviour of individual agglomerates. While observing the entire model filter channel with a high speed camera, a particle-free air flow with a defined inflow velocity at ambient conditions is routed through the filter. The inflow velocity is then slowly increased in small increments until individual agglomerates detach and are transported through the inlet channel. The discrete change in an agglomerates position is extracted by determining its centre from the recording via image processing. Its size is determined by evaluating the longest chord of both length and width at the time of its detachment as a 2D quantity. Due to a single camera perspective, the thickness of such agglomerates cannot be specified.

Two experimental runs with different resulting particle dimensions (500 μm × 300 μm and 800 μm × 400 μm) are considered within a comparison with simulation results. Both detachment events occurred at an inflow velocity of $\bar{u}_{in} = 15.0$ m/s close to the channel inlet. Due to this great value, an inflow velocity of $\bar{u}_{in} = 2.0$ m/s representing the highest one considered in the present work is used for the comparison. As a particle density of $\rho_p = 100.0$ kg/m³ leads to the most pronounced acceleration and deceleration behaviour (cf. Figure 3.19) due to the smallest particle relaxation time according to (3.13), it is selected here.

The temporal velocity evolutions of all runs normalized by their respective peak velocities $u_{p,x,max}$ are displayed in Figure 3.22. In contrast to the inflow velocity considered in the simulation setup, the inflow velocity causing detachment in the experimental runs of $\bar{u}_{in} = 15.0$ m/s is much higher. This difference can directly be attributed to the differing initial conditions, as the continuous layer surrounding the particle fractions increases adhesion and decreases the surface area accessible for the fluid flow. Additionally, the resulting agglomerate sizes are greater than the particle structures' size of 340 μm × 170 μm considered for the simulation setup. Those differences, therefore, impede a comparison of the detachment behaviour. The particles' transport characteristics can, however, be used within a qualitative comparison. Both experimental runs exhibit
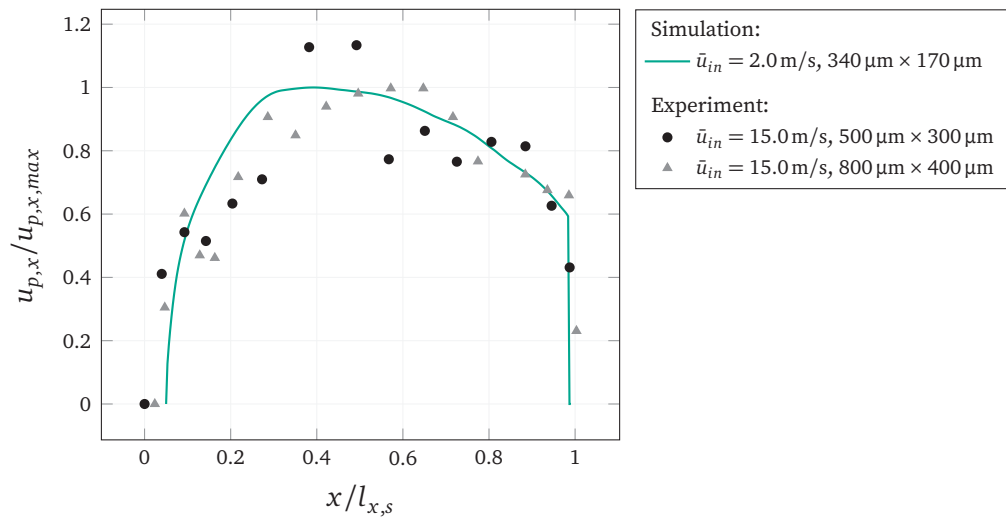
Simulation: $\bar{u}_{in} = 2.0\,\text{m/s}$ $s_l = 0.2$ $x_{p,0}/l_{x,s} = 0.05$ $K = 4.3 \times 10^{-12}\,\text{m}^2$ $\rho_p = 100.0\,\text{kg/m}^3$

Experiment: $\bar{u}_{in} = 15.0\,\text{m/s}$ $K \approx 4.3 \times 10^{-12}\,\text{m}^2$

Figure 3.22: *Comparison of normalized particle velocity in x direction $u_{p,x}/u_{p,x,max}$ between exemplary simulation and experimental results. Determination of $u_{p,x,max}$ of experimental runs by polynomial fit of data points.*

similar features to the simulation results presented above: After a steep increase in the fluid velocity, it reaches a maximum $u_{p,x,max}$, eventually decreases and hits the wall with a non-negligible velocity $u_{p,imp}$. The run closer to the inlet also exposes a higher peak velocity. Due to the small number of data points at this moment, however, the discrete description of the velocity development is subject to high fluctuations.

3.6 Conclusion

This work investigates the detachment and transport behaviour of particle structures during filter regeneration with 3D surface resolved simulations using an LBM. First, the particle-free flow field inside a single wall-flow filter channel was analysed using two different simulation setups. The prior allowed for a pressure drop comparison with experimental investigations and lead to the determination of a physically sensible substrate permeability of $K = 4.3 \times 10^{-12} \, \text{m}^2$. With the second setup, it could be shown that the permeability does not only have an impact on the pressure drop, but also a significant one on the velocity profiles, which can be differentiated by referring to the channel's front and its back section. The influence of the channel scaling on the form of the velocity profile could be shown to be negligible for a permeability of $K = 4.3 \times 10^{-12} \, \text{m}^2$. On this basis, the transient behaviour of single particle structures with a base size of 170 μm and different densities was examined. First, the general transport characteristics were determined identifying several key parameters utilizable for a standardized comparison of different simulation and experiment runs. Those include the peak velocity, the impact velocity and the stopping distance. In order to assess the likelihood of a detachment from the channel surface, the hydrodynamic forces in tangential and normal flow direction were analysed. It could be shown that detachment is more likely caused by a rotational movement induced by tangentially oriented drag forces than by lift forces. Lastly, the particle structure's pneumatic transport through the channel was investigated for different starting positions, substrate permeabilities, inflow velocities and particle densities. It became evident that within the range of considered parameters, the structures always hit the back wall with a non-negligible velocity. The substrate permeability could be shown to lead to non-trivial effects on the structure's trajectories substantiating the necessity of the retrieval of a physically sensible permeability beforehand. Different densities of the particle structures could be observed to directly determine the ability to adapt to

changing flow conditions. The stopping distance was shown to represent an accessible criterion for the structure's likelihood to impact on the back wall without the necessity of examining its exact trajectory. With it, it could be shown that provided the detachment from the channel surface, a particle structure is very likely to always hit the back wall. Experimental observations were then used to show qualitative accordance with the general movement characteristics.

The presented methodology and the respective results represent a step towards a universal and consistent formulation of the relation between relevant input quantities and the formation mechanisms of specific deposition patterns. This eventually enables predictions and modification recommendations regarding operating conditions that can be used to achieve optimizations in engine performance, fuel consumption and service life of wall-flow filters.

4

Scaling of the Channel Model

4.1 Introduction

Wall-flow filters are one of the key components in modern exhaust treatment systems of internal combustion engines, enabling compliance with present emission limits [58]. By means of oppositely arranged inlet and outlet channels, such filters guide the introduced exhaust flow through porous walls, which separate the contained particulate matter (PM), with efficiencies up to 99% [74]. Over time, PM loading increases in the inflow channels, in which continuous deposition layers are formed on the porous wall surfaces, leading to an increase in pressure drop and resulting degradation in engine performance [81, 82, 135]. As the introduced PM mostly consists of combustible soot and small amounts of inorganic non-combustible ash, a filter's regeneration is achieved by continuously or periodically oxidizing its reactive components. Over long-term operation, this leads to an accumulation of ash, which forms agglomerates and affects the deposition layer composition. During regeneration, the resulting inhomogeneities can then lead to a break-up of the continuous layer into in-

dividual fragments, which can potentially detach from the filter surface and relocate inside a channel's domain [81]. As a result, specific deposition patterns are formed, which affect a channel's pressure drop contribution, its loading capacity and the separation efficiency.

Probable causes and influence factors leading to the individual patterns have been determined in various scientific works [50, 82–84]; however, a universal and consistent formulation without partially contradicting statements does not yet exist. Appropriate calculation models that enable a quantification of relevant influence factors are missing completely. This, however, impedes respective predictions on the formation of specific deposition patterns, which eventually affect engine performance, fuel consumption and the service life of wall-flow filters.

In Hafen et al. [1], the authors of the present manuscript demonstrated the applicability of surface-resolved particle simulations on the investigation of particulate matter structure detachment using lattice Boltzmann methods (LBM). Here, they presented a holistic LBM approach, which can be employed both for the simulation of the movement of resolved particles and the flow through porous media, while being based on the same numerical method. In the particle-free case, the presented model could be shown to exhibit super-linear grid convergence for an inflow velocity of $\bar{u}_{in} = 2.0\,\text{m/s}$ and good agreement with a reference solution, which had previously been validated thoroughly by experimental data [112]. Additionally, the approach could also be shown to enable the simulation of a transient detachment and transport process of surface-resolved structures governed by hydrodynamic forces. This work also includes a literature review addressing relevant findings on the deposition pattern formation, general numeric approaches to wall-flow filter modelling and LBM-related research regarding flow through porous media, as well as surface-resolved particle simulations.

In Hafen et al. [2], a holistic LBM approach was then used to investigate the detachment, acceleration and deceleration of individual particulate structures in order to derive clear predictions on the formation of specific deposition patterns. A pressure drop comparison with experimental investigations conducted on the experiment rig described in Thieringer et al. [9] led to the determination of a physically sensible substrate permeability of $K = 4.3 \times 10^{-12}\,\text{m}^2$, which is adopted in the present work as well. General transport characteristics were determined, identifying several key parameters utilizable for a standardized comparison of different simulation and experiment runs. Eventually, the particle structure's pneumatic transport through the channel was investigated for

different starting positions, substrate permeabilities, particle densities and inflow velocities up to $\bar{u}_{in} = 2.0\,\text{m/s}$.

In both works, the hydrodynamic forces acting on individual particulate structures were shown to be responsible for their detachment likelihood and transport characteristics under different operating and geometric conditions. While the described works, therefore, serve as a demonstration of the applicability of the simulation approach, the considered inflow velocities up to $\bar{u}_{in} = 2.0\,\text{m/s}$ only cover a small portion of the real world ranges that include velocities up to $\bar{u}_{in} = 80\,\text{m/s}$ [83]. The main focus of the present work is, therefore, to apply the developed LBM approach to an extended velocity range that covers as much as possible of the physically relevant domain. For a given discretization, however, elevated physical fluid velocities lead to the occurrence of higher LBM-specific lattice velocities, which inevitably drive a simulation closer to the method's inherent stability limit [106]. A discretization refinement increases the distance to the stability limit; however, this comes with the price of drastically increasing the amount of computational cells to be considered for three-dimensional simulations [2]. This, in turn, faces a limit due to the available computational resources, leading to the necessity of running a simulation with elevated fluid velocities in the vicinity of the stability limit. This has two implications: Firstly, the results' accuracy degrades [106] for both the individual quantities of interest and overall mass conservation. Additionally, the anisotropy of the flow (e.g., main flow direction vs. wall-penetration direction) leads to different magnitudes of differently oriented hydrodynamic force and torque contributions and respective different implications for their accuracy. Secondly, local velocity peaks are more likely to break the stability locally, usually causing the simulation to diverge. The occurrence of the peaks is directly dependent on both the geometry of a wall-flow channel and specific deposition patters. As a consequence, a generic LBM discussion does not suffice and a wall-flow specific stability and accuracy examination is indispensable for the consideration of the elevated velocity range in the simulation approach.

One goal of the present work is, therefore, to provide a comprehensive quantification of the stability and accuracy of both particle-free and particle-including flow, considering static, impermeable PM layer fragments attached to the porous substrate's surface. For any future study intended to investigate three-dimensional flow in wall-flow filters with elevated velocities by means of the LBM, this work can serve as a foundation, providing insight into numerical borderline cases that need to be considered. A second goal is the determination of the hydrodynamic forces acting on the particulate structures and the deduc-

tion of the local detachment likelihood of individual layer fragments, including their dependency on local flow conditions and the layer's fragmentation. As the formation of specific deposition patterns is dominated by rearrangement events that require the occurrence of the detachment of such fragments, the present work represents a contribution to respective deposition pattern predictions.

The following sections provide an introduction to the mathematical modelling and relevant numerical methods (cf. Section 4.2), a description of examined simulation cases for three specific scenarios (cf. Section 4.3), and a discussion and interpretation of the study results (cf. Section 4.4). A conclusion in Section 4.5 provides a summary of all the relevant findings and the resulting implications for wall-flow filter applications.

4.2 Mathematical Modelling and Numerical Methods

The present section briefly lays out the theoretical foundation for the simulation approach used in this work. This includes a description of the LBM principles in Section 4.2.1, an explanation of porous media and surface-resolved particle modelling (cf. Section 4.2.3 and Section 4.2.2), and the quantification of errors and convergence behaviour (cf. Section 4.2.4). A more detailed description on most aspects can, however, be found in Hafen et al. [1].

In this work, the evolution of conserved fluid quantities is described with the incompressible Navier–Stokes equations (NSE) [141]. With these, a fluid's velocity $u(x, t)$ and the pressure $p(x, t)$ at a three-dimensional position x in time t can be retrieved inside a specified domain. The fluid flow inside the porous substrate walls is modelled according to Darcy's law [114].

4.2.1 Lattice Boltzmann Method

One way of discretizing the continuous Navier–Stokes equation (NSE) is provided by the LBM in the form of a mesoscopic description of gas dynamics. Instead of individual molecules at the microscale, it considers a particle distribution function f and can be shown to lead to solutions of the equations of fluid dynamics on a macroscopic scale [106]. In this way, the LBM can be used as an alternative to conventional fluid methods, such as the finite volume method (FVM).

The discretization of the fluid domain is achieved by using a uniformly spaced voxel mesh with spacing δx. At time t and position x of the resulting lattice, the velocity space is discretized with lattice velocities c_i, leading to

a set of corresponding discrete-velocity distribution functions f_i. While the size of these sets can be chosen in various ways, in the present work, $q = 19$ discrete velocities covering three spacial dimensions are considered. The lattice Boltzmann equation (LBE) describes the discrete-velocity distribution function f_i after a discrete time step δt at a neighbouring node, where a collision operator Ω_i accounts for the mesoscopic contribution of molecular collisions on the microscale. All lattice-related quantities can then be described in dimensionless lattice units by providing some characteristic quantities inherent to the physics under study [106]. This allows for the commonly adopted choice of $\delta x = \delta t = 1$, leading to the LBE in the form

$$f_i(\boldsymbol{x} + \boldsymbol{c}_i, t + 1) = f_i(\boldsymbol{x}, t) + \Omega_i(\boldsymbol{x}, t). \tag{4.1}$$

While the collisions can be modelled in various ways [122, 138, 139], in the present work, we adopt the choice of the previous works [1, 2, 15] and use a Bhatnagar–Gross–Krook (BGK) collision operator [122] with a lattice relaxation time of $\tau = 0.51$

$$\Omega_i(\boldsymbol{x}, t) = -\frac{1}{\tau} \left(f_i(\boldsymbol{x}, t) - f_i^{(eq)}(\boldsymbol{x}, t) \right). \tag{4.2}$$

It describes the relaxation of the discrete distribution function f_i towards its equilibrium $f_i^{(eq)}$ at a single fluid node

$$f_i^{(eq)}(\boldsymbol{u}, \rho) = w_i \rho \left[1 + \left(\frac{\boldsymbol{c}_i \cdot \boldsymbol{u}}{c_s^2} + \frac{(\boldsymbol{c}_i \cdot \boldsymbol{u})^2}{2c_s^4} + \frac{\boldsymbol{u}^2}{2c_s^2} \right) \right] \tag{4.3}$$

with weights w_i and a lattice speed of sound of $c_s = 1/\sqrt{3}$ inherent to the velocity set chosen in this work [106]. With (4.2) and (4.3), a link to local macroscopic fluid quantities can be established: According to the Chapman–Enskog analysis [140], the macroscopic kinematic viscosity can be shown to depend on the relaxation time as

$$\nu = c_s^2 \left(\tau - \frac{1}{2} \right). \tag{4.4}$$

The equilibrium function $f_i^{(eq)}$ in (4.3), in turn, depends on the macroscopic fluid density ρ and the macroscopic fluid velocity $\boldsymbol{u}$, which can be retrieved via the zeroth- and first-order moments of the discrete distribution function

$$\rho = \sum_{i=0}^{q-1} f_i \quad \text{and} \quad \rho \boldsymbol{u} = \sum_{i=0}^{q-1} \boldsymbol{c}_i f_i. \tag{4.5}$$

With the lattice speed of sound c_s, the density ρ can be related to the pressure p at lattice scale via the isothermal equation of state

$$p = c_s^2 \rho. \tag{4.6}$$

One of the key features of the LBM is the possibility of splitting (4.1) into a purely local collision and a subsequent streaming step. This enables an efficient parallelization strategy, which is realized in the open source software OpenLB [5], used in the present work.

4.2.2 Porous Media Modelling

Within the LBM, the momentum loss that a fluid experiences when passing through a porous medium according to Darcy's law can be accounted for by means of an effective velocity [115]. The relaxation time τ, the kinematic fluid viscosity ν and the medium's permeability K can be expressed in the form of a *confined permeability* $d \in [0, 1]$ [1] as they stay constant throughout a simulation. This leads to

$$\boldsymbol{u}^{eff}(\boldsymbol{x}, t) = d\boldsymbol{u}(\boldsymbol{x}, t) \qquad \text{with} \qquad d = 1 - \tau \frac{\nu}{K}. \tag{4.7}$$

4.2.3 Surface-Resolved Particle Simulations

The homogenized lattice Boltzmann method (HLBM) [7, 95, 121] represents a generalization of (4.7) to surface-resolved particles by considering moving porous media. By associating a local confined permeability $d(\boldsymbol{x}, t)$ with a local weighting factor $B(\boldsymbol{x}, t) \in [0, 1]$ as a *cell saturation*, differentiating between sole liquid ($B = 1$), sole solid ($B = 0$) and mixed ($0 < B < 1$) contributions at every node with position $\boldsymbol{x}$, the approach represents a specific form of the partially saturated method (PSM) [103, 120, 142]. In order to avoid fluctuations, a smooth transition layer of width ϵ is used symmetrically at the boundary of a single particle with index k. The weighting factor in this layer can, thus, be described with the particle's centre of mass $X_k(t)$ and a given point $\boldsymbol{x}$ on an outward-facing normal of the surface via

$$B(\boldsymbol{x}, t) = \cos^2\left(\frac{\pi}{2\epsilon}(\|X_k(t) - \boldsymbol{x}\|_2)\right). \tag{4.8}$$

The factor is then used to determine a weighted average of the fluid velocity $\boldsymbol{u}$ and the solid particle velocity $\boldsymbol{u}^S$ at a single node

$$\boldsymbol{u}^{eff}(\boldsymbol{x}, t) = B(\boldsymbol{x}, t)\boldsymbol{u}(\boldsymbol{x}, t) + (1 - B(\boldsymbol{x}, t))\boldsymbol{u}^S(\boldsymbol{x}, t), \tag{4.9}$$

which then enters the LBE. While the approach enables the simulation of dynamic particle movement [1, 2, 7, 15, 95, 96, 121], the consideration of immobile particles ($u^S = 0$) in the present work simply reduces (4.9) to (4.7). More details on the particle's shape representation providing the respective normal and the HLBM's derivation can be found in Trunk et al. [7, 95].

While the described methodology enables the modelling of the particle's influence on the fluid field, the back coupling is achieved by employing a momentum exchange approach at a particle's surface. Analogously to the previous works [1, 2, 15], the one originally proposed by Wen et al. [126], but extended for smooth interfaces by Trunk et al. [95], is used in the present work. The force contribution of every node x_b in the smooth boundary transition area of a single particle k can be retrieved via

$$F_k(x_b, t) = \sum_{i=0}^{q-1} \left[(c_i - u^S(t)) f_i(\hat{x}_b, t+1) - (c_{\bar{i}} - u^S(t)) f_{\bar{i}}(x_b, t+1) \right] \quad (4.10)$$

by calculating the differences between the discrete velocities c_i and the particle's solid velocity u^S. The next node in the direction of i is denoted $\hat{x}_b$. Index $\bar{i}$ denotes the opposite direction of it. With it, the force F_k and torque T_k acting on a particle's centre of mass X_k can then be retrieved by summing the individual force contributions over all boundary nodes x_b via

$$F_k(t) = \sum_{x_b} F_k(x_b, t) \quad \text{and} \quad T_k(t) = \sum_{x_b} (x_b - X_k(t)) F_k(x_b, t). \quad (4.11)$$

4.2.4 Quantification of Errors and Convergence

In order to assess a simulation's transient convergence behaviour, a respective criterion is defined as the standard deviation σ of a quantity χ being smaller than a predefined residuum r multiplied by the average $\bar{\chi}$ over the last T time steps

$$\sigma(\chi) = \sqrt{\frac{1}{T+1} \sum_{t=1}^{T} (\chi_t - \bar{\chi})^2} < r\bar{\chi}. \quad (4.12)$$

For the convergence evaluation of a particle's surface force, F_k or T_k from (4.11) can be used directly as quantity χ. Convergence of the fluid's velocity and pressure, are, however, evaluated via the kinetic energy and the lattice density averaged by the total cell number M

$$\chi_t(u) = \frac{1}{M} \sum_{m=1}^{M} \left(\frac{1}{2} \|u\|^2 \right)_m \quad \text{and} \quad \chi_t(\rho) = \frac{1}{M} \sum_{m=1}^{M} \rho_m \quad (4.13)$$
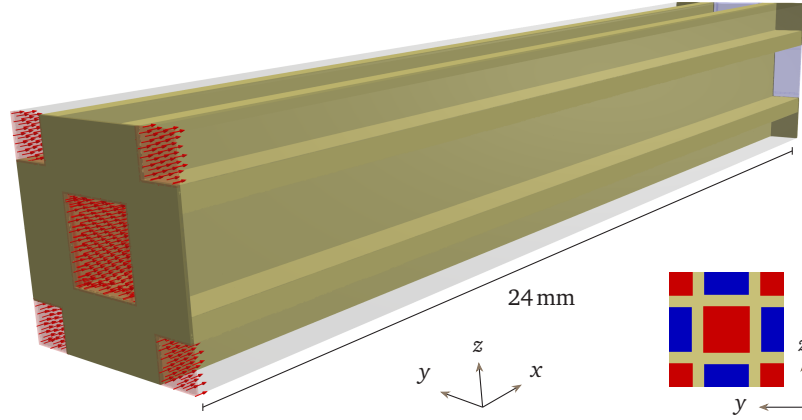
Figure 4.1: *Channel model, including one central inflow channel and fractions of surround-ing inflow and outflow channels. Dark yellow structures represent porous filter substrate, brown structures solid walls. Red colouring indicates inflow sections, blue colouring indicates outflow sections.*

right after being calculated via the moments according to (4.5).

The influence of a discretization refinement is assessed by evaluating the grid convergence, where the error err_{L^2} based on the L^2 norm is used as an error criterion for a quantity χ at a given resolution N

$$err_{L^2}(\chi) = \sqrt{\frac{\sum_{m=1}^{M}\left(\chi_m^{\text{ref}} - \chi_m\right)^2}{\sum_{m=1}^{M}\left(\chi_m^{\text{ref}}\right)^2}}. \tag{4.14}$$

4.3 Application to a Wall-Flow Filter

In this work, the simulation setup of a single wall-flow channel, as described in the previous works [1, 2, 15], is adopted and shown in Figure 4.1.

It consists of a porous structure with a substrate permeability of $K = 4.3 \times 10^{-12}\,\text{m}^2$ and a wall thickness of $l_w = 0.4\,\text{mm}$, which separates a central inflow channel, four additional quarter-sized inlet channels and four half-sized outflow channels. The channels have a width of $l_y = 1.6\,\text{mm}$, which serves as the reference length for the spatial resolution N, defined as the number of cells per channel width. A scaled channel length of $l_{x,s} = 24\,\text{mm}$ is used, which accounts for a fifth of a real world representative of $l_x = 120\,\text{mm}$. This scaling leads to the great reduction in computational demand that enables the extensive studies in

the present work in the first place, while ensuring similar flow characteristics, which is shown in Hafen et al. [2]. It should be noted, however, that, for a given flux, a length reduction leads to a higher wall throughput, which results in an increased overall pressure drop, impeding a direct comparison with experimental results. The temperature in a wall-flow filter can vary significantly both on average and locally depending on the operating conditions [58]. As temperature effects, however, are not part of the present work's scope, ambient conditions are assumed for the whole channel domain.

The model's symmetry enables the application of periodic boundary conditions on the four surrounding sides, which let it serve as a representation of a real wall-flow filter comprised of hundreds of individual channels. A constant velocity at the inlets and a constant pressure at the outlets is imposed using Dirichlet boundary conditions [141]. Solid walls at the channel end caps on both sides are modelled with a no-slip condition. The LBM realization of the latter is performed with a simple bounce-back condition [131], and regularized local boundary conditions [130] are used at the inlets. As the studies in the previous works suffered from severe stability issues for inflow velocities above $\bar{u}_{in} = 2.0\,\mathrm{m/s}$, the local boundary condition at the outflow is exchanged for an interpolated one [143], which has been found to generally yield more stable results.

Three different scenarios are investigated with dedicated purposes for each in the present work:

1. Particle-free flow

2. Single layer fragment

3. Deposition layer during break-up

First, the *particle-free flow* in a clean channel is investigated in order to define and examine the parameter domain that represents a necessary stability criterion for the wall-flow model under study. In the second scenario, a *single layer fragment*, attached to the porous wall's substrate, is considered. For this, the parameter domain is re-evaluated, this time including the individual components of the hydrodynamic force acting on the fragment's surface. The third scenario represents a *deposition layer during break-up*. With it, local effects on the fluid field and the acting forces are investigated for different situations along the channel. The spatial distribution of hydrodynamic forces is evaluated in order to derive predictions on the detachment likelihood of individual layer fragments

and their mutual influence. Independent of the scenario, all simulations are run until either reaching the convergence criteria for the characteristic quantities of interest, diverging or exceeding a defined maximum simulation time when fluctuations emerge. The respective residuals for the average kinetic energy and the average lattice density of $r_u = 10^{-7}$ and $r_\rho = 10^{-6}$ are adopted from the previous works [1, 2, 15]. For particle-related scenarios, the convergence is defined as reaching convergence for both fluid quantities and the normal component of the hydrodynamic force additionally, for which the residuum is set to $r_F = 10^{-7}$.

4.3.1 Particle-Free Flow

In order to investigate the stability and accuracy of the particle-free flow, the wall-flow model including the specified set of boundary conditions and LBM collision dynamics is used for simulations, considering filtration relevant inflow velocities of $\bar{u}_{in} = 2$ m s^{-1} to 60 m s^{-1}. Spatial resolutions between $N = 32$ and 128 are considered, which are defined as the number of cells per channel width l_y. In an attempt to derive clear predictions for an inflow velocity threshold, the macroscopic quantity $\bar{u}_{in}$ is related to its LBM specific lattice counterpart $\bar{u}_{in,L}$ via

$$\bar{u}_{in} = \bar{u}_{in,L} c_u. \tag{4.15}$$

The respective conversion factors for velocity, position and time

$$c_u = \frac{c_x}{c_t} \qquad \text{with} \qquad c_x = \frac{L_{char}}{N} \qquad \text{and} \qquad c_t = (\tau - 0.5) c_{s,L}^2 \frac{1}{\nu} \left(\frac{L_{char}}{N} \right)^2 \tag{4.16}$$

result from the non-dimensionalization approach, commonly employed for the relation between macroscopic and lattice quantities [106].

4.3.2 Single Deposition Layer Fragment

The investigation of a single deposited PM layer fragment allows for the isolated evaluation of the accuracy and velocity dependency of relevant surface forces. While such a fragment only has a minor effect on the global fluid field, it represents an obstacle in the flow that can lead to locally increased velocities. These may, in turn, cause divergence for smaller inflow velocities with respect to the particle-free case. A separate stability evaluation is therefore inevitable. Additionally, it should be considered that the channel's base resolution of $N = 16$ has been chosen in such a way that a constant ratio between channel width and
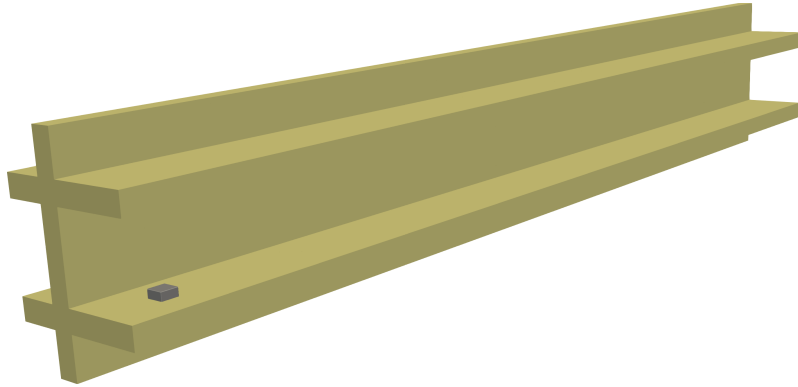
Figure 4.2: *Channel model featuring a single PM layer fragment in gray. Dark yellow structures represent porous filter substrate.*

the thickness of the porous walls can be ensured, while maintaining complete symmetry of the model for multiples of the base resolution [1]. Fragments of the deposition layer, however, are subject to stepwise occurring anisotropic discretization effects of the particle surface, potentially leading to fluctuations in the grid convergence of the force components. Therefore, resolutions up to $N = 176$ are considered to, nevertheless, provide a representative data basis.

Analogously to Hafen et al. [2], a single fragment is placed flush on the substrate's surface. The structure is represented by a cubical disk with an edge ratio of $2 \times 2 \times 1$ and a base size of $d_z = 170\,\mu\text{m}$. At this point, it should be reiterated that, regarding the employed momentum exchange approach, the substrate wall is not considered solid. It is rather part of the global fluid field with a decreased permeability according to (4.7). This ensures that all fluid nodes necessary to prevent failure of the momentum exchange approach are provided. The channel model with a single PM layer fragment is shown in Figure 4.2. In Hafen et al. [2], it could be deduced that the normal forces acting on a fragment's surface cannot contribute much to its detachment. Tangential forces were, in turn, shown to be larger by at least a factor of four in every considered case. This led to the conclusion that, for equally shaped fragments, a lift-off can only be achieved by a rotational movement over the fragment's back-side edge. In order to enhance the modelling of this process, a *rotation-induced normal force* $F_{N,rot}$ is additionally considered in the present work. All relevant forces are outlined in Figure 4.3.

The standard normal and tangential force F_N and F_T are retrieved as components of the force $\boldsymbol{F}_k$ that results from summing the individual contributions of
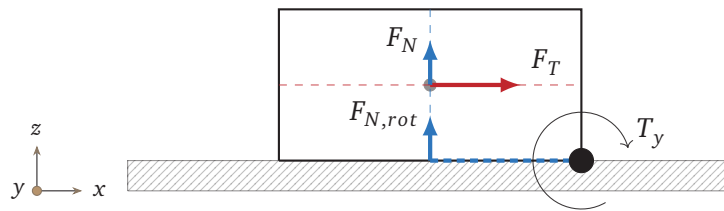
Figure 4.3: *Sketch of single PM layer fragment and considered hydrodynamic forces. Tangential contributions red, normal contributions blue. Torque around y-axis at eccentric contact line.*

the momentum exchange approach at all surface boundary nodes x_b according to (4.11). The calculation of the torque T_k, however, additionally requires the specification of a centre of rotation, usually represented by a particle's centre of mass X_k. Using the actual contact line assumed for a rotational detachment (cf. Figure 4.3) as the centre of rotation instead, the torque T_y can be calculated directly at this position with the momentum exchange approach. Its contribution to a *normal directed detachment* can then be modelled via the *rotation-induced normal force* $F_{N,rot}$, which simply results from dividing the torque T_y by half of the fragment's x-dimension as the rotational lever.

4.3.3 Deposition Layer during Break-Up

As a final scenario, a deposition layer during break-up due to the oxidization of the majority of its soot content [81] is investigated. Analogously to Hafen et al. [1], the layer fragments are modelled as a field of identical cubic discs that cover the porous walls inside an inflow channel. For these, the same characteristics as described in the single particle scenario are assumed. As a base configuration, a uniform field of 3×40 fragments is considered on each of the four porous walls. The channel model with a uniformly fragmented PM layer is shown in Figure 4.4. In order to additionally investigate the effect of the filter loading, non-uniform oxidization kinetics and the temporal evolution of the break-up process, four modifications are considered: By varying the layer height, the amount and predominant deposition location of introduced PM can be accounted for. In this context, the layer height is either varied uniformly or by assuming a predefined transition region, as laid out in Figure 4.5.

While a uniform variation of the layer height in Figure 4.5a is supposed to represent a simple approach to account for the duration of loading and the PM concentration, an initially increasing layer height in Figure 4.5b resembles layer
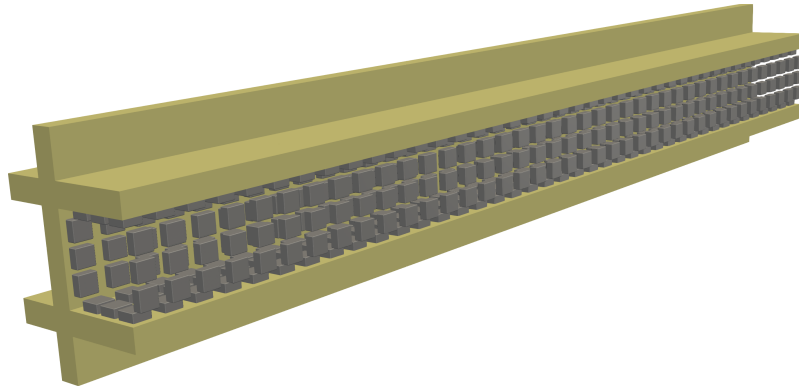
Figure 4.4: *Channel model with uniformly fragmented PM layer in gray. Dark yellow structures represent porous filter substrate.*
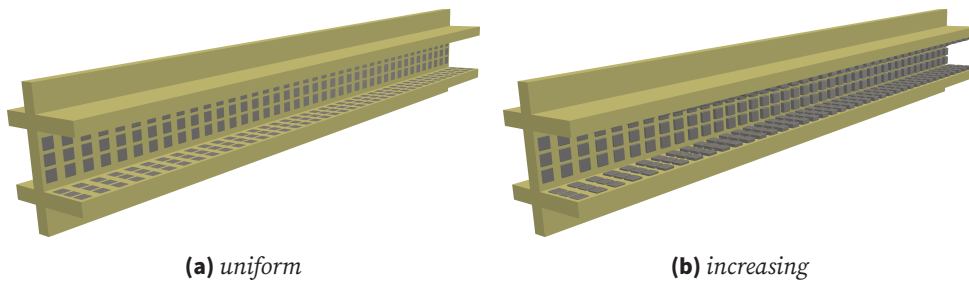
(a) *uniform*

(b) *increasing*

Figure 4.5: *Channel model with modified PM layer height.*

(a) *non-uniform layer fragmentation*   **(b)** *partial detachment*
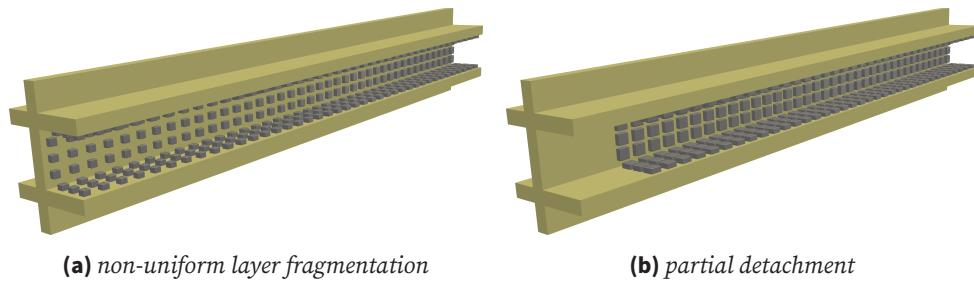
Figure 4.6: *Channel model with modified substrate coverage.*

characteristics reported in the literature [57, 144]. For the latter, a PM layer with increasing height over a relative channel length of x_{rel} in the channel's front section is considered.

With a modification of the substrate coverage, the temporal evolution during regeneration can be modelled by accounting for local differences in the progress of soot oxidization or by regarding an advanced point in time when some detachment has already occurred. This is realized by considering non-uniform layer fragmentation and partial detachment, as shown in Figure 4.6. The non-uniform layer fragmentation in Figure 4.6a features an increasing substrate coverage, beginning from a relative fragment size of $d_{xy,rel}$ to the one assumed in the base configuration. In order to evaluate the impact, each layer configuration is compared against its inverted counterpart, which, respectively, features a decreasing coverage, ending with the relative fragment size at the channel's back. For the partial detachment in Figure 4.6b, layer structures with multiple rows removed over a relative channel length x_{rel} are considered.

4.4 Results and Discussion

In the following, the simulation results will be presented and discussed for all three scenarios described in Sections 4.3.1, 4.3.2 and 4.3.3. While resolutions up to $N = 176$ are considered, flow-field visualizations are generally extracted from $N = 96$ data sets due to much smaller memory consumption.

4.4.1 Particle-Free Flow

The particle-free flow is investigated regarding its transient convergence behaviour of the fluid pressure and velocity (cf. Section 4.4.1.1), the resulting flow
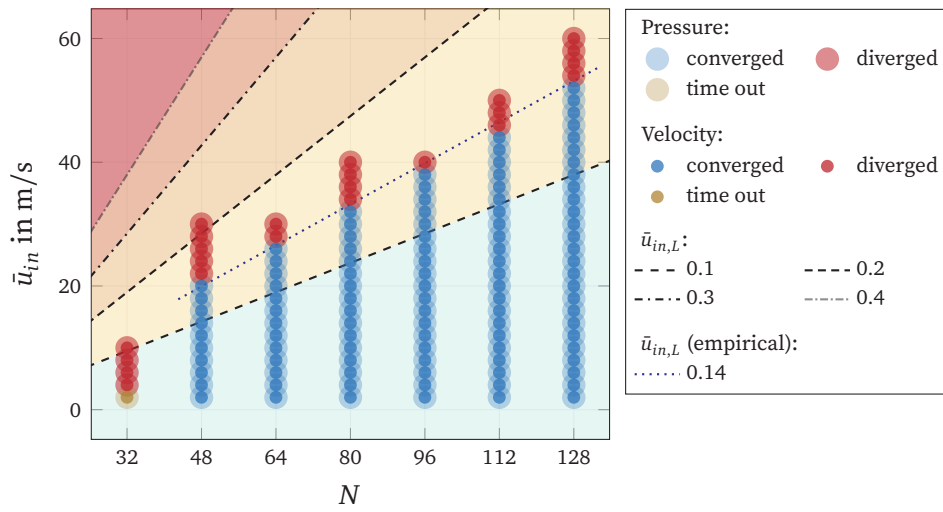
Figure 4.7: *Stability map for pressure and velocity convergence in particle-free flow. Contour lines show stability-relevant and empirically determined velocities at lattice scale. Background colouring indicates distance to theoretical LBM stability limits (green to red).*

field (cf. Section 4.4.1.2) and the grid convergence as a measure of accuracy (cf. Section 4.4.1.3).

4.4.1.1 Transient Convergence Behaviour

In order to determine the necessary stability domain, simulations with different combinations of average inflow velocity $\bar{u}_{in}$ and resolution N are run until completion (cf. Section 4.3). The actual value of each convergence quantity is then evaluated, considering three possible states: *convergence* is assumed if the value has passed its predefined residuum. Undefined values due to a division by zero are counted as *diverged*. A completion triggered by the specified maximum simulation time of $t_{max} = 0.1\,\text{s}$, is considered a *timeout*, which can be caused by both continuously fluctuating quantities or a very slow convergence behaviour, rendering the simulation unfeasible. The resulting stability map is shown in Figure 4.7. Generic LBM limits according to (4.15) assuming relevant lattice velocities are included as well. The resulting stability map is shown in Figure 4.7. The first thing to note is that pressure and velocity exhibit synchronous convergence behaviour. For a resolution of $N = 32$ cells per channel diameter, no convergence can be achieved within the considered duration. With a resolution
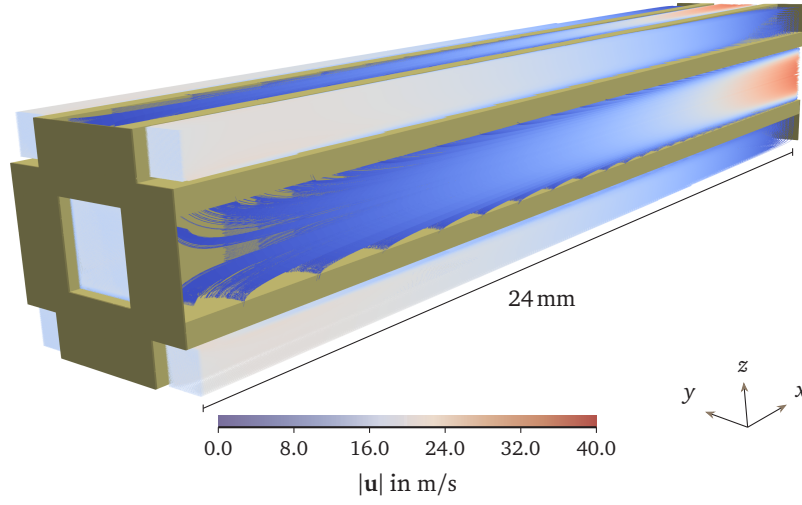
Figure 4.8: *Particle-free flow with an inflow velocity of $\bar{u}_{in} = 20.0$ m/s and a resolution of $N = 96$. Dark yellow structures represent porous filter substrate, brown structures solid walls. Streamlines exhibit local flow direction. Colour scale indicates local velocity magnitude.*

of $N = 48$, inflow velocities up to $\bar{u}_{in} = 20$ m/s can be realized. Increasing resolutions, then, enable convergence for higher inflow velocities as well, reaching up to $\bar{u}_{in} = 52$ m/s at $N = 128$. It becomes apparent that the resulting stability threshold follows a linear course with a slope that fits well between those of the contour lines for $\bar{u}_{in,L} = 0.1$ and 0.2. The considered wall-flow model can, accordingly, generally be assumed to be capable of handling inflow velocities that lead to an average lattice velocity smaller than $\bar{u}_{in,L,max} \approx 0.14$. Taking (4.16) into account, this allows the formulation of a resolution-dependent maximum inflow velocity via

$$\bar{u}_{in,max}(N) = AN \qquad \text{with} \qquad A = \bar{u}_{in,L,max}\frac{c_u}{N} = 0.14\frac{\nu}{(\tau - 0.5)c_{s,L}^2 L_{char}} = 0.415$$

(4.17)

4.4.1.2 Flow Field

The resulting flow field for an inflow velocity of $\bar{u}_{in} = 20.0$ m/s and a resolution of $N = 96$ is shown in Figure 4.8.

The channel model from Figure 4.1 shows coloured streamlines according to the local flow direction and magnitude. Starting with the prescribed inflow
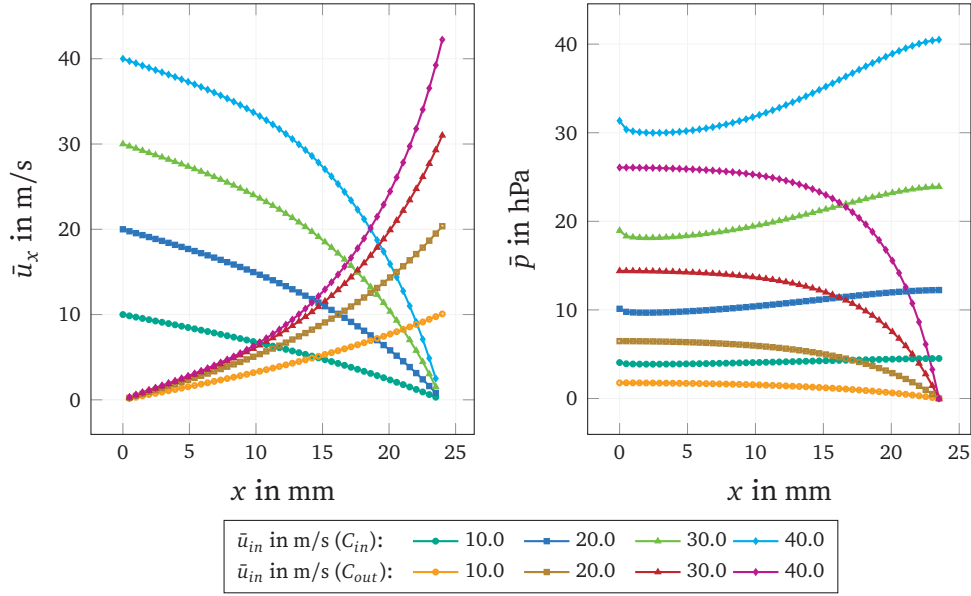
Figure 4.9: *Velocity profiles $\bar{u}_x(x)$ and pressure profiles $\bar{p}(x)$ in inlet channel domain C_{in} and outlet channel domain C_{out} with a resolution of $N = 128$.*

velocity, the five inlet channels exhibit a decreasing velocity magnitude and streamline density along their length. The outflow channels, in turn, show a continuous magnitude and density increase, eventually forming a developed channel profile at the outflow. The parabolically shaped profile solely results from the momentum loss in the enclosing porous walls, as no specific modelling of friction is considered. The resulting presence of elevated velocities of up to $|\mathbf{u}| = 32.8\,\text{m/s}$ drives the simulation closer to the stability limit, proving the necessity for a model-specific stability discussion.

The axial fluid velocity and the pressure averaged at discrete locations over the inflow and outflow channels' cross-sections $\bar{u}_x$ and $\bar{p}$, are shown in Figure 4.9 for different inflow velocities. In order to include inflow velocities up to $\bar{u}_{in} = 40.0\,\text{m/s}$, a resolution of $N = 128$ is considered here. Due to their location inside the solid wall, the last position in the inflow channel ($x = 24\,\text{mm}$) and the first one in the outflow channel ($x = 0\,\text{mm}$) do not produce any fluid information. The velocity $\bar{u}_x$ in the inflow channel domain C_{in} transitions from the imposed one at the inlet $\bar{u}_{in}$ to zero at the channel end in the form of a distinctive curve for all inflow velocities considered. The fluid passing through the porous filter walls then accumulates in the outflow channel domain C_{out}, which exhibits

the opposite behaviour accordingly. For velocities in the close vicinity of the stability limit, mass conservation degrades, leading to a difference between the resulting average axial fluid velocity at the outlets and the imposed one at the inlets. The pressure profile of the inlet channel also exhibits a distinctive form at a pressure level resulting from the momentum loss due to the porous walls between the channels. Near the inflow channel's back wall, the pressure reaches its maximum value. The average pressure in the outflow channel decreases continuously with a decreasing slope. In this way, the pressure difference between the inflow and outflow channel continuously increases over the channel length.

4.4.1.3 Grid Convergence

The final values of the average kinetic energy $\bar{E}_{kin}$ and average lattice density $\bar{\rho}$, as representatives of the velocity and pressure convergence, are then used to calculate the respective $err_{L^2}(\chi)$ according to (4.14), with the highest resolution of $N = 128$ as the reference solution χ^{ref}. The grid convergence for four different inflow velocities is shown in Figure 4.10.

Both quantities can be shown to exhibit a quadratic or super-quadratic experimental order of convergence (EOC) over the considered resolution range. The velocity convergence, however, features a relatively large error level, which is nearly identical for all inflow velocities. The pressure convergence, in turn, exhibits a smaller error level, which increases significantly for greater inflow velocities. Based on this, it can be assumed that the wall-flow model including the porosity approach is consistent with respect to the chosen grid resolution and is generally able to recover the flow for velocities up to $\bar{u}_{in} = 40\,\text{m/s}$. Due to the in-part high error level, however, the highest resolution feasible should always be used. From the average density's error, it can additionally be deduced that mass conservation might depend slightly on the inflow velocity.

4.4.2 Single Deposition Layer Fragment

Analogously to the particle-free flow, the transient convergence behaviour (cf. Section 4.4.2.1), the resulting flow field (cf. Section 4.4.2.2) and the grid convergence (cf. Section 4.4.2.3) are investigated for a single layer fragment attached to the porous wall's substrate.
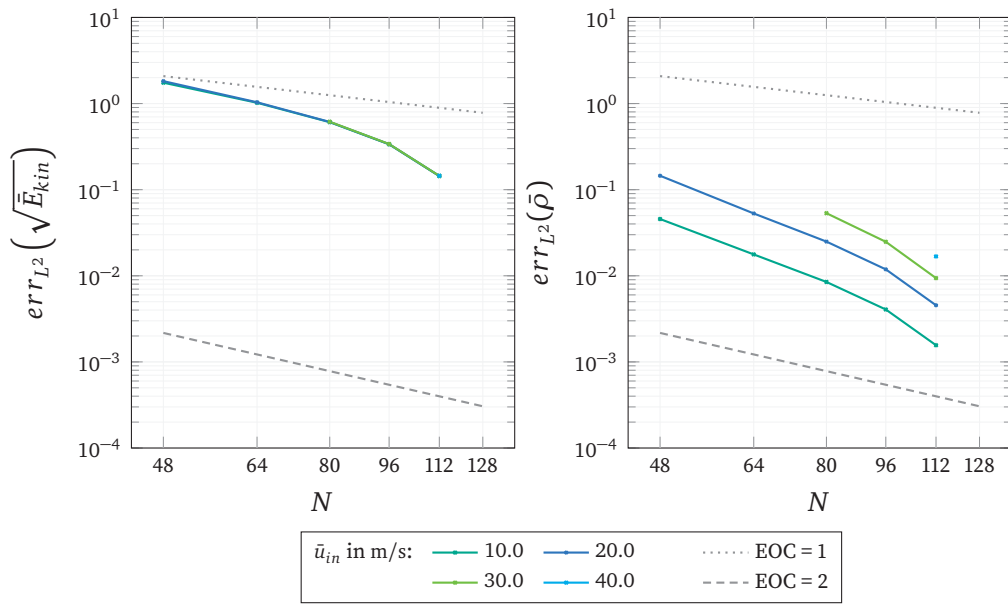
Figure 4.10: *Error err_{L^2} of final values of average kinetic energy and average lattice density for different inflow velocities $\bar{u}_{in}$. Reference solution χ^{ref} at $N = 128$. Quadratic and linear EOC as guidelines.*
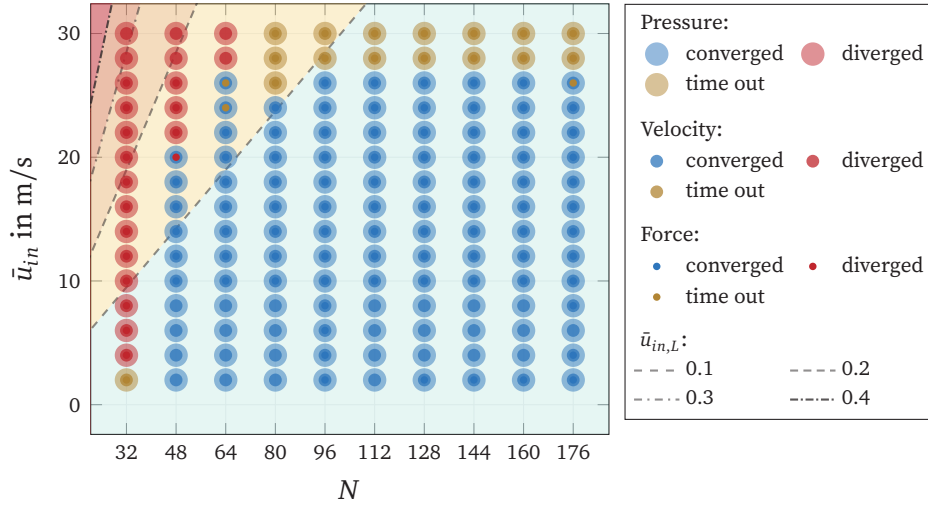
Figure 4.11: *Stability map for pressure, velocity and force convergence in flow with single layer fragment. Contour lines show stability-relevant velocities at lattice scale. Background colouring indicates distance to theoretic LBM stability limit (green to red).*

4.4.2.1 Transient Convergence Behaviour

The final state of the transient convergence behaviour is evaluated for different inflow velocities $\bar{u}_{in}$ and resolutions up to $N = 176$. As laid out in Section 4.3, the normal component of the force acting on a fragment's surface is used additionally as a third convergence quantity. The resulting stability map is shown in Figure 4.11.

For resolutions up to $N = 64$, the same convergence threshold can be observed for the flow as in the particle-free scenario. Larger resolutions, however, do not enable the flow convergence for inflow velocities greater than $\bar{u}_{in} = 26\,\text{m/s}$ due to persisting fluctuations in the fluid field. These can be reasoned rather to represent a physically correct behaviour than numerical artefacts as an increase in the grid resolution does not change their occurrence. The force convergence mostly shares the same behaviour as the pressure and velocity, but, for some specific cases, exhibits time out and divergence states for slightly smaller inflow velocities. As a result, the following particle-related studies are limited to inflow velocities smaller than $\bar{u}_{in} = 28\,\text{m/s}$.

In order to confirm these observations, the transient behaviour of the velocity criterion is shown in Figure 4.12 for a resolution of $N = 96$ and different
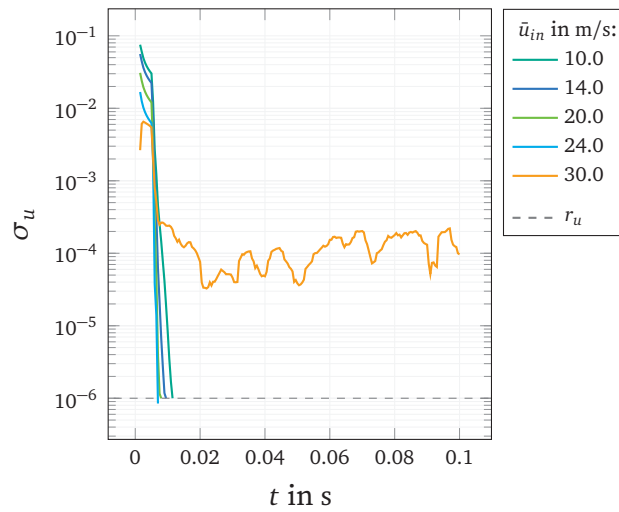
Figure 4.12: *Transient development of velocity convergence with a resolution of $N = 96$ for different inflow velocities $\bar{u}_{in}$. Dashed line represents residuum $r_{\bar{u}}$.*

inflow velocities. For inflow velocities up to $\bar{u}_{in} = 26\,\text{m/s}$, convergence can be achieved within less than $t = 0.02\,\text{s}$, while smaller velocities generally lead to a slower convergence. An inflow velocity of $\bar{u}_{in} = 30\,\text{m/s}$, in contrast, results in a continuously fluctuating behaviour around $\sigma_u = 1 \times 10^{-4}$, rendering it impossible to obtain a converged fluid field with respect to the specified residuum of $r_u = 1 \times 10^{-6}$. In order to ensure convergence with a sufficient distance to the convergence limit, an inflow velocity of $\bar{u}_{in} = 20\,\text{m/s}$ is used for all following particle-related studies. The respective transient behaviour of all three convergence quantities for a resolution of $N = 96$ is shown in Figure 4.13. All convergence quantities show a similar behaviour: After a short transition period, the quantities head towards their respective residuum with a similar slope. The fluid field converges first at $t = 7.5\,\text{ms}$, but is followed shortly by the convergence of the hydrodynamic force on the particle surface at $t = 8.65\,\text{ms}$. This shows that all quantities are strongly coupled, but suggests that fluid convergence generally has to be ensured first.

4.4.2.2 Flow Field

The flow field around the single fragment is shown in Figure 4.14 for an inflow velocity of $\bar{u}_{in} = 20.0\,\text{m/s}$ and a resolution of $N = 96$. Due to its small dimensions, the fragment does not lead to great differences in the global fluid field with
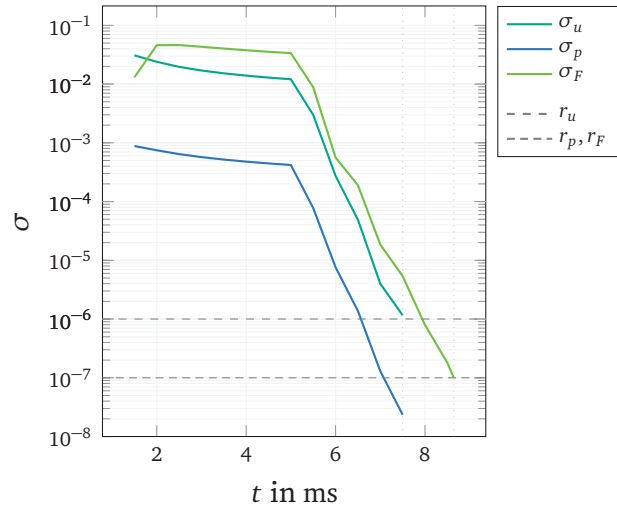
Figure 4.13: *Transient development of velocity, pressure and force convergence for an inflow velocity of $\bar{u}_{in} = 20\,\text{m/s}$ with a resolution of $N = 96$. Dashed lines represent residuals r_u, r_p and r_F. Dotted lines indicate time of flow and force convergence.*
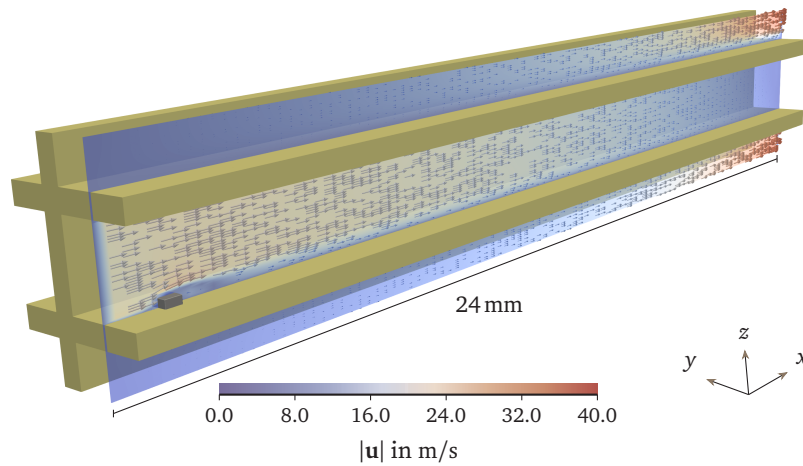
Figure 4.14: *Flow field with an inflow velocity of $\bar{u}_{in} = 20.0\,\text{m/s}$ and a resolution of $N = 96$ featuring a single PM layer fragment in gray. Dark yellow structures represent porous filter substrate. Colour scale indicates local velocity magnitude.*
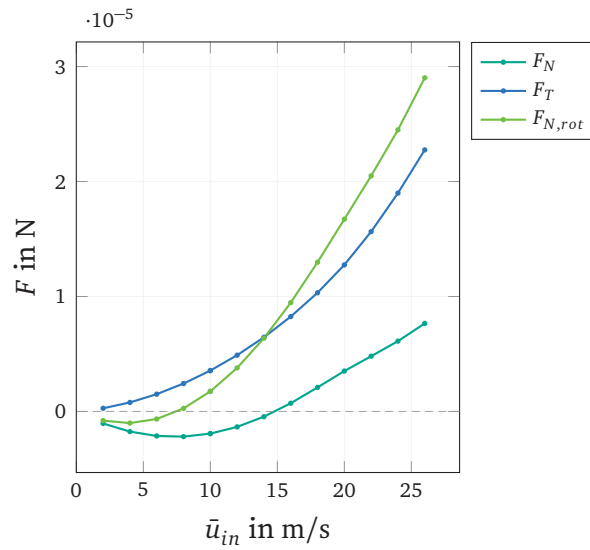
Figure 4.15: *Comparison of standard normal force F_N, tangential force F_T and rotation-induced normal force $F_{N,rot}$ at convergence with a resolution of $N = 96$ for different inflow velocities.*

respect to the one in the particle-free case. In the direct vicinity of the fragment, however, an acceleration of the local fluid velocity can be observed on the fragment's upper side. In the shielded area right behind it, a region of greatly reduced velocity can be found, which is large enough to potentially influence the flow conditions at neighbouring fragments.

The influence of the inflow velocity on all three force variants is shown in Figure 4.15. All forces feature small values for velocities close to zero, but increase continuously for higher velocities. While the tangential force F_T is always positive, the standard normal and rotation-induced normal forces F_N and $F_{N,rot}$ only exhibit positive values for inflow velocities greater than $\bar{u}_{in} = 15\,\text{m/s}$ and $\bar{u}_{in} = 8\,\text{m/s}$, respectively. In accordance with the observations in Hafen et al. [2], this shows that detachment of particle structures with similar form can most likely only be caused by tangential forces when considering smaller inflow velocities. The rotation-induced normal force is always greater than the standard normal force and even becomes greater than the tangential one after $\bar{u}_{in} = 15\,\text{m/s}$. Normal induced detachment assuming a non-slipping eccentric centre of rotation can, therefore, be reasoned to only depend on the rotation-induced normal force $F_{N,rot}$, leading to neglect of the standard normal force F_N in the remainder of this work.
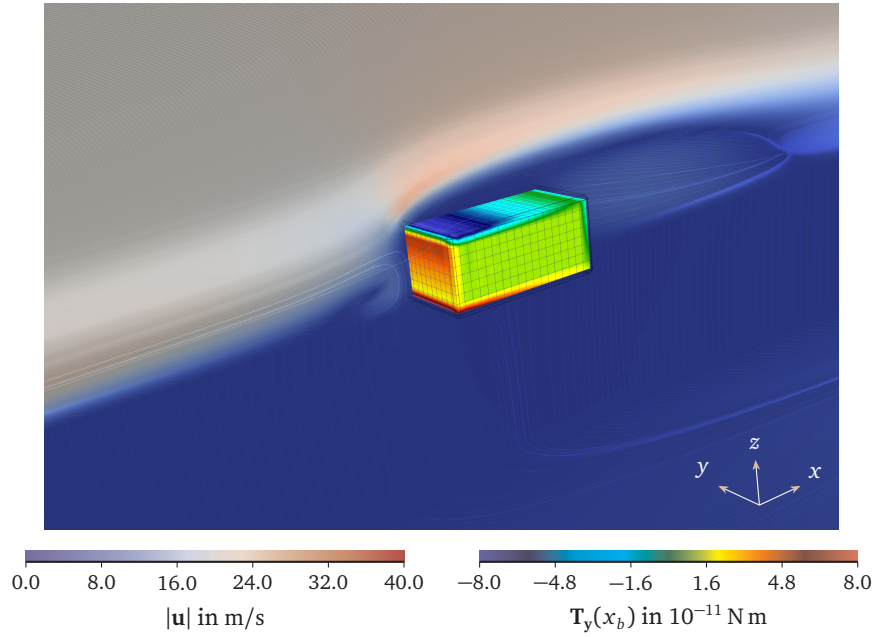
Figure 4.16: *Detailed flow field featuring a single PM layer fragment coloured according to local contribution to torque $\mathbf{T_y}(x_b)$. Streamlines exhibit local flow direction. Left colour scale indicates local flow velocity magnitude $|\mathbf{u}|$. Porous substrate removed for visual clarity.*

In order to investigate the fluid's local influence on the rotation-induced normal force $F_{N,rot}$, the local contributions of the torque T_y on the fragment surface are visualized in Figure 4.16, assuming an eccentric centre of rotation. It can be observed that the highest force magnitude is found near the front upper edge (dark blue, dark red), which forms the starting point for the elevated fluid velocity on the fragment's upper side. The edge also represents the inflection point between positive and negative values that either contribute to the fragment's detachment or an additional support of adhesive forces that keep the fragment attached to the porous substrate. Flow conditions in this region, and all factors potentially influencing them before reaching this position, are, therefore, of specific interest for the fragment's detachment behaviour.

4.4.2.3 Grid Convergence

In order to access the accuracy of the hydrodynamic force, the grid convergence for the tangential and the rotation-induced normal force F_T and $F_{N,rot}$ is
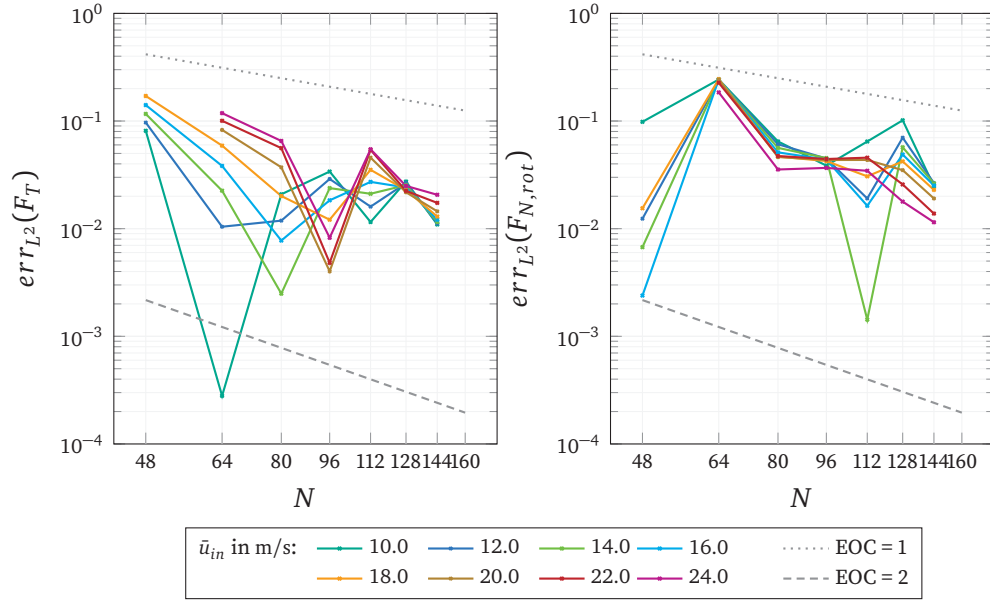
Figure 4.17: *Error err_{L^2} of tangential and standard normal force for different inflow velocities $\bar{u}_{in}$. Reference solution χ^{ref} at $N = 160$. Quadratic and linear EOC as guidelines.*

evaluated for different inflow velocities $\bar{u}_{in}$ and shown in Figure 4.17.

As predicted, it can be observed that both forces are subject to much larger fluctuations than the flow convergence quantities in the particle-free case in Figure 4.10 due to anisotropic discretization effects. For most velocities, however, both forces exhibit linear to quadratic convergence behaviour with a general error level below $err_{L^2} = 10^{-1}$. Considering that the presented model rather represents a real application case than a simplified benchmark case (as, e.g., considered in Trunk et al. [95] and Haussmann et al. [6]), while including both porous media modelling and the surface-resolved particle approach, this represents satisfactory accuracy. When comparing results with different inflow velocities, their apparent influence on the convergence behaviour should, nonetheless, be kept in mind. This limitation, however, is irrelevant for the following section, as an inflow velocity of $\bar{u}_{in} = 20\,\text{m/s}$ is considered for all studies.

The presented quantification of stability and accuracy for both the particle-free flow in Section 4.3.1 and the single-layer fragment in Section 4.3.2 justify confidence in using the wall-flow model with elevated inflow velocities. This statement includes the specific set of boundary conditions, as well as the porous
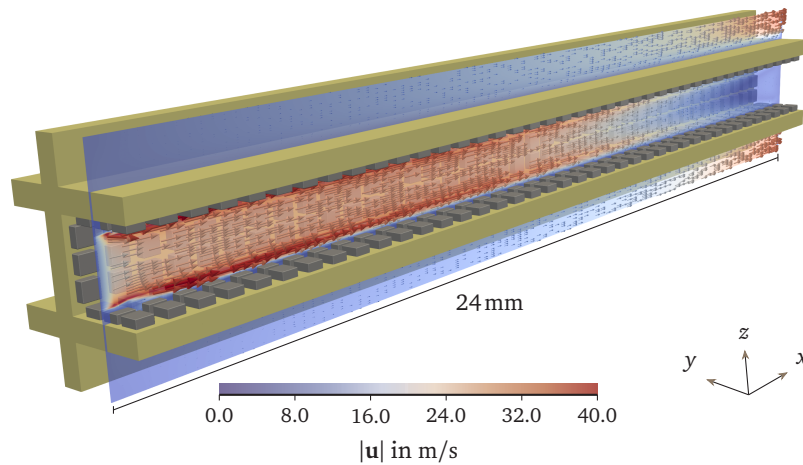
Figure 4.18: *Flow field with uniformly fragmented PM layer in gray. Dark yellow structures represent porous filter substrate. Colour scale indicates local velocity magnitude.*

media and the resolved particle approach.

4.4.3 Deposition Layer During Break-up

In this section, the results from investigating a uniformly fragmented deposition layer, as well as the impacts of the modifications described in Section 4.3.3, are presented. The latter comprise the influence of a uniform or increasing layer height (cf. Sections 4.4.3.2 and 4.4.3.3), non-uniform layer fragmentation (cf. Section 4.4.3.4) and partial detachment (cf. Section 4.4.3.5). A resolution of $N = 96$ and an inflow velocity of $\bar{u}_{in} = 20\,\text{m/s}$ are selected for all studies to ensure a sufficient distance to the stability limit and feasible computation times.

4.4.3.1 Uniformly Fragmented Deposition Layer

A deposition layer with a significant height, covering the majority of an inlet channel's cross-section, leads to a great reduction in the volume available for the gaseous flow. The resulting flow field for such a layer is shown in Figure 4.18. Compared to the flow field in Figure 4.14, much higher fluid velocities of up to $|\mathbf{u}| = 40\,\text{m/s}$ emerge in the reduced cross-section. These form into a somewhat continuous layer of elevated fluid velocity closely above the fragmented layer over most of the channel length. Due to the cross-section's sudden reduction near the channel inlet, the flow is initially directed towards the channel's centre,
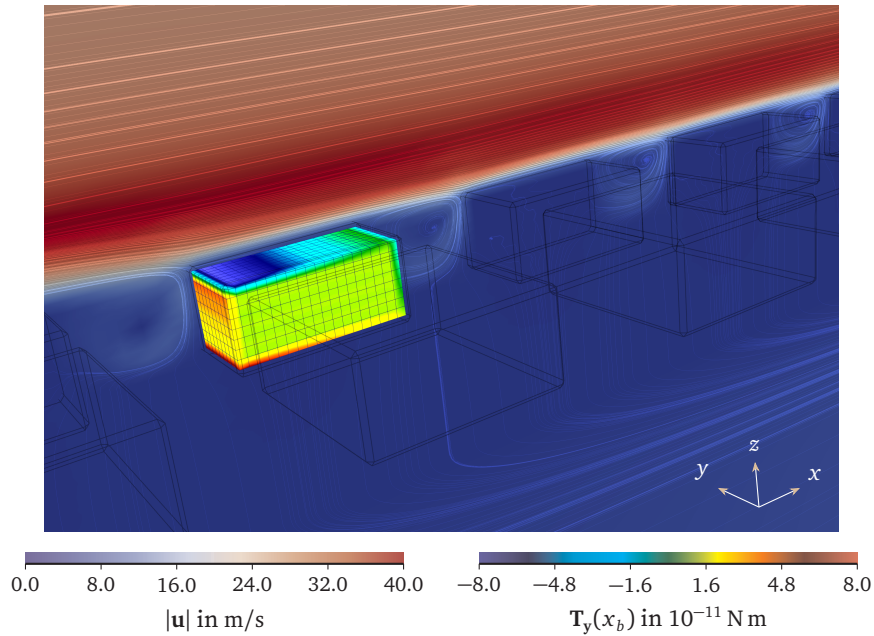
Figure 4.19: *Detailed flow field with uniformly fragmented PM layer. Exemplary fragment coloured according to local contribution to torque $\mathbf{T_y}(x_b)$. Streamlines exhibit local flow direction. Left colour scale indicates local flow velocity magnitude $|\mathbf{u}|$. Porous substrate removed for visual clarity.*

leading to an arch over the first three fragment rows. A close-up, focusing on the centre fragment of the third row, is shown in Figure 4.19. The exemplary fragment can be observed to exhibit a similar distribution of torque contributions as in the single fragment case in Figure 4.16. The magnitude of positive contributions on the exposed front side, however, is much smaller. The elevated velocity layer can clearly be identified on the particle's upper side, with a relatively sharp transition zone. Between the individual fragments, distinct flow structures occur, which show some resemblance to the ones obtained in a lid-driven cavity problem [145].

In order to derive predictions on the detachment likelihood of individual layer fragments, the spatial distribution of the hydrodynamic force acting on the fragments on one of the four substrate walls is retrieved. In Figure 4.20, the tangential force F_t and the rotation-induced normal force $F_{n,rot}$ are shown for each individual fragment along the channel length for the right, centre and left rows of the fragment field.
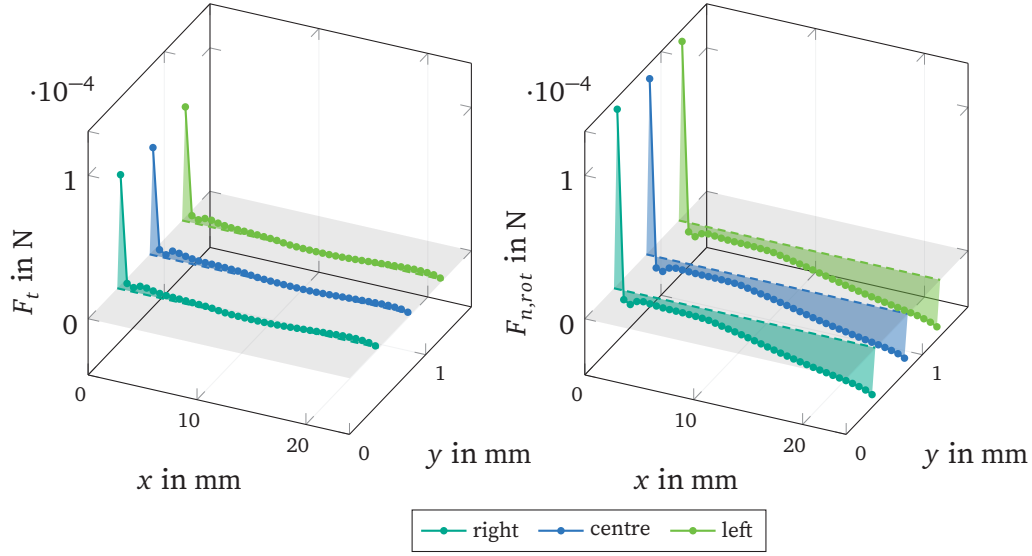
Figure 4.20: *Two-dimensional distribution of tangential forces F_t and rotation-induced normal forces $F_{n,rot}$ in a fragmented PM layer on one of four substrate walls. Differentiation between three lateral rows. Gray plane at zero crossing.*

It becomes apparent that, contrary to the observations at smaller velocities in Hafen et al. [1], the y-position has a negligible influence, as all three rows feature a very similar profile. For both forces, the frontmost fragment row experiences much higher values, while the ones for the rotation-induced normal component exceed the tangential ones. Due to the main flow direction along the channel length, all tangential values are positive with a small decrease in the mid-channel.

However, all rotation-induced normal force values after the first fragment row stay below zero. This already implies that, independent of any normal-directed adhesion force, no detachment can occur in that region for similar configurations as long as the centre of rotation in Figure 4.3 does not slip. The effect of the initial arch of elevated velocities on top of the first three fragment rows, shown in Figure 4.18, is visible in the force values as well.

A close-up of the different force contributions after the first row, including the standard normal force component F_N is shown in Figure 4.21. It can be observed that the values of the centre line and the outer row indeed differ in such a small way that only the centre row is considered for all following studies. The close-up additionally reveals that the rotation-induced normal force
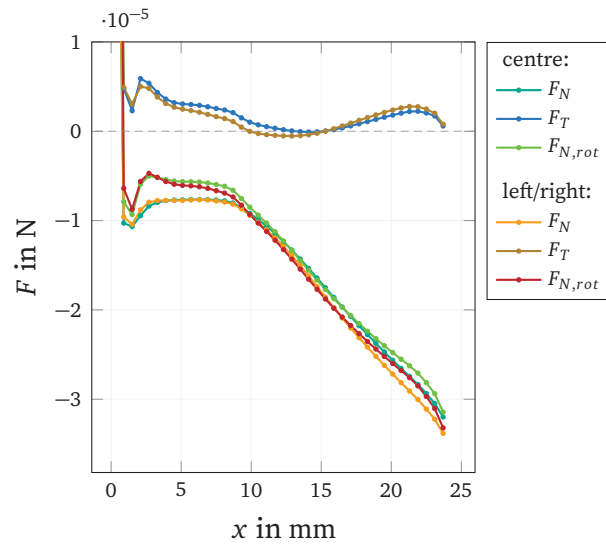
Figure 4.21: *Distribution of tangential forces F_t, standard normal forces F_n and rotation-induced normal forces $F_{n,rot}$ in central and outer PM fragment rows.*

always exceeds the standard normal force, serving as another reason to use it as the proper representative for the evaluation of *normal-directed detachment* (cf. Section 4.3.2) in the following.

4.4.3.2 Influence of Uniform Layer Height

A change in the height of the fragmented deposition layer changes both the hydrodynamic force on the surface of a single fragment and the overall flow field due to increase in the available channel cross-section. The flow field for the smallest considered height of $d_z = 21.0\,\mu\mathrm{m}$ is shown in Figure 4.22. The thin layer results in a more homogeneous flow field with no distinct layer of elevated velocities on the fragment's upper side. A comparison of the velocity profile for different layer heights is shown in Figure 4.23. It should be noted at this point that all velocity contributions are still averaged over the whole channel cross-section. It can be observed that the development of the averaged fluid velocity in the main flow direction is not influenced significantly, despite potentially large differences in local velocity contributions. The resulting hydrodynamic forces for different layer heights are shown in Figure 4.24.

The greatest impact of the fragment height can be found in the first row due to the great flow exposition, while the following fragments are less affected.
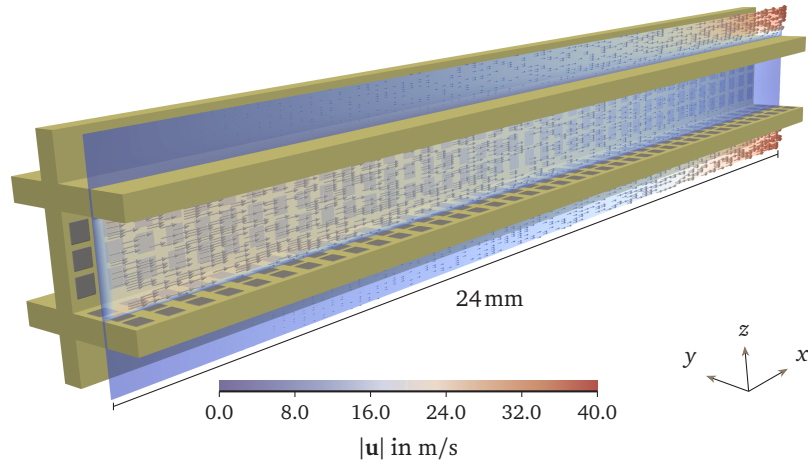
Figure 4.22: *Flow field with fragmented PM layer assuming a height of $d_z = 21.0\,\mu m$ in gray. Dark yellow structures represent porous filter substrate. Colour scale indicates local velocity magnitude.*
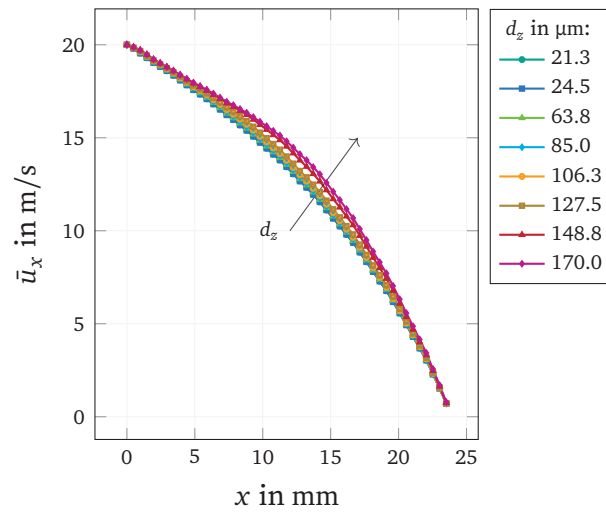
Figure 4.23: *Velocity profiles $\bar{u}_x(x)$ in inlet channel domain.*
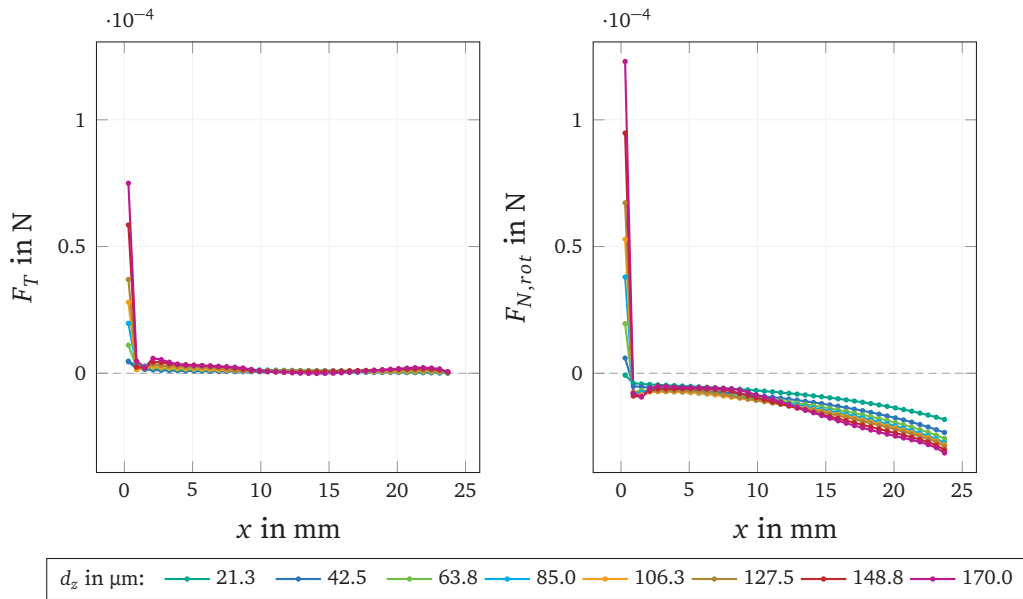
Figure 4.24: *Distribution of tangential forces F_t and rotation-induced normal forces $F_{n,rot}$ in central PM fragment row for different uniform layer heights d_z.*

These exhibit only negative contributions for the rotation-induced normal force, independent of the considered layer height. For the thinnest layer, this is additionally true for the first row, rendering normal-directed detachment unlikely.

4.4.3.3 Influence of Increasing Layer Height

A less prominent flow exposition of the first particle row results from a less abrupt decrease in the channel's cross-section due to a gradually increasing layer height. The flow field for a smooth transition from $d_z = 0.0425\,\text{mm}$ to $0.17\,\text{mm}$ over a relative channel length of $x_{rel} = 0.4$ is shown in Figure 4.25. The channel's front appears similar to the uniform thin layer in Figure 4.22; however, an increase in the velocity magnitude can be observed in the mid-channel.

As the fluid slows down again towards the channel's back, entrained PM fragments are expected to experience the strongest acceleration in the channel's mid-section once detached. The force distribution is shown in Figure 4.26. The distribution of both forces is more homogeneous with respect to the previously investigated layers. While the rotation-induced normal force $F_{N,rot}$ still features
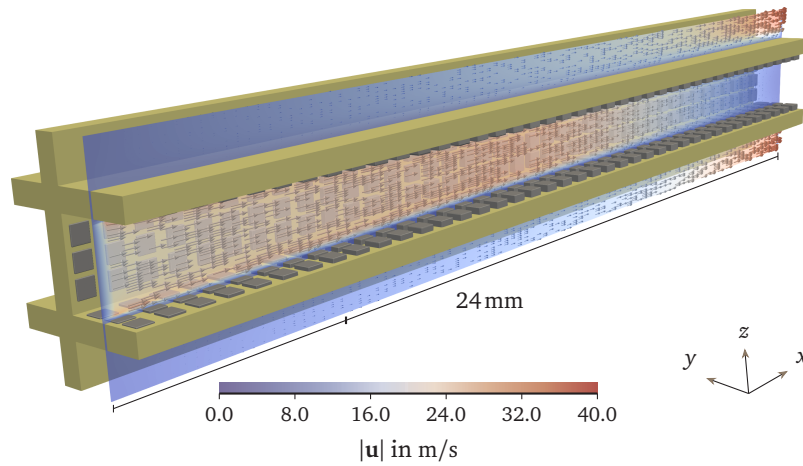
Figure 4.25: *Flow field with fragmented PM layer assuming an increasing height over a relative channel length of $x_{rel} = 0.4$ in gray. Dark yellow structures represent porous filter substrate. Colour scale indicates local velocity magnitude.*
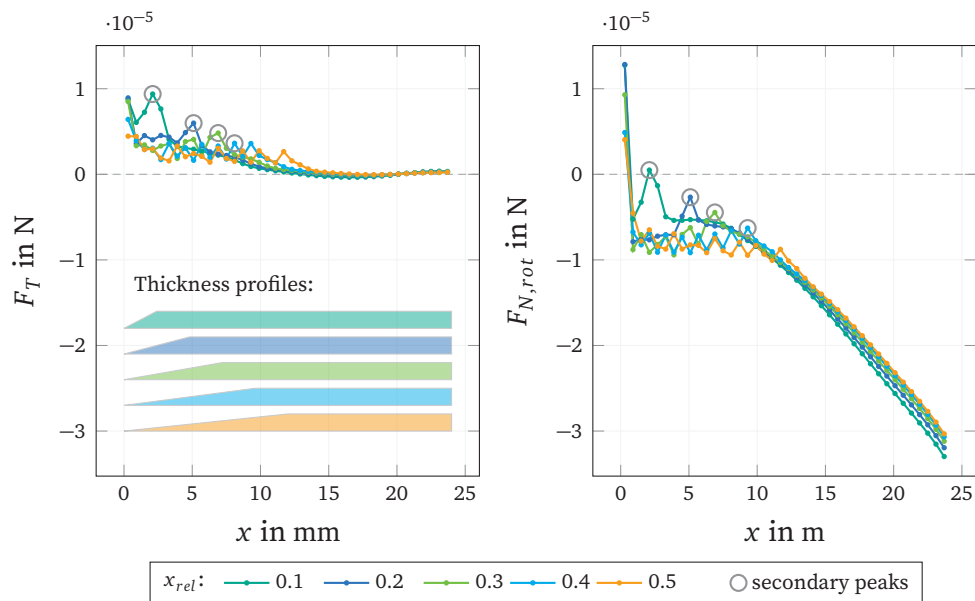
Figure 4.26: *Distribution of tangential forces F_t and rotation-induced normal forces $F_{n,rot}$ in central PM fragment row with increasing height over different relative channel lengths x_{rel}. Sketches (**left**) lay out height profiles. Circular marks indicate secondary peaks.*
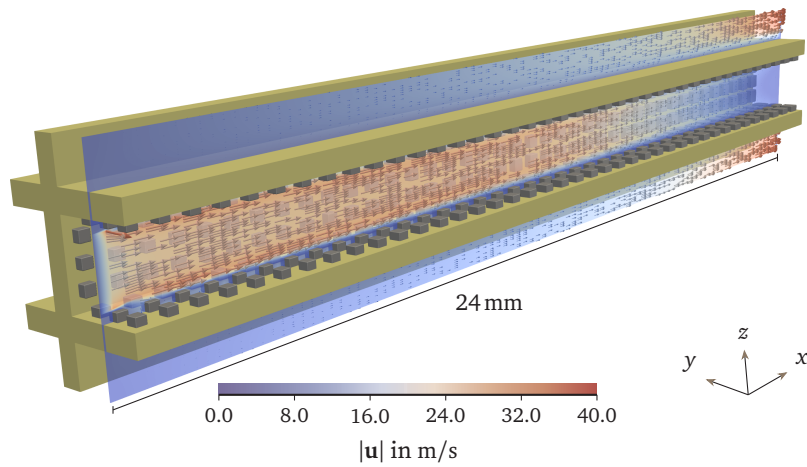
Figure 4.27: *Flow field with fragmented PM layer assuming an increasing substrate coverage beginning from a relative fragment size of $d_{xy,rel} = 0.6$ in gray. Dark yellow structures represent porous filter substrate. Colour scale indicates local velocity magnitude.*

the distinct force signal in the first row, the tangential force F_T shows a rather gradual decrease. When considering a sufficiently steep increase in height ($x_{rel} \leq 0.4$), a secondary peak emerges in both force signals at the transition point to a uniform layer height. None of the peaks, however, features significant positive values for the rotation-induced normal force to favour detachment.

4.4.3.4 Influence of Non-Uniform Layer Fragmentation

All the previously investigated layer variants represent the same coverage of the porous filter substrate. In order to investigate the coverage influence on both the fluid field and the hydrodynamic forces, linearly increasing or decreasing fragment sizes are considered while assuming the same height. Figure 4.27 shows the flow field for an increasing coverage, starting with a relative fragment size of $d_{xy,rel} = 0.6$ with respect to the standard dimension of $340 \times 340 \times 170\,\mu m^3$ (cf. Section 4.3.2). It can be observed that the increased cross-section in the channel's front prevents the formation of an elevated velocity layer, as found in Figure 4.18. The distribution of the velocity magnitude, therefore, appears very homogeneous over the first two-thirds of the channel length, leading to a nearly constant acceleration regime detached particles would be exposed to.

In order to quantify the coverage influence for each relative fragment size
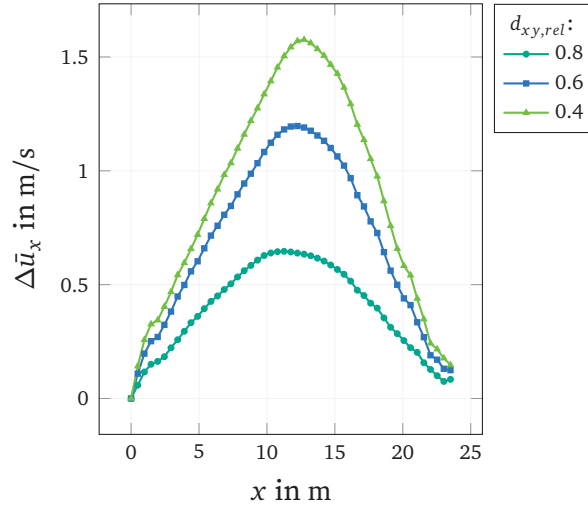
Figure 4.28: *Difference between velocity profiles $\bar{u}_x(x)$ of increasing and decreasing coverage for different relative fragment sizes $d_{xy,rel}$ in inlet channel domain.*

$d_{xy,rel}$, the decreasing case is related to the increasing one by subtracting the velocity profiles of the latter from the prior. The velocity differences are shown in Figure 4.28. It can be seen that the subtraction of the profiles yields only positive values. This means that a smaller fragment size in the front section (in the increasing case) leads to a smaller average fluid velocity over most of the channel length. The maximum of the velocity difference $\Delta\bar{u}_x$ can be found in the mid-section of the channel. This represents a wall-flow-specific feature, as the coverage between increasing and decreasing configuration for the same relative fragment size $d_{xy,rel}$ differs most at the channel's front and its back, but is in fact identical in mid-channel. This implies that more of the flow passes through the substrate's front section when the coverage is smaller in this area. With larger differences in the particle dimensions, the peak increases and slightly moves towards the back of the channel. In any case, the values of the velocity difference $\Delta\bar{u}_x$ can be considered relatively small with respect to the inflow velocity of $\bar{u}_{in} = 20\,\text{m/s}$.

The respective force distributions are shown in Figure 4.29. The values of the first row are not affected by the decreasing coverage, which mainly leads to differences in the channel back. In the increasing case, in turn, the values of the first row directly depend on the fragment size and exhibit smaller force signals accordingly when considering smaller relative fragment sizes $d_{xy,rel}$. It is, however, noteworthy that, for sufficiently small fragment sizes below $d_{xy,rel} =$
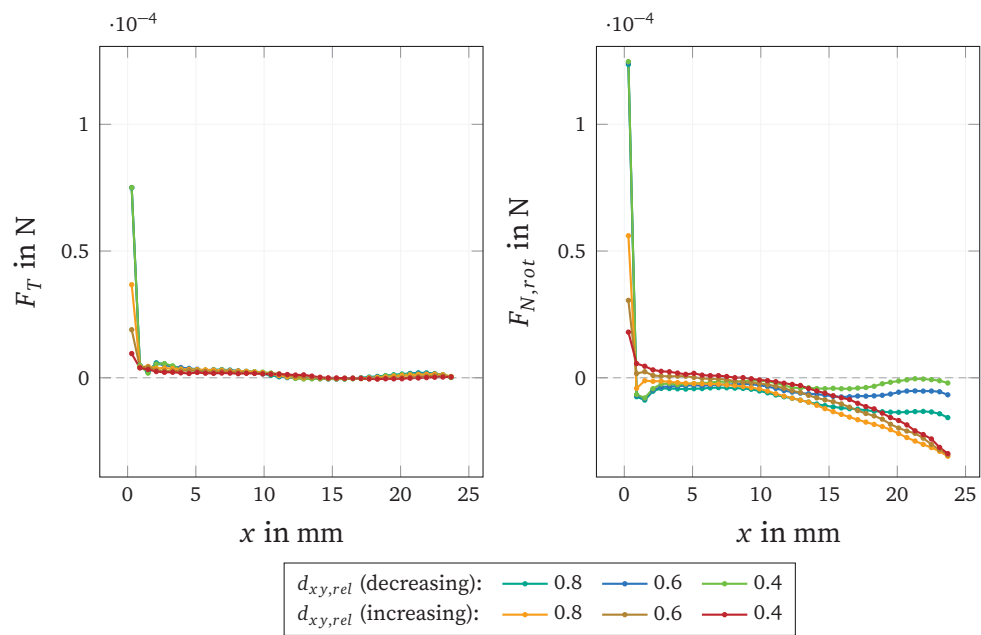
Figure 4.29: *Distribution of tangential forces F_t and rotation-induced normal forces $F_{n,rot}$ in central PM fragment row with increasing and decreasing substrate coverage beginning from or ending with different relative fragment sizes $d_{xy,rel}$.*
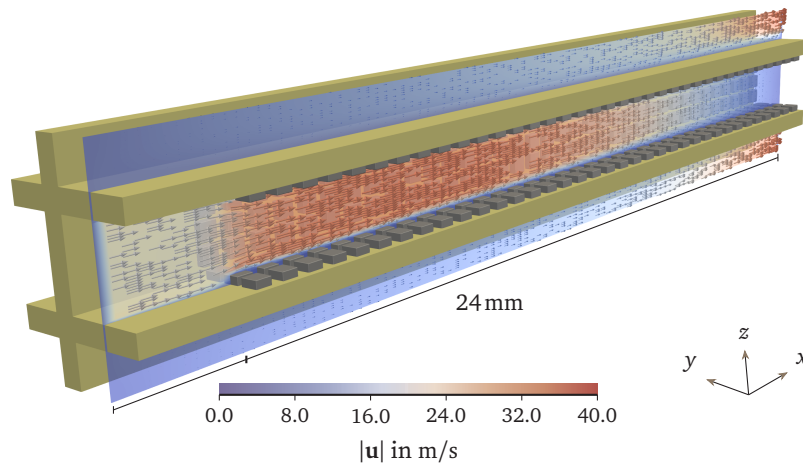
Figure 4.30: *Flow field with fragmented PM layer assuming partial detachment over a relative channel length of $x_{rel} = 0.1$ in gray. Dark yellow structures represent porous filter substrate. Colour scale indicates local velocity magnitude.*

0.6, a significant amount of slightly positive values of the rotation-induced normal force can be found even after the first row. Provided there are very small adhesive forces, this potentially enables the simultaneous detachment of multiple fragments in this region.

4.4.3.5 Influence of Partial Detachment

Due to the prominent role of the first fragment row in all previous studies, the effect of a fragmented layer with significant partial detachment in the front section is investigated. The flow field assuming a partial detachment up to a relative channel length of $x_{rel} = 0.1$ is shown in Figure 4.30. The transition point between the particle free substrate area to the first fragment row is characterized by a great increase in the fluid velocity magnitude due to the abrupt change in the cross-section available for the gaseous flow. Unlike the full uniformly fragmented deposition layer in Figure 4.18, however, a layer of elevated velocity does not appear and the fluid velocity features a homogeneous cross-section over the whole inflow channel. Considering the fact that the layer of elevated fluid velocity in the full layer case was observed over most of the channel length, it can be reasoned that a partial detachment of the first fragment rows leads to a homogenization of the whole fluid field. The force distributions assuming partial detachment up to various relative channel lengths x_{rel} are shown in
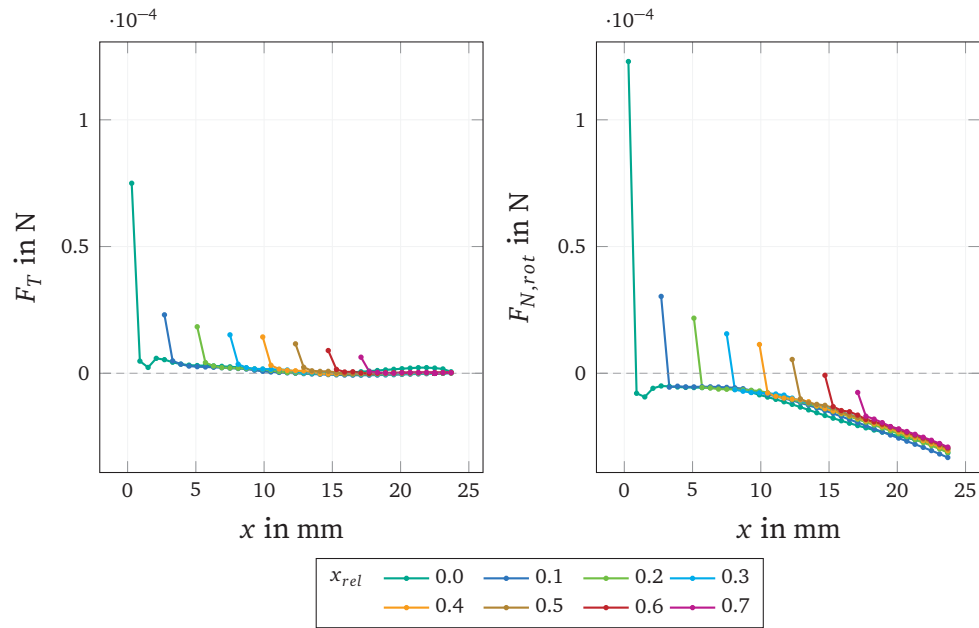
Figure 4.31: *Distribution of tangential forces F_t and rotation-induced normal forces $F_{n,rot}$ in central PM fragment row with partial detachment over different relative channel lengths x_{rel}.*

Figure 4.31.

It can be observed that the appearance of relatively high force values at the first row do not depend on its overall position in the existing flow field, but can be attributed to its exposed position in the flow. First rows located further towards the channel end do, however, experience smaller forces. The trend continues until negative values result for the rotation-induced normal force $F_{n,rot}$ after a relative channel length of $x_{rel} = 0.5$. This implies that PM fragments in a uniformly fragmented layer most likely detach one row after another until a threshold position is reached beyond which detachment can not occur any more.

4.5 Conclusions

The present work investigates the PM structure detachment from surfaces of wall-flow filters for elevated velocities using a previously developed LBM approach. Three different scenarios were investigated: The *particle-free flow*

in a clean channel was examined with respect to the parameter domain that ensures sufficient stability and accuracy. By evaluating the simulations' final states, a necessary stability domain was defined and a resolution-dependent expression for a stability threshold for the average inflow velocity was obtained. For grid resolutions of at least $N = 96$ cells per channel diameter, reasonable velocity and pressure accuracy could be achieved, including a satisfactory mass conservation. The parameter domain was then reevaluated for the flow around a *single layer fragment*, attached to the porous wall's substrate, including the individual components of the hydrodynamic surface force. It could be shown that the suitable parameter domain was limited to inflow velocities below $\bar{u}_{in} = 28\,\mathrm{m/s}$. The flow field was shown to feature distinct regions of increased and decreased local fluid velocities in the fragment's vicinity. Furthermore, the rotation-induced normal force was reasoned to be the relevant one for the prediction of fragment detachment. The force contributions could be shown to feature satisfactory accuracy for the wall-flow model with porous media and the surface-resolved particle approach included. With the wall-flow model's stability and accuracy for elevated velocities ensured, a *deposition layer during break-up* was investigated regarding local effects on the fluid field and the acting forces for different situations. Predictions on the detachment likelihood of individual layer fragments and their mutual influence were derived based on the spatial distribution of hydrodynamic forces. A uniformly fragmented PM layer of considerable height could be shown to lead to local velocity magnitudes of up to twice as large as the average inflow velocity. The first fragment row was identified as especially prone to detachment, with the following fragments being rather shielded. Contrary to previous observations [1], in low-velocity regimes, no significant dependency on the y-position along the channel width was noticeable. The layer height could be shown to predominantly have an effect on the first fragment row, while the impact could be observed to be diminished when considering continuously increasing layer heights. The substrate coverage turned out to have a minor effect on the velocity profile along the channel length, but was shown to potentially enable simultaneous detachment over multiple fragment rows when considering a sufficiently small coverage in the channel's front. Eventually, it could be shown that all considered cases do not significantly change the fact that normal directed detachment most likely occurs row-for-row until non-detachable rows are reached in the channel back.

The presented work provides a detailed quantification of stability and accuracy for static, impermeable PM layer fragments attached to the porous substrate's surface inside a single channel of a wall-flow filter. Furthermore, it

provides relevant insights into the nature of the hydrodynamic forces acting on the particulate structures and the local detachment likelihood of individual layer fragments depending on local flow conditions and the layer's fragmentation. As these represent key factors for rearrangement events and respective deposition pattern predictions, they contribute to potential optimizations in engine performance, fuel consumption and the service life of wall-flow filters.

5

Investigation of Dynamic Plug Formation

5.1 Introduction

Modern exhaust treatment systems of internal combustion engines rely on wall-flow filters as one of the key components for enabling compliance with present emission limits [58]. In such filters, a porous structure comprised of oppositely arranged inlet and outlet channels traps the contained particulate matter (PM) with efficiencies of up to 99% [74]. With increased filter loading, deposition layers are formed on the porous walls' surfaces and the filter's pressure drop increases, accompanied by a degradation of engine performance [81, 82, 135]. The introduced PM mostly consists of combustible soot and small amounts of inorganic non-combustible ash, which allows the filter's regeneration by continuously or periodically oxidizing its reactive components. The regeneration affects the deposition layer composition over the long term, as it leads to an accumulation of ash, which eventually forms larger agglomerates. The resulting inhomogeneities can then lead to a break-up of the continuous layer into individual PM layer fragments, which potentially detach from the filter

surface and relocate inside a channel [81]. This leads to the formation of specific deposition patterns, which affect a single channel's pressure drop contribution, its loading capacity and the separation efficiency.

Various scientific works [50, 82–84] contribute to the identification of probable causes and influence factors leading to the individual patterns, but a universal and consistent formulation without partially contradictory statements cannot be found. Calculation models that enable a consistent quantification of relevant influence factors on the individual parts of the regeneration process are missing completely. Those are, however, vital for respective predictions on the formation of specific deposition patterns, which impact engine performance, fuel consumption and service life of wall-flow filters.

In order to close this gap, the authors of the present manuscript approached different relevant aspects in three previous, consecutive works [1–3]: In an initial work [1], a holistic lattice Boltzmann method (LBM) approach was presented, which can be employed both for the simulation of the movement of surface resolved particles and the flow through porous media. With it, the gas flow and the movement of PM layer fragments was simulated with the open source software OpenLB [5, 27], while super-linear grid convergence and good agreement with a reference solution [112] could be shown. A literature review addressing relevant findings on the deposition pattern formation, general numeric approaches to wall-flow filter modelling and LBM-related research regarding flow through porous media, as well as surface resolved particle simulations, can be found in this work. The approach was then used in a following work [2] for the investigation of the detachment, acceleration and deceleration of individual PM layer fragments, resulting from the fragmentation of a continuous PM deposition layer during the filter's regeneration. This work includes a pressure drop comparison with investigations conducted on an experiment rig described in Thieringer et al. [9]. In the most recent work [3], a comprehensive quantification of the stability and accuracy of both particle-free and particle-including flow was provided for elevated inflow velocities of up to 60 m/s. By considering static, impermeable PM layer fragments attached to the porous substrate's surface, the detachment likelihood of individual layer fragments, including its dependency on local flow conditions and the layer's fragmentation, was determined.

The present and fourth work represents a direct sequel to Hafen et al. [3] by additionally considering the PM fragments' dynamic behaviour following the layer fragmentation. This includes the investigation of the detachment and transport of the fragments along the channel, as well as the subsequent formation of a channel plug. The latter represents a porous, unordered packing,

resulting from the accumulation of PM fragments, which can occupy a significant amount of the available channel volume [83, 84, 98, 99]. This can only be achieved by considering the interaction of moving fragments with each other, of moving fragments with a static fragment accumulation and of fragments with the substrate walls.

One goal of this work is therefore the extension of the resolved particle methodology [1–3, 15] by a previously developed and thoroughly validated discrete method to treat particle–particle and particle–wall interactions [96] and its application to dynamic rearrangement events in wall-flow filters. A second goal is the evaluation of the influence of the fragmented layer topology, PM properties and operating conditions on the described process itself and the determination of relevant key quantities. The latter include the final pressure drop, as well as the size and the mean density of resulting channel plugs.

Contrary to previous works in which the simulations' stability, accuracy and validity was accessed with convergence studies, literature findings and experimental results, the present work does not attempt such evaluations, but rather focusses on the derivation of quantitative statements. The challenges inherent to experimental investigations of the transient processes of interest [9], which are the motivation behind the present study in the first place, impede a thorough validation of the simulation results at this point. Single-valued key quantities, such as the plug density, are, however, compared to literature findings.

The remainder of the present work is structured as follows: A brief elaboration on the mathematical modelling and relevant numerical methods can be found in Section 5.2. Their application to a wall-flow filter is then described in Section 5.3, followed by the discussion and interpretation of the studies' results in Section 5.4. A summary of all relevant findings and resulting implications can then be found in Section 5.5. As the considered rearrangement process consists of multiple individual sub-processes, the present work contains a large number of flow field visualizations accompanying the quantitative evaluations in order to improve overall comprehension.

5.2 Mathematical Modelling and Numerical Methods

Analogous to the previous work [3], the evolution of conserved fluid quantities is described with the incompressible Navier-Stokes equations (NSE) [141] by using the LBM as a discretization approach in form of a mesoscopic description of gas dynamics. As an alternative to conventional computational fluid dynamics

(CFD) methods, this enables the retrieval of a fluid's velocity $u(x, t)$ and the pressure $p(x, t)$ at a three-dimensional position x in time t inside a specified domain.

In order to avoid a sole duplication of the existing modelling description, the respective equations are not carried over from Hafen et al. [3], but rather are referenced here. This includes a description of the LBM principles, an explanation of porous media and surface resolved particle modelling and the quantification of errors and convergence behaviour. As the modelling of discrete particle contacts according to [96] was not part of the previous works, however, it is laid out in the following:

5.2.1 Discrete Contact Modelling

In contrast to the contact treatment of spherical particles, the respective treatment for arbitrarily shaped ones comes with a significantly increased complexity, as the distance between surfaces cannot simply be deduced from their position and diameter. A model accounting for the interaction of arbitrary geometries including the computation of the contact normal n_c can be found in Nassauer and Kuna [146]. With it, the magnitude of the normal contact force

$$F_{c,n} = 0.75E^* \sqrt{V_c d_c} \left(1 + c\dot{d}_n\right) \tag{5.1}$$

can be obtained by means of the overlap volume V_c, the indentation depth d_c, the damping factor c and the magnitude of the relative velocity between two objects in contact in the direction of the normal force $\dot{d}_n$. Those parameters are computed following the method described in Marquardt et al. [96]. The effective modulus of elasticity E^* accounts for the material properties of both objects. With

$$E^* = \left(\frac{1 - v_A^2}{E_A} + \frac{1 - v_B^2}{E_B} \right)^{-1} \tag{5.2}$$

the moduli of elasticity E_A and E_B as well as the Poisson's ratios v_A and v_B of two colliding objects A and B are combined into a single effective value. According to Carvalho and Martins [147], the damping factor

$$c = 1.5\frac{(1-e)(11-e)}{(1+9e)}\frac{1}{v_0} \qquad\qquad v_0 > 0,$$
$$c = 0 \qquad\qquad v_0 \leq 0 \tag{5.3}$$

depends on the initial relative velocity magnitude at contact v_0 and the coefficient of restitution e. The force's three-dimensional vector components can be

Figure 5.1: *Sketch of wall-flow filter model, consisting of one central inflow (red) channel with fractions of surrounding inflow and outflow (blue) channels separated by porous walls.*

obtained via

$$F_{c,n} = n_c F_{c,n}. \tag{5.4}$$

Inside a dense packing, a particle's kinetic energy

$$\Upsilon_{p,kin} = \Upsilon_{p,trans} + \Upsilon_{p,rot} = \frac{m_p \mathbf{u}_p^2}{2} + \frac{\mathbf{I}_p \boldsymbol{\omega}_p^2}{2} \tag{5.5}$$

can be used as a threshold to avoid a never-ending evaluation of particle contacts. It depends on the particle's moment of inertia $\mathbf{I}_p$, its mass m_p, its velocity $\mathbf{u}_p$ and its rotational velocity $\boldsymbol{\omega}_p$, which represent its translational and rotational energy $\Upsilon_{p,trans}$ and $\Upsilon_{p,rot}$.

5.3 Application to a Wall-Flow Filter

The simulation setup of a single wall-flow filter channel used in previous works [1–3, 15] is considered in the present one as well. Figure 5.1 shows a sketch of the model, which represents a hashtag-shaped porous structure with a wall thickness of $l_w = 0.4\,\text{mm}$, which separates a central inflow channel, four additional quarter-sized inlet channels and four half-sized outflow channels. It features solid walls at the end of all inflow channels and at the beginning of all outflow channels, resulting in the described layout of oppositely arranged inlet and outlet channels. Within this model, a channel width of $l_y = 1.6\,\text{mm}$ and a scaled channel length of $l_{x,s} = 24\,\text{mm}$ is used. The latter accounts for a fifth of a real world representative of $l_x = 120\,\text{mm}$ in order to achieve a reduction in computational load that enables the computationally demanding studies in the present work in the first place [3]. All pressure-related quantities in the present work can therefore be related to each other, but should not be considered for a quantitative comparison of their absolute value with those reported in different

studies. The model's general capability in recovering the correct pressure drop when considering a full-length channel could, however, be ensured by showing quantitative accordance with literature findings in Hafen et al. [1] and measurements on an experimental test rig in Hafen et al. [2]. The explicit influence of the gas temperature is not considered in this work and ambient conditions are assumed for the whole channel domain.

The model domain is spatially discretized with a resolution N that is defined as the number of cells per channel width l_y. Periodic boundary conditions are then applied on the four surrounding sides, which let it serve as a representation of a real wall-flow filter comprised of hundreds of individual channels. Dirichlet boundary conditions [141] are used to impose a constant velocity at the inlets and a constant pressure at the outlets. No-slip conditions are assumed for the solid walls at the channel end caps on both sides. For the LBM-specific consideration, a simple bounce-back condition [131] is used for no-slip wall, regularized local boundary conditions [130] at the inlets and interpolated boundary conditions [143] at the outlets.

As the present work directly builds upon the results of its predecessor [3], a deposition layer during break-up due to the oxidization of the majority of its soot content [81] is considered as well. The individual layer fragments are modelled as a field of identical cubic discs that cover the porous walls inside an inflow channel. Here, a uniform field of 3×40 fragments is considered as a base configuration on each of the four porous walls of the central inflow channel.

In order to avoid numerical instabilities from initially large gradients, all simulation runs are conducted by smoothly ramping up the inflow velocity to the prescribed one, while the fragments are artificially held in place. Afterwards, convergence of velocity, pressure and hydrodynamic force are evaluated in reoccurring steps in the whole fluid field analogously to [3]. Contrary to the previous work, however, simulations are not concluded when reaching a converged state, defined by the convergence criteria for velocity, pressure and hydrodynamic force. Instead, the fragments are released from their static state, which enables them to potentially detach and move through the channel when sufficient hydrodynamic forces are present. In order to retain reproducibility, no artificial randomness is considered either for the fragmented layer creation or during detachment. Due to the channel's symmetry, this leads to the simultaneous detachment of multiple uniform fragments, which results in an accelerated rearrangement process with respect to a real-world counterpart. As reproducibility represents one of the prime advantages of simulations over experiments, this trade-off is chosen deliberately. A simulation is concluded when the cumulated

Table 5.1: *Relevant quantities with base value and variation range considered in the respective investigations .*

Quantity	Symbol	Base Value	Variation Range (min, max)
Fragment height	d_z	$170.0\,\mu m$	$42.5\,\mu m$, $212.5\,\mu m$
Equilateral fragment width	d_{xy}	$340.0\,\mu m$	$170.0\,\mu m$, $425.0\,\mu m$
Fragment rows along channel	$n_{f,x}$	40	20, 60
Fragment density	ρ_p	$500\,kg/m^3$	$100\,kg/m^3$, $800\,kg/m^3$
Fragment's modulus of elasticity	E_p	$1 \times 10^{-1}\,MPa$	$5 \times 10^{-2}\,MPa$, $5\,MPa$
Adhesion in normal direction	F_N	$0\,\mu N$	$0\,\mu N$, $25\,\mu N$
Inflow velocity	$\bar{u}_{in}$	$10\,m/s$	$4\,m/s$, $14\,m/s$

kinetic energy over all fragments according to (5.5) falls below a predefined energy threshold. Every simulation run can accordingly be divided into four consecutive parts:

1. Fluid velocity ramp-up and convergence with static fragmented layer

2. Detachment of fragments

3. Transport of fragments

4. Plug formation.

While the first one has been thoroughly investigated in the previous work, the present one focusses specifically on the last one. The conclusion of both periods is denoted *fragmented layer state* and *plug state*, respectively, and will be referenced throughout this work accordingly.

While such a rearrangement process may depend on many influence factors, the ones listed in Table 5.1 are investigated in this work. The first three factors cause modifications in the initial fragmented layer topology and the converged fluid field, respectively. They thus affect the complete rearrangement process. While the layer height depends on the loading time and PM concentration in the entering exhaust stream, the variation of fragment dimensions and the layer structure provides a simplified approach to account for the impact of the local distribution of ash and soot inside the PM layer. The latter four factors represent additional changes in PM properties and operating conditions, which impact the individual parts of a rearrangement process differently. The choice of base values and variation ranges results from a combined attempt to ensure

stability, to keep the analogy to previous studies, to respect physical limitations and to maximize the sensitivity of the individual factors on the process.

In the previous work [3], an inflow velocity of $\bar{u}_{in} = 20\,\text{m/s}$ and a resolution of $N = 96$ was selected for all studies of a deposition layer during break-up. Due to the significantly increased computational demand resulting from the additional consideration of the transient effects, the present work adopts a smaller inflow velocity of $\bar{u}_{in} = 10\,\text{m/s}$, which enables a lower resolution of $N = 64$ in order to avoid exceeding the available computational resources.

The discrete contact model, described in Section 5.2.1, requires the specification of respective material and mechanical properties. While those are in part subject to some uncertainty, they are kept constant in all studies to nonetheless ensure consistency throughout all investigations. For the porous substrate, a modulus of elasticity of $E_w = 10.0\,\text{GPa}$ and a Poisson's ratio of $v_w = 0.2$ can be assumed, following experimental measurements of Cordierite wall-flow filters [100, 148]. Due to the lack of respective measurements for the PM under study, in this work, a Poisson's ratio of $v_p = 0.4$ is assumed for the PM layer fragments, adopting the properties of saturated clay [149]. It is worth noting at this point, however, that the effective modulus of elasticity E^* in (5.2) exhibits a minor sensitivity to changes in the Poisson's ratio of the fragments, owing to the large magnitudes associated with the moduli of elasticity in the denominators. Based on its minor stiffness, we assume a fragment's modulus of elasticity of $E_p = 0.1\,\text{MPa}$. Due to the contact model's sensitivity to this parameter and the lack of existing data to substantiate this assumption, its impact is investigated as representative for the mechanical properties of PM as well (cf. Table 5.1). In order to ensure sufficient dissipation for the comparably coarse temporal resolution in the present work ($\Delta t = 1.32 \times 10^{-7}\,\text{s}$), a coefficient of restitution of $e = 0.3$ is used.

Analogous to the previous works [1–3, 15], some relevant quantities are averaged at discrete locations over the cross-section of the central inlet channel and one representative outlet channel (denoted as C_{in} and C_{out}) at recurring intervals and significant points in time. Next to the axial fluid velocity u_x and the pressure p, this work now additionally considers the PM density ρ, eventually providing a velocity, pressure and density profile $\bar{u}_x(x)$, $\bar{p}(x)$ and $\bar{\rho}(x)$ along the channel length both at the converged fragmented layer state and the plug state. Such a density profile can then provide information about:

- Areas of complete detachment

- Areas of incomplete detachment and re-deposition

- Volume occupied by the plug

- Local compactness inside the plug

In order to enable a consistent quantification of the plug extent and its properties, a mean density profile $\varrho(x)$ is evaluated at the plug state. For this, the raw profile at plug state is smoothed by applying a Savitzky–Golay filter [150] with an order of 2 and a window size of 40 discrete points. The largest gradient in the smoothed profile is then interpreted as the transition point on the x-axis between layer and plug region. The original raw profile is averaged separately in both regions, yielding the mean density profile. This way, the plug starting position and its average density can be obtained as single-valued quantities, available for the comparison with other simulation. The individual steps are laid out at the first occurring of a density profile in Figure 5.7.

5.4 Results and Discussion

In the present section, the results from all simulation runs are presented, discussed and related to each other. First, the rearrangement process assuming the base configuration in Table 5.1 is evaluated in detail with respect to initial flow conditions in the converged state, the transient behaviour during rearrangement events and the final state in Section 5.4.1. Afterwards, the impact of influence factors that lead to a change in the fragmented layer topology on both the initial flow condition and the rearrangement process are laid out in Section 5.4.2. Additional PM properties and operating conditions that do not alter the initial state are then investigated in Section 5.4.3.

5.4.1 Rearrangement in Base Configuration

The base configuration represents the channel model with a fragmented deposition layer, assuming the exact values listed in Table 5.1. Its converged fragmented layer state (cf. Section 5.4.1.1), the following transient behaviour during rearrangement (cf. Section 5.4.1.2) and the final plug state are investigated separately in the following (cf. Section 5.4.1.3).

5.4.1.1 Fragmented Layer State

The flow field inside the channel including the fragmented layer at the converged state is shown in Figure 5.2.

24 mm

0.0   4.0   8.0   12.0   16.0   20.0

|**u**| in m/s
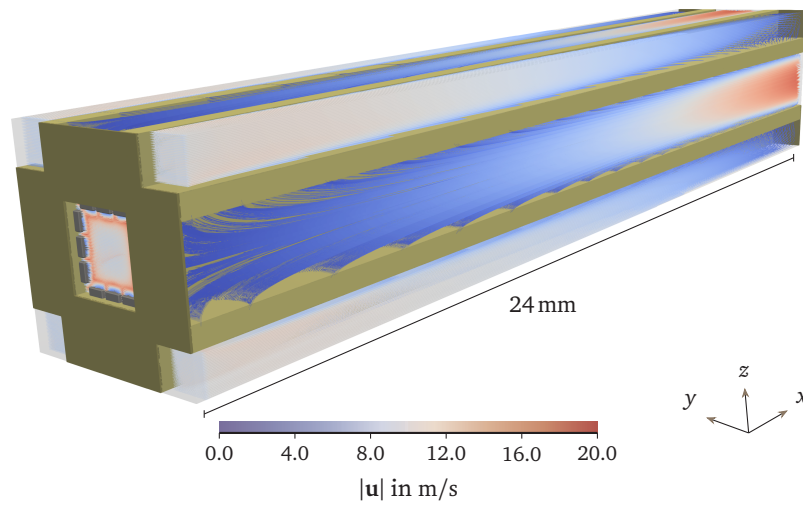
Figure 5.2: *Flow field with uniformly fragmented PM layer in gray. Dark yellow structures represent porous filter substrate, brown structures solid walls. Streamlines exhibit local flow direction. Colour scale indicates local velocity magnitude.*

The flow field is represented by streamlines, which indicate the local flow direction and are coloured according to the local velocity magnitude. With those, the decrease in velocity magnitude inside the inlet channels can be identified over the channel length. A continuous magnitude increase can in turn be found in the outflow channels, eventually forming a developed channel profile at the outflow. As the fragmented deposition layer covers a large part of the central inlet channel's cross-section, the area available for the flow is reduced, leading to significantly elevated velocities of up to $|\mathbf{u}| = 16\,\mathrm{m/s}$ with respect to the imposed average inflow velocity of $\bar{u}_{in} = 10\,\mathrm{m/s}$.

The determination of the hydrodynamic forces acting on the particulate structures and the deduction of the local detachment likelihood of individual layer fragments, including their dependency on local flow conditions and the layer's fragmentation, have been the subject of the predecessor work [3]. The corresponding velocity and pressure profiles $\bar{u}_x(x)$ and $\bar{p}(x)$ in the converged fragmented layer state can thus be found there, but have, additionally, been added as a reference to Figure 5.8.

5.4.1.2 Transient Behaviour

The transition from a uniformly fragmented deposition layer to an immobile plug configuration consists of detachment and transport of the individual fragments as well as the plug formation. The transient process in the central inlet channel is shown in Figure 5.3 at four exemplary points in time **T1**, **T2**, **T3** and **T4**.

Time **T1** represents the inner view of Figure 5.2, with the uniformly fragmented PM layer and a somewhat continuous layer of elevated fluid velocity closely above the fragmented layer over most of the channel length [3]. The fragments are then released (cf. Section 5.2), leading to a consecutive row-by-row detachment, which is caused by both increased flow exposition of initially shielded fragments and tear-off due to contact with suspended fragments flying by. This way, the number of simultaneously suspended fragments increases continuously until a major portion of the channel's cross-section is occupied by them at **T2**. Due to the restored channel cross-section in the channel's front, the local velocity magnitude decreases significantly here. At time **T3**, re-deposited fragments can be observed in the channel-mid, as fragment–fragment contact rather causes interception than tear-off due to the different flow conditions here. In a previous study on single fragment behaviour [2], fragments were found to always travel to the channel end once detached. When considering multi-fragment environments, this statement has to be extended with the possibility of interception, respectively. Time **T4** shows the channel's final state, where no fragments are suspended any more and a compact plug has formed at the channel end with a small region of undetachable fragments in front of it. Summing the kinetic energy $\Upsilon_{p,kin}$ in (5.5) over all individual layer fragments results in the cumulated kinetic energy Υ_{kin}, which provides a measure of the progress of the rearrangement process. Its temporal development is shown in Figure 5.4.

The cumulated kinetic energy features a steep increase following the fragment's release after fluid convergence, as fragments continuously detach and resuspend into the flow. A maximum is reached when the number of simultaneously suspended fragments is the highest and detaching fragments approximately equals those joining the plug formation or being intercepted mid-way. The cumulated kinetic energy then starts to decrease until reaching a level at around $t \approx 40\,\text{ms}$, where it approaches zero with a shallow slope. During this period, fragments steadily arrange inside the newly formed plug, whose compactness continuously increases. The transient development of the cumu-

24 mm

① $t = 10.8$ ms

② $t = 16.0$ ms

③ $t = 24.5$ ms

④ $t = 80.0$ ms

0.0   4.0   8.0   12.0   16.0   20.0

$|\mathbf{u}|$ in m/s

z

x
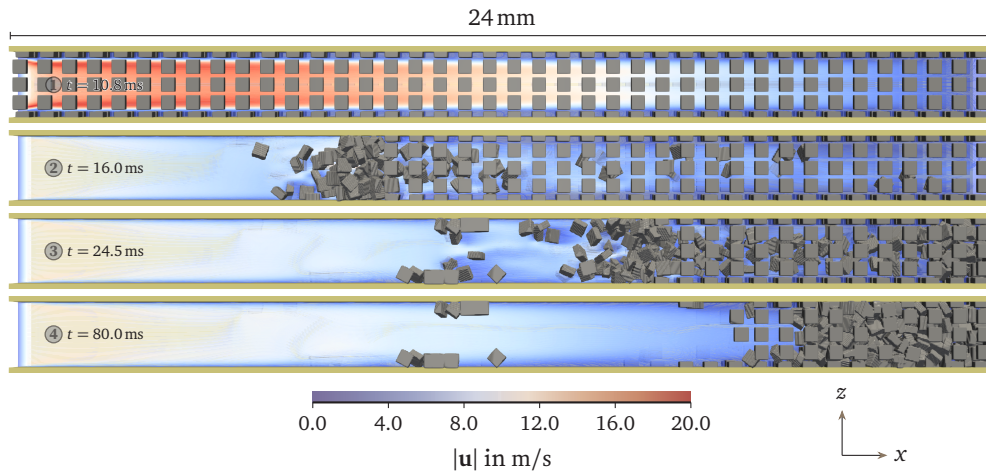
Figure 5.3: *Time series of detachment, transport and plug formation. Dark yellow structures represent porous filter substrate. Streamlines exhibit local flow direction. Colour scale indicates local velocity magnitude.*

t_{frag} t_{plug}

t in ms
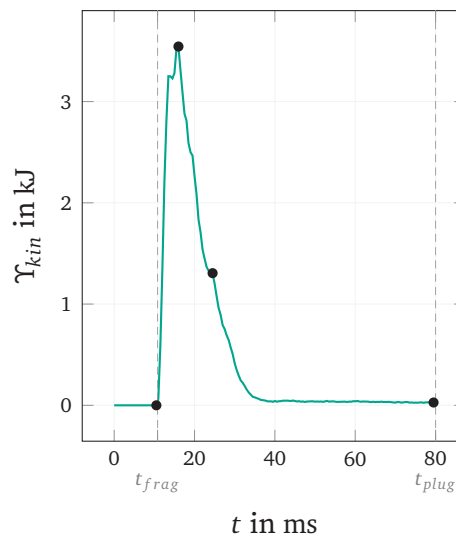
Figure 5.4: *Transient behaviour of fragments' cumulated kinetic energy Υ_{kin}. Black dots represent relevant times in Figure 5.3. Dashed lines indicate time of converged fragmented layer state t_{frag} and final plug state t_{plug}.*
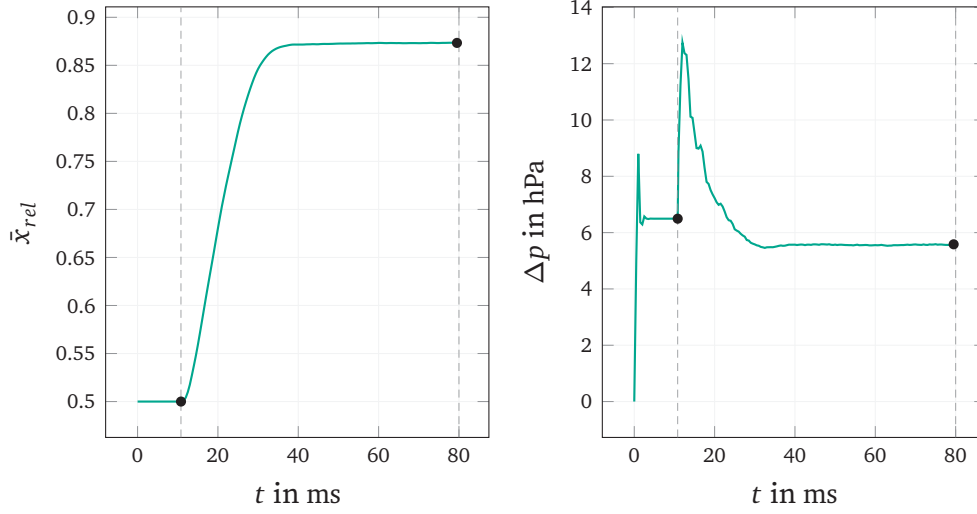
Figure 5.5: *Transient development of relative average PM position $\bar{x}_{rel}$ and pressure drop Δp. Dashed lines indicate time of converged fragmented layer state t_{frag} and final plug state t_{plug}. Black dots represent sampling points at relevant states.*

lated kinetic energy differs in part significantly throughout the different studies considered in this work. In order to ensure the comparability, a maximum simulation time of $t_{plug} = 80\,\text{ms}$ is identified as sufficient to capture all relevant transient effects in all simulation runs. That way, it simultaneously represents the time assumed for the evaluation of the *plug state*.

By averaging the discrete positions of all layer fragments, the average relative position of the total PM mass in the channel $\bar{x}_{rel}$ can be determined, which provides a simple single-valued measure for the spatial development during the rearrangement process.It can also provide some information about a continuing compaction, which reduces the channel volume occupied by the plug and may affect the total pressure drop. The temporal evolution of the relative average PM position $\bar{x}_{rel}$ and the pressure drop Δp is shown in Figure 5.5.

Due to its symmetry around the x-axis, a uniformly fragmented layer leads to an initial relative average PM position of $\bar{x}_{rel} = 0.5$. When the fragments are released after convergence and start to detach (cf. Section 5.3), the value increases steeply. The apparent smoothness of the course shows that the considered total number of fragments of $n = 480$ can be reasoned to be statistically representative. After the first fragments hit the channel's back wall, the slope decreases and starts to gradually approach a constant value, analogously to the

cumulated kinetic energy in Figure 5.4.

The pressure drop, in turn, settles at a constant value of $\Delta p = 6.50\,\mathrm{hPa}$ right after a start-up-induced fluctuation. When the fragments start to detach, the additional cross-section reduction observable at **T2** in Figure 5.3 causes more flux to be redirected through the porous walls with an elevated wall-penetrating velocity. Here, the momentum loss increases, causing the pressure drop to rise as well. When the cross-section starts to clear up due to fewer particles detaching, the pressure starts decreasing again and continues to get smaller as more volume becomes available again for the flow. Analogously to the cumulated kinetic energy and the average PM position, the pressure drop then approaches a constant value. The resulting pressure drop of $\Delta p = 5.58\,\mathrm{hPa}$ is smaller than the one at the converged layer state, with a difference of $\Delta p = 92\,\mathrm{Pa}$. This value is defined by the relation between an increase in the channel's cross-section and the open flow area through the filter substrate on the one hand and a decrease in the available channel volume on the other hand. Both quantities in Figure 5.5 are sampled at the converged fragmented layer state and the final plug state for the comparison between different simulations in Sections 5.4.2 and 5.4.3.

5.4.1.3 Plug State

The transient behaviour is concluded when reaching the plug state. A detailed view of the resulting plug packing is shown in Figure 5.6. All surfaces are coloured according to the magnitude of the local hydrodynamic force.

It can be observed how the transported fragments form a dense packing over multiple fragment rows. Some undetached fragments can be found right in front of it, where the hydrodynamic forces in the normal direction of the substrate's surface are not large enough to cause detachment. It also shows some redeposited particles, which have been intercepted during transport when loosing momentum due to contact with undetached fragments. The hydrodynamic force's magnitude $|\mathbf{F}_{hyd}|$ can be seen to decrease quickly when advancing further into the packing, indicating a continuously decreasing amount of fluid penetrating the plug. As the filter walls are permeable, they are subject to small currents inside them, causing a non-zero force contribution on each fragment's bottom side.

The density profile for both fragmented layer and plug state is shown in Figure 5.7. The methodology for the evaluation of a mean density profile as described in Section 5.2 is outlined as well.
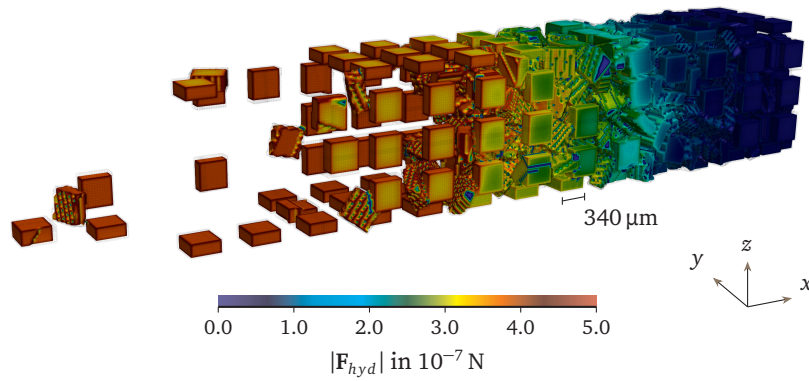
Figure 5.6: *Packing at plug state. Fragment surfaces coloured according to local contribution to hydrodynamic force magnitude $|\mathbf{F}_{hyd}|$. Porous substrate and flow removed for visual clarity.*
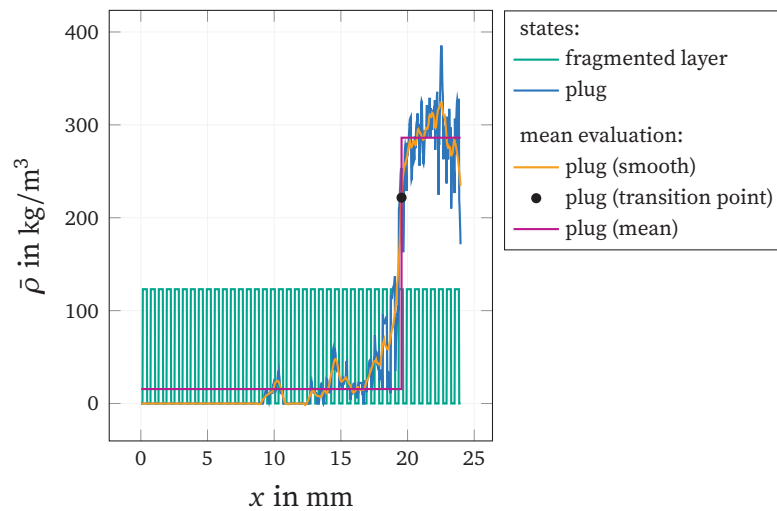
Figure 5.7: *PM density profile $\bar{\rho}(x)$ at fragmented layer and plug state. Additionally, layout of mean evaluation methodology according to Section 5.2.*
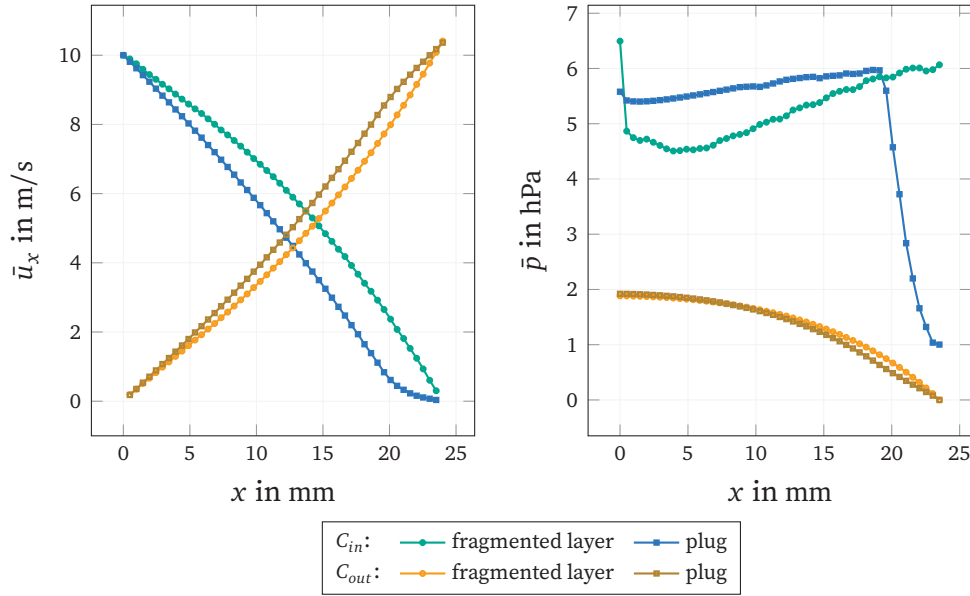
Figure 5.8: *Velocity profile $\bar{u}_x(x)$ and pressure profile $\bar{p}(x)$ in inlet channel domain C_{in} and outlet channel domain C_{out} at fragmented layer and plug state.*

It can be seen that the fragmented layer state is characterized by a non-negligible density which exhibits a periodic nature with a constant maximum, directly reflecting the PM layer height. The plug state, in turn, features a distinct profile, which shows no density in the frontal part of the channel, a small one in the channel-mid and a clearly identifiable plug region in the rear part of the channel beginning. The density reaches its maximum in the middle of the plug and decreases slightly both towards its front and the channel back wall.

The transition between layer and plug according to the mean density methodology lies at $x = 19.6\,\text{mm}$, which reveals that the plug occupies approximately 18% of the central inflow channel's volume at plug state. The resulting mean density profile (denoted $\varrho(x)$ in the following) exhibits an average plug density of $\varrho = 286\,\text{kg/m}^3$, which lies well in the ranges of $220\,\text{kg/m}^3$ to $330\,\text{kg/m}^3$ [83] and $160\,\text{kg/m}^3$ to $400\,\text{kg/m}^3$ [98, 99] reported in the literature for unsintered lube oil-derived ash.

The respective velocity and pressure profiles $\bar{u}_x(x)$ and $\bar{p}(x)$ in the central inlet channel and the representative outlet channel (cf. Section 5.3) are shown in Figure 5.8 for both fragmented layer and plug state.

In the predecessor work [3], distinct profiles were identified in the frag-

mented layer state: The velocity is characterized by a transition from the imposed one $\bar{u}_{in}$ to zero in the inflow channel domain $C_{in} = 10\,$m/s and exhibits the opposite behaviour in the outflow channel domain C_{out}. It should be noted at this point that all averaging is performed on the full channel cross-section. That way, an increase in the axial velocity due to a reduced area available for the flow does not impact the velocity profile, as fewer but higher velocities lead to the same average. It consequently represents a measure of the x-directed flux at a specific position. The pressure, however, decreases at a reduced available cross-section, as the velocity effectively increases. This results in a sudden pressure drop close to the inlet in the fragmented layer state. The pressure then gradually increases until reaching a local maximum near the back wall. The overall pressure level in the inflow channel results from the momentum loss due to the porous walls between the channels. In the outflow channel, in turn, the pressure decreases continuously with a decreasing slope, leading to a continuously increasing pressure difference between the inflow and outflow channel over its length. At the plug state, the velocity profile in the inflow channel changes significantly, as the rear part of the channel becomes occupied and the effective volume available for the flow decreases. As the flow resistance in the remaining part decreases additionally due to the increase in free substrate surface area, more fluid passes through the walls in the channel front and the mid-section. This becomes evident when considering the significantly decreased axial velocity in the inflow channel and the increased velocity over the whole length of the outflow channel. According to the observations made on Figure 5.7, the plug is not completely impenetrable, but rather exhibits a quickly decreasing permeability, which results in the observed continuously decreasing hydrodynamic surface force on the fragments. As derived from Figure 5.5, the pressure in the inlet decreases by $\Delta p = 93.2\,$Pa at the plug state. Due to the complete detachment of the first fragment row, the sudden drop in pressure near the inlet vanishes. The profile then exhibits a shallow and nearly linear increase until reaching the plug's beginning. Inside the plug, the pressure drops quickly to a level that lies even below the average outflow channel pressure.

5.4.2 Influence of Fragmented Layer Topology

In the following, the influence of the layer topology on the complete rearrangement process is investigated by considering differences in the layer height in Section 5.4.2.1, the fragment dimensions in Section 5.4.2.2 and the layer structure in Section 5.4.2.3. Next to quantitative evaluations, flow fields are shown for
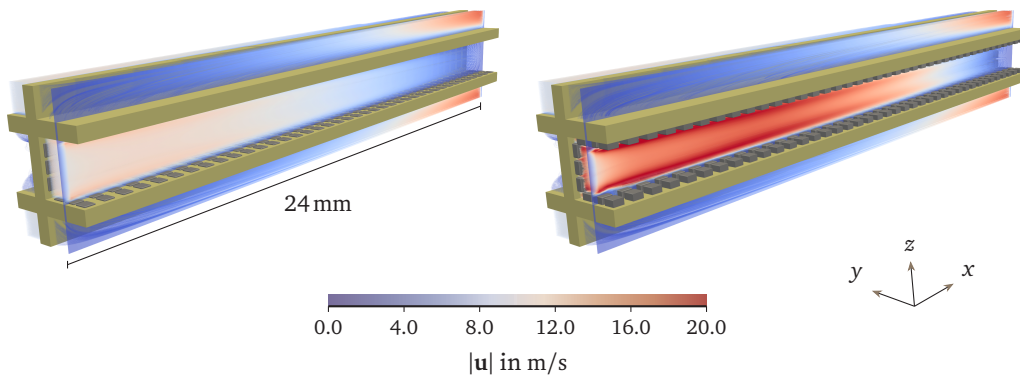
Figure 5.9: *Converged flow fields with uniformly fragmented PM layer in gray for layer heights $d_z = 63.8\,\mu m$ (**left**) and $d_z = 212.5\,\mu m$ (**right**) at fragmented layer state. Dark yellow structures represent porous filter substrate. Streamlines exhibit local flow direction. Colour scale indicates local velocity magnitude.*

both the converged layer state and the final plug state.

5.4.2.1 Influence of Layer Height

A layer as thin as $d_z = 42.5\,\mu m$ does not enable any detachment. The remaining range of considered PM layer heights in Table 5.1 is enclosed by the borderline cases $d_z = 63.8\,\mu m$ and $d_z = 212.5\,\mu m$, for which the resulting flow field is shown in Figure 5.9 at the converged fragmented layer stage.

A direct comparison reveals large differences in the fluid velocity over the major part of the central inlet channel, as a cross-section reduction leads to significantly increased local and averaged axial fluid velocities. Those already hint at more fragment detachment due to an increased detachment likelihood [3] and faster fragment transport. The resulting flow fields at the final plug state are shown in Figure 5.10.

The formulated assumption can be confirmed, as detachment only occurred at the very first fragment rows for a layer height of $d_z = 63.8\,\mu m$, but over the whole channel length for a layer height of $d_z = 212.5\,\mu m$. The PM density $\bar{\rho}(x)$ profile and mean density profile $\varrho(x)$ (as laid out in Figure 5.7) are shown in Figure 5.11 for the considered range of layer heights.

The profile exposes regions of different detachability: while for small layer heights, only the first few fragment rows detach, nearly complete detachment can be found for the largest height. The volume occupied by the resulting plug
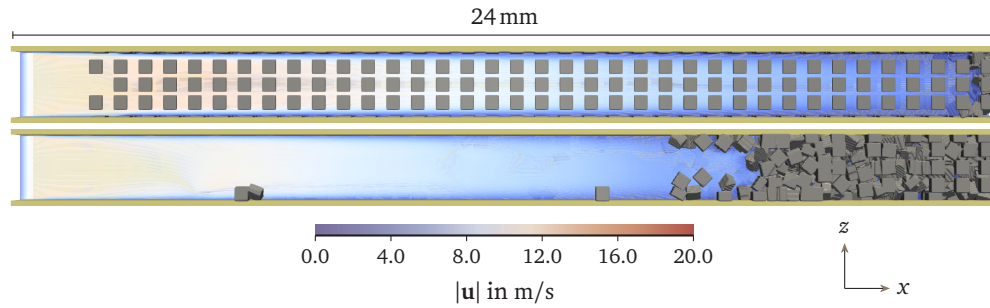
Figure 5.10: *Final flow fields with PM fragments in gray for layer heights $d_z = 63.8\,\mu m$ (**top**) and $d_z = 212.5\,\mu m$ (**bottom**) at plug state. Dark yellow structures represent porous filter substrate. Streamlines exhibit local flow direction. Colour scale indicates local velocity magnitude.*
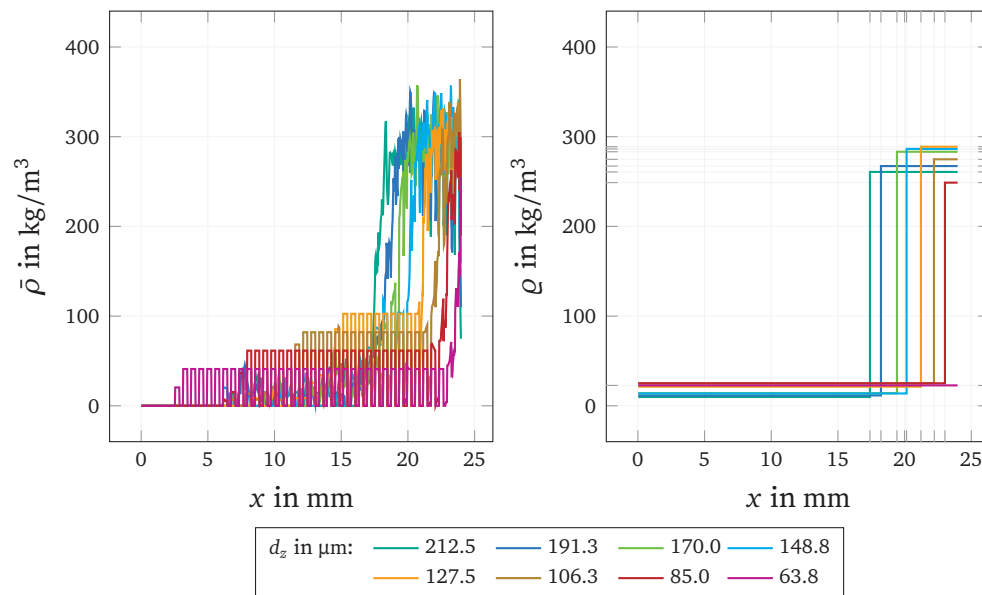
Figure 5.11: *PM density profile $\bar{\rho}(x)$ (**left**) and mean density profile $\varrho(x)$ (**right**) at plug state for different layer heights d_z.*
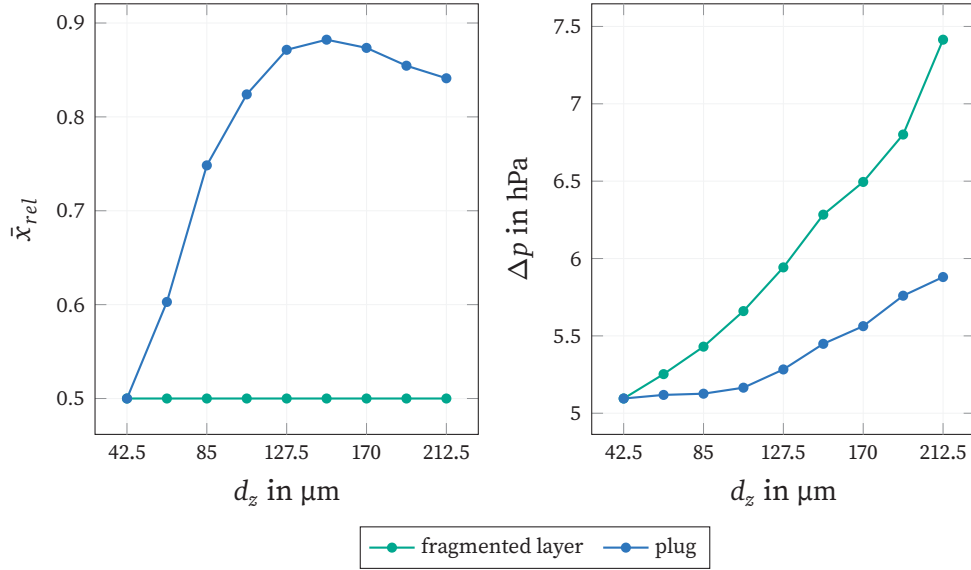
Figure 5.12: *Relative average PM position $\bar{x}_{rel}$ and pressure drop Δp for different layer heights d_z at fragmented layer and plug state.*

differs accordingly, as more detachment leads to more PM available for the plug formation, which gradually extends towards the inlet.

The dependency of the relative average PM position $\bar{x}_{rel}$ and the pressure drop Δp on the layer height at both fragmented layer and plug state (cf. Figure 5.5) is laid out in Figure 5.12.

As no detachment occurs for $d_z = 42.5\,\mu m$, both quantities are identical between the states. With increasing layer height, the relative average PM position then shifts towards the channel back at plug state due to the increasing number of detachable fragments. After reaching a maximum position of $\bar{x}_{rel} = 0.88$ for $d_z = 148.75\,\mu m$, it decreases for larger layer heights as the plug continues to grow in negative x-direction. Such a local maximum can consequently only be found for quantities that impact the detachment likelihood in a similarly pronounced way. The pressure drop increases continuously for both states, while exposing a much steeper slope at the fragmented state. This way, the difference becomes larger with increasing layer heights, with a maximum of $\Delta p = 153\,Pa$ for $d_z = 212.5\,\mu m$.
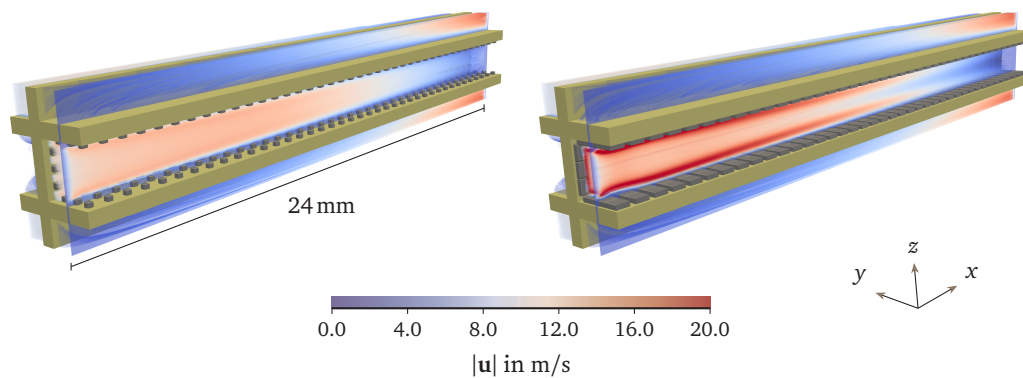
Figure 5.13: *Converged flow fields with uniformly fragmented PM layer in gray for fragment dimensions $d_{xy} = 170\,\mu m$ (**left**) and $d_{xy} = 425\,\mu m$ (**right**) at fragmented layer state. Dark yellow structures represent porous filter substrate. Streamlines exhibit local flow direction. Colour scale indicates local velocity magnitude.*

5.4.2.2 Influence of Fragment Dimensions

The flow fields for the lower and upper end of the considered fragment dimension range in Table 5.1 is shown in Figure 5.13.

Similarly to the relation in Figure 5.9, the larger fragment dimension leads to higher magnitudes of the fluid velocity due to the reduction in the channel's cross-section. Additionally, the free surface area on the substrate is greatly reduced, which leads to an inhomogeneous velocity distribution of the channel cross-section with a pronounced layer of elevated fluid velocity closely above the fragmented layer. The resulting flow fields at the final plug state are shown in Figure 5.14.

Due to the large difference in available PM mass, the resulting plug size differs accordingly. For fragment dimensions of $d_{xy} = 170\,\mu m$, a larger volume remains available for the flow. Complete detachment in the front and mid-section of the channel can be found in both cases, while the smaller fragment size exhibits an undetachable region in the additional flow volume due to insufficient axial flow velocities. The density profile for all considered fragment dimensions is shown in Figure 5.15.

Contrary to the observations made in Figure 5.11, no regions of undetachable fragments can be identified in the front and mid-section, even for small fragment dimensions. Detachability can consequently be assumed to feature a negligible sensitivity to the fragment dimensions in the considered range.
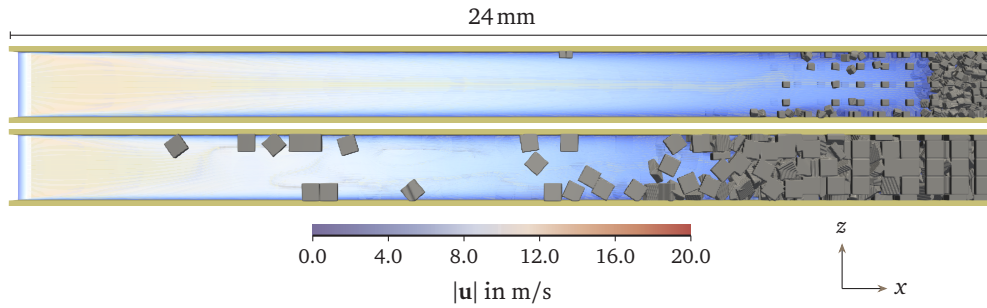
Figure 5.14: *Final flow fields with PM fragments in gray for fragment dimensions $d_{xy} = 170\,\mu m$ (**top**) and $d_{xy} = 425\,\mu m$ (**bottom**) at plug state. Dark yellow structures represent porous filter substrate. Streamlines exhibit local flow direction. Colour scale indicates local velocity magnitude.*
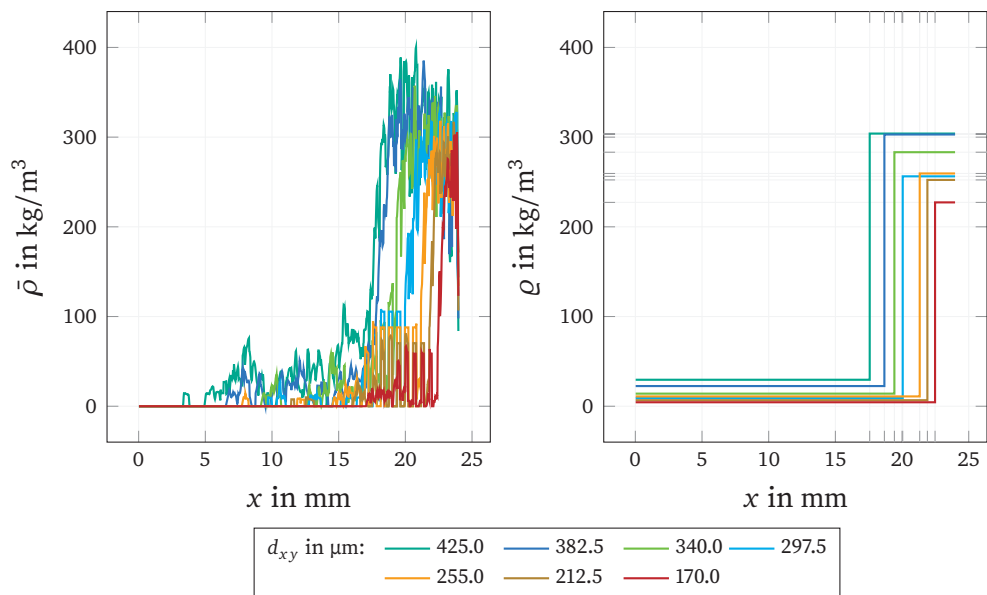
Figure 5.15: *PM density profile $\bar{\rho}(x)$ (**left**) and mean density profile $\varrho(x)$ (**right**) at plug state for different fragment dimensions d_{xy}.*
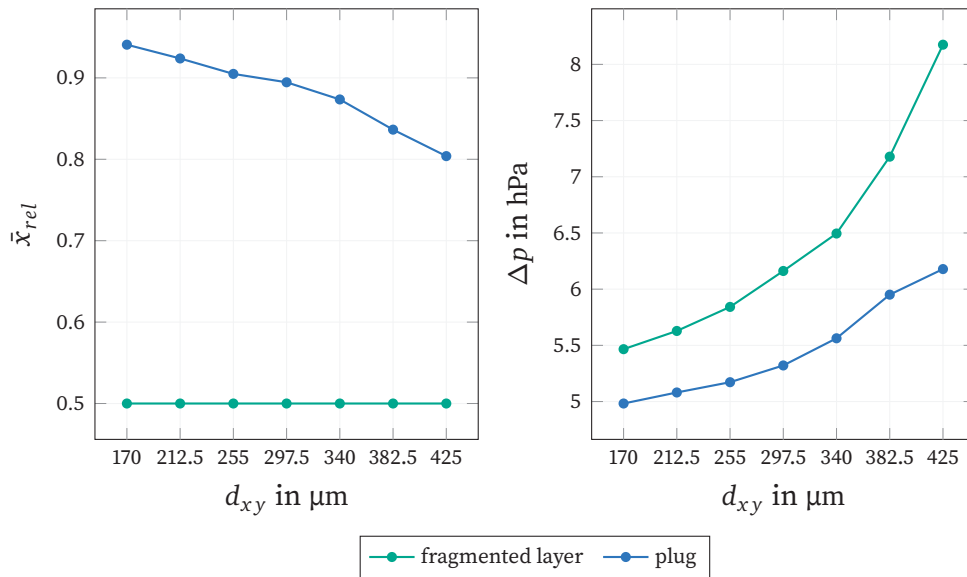
Figure 5.16: *Relative average PM position $\bar{x}_{rel}$ and pressure drop Δp for different fragment dimensions d_{xy} at fragmented layer and plug state.*

Larger fragments, however, seem to be associated with a higher likelihood for interception during the transport, as non-zero density values reach further towards the inlet at the plug state. Inside the plug, differences are similar to those observed for the layer height, as the cumulated mass, hence the mean density, increases in both cases with larger fragments. The dependency of the relative average PM position $\bar{x}_{rel}$ and the pressure drop Δp on the fragment dimensions at both states is shown in Figure 5.16. Contrary to a variation of the layer height in Figure 5.12 the average PM position continuously decreases with increasing fragment dimension. Due to negligible differences in the detachability, no inflection point can be found here and the average PM position directly reveals how far the plug reaches into the channel. The pressure increases for both states, with the difference between them continuously becoming larger. A fragment size of $d_{xy} = 425\,\mu m$ eventually results in a difference of $\Delta p = 199.6\,Pa$.

5.4.2.3 Influence of Layer Structure

Depending on the amount and nature of inhomogeneities in the local distribution of reactive (soot) and inert (ash) components in a PM layer, a fragmentation due to the oxidation of the reactive components can lead to different amounts
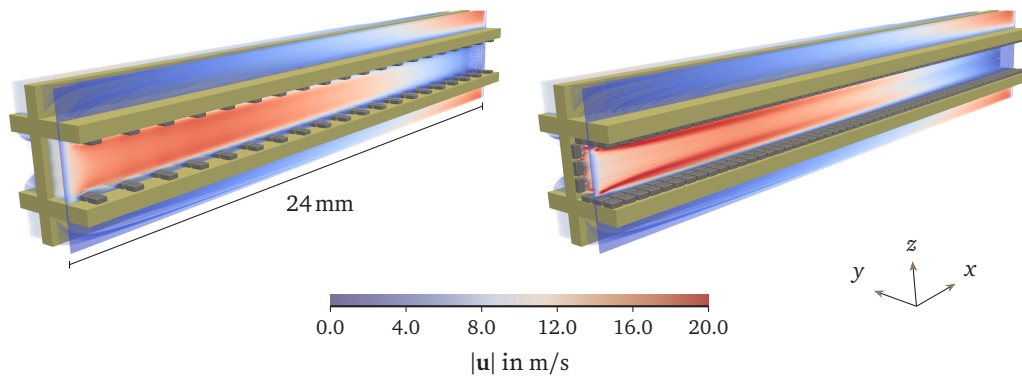
Figure 5.17: *Converged flow fields with uniformly fragmented PM layer in gray for numbers of fragment rows $n_{f,x} = 20$ (**left**) and $n_{f,x} = 60$ (**right**) at fragmented layer state. Dark yellow structures represent porous filter substrate. Streamlines exhibit local flow direction. Colour scale indicates local velocity magnitude.*

of equally sized PM fragments [81]. The borderline cases for the resulting layer structures are displayed in Figure 5.17. While the cross-section at the position of fragment rows remains identical, the free surface area on the porous substrate differs significantly. Analogously to the observations in Figure 5.13, a reduction in free surface area leads to the development of a more inhomogeneous velocity distribution over the channel's cross-section. A layer structure of $n_{f,x} = 20$ shows the trailing fluid structures observed in Hafen et al. [3] behind each fragment row due to the large distance to the next one. When considering $n_{f,x} = 60$, in turn, each fragment row is shielded from the flow by the surrounding ones.

At plug state, the two borderline cases yield the flow fields shown in Figure 5.18. The plug size, again, directly reflects the difference in available PM mass. The influence of the layer structure on the density profiles is shown in Figure 5.19.

It shows similar tendencies as the fragment dimension in Figure 5.15: Full detachment can be found for all variations in the channel's front and mid-section. Solely a small section right in front of the plug shows a reduced detachability for a greater number of fragment rows $n_{f,x}$ due to the reduced exposition to the hydrodynamic forces at this position. Contrary to the influence of the fragment dimensions, the plug's mean density exhibits a smaller sensitivity.

The relative average PM position in Figure 5.20 directly reflects the cumulated PM mass provided at the fragmented layer state, as it depicts plug growth
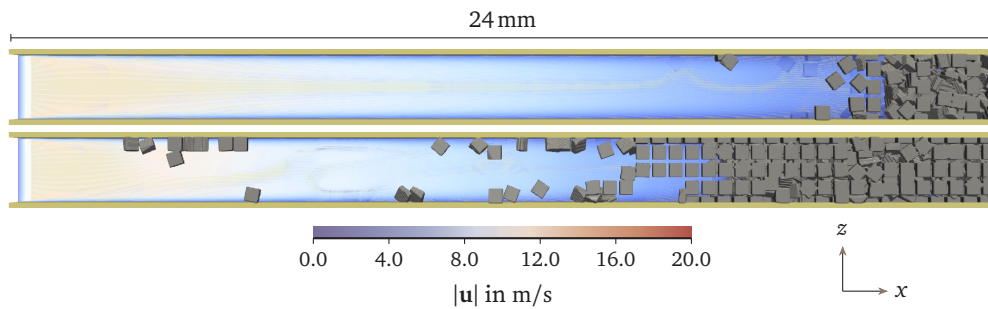
Figure 5.18: *Final flow fields with PM fragments in gray for numbers of fragment rows $n_{f,x} = 20$ (**top**) and $n_{f,x} = 60$ (**bottom**) at plug state. Dark yellow structures represent porous filter substrate. Streamlines exhibit local flow direction. Colour scale indicates local velocity magnitude.*

towards the inlet. This growth leads to a nearly linear increase in the pressure drop at plug state. The pressure drop at the fragmented layer state exhibits a steeper slope and rises to larger values when the free substrate surface area becomes smaller. This rise eventually leads to a pressure drop difference of $p = 442\,\text{Pa}$ at $n_{f,x} = 60$ between both states.

Some intermediate conclusions can be drawn from the investigation of all three topology variations, which can be attributed to two major causes: Firstly, the total PM mass present in the channel. As no continuing soot oxidization is considered, this mass stays constant throughout each simulation. Secondly, the free substrate surface area available for the flow at fragmented layer state. A reduction in this area leads to an inhomogeneity in the velocity distribution over the channel's cross-section, which includes the development of a layer of elevated velocities closely above the fragments. This potentially leads to larger hydrodynamic forces on the deposited fragments and less propulsion in the channel's centre during transport. In general, it can be stated that the topology at the fragmented layer state affects the final plug structure, while the impact on the pressure drop is smaller at plug state. The pressured dependency at plug state shows a more linear behaviour than the part super-linearly increasing fragmented layer state with potential jumps (cf. Figure 5.20). More specifically, larger layer heights, which represent longer loading times or higher PM concentrations, lead to greater pressure drops at plug state and an increased difference between both states. Larger fragment dimensions, associated with a smaller soot-to-ash ratio, lead to the same result. The more fragments remain
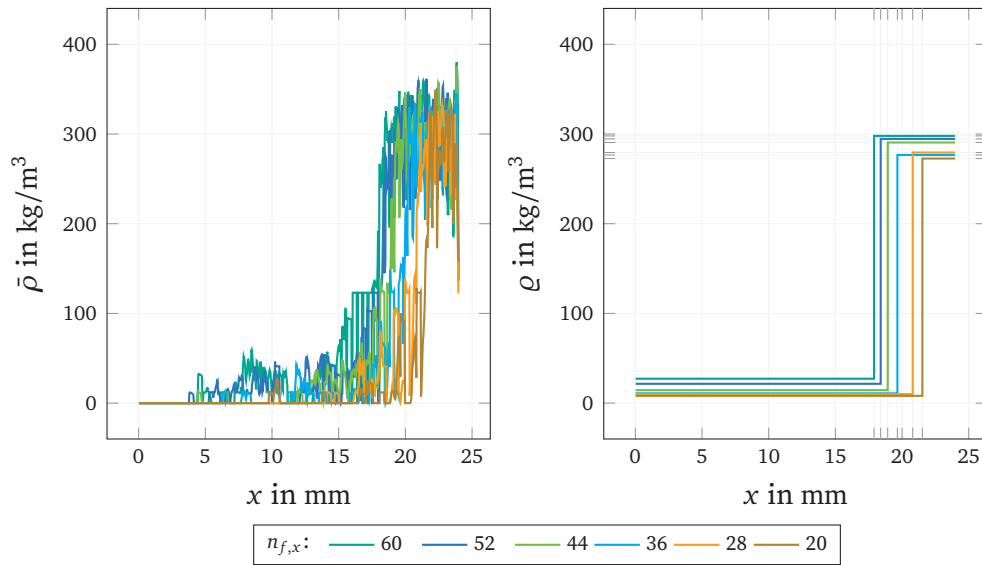
Figure 5.19: *PM density profile $\bar{\rho}(x)$ (**left**) and mean density profile $\varrho(x)$ (**right**) at plug state for different numbers of fragment rows $n_{f,x}$*
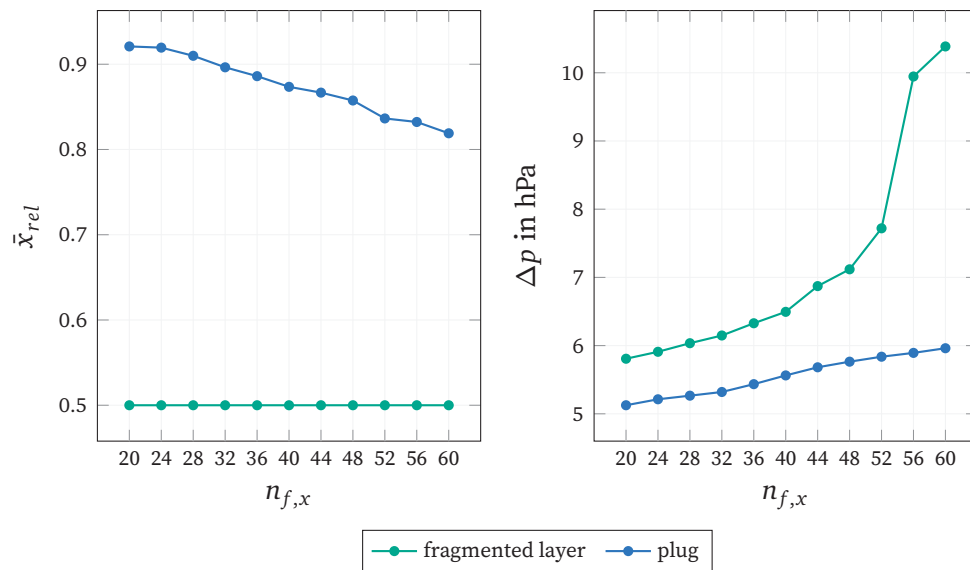
Figure 5.20: *Relative average PM position $\bar{x}_{rel}$ and pressure drop Δp for different numbers of fragment rows $n_{f,x}$ at fragmented layer and plug state.*

after the soot oxidization, the larger the final pressure drop, with a pressure jump at $n_{f,x} = 65$ and a substrate surface coverage of approximately 50%. For a given PM mass present in the channel, the transition towards a plug becomes especially beneficial for the pressure drop when the fragmented PM layer only provides a small free substrate surface area available for the flow.

5.4.3 Influence of Particulate Matter Properties and Operating Conditions

In addition to the investigation of the layer topology's influence, the four remaining factors in Table 5.1, which do not alter the fragmented layer state, are considered in the following. Those include the PM density in Section 5.4.3.1, the fragments' mechanical properties in Section 5.4.3.2, the adhesion between fragments and the porous substrate in Section 5.4.3.3 and the inflow velocity in Section 5.4.3.4.

5.4.3.1 Influence of PM density

As a variation in the PM density represents a change in the fragment's properties that eventually join the plug formation, the plug's average density directly depends on the prescribed one. The volume occupied by the plug shows a non-negligible sensitivity, as it slightly grows with decreasing PM density (cf. Figure 5.21). Due to the fact that the PM density neither impacts the hydrodynamic surface force nor the contact forces in (5.1), it only affects a fragment's inertia, which is solely relevant for the detachment and transport process. Fragments with higher densities accordingly hit an existing plug structure with more momentum, causing a small compaction. Such a compaction can clearly be identified in the behaviour of the relative average PM position $\bar{x}_{rel}$ in Figure 5.22.

The pressure drop at plug state decreases respectively with decreasing plug volume. A larger PM density, therefore, leads to a smaller pressure drop at plug state due to the formation of a more compact plug as a result of higher inertia.

5.4.3.2 Influence of Mechanical Properties

The fragments' mechanical properties neither affect the fragmented layer state nor the detachment process. While not directly impacting the transport either, any contact with the substrate wall or other fragments on their way can cause a change in trajectory or velocity. The density profile in Figure 5.23 therefore exhibits no distinct difference in the detachability.
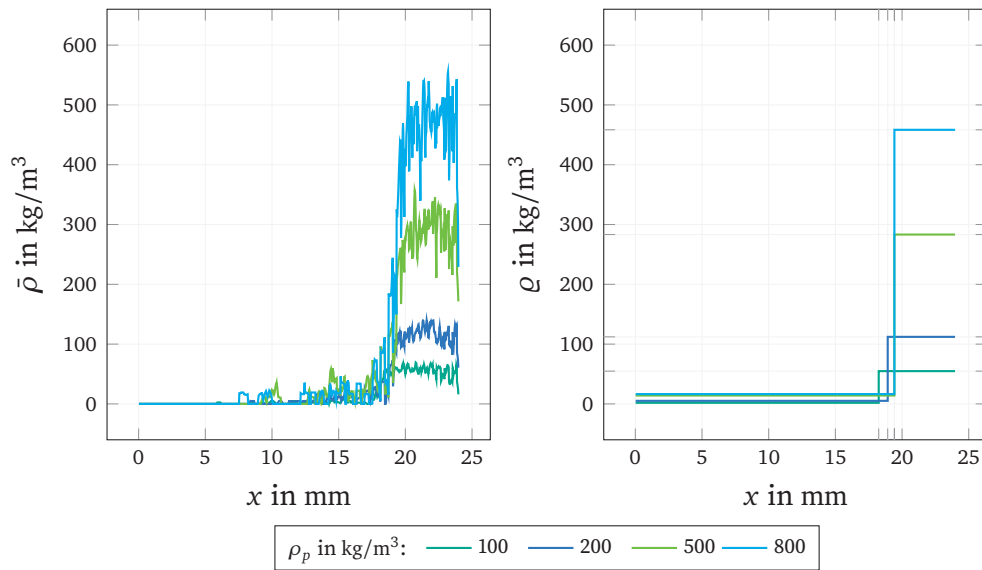
Figure 5.21: *PM density profile $\bar{\rho}(x)$ (**left**) and mean density profile $\varrho(x)$ (**right**) at plug state for different PM densities ρ_p.*
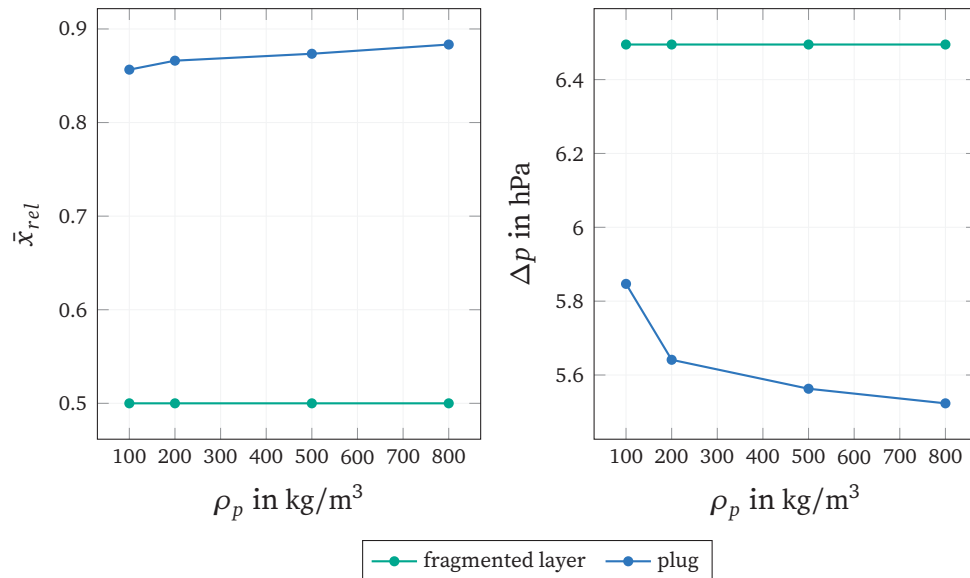
Figure 5.22: *Relative average PM position $\bar{x}_{rel}$ and pressure drop Δp for different PM densities ρ_p at fragmented layer and plug state.*
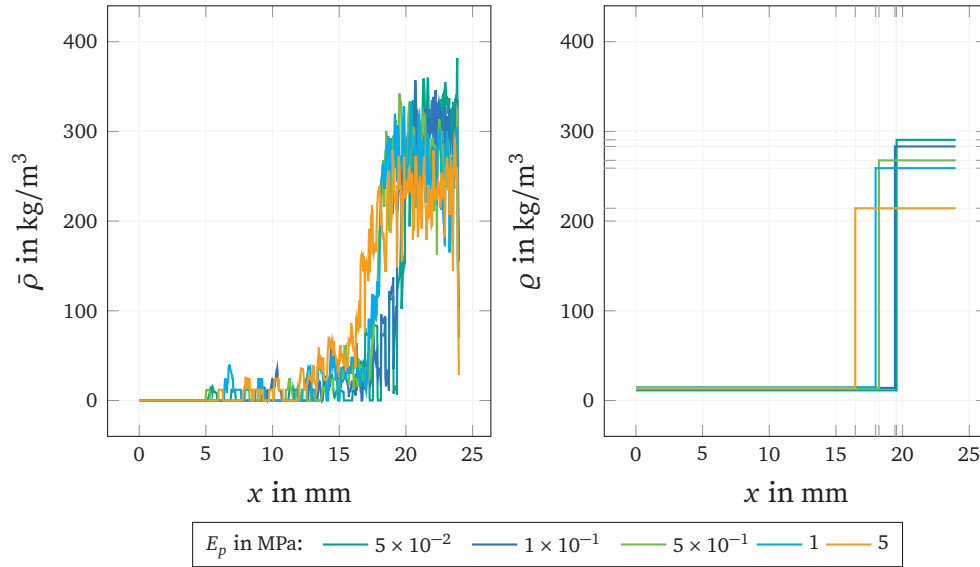
Figure 5.23: *PM density profile $\bar\rho(x)$ (**left**) and mean density profile $\varrho(x)$ (**right**) at plug state for different fragment moduli of elasticity E_p.*

It can be observed that a large elasticity of $E_p \geq 1\,\text{MPa}$ leads to an increase in the plug volume, as repulsion forces become larger at fragment–fragment contacts according to (5.1) and counteract further compaction. As the density inside the plug becomes smaller for those as well, the plug's porosity increases additionally. The relative average PM position in Figure 5.24 directly reflects the volume increase due to the less compact packing.

The pressure drop at plug state initially increases with the plug volume. It then transitions into a nearly constant value of $\Delta p \approx 5.9\,\text{hPa}$ at $E_p = 5 \times 10^{-1}\,\text{MPa}$ due to the continuous increase in the plug's porosity, which compensates for the reduced volume available for the flow. The results suggest that using additives, which decrease the fragments' stiffness, would be beneficial for the reduction in the pressure drop due to a more compact plug.

5.4.3.3 Influence of Adhesive Forces

According to the studies conducted in Hafen et al. [3], detachment of the fragments in the first row is assisted by a hydrodynamic force of $F_N = 29.2\,\mu\text{N}$ assuming an inflow velocity of $\bar u_{in} = 10\,\text{m/s}$. As the acting forces are significantly smaller for all other rows, no detachment occurs with adhesion forces
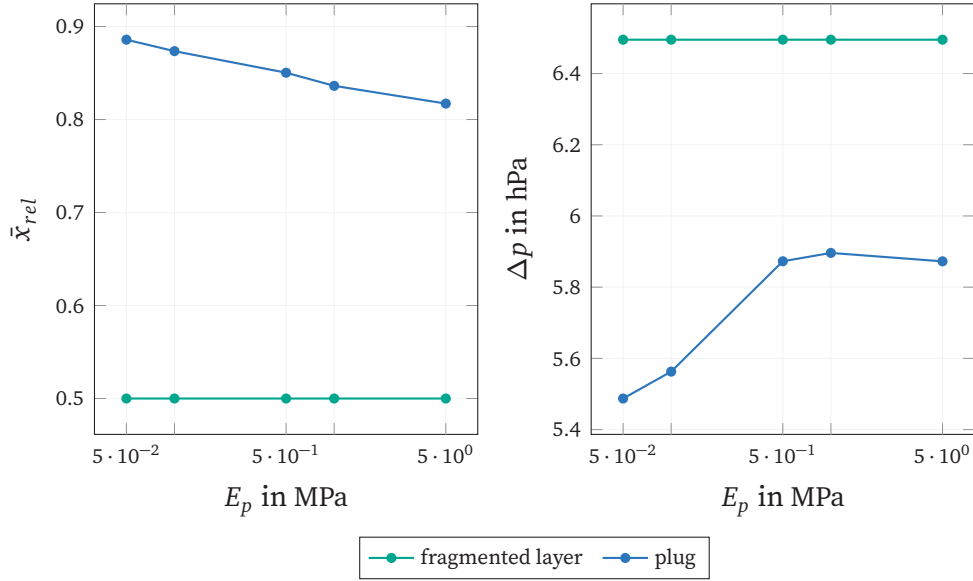
Figure 5.24: *Relative average PM position $\bar{x}_{rel}$ and pressure drop Δp for different fragment moduli of elasticity E_p at fragmented layer and plug state.*

in normal direction of the substrate's surface of $F_N = 30\,\mu\text{N}$ or larger present. For the remaining range of considered adhesion forces in Table 5.1, the density profile is shown in Figure 5.25.

As predicted by the detachment likelihood formulated in Hafen et al. [3], the fragment rows closest to the inlet detach first when reducing the adhesion force to $F_N < 29.2\,\mu\text{N}$. With a continuous adhesion reduction, more neighbouring fragment rows become detachable. While the plug volume stays similar for higher values, it increases for $F_N \leq 5\,\mu\text{N}$. Thus, the relative average PM position in Figure 5.26 can at smaller adhesive forces be attributed to the plug volume only. At larger ones, it then reflects regions of partial detachment and fragment interception, similarly to findings in Figure 5.12 between $d_z = 42.5\,\mu\text{m}$ and $d_z = 148.75\,\mu\text{m}$.

The pressure drop at the plug state revolves around a small range between 5.40 hPa and 5.59 hPa and stays nearly constant for adhesion forces of $F_N \geq 10.0\,\mu\text{N}$, which corresponds to the observed similar plug volume. For smaller adhesion forces, the pressure drop increases slightly due to the increased plug volume. It becomes clear that the removal of the first few fragment rows already causes the major part of the pressure drop reduction with respect to the fragmented layer state. Additionally, it can be observed that adhesive
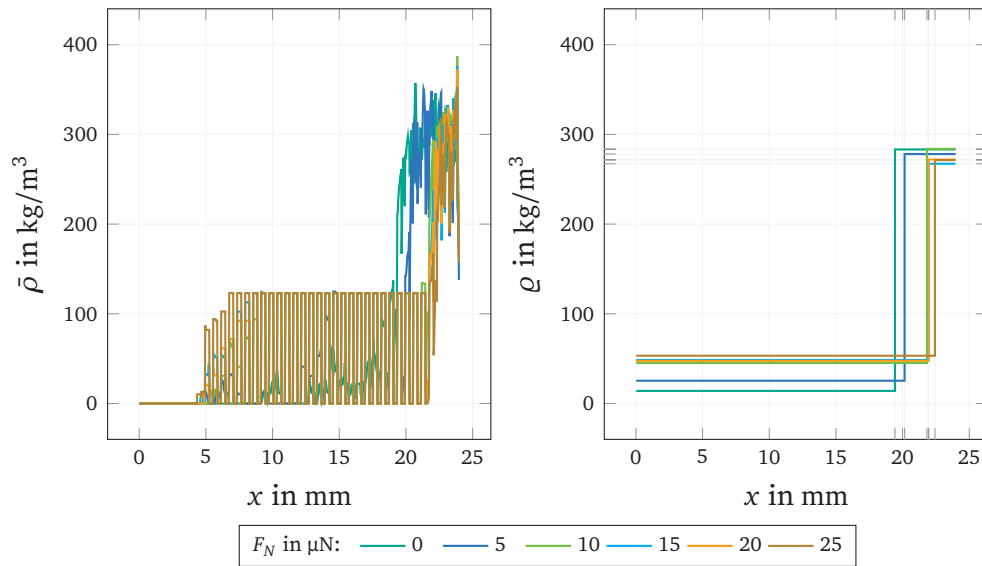
Figure 5.25: *PM density profile $\bar{\rho}(x)$ (**left**) and mean density profile $\varrho(x)$ (**right**) at plug state for different adhesive forces F_N.*

forces are only relevant around the detachment threshold of the first fragment row, as a further reduction has a negligible influence on the detachment and the pressure drop accordingly.

5.4.3.4 Influence of Inflow Velocity

The inflow velocity $\bar{u}_{in}$ is directly responsible for the magnitude of the hydrodynamic forces present in the channel. It accordingly impacts the fragmented layer state, the detachment process, the pneumatic transport and the plug formation. A velocity of $\bar{u}_{in} \leq 8\,\text{m/s}$ shows a significant number of undetachable fragments in Figure 5.27.

For higher inflow velocities, the plug's density profile exhibits a very similar structure, with small differences in the plug's mean density. The relative average PM position in Figure 5.28 does not show a large sensitivity on the inflow velocity either.

A slight increase is caused by the continuously increasing inertia of fragments hitting the plug and causing a compaction similarly to the observations in Figure 5.22. At smaller velocities, this effect is superimposed by the increasing number of detachable fragments. As a result of an increased momentum loss due to a higher wall through-put, the pressure drop shows a strong sensitivity to
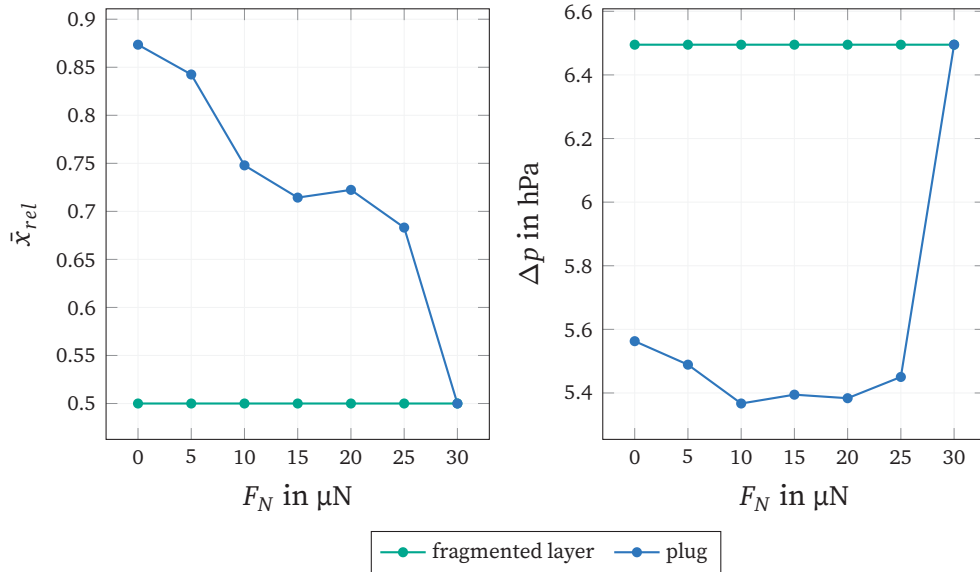
Figure 5.26: *Relative average PM position $\bar{x}_{rel}$ and pressure drop Δp for different adhesive forces F_N at fragmented layer and plug state.*
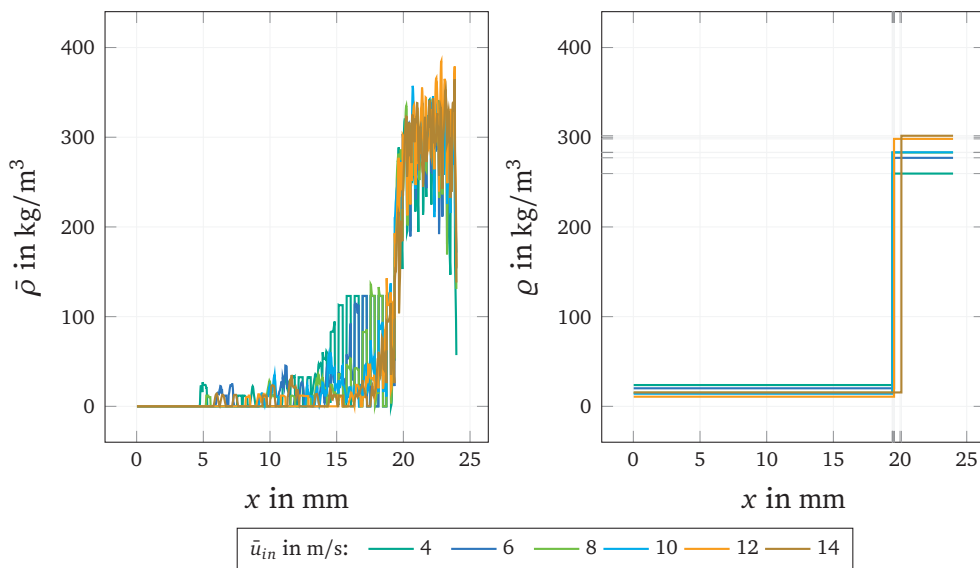
Figure 5.27: *PM density profile $\bar{\rho}(x)$ (**left**) and mean density profile $\varrho(x)$ (**right**) at plug state for different inflow velocities $\bar{u}_{in}$.*
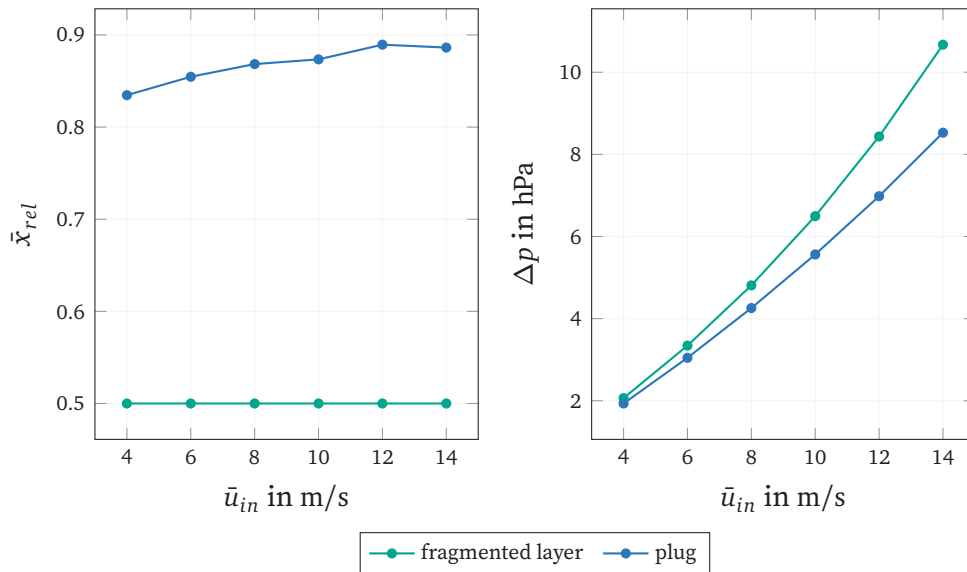
Figure 5.28: *Relative average PM position $\bar{x}_{rel}$ and pressure drop Δp for different inflow velocities $\bar{u}_{in}$ at fragmented layer and plug state.*

the inflow velocity for both states. While the plug state exhibits a nearly linear profile, the fragmented layer state increases super-linearly, leading to a continuously growing difference between both states until reaching $\Delta p = 214.3$ Pa at $\bar{u}_{in} = 14$ m/s. In comparison with the strong relation between gas velocity and momentum loss in the filter substrate, however, the superposed pressure drop dependency at plug state proves to be less relevant.

5.5 Conclusions

In this work, the dynamic rearrangement process during the regeneration of a wall-flow filter channel was investigated using the open source software OpenLB [5, 27]. As a direct sequel to the investigation of the static fragmented layer exposed to elevated fluid velocities in Hafen et al. [3], the present work additionally investigated the dynamic behaviour during fragment detachment, fragment transport and plug formation. First, the complete rearrangement process was evaluated in detail, considering a constant base configuration for the influence factors (cf. Section 5.4.1). With it, it could be shown that fragments detach row-by-row, confirming the assumption of the predecessor work. Fragment–fragment contact in the channel's front turned out to potentially

cause tear-off, while it causes interception in the channel-mid. The inclusion of the discrete contact model proved to enable the successful formation of an end plug occupying a significant amount of the available channel volume. A simple mean density methodology was presented and could be shown to represent a reproducible way of determining the plug extent and its average density, which agrees well with values reported by Kimura et al. [98], Sappok et al. [99] and Dittler [83]. Afterwards, the impact of influence factors that lead to a change in the fragmented layer topology on both the initial flow condition and the rearrangement process were laid out (cf. Section 5.4.2). While the topology of the fragmented layer could be shown to affect the final plug structure, its pressure drop impact on the initial fragmented layer state was identified to be greater. Larger layer heights, which represent longer loading times or higher PM concentrations, could be shown to lead to greater pressure drops at plug state and an increased difference between both states. Larger fragment dimensions, associated with a smaller soot-to-ash ratio, were shown to lead to the same result. It turned out that a larger number of fragments remaining after the soot oxidization leads to a larger final pressure drop. For a given mass of PM present in the channel, the transition towards a PM plug was shown to be especially beneficial when the fragmented layer only provides a small free substrate surface area available for the flow. Lastly, additional PM properties and operating condition that do not alter the initial fragmented layer topology were investigated (cf. Section 5.4.3). A larger PM density could be shown to lead to a smaller pressure drop at plug state due to the formation of a more compact plug as a result of higher fragment inertia. It was reasoned that the use of additives, which decrease the fragments' stiffness, would be beneficial for the reduction in the pressure drop due to a more compact plug. It could be shown that the removal of the first few fragment rows already causes the major part of the pressure drop reduction with respect to the fragmented layer state. Additionally, it could be shown that adhesive forces are only relevant around the detachment threshold of the first fragment row, as a further reduction has a negligible influence on the detachment and the pressure drop accordingly. In comparison with the strong relation between gas velocity and momentum loss in the filter substrate, the superposed pressure drop dependency at plug state was identified as less relevant.

While not attempting a systematic comparison of the different influence factors with each other, it can be argued that the inflow velocity (cf. Section 5.4.3.4) and the layer structure (cf. Section 5.4.2.3) have the largest impact on the final pressure drop. They can, accordingly, be designated as the most crucial ones

for the dynamic rearrangement process in wall-flow filters.

The present work demonstrated the successful extension of the resolved particle methodology via a discrete method to treat particle–particle and particle–wall interactions and its application to the transient rearrangement process in wall-flow filters. Additionally, it reveals the sensitivity of relevant influence factors related to the fragmented layer topology, the PM properties and the operating conditions, and quantifies their impact on the rearrangement process. This way, it contributes to the formulation of respective predictions on the deposition pattern formation, which impact engine performance, fuel consumption and service life of wall-flow filters.

6

Conclusion and Outlook

6.1 Conclusion

In this work, a *fundamental investigation of particle-layer rearrangement events in ceramic wall-flow filters* is presented. For that, a resolved particle simulation approach was developed and implemented in the open source framework OPENLB. This approach was applied for the determination of the sensitivity of engineering-related influence factors and a quantification of their impact on the transient rearrangement process. That way, the present work contributes to an understanding of deposition pattern formation in wall-flow filters. This contribution is summarized in the following with respect to the individual contribution components *Modelling and Methodology*, *Validation and Assessment of Applicability* as well as *Application and Investigation* (cf. Figure 1.4):

Modelling and methodology   In a first step, presented in Chapter 2, an LBM approach was developed which is capable of capturing the gaseous flow field inside a single wall-flow filter channel and the dynamics of surface resolved layer fragments during filter regeneration. The approach includes the consideration of flow through the porous substrate walls and provides full coupling between fluid flow and fragment movement. A first application setup (*four-channel* setup), which represents a single filter channel embedded into fractions of neighbouring inflow and outflow channels, was defined with appropriate operating and boundary conditions. A second setup (*two-channel* setup) was

then added in Chapter 3. In this chapter, the methodology was extended addi-
tionally by a set of general transport parameters, intended for a standardized
comparison of different simulation and experiment runs. Those were defined,
such as the peak and impact velocity, and adapted from existing ones, such as
the stopping distance according to Hinds [110]. The model was then stabilized
for the use of higher inflow velocities and smaller permeabilities in Chapter 4,
by adapting the boundary conditions. In order to additionally enable inves-
tigations on the process of plug formation, a discrete contact model for the
consideration of fragment–wall and fragment–fragment contact was eventually
added in Chapter 5.

   The resulting holistic model enables the examination of the complete re-
generation process, including the break-up and fragmentation of a coherent
particle layer, the dynamic behaviour of separated layer fragments and the
formation of a channel-plug. In this state, it can readily be used for further
investigations, as discussed in the outlook in Section 6.2. The model's different
development stages are listed in Section A of the appendix and can each be
retrieved accordingly.

Validation and assessment of applicability   While the developed model enables
the envisaged studies in this work, the significance of their results mainly de-
pends on how accurately the model represents a real-world counterpart. In
order to provide the respective confidence in the model's validity and the actual
applicability, a large share was dedicated to this contribution component in all
four solution steps (cf. Figure 1.4).

   At first, the choice of using a simplified porous media model for the flow
through the porous substrate walls was examined in Chapter 2. It was shown
that the permeability and the inflow velocity used in this step led to a sufficiently
small error caused by the neglection of non-linear pressure drop contributions.
It could also be shown that when considering smaller permeabilities, as done
in the more advanced steps, a small error can also be guaranteed with veloci-
ties in the upper velocity range. Afterwards, the model's order of accuracy in
the particle-free case was examined and the flow field was compared to a well
validated reference solution [112]. Here, the model could be shown to exhibit
super-linear grid convergence and good agreement with the reference solution.
In Chapter 3, the two-channel setup was used for the comparison with results
from the experimental test rig used in Thieringer et al. [9]. A pressure drop
comparison led to the determination of a physically sensible substrate perme-

ability of $K = 4.3 \times 10^{-12}\,\mathrm{m}^2$, which was used throughout the following steps. For the general movement characteristics of individual layer fragments, qualitative accordance could be shown between experiments and simulations. Due to the consideration of elevated inflow velocities in Chapter 4, the particle-free flow in a clean channel was examined with respect to the parameter domain that ensures sufficient stability and accuracy. By evaluating the simulations' final states, a necessary stability domain was defined and a resolution-dependent expression for a stability threshold for the average inflow velocity was obtained. Reasonable velocity and pressure accuracy as well as satisfactory mass conservation could be achieved for grid resolutions of at least $N = 96$ cells per channel diameter. For the flow around a single layer fragment, the suitable parameter domain turned out to be limited to inflow velocities below $\bar{u}_{in} = 28\,\mathrm{m/s}$ due to persisting fluctuations in the velocity and pressure field. The force contributions could be shown to feature satisfactory accuracy. When considering the investigation of the dynamic process of plug formation in Chapter 5, the evaluated average plug densities could be shown to agree well with values reported in the literature.

Based on those results, the developed approach can confidently be assumed to accurately represent the processes of interest in a real-world wall-flow filter channel within a specified parameter domain with its limits known. While the exceedance of those limits is likely accompanied by a degradation of the model's accuracy, stability and applicability, some further model extension, as discussed in the outlook in Section 6.2, provide the potential of expanding the parameter domain even further.

Application and investigation With the properly validated simulation model, detailed investigations were conducted with a focus on the closure of the research gaps formulated in Section 1.3. In a first step in Chapter 2, the characteristics of a static fragmented layer were examined regarding the spatial distribution of the acting hydrodynamic forces and the impact on the fluid field. Both tangential and normal component of the hydrodynamic force revealed a distinct profile over the channel length, covering high values at the inflow and slightly negative ones close to the back wall. The tangential forces could, however, be identified as much greater than the ones in normal direction. It could be shown that, in order to enable a fragment to detach, the hydrodynamic forces on its surface need to lead to a net force or torque which are directed in such a way that they facilitate detachment rather than additional surface

contact. Additionally, the influence of fragment clusters was evaluated. This revealed clusters in the channel rear as favourable regarding a pressure drop optimization and indicated a self-reinforcing effect during rearrangement events. Afterwards, some first transient simulations of fragment detachment were conducted in a low velocity regime ($\bar{u}_{in} \leq 2\,\text{m/s}$) and the impact of some assorted layer properties on the detachment characteristics were examined. In this context, it could be shown that the fragments are likely to engage in a rotational movement quickly after detachment due to comparably large tangential forces. This enables the fluid to attack their bottom face and cause an upward motion towards the core flow.

Those observations could be confirmed by a detailed analysis of the detachment mechanics in the single fragment investigations in Chapter 3. Here, a fragment's pneumatic transport through the channel was investigated for different starting positions, substrate permeabilities, inflow velocities and particle densities. The transient development of the hydrodynamic surface force was evaluated for the tangential and normal component separately during transport as well. Different PM densities were observed to directly determine the ability to adapt to changing flow conditions. The stopping distance proved to represent an accessible criterion for the fragment's likelihood to impact on the back wall without the necessity of examining its exact trajectory. Within the range of considered parameters, the stopping distance revealed that, provided the detachment from the channel surface, a single layer fragment is very likely to always hit the back wall.

In Chapter 4, the single fragment was then exposed to elevated inflow velocities of up to $\bar{u}_{in} = 26\,\text{m/s}$ within the stable domain determined previously. In order to account for the detachment dynamics more accurately, the rotation-induced normal force was introduced and compared to the normal and tangential component of the original surface force. It could be shown to represent a superior measure for the prediction of fragment detachment. Additionally, a deposition layer during break-up was investigated regarding local effects on the fluid field and the acting forces for different situations. Analogously to the low velocity regime considered in Chapter 2, the spatial distribution of the acting hydrodynamic forces was examined for the upper velocity domain. Based on this distribution, predictions on the detachment likelihood of individual layer fragments and their mutual influence were then derived. Provided a considerable height, a uniformly fragmented particle layer could be shown to lead to local velocity magnitudes of up to twice as large as the average inflow velocity.

In the final step, presented in Chapter 5, the complete transient rearrange-

ment process, including the plug-formation, was evaluated. As predicted in the previous chapter, the fragments could be confirmed to detach row-by-row. Contrary to the observation of isolated fragments in Chapter 3, however, fragment–fragment contact during transport turned out to potentially cause interception mid-way. While this is the case in the channel mid, it could be shown that in its front part, such contact rather causes a tear-off of attached fragments. When investigating the impact of layer topology, geometric properties and the operating conditions, a focus was placed on the comparison between an initial fragmented layer state and the final plug state. The layer topology could be observed to affect the final plug structure, while its pressure drop impact on the initial fragmented layer state was identified to be much greater. Influence factors associated with longer loading times as well as higher PM concentrations and smaller soot-to-ash ratios in the entering exhaust stream led to greater pressure drops at plug state and an increased difference between both states. Considering a given particle mass in the channel, a transition towards a plug turned out to be especially beneficial when the fragmented layer only provides a small free substrate surface area available for the flow. This implies that any means (e. g. specific additives) that promote cohesive forces between ash precursors (cf. Section 1.2.3) mitigate this effect and represent potential for a pressure drop optimization.

Eventually, the influence of assorted material properties and operating conditions was investigated. A larger PM density turned out to cause a more compact plug due to higher fragment inertia, which led to a smaller pressure drop at plug state. The plug's compactness could also be shown to directly depend on the fragments' stiffness. A reduction of this stiffness, by e. g. additives, could, respectively, lead to a pressure drop reduction due to a more compact plug. Adhesive forces turned out to only be relevant in a range revolving around the detachment threshold of the first fragment row, as a further reduction has a negligible influence. This implies that the complexity that comes with the consideration of adhesion can be reduced to a single-valued threshold quantity in this context. Overall, a focus on the first few fragment rows turned out to be sufficient in most cases, as their removal already causes the major part of the pressure drop reduction with respect to the fragmented layer state. This might motivate respective geometric modifications (e. g. by enlarging the inflow cross-section). The investigation of the inflow velocity's impact revealed that, in comparison with the strong relation between gas velocity and momentum loss in the filter substrate, the superposed pressure drop dependency at plug state is less relevant.

The presented results represent a comprehensive quantification of the impact of the considered influence factors listed in Section 1.3 on various aspects of the transient rearrangement process in wall-flow filters. The developed approach, respectively, represents the achievement of the thesis's main goal and all sub-goals formulated in Section 1.4. By identifying the relevant influence factors that affect the deposition pattern formation, the work, eventually, represents a significant contribution to the research gaps laid out in Section 1.3.

6.2 Outlook

In light of the limitations experienced during the development and application of the presented wall-flow model, the following three adaptions represent some means to extend the model's domain of validity:

Consideration of turbulence   As shown in Chapter 4, the developed approach cannot guarantee stable simulations over the complete range of inflow velocities from 1 m/s to 80 m/s, as originally intended. While not exactly applicable to wall-flow filter channels, this range would lead to channel Reynolds numbers of approximately $\mathrm{Re} = 100$ to $\mathrm{Re} = 8000$. The experienced limitation is predominantly caused by fluctuations in the velocity and pressure field, which in the four-channel setup occurs above inflow velocities of $\bar{u}_{in} = 45\,\mathrm{m/s}$ in particle-free flows and at $\bar{u}_{in} = 28\,\mathrm{m/s}$ in particle-laden flows. In the two-channel setup, those occur even earlier. When aiming at enabling particle-laden flows in both setups over the entire, relevant range of inflow velocities, turbulent effects have to be considered. This could be realized by means of a large eddy simulation (LES) approach, which has been implemented and validated in OPENLB for single-phase flows [5, 151, 152]. As the homogenized lattice Boltzmann method (HLBM), accounts for the influence of hydrodynamic forces on particle surfaces in the collision step of the lattice Boltzmann equation (LBE) in (2.1), a respective extension has to be approached at this point.

Consideration of temperature   While not particularly considered in the present work, the temperature significantly affects the reaction rate of the soot oxidation [153] with large local differences within the deposition layer and the porous substrate during the regeneration process. Due to the exothermic nature of the oxidization process, particle layer fragments additionally act as heat sources, which also affect the temperature field [154]. It is also known [98] that the

modulus of elasticity, which affects the entire contact behaviour including the compactness of the plug (cf. Chapter 5) is temperature dependent. In order to account for those effects, local gradients of the reaction rate could be considered in each particle layer fragment. This would enable the quantification of the gas temperature as well as the influence of the exothermic soot reaction when flowing through and around the layer fragments and the porous filter walls. Assuming the turbulent extension described above, inflowing and outflowing gases in the particle-free region could be treated as isothermal due to turbulent mixing. For a concrete realization, a three-dimensional temperature field has to be evaluated using methods for calculating heat transfer that already exist in OPENLB [151]. For this, the discrete lattice (cf. Section 2.2.1) has to be extended to enable the calculation of the additional advection-diffusion equation with an added source term in the region of the deposition layer and the porous substrate. With the temperature field known, integral temperature values averaged over the respective fragment volumes can then be assigned to the individual fragments. This eventually enables the back-coupling of the local temperature to the reaction rate of the soot oxidation as well as to the modulus of elasticity. The resolved-particle data structure has to be adapted additionally, as reaction related data has to be available locally. With the proposed extension, the reaction process can be considered separately for each fragment.

Multiscale extension   As described in Chapter 1, a vehicle's after-treatment system consist of multiple components, including a wall-flow filter. When considering processes in such a system outside the actual filter, a differentiation between *system scale*, *filter scale* and *channel scale* allows for a separate consideration of the differing length and time scales. Such a multiscale approach, however, mandates the determination of a standardized procedure for linking relevant process-related input variables (operating conditions, aerosol and filter properties) and target variables (layer properties, detachment and resuspension behaviour as well as deposition pattern properties) between the different scales. With those, a comparison between integral measurement data on large scales and local effects on small scales could be realized. It would also simplify comparisons with literature data, which has mostly been determined on the system scale. The integration of a single channel into the ceramic filter monolith could be realized as a function of the radial position. In this case, the local distribution of inflow velocity and temperature on the filter scale [129] has to be assumed as the initial condition of individual simulations on the channel scale. With

a known number of individual channels, the total volume flow could then be calculated (e. g. by assuming an average weighting). The same applies to the pressure drop that results at the filter outlet. Here, local influences on the filter scale, such as those formed by turbulent jets on the downstream side of the filter [155] or by expansion of an upstream distribution funnel [129], have to be taken into account on the channel scale. On the system scale, additional pressure drop contributions of upstream and downstream components as well as potential changes in the PM concentration could be considered. In addition to the described conceptual developments, it is also indispensable, in the context of such a multiscale approach, to develop a consistent save and load procedure of the particle data, which enables a restart of a simulation from a previously calculated state. This allows for inter- or extrapolation between scales and a reduction of computational time when performing parameter studies starting from the same base state.

Acknowledgment

List of Puplications

Peer-Reviewed Publications

[1] **Hafen**, **N.**, Dittler, A., and Krause, M. J. "Simulation of particulate matter structure detachment from surfaces of wall-flow filters applying lattice Boltzmann methods." In: *Computers & Fluids* 239 (2022), p. 105381. DOI: 10.1016/j.compfluid.2022.105381.

[2] **Hafen**, **N.**, Thieringer, J. R., Meyer, J., Krause, M. J., and Dittler, A. "Numerical investigation of detachment and transport of particulate structures in wall-flow filters using lattice Boltzmann methods." In: *Journal of Fluid Mechanics* 956 (2023), A30. DOI: 10.1017/jfm.2023.35.

[3] **Hafen**, **N.**, Marquardt, J. E., Dittler, A., and Krause, M. J. "Simulation of Particulate Matter Structure Detachment from Surfaces of Wall-Flow Filters for Elevated Velocities Applying Lattice Boltzmann Methods." In: *Fluids* 8.3 (2023). DOI: 10.3390/fluids8030099.

[4] **Hafen**, **N.**, Marquardt, J. E., Dittler, A., and Krause, M. J. "Simulation of Dynamic Rearrangement Events in Wall-Flow Filters Applying Lattice Boltzmann Methods." In: *Fluids* 8.7 (2023). DOI: 10.3390/fluids8070213.

[5] Krause, M. J., Kummerländer, A., Avis, S. J., Kusumaatmaja, H., Dapelo, D., Klemens, F., Gaedtke, M., **Hafen**, **N.**, Mink, A., Trunk, R., Marquardt, J. E., Maier, M.-L., Haussmann, M., and Simonis, S. "OpenLB—Open source lattice Boltzmann code." In: *Computers & Mathematics with Applications* 81 (2021). Development and Application of Open-source Software for Problems with Numerical PDEs, pp. 258–288. DOI: 10.1016/j.camwa.2020.04.033.

[6] Haussmann, M., **Hafen, N.,** Raichle, F., Trunk, R., Nirschl, H., and Krause, M. J. "Galilean invariance study on different lattice Boltzmann fluid–solid interface approaches for vortex-induced vibrations." In: *Computers & Mathematics with Applications* 80.5 (2020), pp. 671–691. DOI: 10.1016/j. camwa.2020.04.022.

[7] Trunk, R., Weckerle, T., **Hafen, N.,** Thäter, G., Nirschl, H., and Krause, M. J. "Revisiting the Homogenized Lattice Boltzmann Method with Applications on Particulate Flows." In: *Computation* 9.2 (2021). DOI: 10.3390/ computation9020011.

[8] Reinke, F., **Hafen, N.,** Haussmann, M., Novosel, M., Krause, M. J., and Dittler, A. "Applied Geometry Optimization of an Innovative 3D-Printed Wet-Scrubber Nozzle with a Lattice Boltzmann Method." In: *Chemie Ingenieur Technik* 94.3 (2022), pp. 348–355. DOI: 10.1002/cite.202100151.

[9] Thieringer, J. R. D., **Hafen, N.,** Meyer, J., Krause, M. J., and Dittler, A. "Investigation of the Rearrangement of Reactive ash; Inert Particulate Structures in a Single Channel of a Wall-Flow Filter." In: *Separations* 9.8 (2022). DOI: 10.3390/separations9080195.

[10] Marquardt, J. E., **Hafen, N.,** and Krause, M. J. "A novel particle decomposition scheme to improve parallel performanceof fully resolved particulate flow simulations [Submitted]." In: *Journal of Computational Science* (2024). DOI: 10.48550/arXiv.2312.14172.

[11] Prinz, F., Pokorný, J., Elcner, J., Lízal, F., Mišík, O., Malý, M., Bělka, M., **Hafen, N.,** Kummerländer, A., Krause, M. J., Jedelský, J., and Jícha, M. "Comprehensive experimental and numerical validation of Lattice Boltzmann fluid flow and particle simulations in a child respiratory tract." In: *Computers in Biology and Medicine* 170 (2024), p. 107994. DOI: doi.org/10.1016/j.compbiomed.2024.107994.

[12] Gaćina, M., Vulin, D., **Hafen, N.,** Greif, M. T., Krause, M. J., and Katić, M. "Digital Rock Permeability and REV Validation Using 2D Pore Morphology Approach [In Preparation]." In: *energies* (2023).

[13] Simonis, S., **Hafen, N.,** Jeßberger, J., Dapelo, D., Thäter, G., and Krause, M. J. "Homogenized lattice Boltzmann methods for fluid flow through porous media - part I: model derivation and numerical methodology [Submitted]." In: *ESAIM: M2AN* (2024). DOI: 10.48550/arXiv.2310.14746.

[14] Marquardt, J. E., **Hafen**, **N.**, and Krause, M. J. "A novel model for direct numerical simulation of suspension dynamicswith arbitrarily shaped convex particles [Submitted]." In: *Computer Physics Communications* (2024). DOI: 10.48550/arXiv.2401.10878.

Other Publications

[15] **Hafen**, **N.**, Krause, M. J., and Dittler, A. "Simulation of Particle-Agglomerate Transport in a Particle Filter using Lattice Boltzmann Methods." In: *22. Internationales Stuttgarter Symposium*. Wiesbaden, 2022, pp. 292–303. DOI: 10.1007/978-3-658-37011-4_24.

[16] Kummerländer, A., Avis, S., Kusumaatmaja, H., Bukreev, F., Crocoll, M., Dapelo, D., Großmann, S., **Hafen**, **N.**, Ito, S., Jeßberger, J., Kummer, E., Marquardt, J. E., Mödl, J., Pertzel, T., Prinz, F., Raichle, F., Sadric, M., Schecher, M., Teutscher, D., Simonis, S., and Krause, M. J. *OpenLB User Guide: Associated with Release 1.6 of the Code*. 2023. DOI: 10.48550/arXiv. 2307.11752. URL: https://doi.org/10.48550/arXiv.2307.11752.

Conference Talks

[17] **Hafen**, **N.**, Dittler, A., and Krause, M. J. "Umlagerungsvorgänge reaktivinerter Partikelschichten in keramischen Querstromfiltern – Aufklärung mittels aufgelöster Partikel-Simulationen." In: *Jahrestreffen der ProcessNet-Fachgruppen Mechanische Flüssigkeitsabtrennung und Gasreinigung*. Bamberg, Germany, 2019.

[18] **Hafen**, **N.**, Dittler, A., and Krause, M. J. "Simulation of the particle layer rearrangement in ceramic wall-flow filters – Lattice Boltzmann Methods employing resolved particle simulations." In: *Partek 2019 – International Congress on Particle Technology*. Nurnberg, Germany, 2019.

[19] **Hafen**, **N.**, Dittler, A., and Krause, M. J. "Investigation of particle detachments in wall-flow filters employing resolved particle simulations – Moving porous media modelling with Lattice Boltzmann Methods." In: *DSGD 2020 – 29th International Conference on Discrete Simulation of Fluid Dynamics*. Viterbo, Italy, 2020.

[20]   **Hafen**, **N.**, Dittler, A., and Krause, M. J. "Simulation von Umlagerungsvorgän-gen reaktiv-inerter Partikelstrukturen in Wandstromfiltern – Aufgelöste Partikelsimulationen mittels Lattice Boltzmann Methoden." In: *Online-Industrieworkshop Digitalisierung in der Trenntechnik – Simulation, Machine Learning, Industrie 4.0*. Online, 2020.

[21]   **Hafen**, **N.**, Dittler, A., and Krause, M. J. "Simulation von Umlagerungsvorgän-gen reaktiv-inerter Partikelstrukturen in Wandstromfiltern – Aufgelöste Partikelsimulationen mittels Lattice Boltzmann Methoden." In: *Jahre-streffen der ProcessNet-Fachgruppen Gasreinigung und Partikelmesstechnik*. Bamberg, Germany, 2021.

[22]   **Hafen**, **N.**, Dittler, A., and Krause, M. J. "Simulation of Particulate Matter Detachment and Transport in Wall-Flow Filters using Lattice Boltzmann Methods." In: *Filtech 2022*. Cologne, Germany, 2022.

[23]   **Hafen**, **N.**, Krause, M. J., and Dittler, A. "Simulation of Particle-Agglomerate Transport in a Particle Filter using Lattice Boltzmann Methods." In: *22. Internationales Stuttgarter Symposium – Automobil- und Motorentechnik*. Stuttgart, Germany, 2022.

Software Releases

[24]   Krause, M., Avis, S., Dapelo, D., **Hafen**, **N.**, Haußmann, M., Gaedtke, M., Klemens, F., Kummerländer, A., Maier, M.-L., Mink, A., Ross-Jones, J., Si-monis, S., and Trunk, R. *OpenLB Release 1.3: Open Source Lattice Boltzmann Code*. Version 1.3. 2019. DOI: 10.5281/zenodo.3625967.

[25]   Krause, M., Avis, S., Kusumaatmaja, H., Dapelo, D., Gaedtke, M., **Hafen**, **N.**, Haußmann, M., Jeppener-Haltenhoff, J., Kronberg, L., Kummerlän-der, A., Marquardt, J., Pertzel, T., Simonis, S., Trunk, R., Wu, M., and Zarth, A. *OpenLB Release 1.4: Open Source Lattice Boltzmann Code*. Ver-sion 1.4. 2020. DOI: 10.5281/zenodo.4279263.

[26]   Kummerländer, A., Avis, S., Kusumaatmaja, H., Bukreev, F., Dapelo, D., Großmann, S., **Hafen**, **N.**, Holeksa, C., Husfeldt, A., Jeßberger, J., Kronberg, L., Marquardt, J., Mödl, J., Nguyen, J., Pertzel, T., Simonis, S., Springmann, L., Suntoyo, N., Teutscher, D., Zhong, M., and Krause, M. *OpenLB Release 1.5: Open Source Lattice Boltzmann Code*. Version 1.5. 2022. DOI: 10.5281/zenodo.6469606.

[27] Kummerländer, A., Avis, S., Kusumaatmaja, H., Bukreev, F., Crocoll, M., Dapelo, D., **Hafen, N.,** Ito, S., Jeßberger, J., Marquardt, J. E., Mödl, J., Pertzel, T., Prinz, F., Raichle, F., Schecher, M., Simonis, S., Teutscher, D., and Krause, M. J. *OpenLB Release 1.6: Open Source Lattice Boltzmann Code.* Version 1.6. 2023. DOI: 10.5281/zenodo.7773497.

Bibliography

[28] Merkisz, J. and Pielecha, J. "The Process of Formation of Particulate Mat-
      ter in Combustion Engines." In: *Nanoparticle Emissions From Combustion
      Engines*. 2015, pp. 19–25. DOI: 10.1007/978-3-319-15928-7_3.

[29] Kontses, A., Triantafyllopoulos, G., Ntziachristos, L., and Samaras, Z.
      "Particle number (PN) emissions from gasoline, diesel, LPG, CNG and
      hybrid-electric light-duty vehicles under real-world driving conditions."
      In: *Atmospheric Environment* 222 (2020), p. 117126. DOI: 10.1016/j.atmosenv.
      2019.117126.

[30] World Health Organization. *WHO global air quality guidelines: particulate
      matter (PM2.5 and PM10), ozone, nitrogen dioxide, sulfur dioxide and carbon
      monoxide*. en. World Health Organization, 2021.

[31] Chen, J. and Hoek, G. "Long-term exposure to PM and all-cause and
      cause-specific mortality: A systematic review and meta-analysis." In:
      Environment International 143 (2020), p. 105974. DOI: 10.1016/j.envint.2020.
      105974.

[32] Mazzarella, G., Ferraraccio, F., Prati, M., Annunziata, S., Bianco, A.,
      Mezzogiorno, A., Liguori, G., Angelillo, I., and Cazzola, M. "Effects of
      diesel exhaust particles on human lung epithelial cells: An in vitro study."
      In: *Respiratory Medicine* 101.6 (2007), pp. 1155–1162. DOI: 10.1016/j.rmed.
      2006.11.011.

[33] Atkinson, R. W., Kang, S., Anderson, H. R., Mills, I. C., and Walton, H. A.
      "Epidemiological time series studies of PM2.5 and daily mortality and
      hospital admissions: a systematic review and meta-analysis." In: *Thorax*
      69.7 (2014), pp. 660–665. DOI: 10.1136/thoraxjnl-2013-204492.

[34]   Balakrishnan, K. et al. "The impact of air pollution on deaths, disease burden, and life expectancy across the states of India: the Global Burden of Disease Study 2017." In: *The Lancet Planetary Health* 3.1 (2019), e26–e39. DOI: 10.1016/S2542-5196(18)30261-4.

[35]   German National Academy of Sciences Leopoldina. *Clean air. Nitrogen oxides and particulate matter in ambient air: Basic principles and recommendations.* Tech. rep. 2019.

[36]   Kurtyka, K. and Pielecha, J. "The evaluation of exhaust emission in RDE tests including dynamic driving conditions." In: *Transportation Research Procedia* 40 (2019). TRANSCOM 2019 13th International Scientific Conference on Sustainable, Modern and Safe Transport, pp. 338–345. DOI: 10.1016/j.trpro.2019.07.050.

[37]   Council of the European Union. *Regulation (EC) No 715/2007 of the European Parliament and of the Council of 20 June 2007 on type approval of motor vehicles with respect to emissions from light passenger and commercial vehicles (Euro 5 and Euro 6) and on access to vehicle repair and maintenance information.* Sept. 1, 2020. URL: http://data.europa.eu/eli/reg/2007/715/2020-09-01 (visited on 06/14/2023).

[38]   Parkers. *Full guide to Euro 6 for vans and pickups, including Euro 6d and Euro VI.* Nov. 6, 2021. URL: https://www.parkers.co.uk/vans-pickups/advice/euro-6-guide/ (visited on 06/14/2023).

[39]   DieselNet. *Russia and EAEU.* Jan. 2018. URL: https://dieselnet.com/standards/ru/ (visited on 06/14/2023).

[40]   Miller, J. and Braun, C. *Cost-Benefit Analysis of Euro VI Heavy-Duty Emission Standards in Argentina.* Apr. 2020. URL: https://theicct.org/wp-content/uploads/2021/06/ArgentinaCBA-HDV-Eng.pdf (visited on 06/14/2023).

[41]   Environmental Protection Agency. *Control of Air Pollution From Motor Vehicles: Tier 3 Motor Vehicle Emission and Fuel Standards.* June 30, 2014. URL: https://www.govinfo.gov/content/pkg/FR-2014-06-30/pdf/C1-2014-06954.pdf (visited on 06/14/2023).

[42]   Government of Canada. *Air pollution: regulations for vehicles and engines.* July 17, 2013. URL: https://www.canada.ca/en/environment-climate-change/services/air-pollution/sources/transportation/regulations-vehicles-engines.html (visited on 06/14/2023).

[43] DieselNet. *China: Cars and Light Trucks*. May 2023. URL: https://dieselnet.com/standards/cn/ld.php (visited on 06/14/2023).

[44] DieselNet. *India: Cars and Light Trucks*. Dec. 2022. URL: https://dieselnet.com/standards/in/ld.php (visited on 06/14/2023).

[45] DieselNet. *Australia: On-Road Vehicles and Engines*. July 2011. URL: https://dieselnet.com/standards/au/ (visited on 06/14/2023).

[46] Wallington, T. J., Anderson, J. E., Dolan, R. H., and Winkler, S. L. "Vehicle Emissions and Urban Air Quality: 60 Years of Progress." In: *Atmosphere* 13.5 (2022). DOI: 10.3390/atmos13050650.

[47] European Comission. *Commission proposes new Euro 7 standards to reduce pollutant emissions from vehicles and improve air quality*. Nov. 10, 2022. URL: https://ec.europa.eu/commission/presscorner/detail/en/ip_22_6495 (visited on 06/13/2023).

[48] European Comission. *European Green Deal: Commission proposes rules for cleaner air and water*. Oct. 26, 2022. URL: https://ec.europa.eu/commission/presscorner/detail/en/ip_22_6278 (visited on 06/13/2023).

[49] Council of the European Union. *Regulation (EU) 2016/1628 of the European Parliament and of the Council of 14 September 2016 on requirements relating to gaseous and particulate pollutant emission limits and type-approval for internal combustion engines for non-road mobile machinery, amending Regulations (EU) No 1024/2012 and (EU) No 167/2013, and amending and repealing Directive 97/68/EC*. July 17, 2022. URL: http://data.europa.eu/eli/reg/2016/1628/2022-07-17 (visited on 06/14/2023).

[50] Dittler, A. *Abgasnachbehandlung mit Partikelfiltersystemen in Nutzfahrzeugen*. 1st ed. Shaker, 2014.

[51] Thring, R. H. "Homogeneous-Charge Compression-Ignition (HCCI) Engines." In: *1989 SAE International Fall Fuels and Lubricants Meeting and Exhibition*. 1989. DOI: 10.4271/892068.

[52] Reitz, R. D. and Duraisamy, G. "Review of high efficiency and clean reactivity controlled compression ignition (RCCI) combustion in internal combustion engines." In: *Progress in Energy and Combustion Science* 46 (2015), pp. 12–71. DOI: 10.1016/j.pecs.2014.05.003.

[53]   Yan, Z., Gainey, B., and Lawler, B. "A parametric modeling study of thermal barrier coatings in low-temperature combustion engines." In: *Applied Thermal Engineering* 200 (2022), p. 117687. DOI: 10.1016/j.applthermaleng.2021.117687.

[54]   Li, Y., Tang, W., Abubakar, S., and Wu, G. "Construction of a compact skeletal mechanism for acetone–n–butanol–ethanol (ABE)/diesel blends combustion in engines using a decoupling methodology." In: *Fuel Processing Technology* 209 (2020), p. 106526. DOI: 10.1016/j.fuproc.2020.106526.

[55]   Cai, T. and Zhao, D. "Temperature Dependence of Laminar Burning Velocity in Ammonia/Dimethyl Ether-air Premixed Flames." In: *Journal of Thermal Science* 31.1 (2022), pp. 189–197. DOI: 10.1007/s11630-022-1549-1.

[56]   Tan, D., Wu, Y., Lv, J., Li, J., Ou, X., Meng, Y., Lan, G., Chen, Y., and Zhang, Z. "Performance optimization of a diesel engine fueled with hydrogen/biodiesel with water addition based on the response surface methodology." In: *Energy* 263 (2023), p. 125869. DOI: 10.1016/j.energy.2022.125869.

[57]   Zhao, C., Zhu, Y., and Huang, S. "Pressure Drop and Soot Accumulation Characteristics through Diesel Particulate Filters Considering Various Soot and Ash Distribution Types." In: *WCX™ 17: SAE World Congress Experience*. 2017. DOI: 10.4271/2017-01-0959.

[58]   Wang, Y., Kamp, C. J., Wang, Y., Toops, T. J., Su, C., Wang, R., Gong, J., and Wong, V. W. "The origin, transport, and evolution of ash in engine particulate filters." In: *Applied Energy* 263 (2020), p. 114631. DOI: 10.1016/j.apenergy.2020.114631.

[59]   Haralampous, O. and Koltsakis, G. C. "Intra-layer temperature gradients during regeneration of diesel particulate filters." In: *Chemical Engineering Science* 57.13 (2002), pp. 2345–2355. DOI: 10.1016/S0009-2509(02)00135-5.

[60]   Kamp, C. J., Bagi, S., and Wang, Y. "Phenomenological Investigations of Mid-Channel Ash Deposit Formation and Characteristics in Diesel Particulate Filters." In: *WCX SAE World Congress Experience*. 2019. DOI: 10.4271/2019-01-0973.

[61]   Eakle, S., Avery, S., Weber, P., and Henry, C. "Comparison of Accelerated Ash Loading Methods for Gasoline Particulate Filters." In: *International Powertrains, Fuels & Lubricants Meeting*. 2018. DOI: 10.4271/2018-01-1703.

[62]   Rubino, L., Piotr Oles, J., and La Rocca, A. "Evaluating Performance of Uncoated GPF in Real World Driving Using Experimental Results and CFD modelling." In: *13th International Conference on Engines & Vehicles*. 2017. DOI: 10.4271/2017-24-0128.

[63]   Becker, C., Reinsch, B., Strobel, M., Frisse, H.-P., and Fritsch, A. "Diesel-partikelfilter aus Cordierit." In: *MTZ - Motortechnische Zeitschrift* 69.6 (2008), pp. 494–501. DOI: 10.1007/BF03227461.

[64]   Motoki, K., Suenobu, H., and Kodama, E. "Honeycomb filter, and manufacturing method of the same." U.S. pat. 8747511B2. 2014.

[65]   Ohno, K., Shimato, K., Taoka, N., Santae, H., Ninomiya, T., Komori, T., and Salvat, O. "Characterization of SiC-DPF for Passenger Car." In: *SAE 2000 World Congress*. 2000. DOI: 10.4271/2000-01-0185.

[66]   Stobbe, P., Petersen, H. G., Sorenson, S. C., and Høj, J. W. "A New Closing Method for Wall Flow Diesel Particulate Filters." In: *SAE Transactions* 105 (1996), pp. 1–8. (Visited on 08/03/2023).

[67]   Ogunwumi, S. B., Tepesch, P. D., Chapman, T., Warren, C. J., Melscoet-Chauvel, I. M., and Tennent, D. L. "Aluminum Titanate Compositions for Diesel Particulate Filters." In: *SAE 2005 World Congress & Exhibition*. 2005. DOI: 10.4271/2005-01-0583.

[68]   Ogunwumi, S. B., Tepesch, P. D., and Wusirika, R. R. "Ceramic body based on aluminum titanate." U.S. pat. 6942713B2. 2005.

[69]   Frost, R. and Holleran, L. M. "Method of making monolithic honeycombed structures." U.S. pat. 3899326A. 1975.

[70]   Hammond, D. C. and Vickers, J. T. "Wall-flow monolith filter." U.S. pat. 4390355A. 1983.

[71]   Hammond, D. C. and Vickers, J. P. T. "Method of making wall-flow monolith filter." U.S. pat. 4423090A. 1983.

[72]   Choi, S., Oh, K.-C., and Lee, C.-B. "The effects of filter porosity and flow conditions on soot deposition/oxidation and pressure drop in particulate filters." In: *Energy* 77 (2014), pp. 327–337. DOI: 10.1016/j.energy.2014.08.049.

[73]   Sappok, A., Santiago, M., Vianna, T., and Wong, V. W. "Characteristics and Effects of Ash Accumulation on Diesel Particulate Filter Performance: Rapidly Aged and Field Aged Results." In: *SAE World Congress & Exhibition*. 2009. DOI: 10.4271/2009-01-1086.

[74] Gaiser, G. "Berechnung von Druckverlust, Ruß- und Ascheverteilung in Partikelfiltern." In: *MTZ - Motortechnische Zeitschrift* 66.2 (2005), pp. 92–102. DOI: 10.1007/BF03227250.

[75] Konstandopoulos, A. G. and Johnson, J. H. "Wall-Flow Diesel Particulate Filters—Their Pressure Drop and Collection Efficiency." In: *SAE International* (1989). DOI: 10.4271/890405.

[76] Sappok, A., Rodriguez, R., and Wong, V. "Characteristics and Effects of Lubricant Additive Chemistry on Ash Properties Impacting Diesel Particulate Filter Service Life." In: *SAE International Journal of Fuels and Lubricants* 3.1 (2010), pp. 705–722. DOI: 10.4271/2010-01-1213.

[77] Sappok, A. and Wong, V. W. "Lubricant-Derived Ash Properties and Their Effects on Diesel Particulate Filter Pressure Drop Performance." In: *Journal of Engineering for Gas Turbines and Power* 133.3 (2011). DOI: 10.1115/icef2009-14080.

[78] Bissett, E. J. "Mathematical model of the thermal regeneration of a wall-flow monolith diesel particulate filter." In: *Chemical Engineering Science* 39.7 (1984), pp. 1233–1244. DOI: 10.1016/0009-2509(84)85084-8.

[79] Morcos, M., Ayyappan, P., and Harris, T. "Characterization of DPF Ash for Development of DPF Regeneration Control and Ash Cleaning Requirements." In: *SAE 2011 World Congress & Exhibition*. 2011. DOI: 10.4271/2011-01-1248.

[80] Konstandopoulos, A. G., Kostoglou, M., Skaperdas, E., Papaioannou, E., Zarvalis, D., and Kladopoulou, E. "Fundamental Studies of Diesel Particulate Filters: Transient Loading, Regeneration and Aging." In: *SAE 2000 World Congress*. 2000. DOI: 10.4271/2000-01-1016.

[81] Sappok, A., Govani, I., Kamp, C., Wang, Y., and Wong, V. "In-Situ Optical Analysis of Ash Formation and Transport in Diesel Particulate Filters During Active and Passive DPF Regeneration Processes." In: *SAE International Journal of Fuels and Lubricants* 6.2 (2013), pp. 336–349. DOI: 10.4271/2013-01-0519.

[82] Ishizawa, T., Yamane, H., Satoh, H., Sekiguchi, K., Arai, M., Yoshimoto, N., and Inoue, T. "Investigation into Ash Loading and Its Relationship to DPF Regeneration Method." In: *SAE International Journal of Commercial Vehicles* 2.2 (2009), pp. 164–175. DOI: 10.4271/2009-01-2882.

[83]   Dittler, A. "Ash Transport in Diesel Particle Filters." In: *SAE 2012 International Powertrains, Fuels & Lubricants Meeting*. 2012. DOI: 10.4271/2012-01-1732.

[84]   Wang, Y. and Kamp, C. "The Effects of Mid-Channel Ash Plug on DPF Pressure Drop." In: *SAE 2016 World Congress and Exhibition*. 2016. DOI: 10.4271/2016-01-0966.

[85]   Zhang, Z., Dong, R., Lan, G., Yuan, T., and Tan, D. "Diesel particulate filter regeneration mechanism of modern automobile engines and methods of reducing PM emissions: A review." In: *Environmental Science and Pollution Research* 30.14 (2023), pp. 39338–39376.

[86]   Luo, J., Tie, Y., Tang, L., Li, Y., Xu, H., Liu, Z., Li, M., Zhang, H., and Zhang, Z. "Effect of regeneration method and ash deposition on diesel particulate filter performance: A review." In: *Environmental Science and Pollution Research* 30.16 (2023), pp. 45607–45642.

[87]   Zhang, Z., Dong, R., Tan, D., Duan, L., Jiang, F., Yao, X., Yang, D., Hu, J., Zhang, J., Zhong, W., and Zhao, Z. "Effect of structural parameters on diesel particulate filter trapping performance of heavy-duty diesel engines based on grey correlation analysis." In: *Energy* 271 (2023), p. 127025. DOI: 10.1016/j.energy.2023.127025.

[88]   Konstandopoulos, A. G. "Flow Resistance Descriptors for Diesel Particulate Filters: Definitions, Measurements and Testing." In: *SAE 2003 World Congress & Exhibition*. 2003. DOI: 10.4271/2003-01-0846.

[89]   Masoudi, M. "Pressure Drop of Segmented Diesel Particulate Filters." In: *SAE Transactions* 114 (2005), pp. 503–511.

[90]   Konstandopoulos, A. G., Skaperdas, E., and Masoudi, M. "Inertial Contributions to the Pressure Drop of Diesel Particulate Filters." In: *SAE 2001 World Congress*. 2001. DOI: 10.4271/2001-01-0909.

[91]   Sutera, S. P. and Skalak, R. "The History of Poiseuille's Law." In: *Annual Review of Fluid Mechanics* 25.1 (1993), pp. 1–20. DOI: 10.1146/annurev.fl.25.010193.000245.

[92]   Young, D. M., Hickman, D. L., Bhatia, G., and Gunasekaran, N. "Ash Storage Concept for Diesel Particulate Filters." In: *SAE 2004 World Congress & Exhibition*. 2004. DOI: 10.4271/2004-01-0948.

[93] Yamamoto, K. and Nakamura, M. "Simulation on Flow and Heat Transfer in Diesel Particulate Filter." In: *Journal of Heat Transfer* 133.6 (2011). DOI: 10.1115/1.4003448.

[94] Yamamoto, K. and Sakai, T. "Simulation of continuously regenerating trap with catalyzed DPF." In: *Catalysis Today* 242 (2015). Memorial Issue for the late Prof. Yasutake Teraoka: Proceedings of the 6 th Japan-China Workshop on Environmental Catalysis and Eco-materials, pp. 357–362. DOI: 10.1016/j.cattod.2014.07.022.

[95] Trunk, R., Marquardt, J., Thäter, G., Nirschl, H., and Krause, M. J. "Towards the simulation of arbitrarily shaped 3D particles using a homogenised lattice Boltzmann method." In: *Computers & Fluids* 172 (2018), pp. 621–631. DOI: 10.1016/j.compfluid.2018.02.027.

[96] Marquardt, J. E., Römer, U. J., Nirschl, H., and Krause, M. J. "A discrete contact model for complex arbitrary-shaped convex geometries." In: *Particuology* 80 (2023), pp. 180–191. DOI: 10.1016/j.partic.2022.12.005.

[97] Kamp, C. J., Sappok, A., Wang, Y., Bryk, W., Rubin, A., and Wong, V. "Direct Measurements of Soot-Ash Affinity in the Diesel Particulate Filter by Atomic Force Microscopy and Implications for Ash Accumulation and DPF Degradation." In: (2014). DOI: 10.4271/2014-01-1486.

[98] Kimura, K., Lynskey, M., Corrigan, E. R., Hickman, D. L., Wang, J., Fang, H. L., and Chatterjee, S. "Real World Study of Diesel Particulate Filter Ash Accumulation in Heavy-Duty Diesel Trucks." In: *Powertrain & Fluid Systems Conference and Exhibition*. 2006. DOI: 10.4271/2006-01-3257.

[99] Sappok, A., Santiago, M., Vianna, T., and Wong, V. W. "Controlled Experiments on the Effects of Lubricant/Additive (Low-Ash, Ashless) Characteristics on DPF Degradation." In: *Diesel Engine-Efficiency and Emissions Research (DEER) Conference*. 2008.

[100] Cooper, R. C., Bruno, G., Onel, Y., Lange, A., Watkins, T. R., and Shyam, A. "Young's modulus and Poisson's ratio changes due to machining in porous microcracked cordierite." In: *Journal of Materials Science* 51.21 (2016), pp. 9749–9760. DOI: 10.1007/s10853-016-0209-9.

[101] Thieringer, J. R. D., Watzek, A. K., Meyer, J., and Dittler, A. "Generation of ash particles from different lube oil mists." In: *Aerosol Science and Technology* 56.8 (2022), pp. 744–756. DOI: 10.1080/02786826.2022.2073192.

[102]   Corbly, J. E. "The Free Software Alternative: Freeware, Open Source Software, and Libraries." In: *Information Technology and Libraries* 33.3 (2014), pp. 65–75. DOI: 10.6017/ital.v33i3.5105.

[103]   Rettinger, C. and Rüde, U. "A comparative study of fluid-particle coupling methods for fully resolved lattice Boltzmann simulations." In: *Computers & Fluids* 154 (2017). ICCFD8, pp. 74–89. DOI: 10.1016/j.compfluid.2017.05.033.

[104]   Feichtinger, C., Habich, J., Köstler, H., Hager, G., Rüde, U., and Wellein, G. "A flexible Patch-based lattice Boltzmann parallelization approach for heterogeneous GPU–CPU clusters." In: *Parallel Computing* 37.9 (2011). Emerging Programming Paradigms for Large-Scale Scientific Computing, pp. 536–549. DOI: 10.1016/j.parco.2011.03.005.

[105]   Raase, S. and Nordström, T. "On the Use of a Many-core Processor for Computational Fluid Dynamics Simulations." In: *Procedia Computer Science* 51 (2015). International Conference On Computational Science, ICCS 2015, pp. 1403–1412. DOI: 10.1016/j.procs.2015.05.348.

[106]   Krüger, T., Kusumaatmaja, H., Kuzmin, A., Shardt, O., Silva, G., and Viggen, E. M. *The Lattice Boltzmann Method - Principles and Practice*. Springer Cham, 2016. DOI: 10.1007/978-3-319-44649-3.

[107]   Conklin, A. A. and Kumar, S. "Solving the big computing problems in the twenty-first century." In: *Nature Electronics* 6.7 (2023), pp. 464–466. DOI: 10.1038/s41928-023-00985-1.

[108]   Guo, Z. and Zhao, T. S. "Lattice Boltzmann model for incompressible flows through porous media." In: *Phys. Rev. E* 66 (3 2002), p. 036304. DOI: 10.1103/PhysRevE.66.036304.

[109]   Thieringer, J. R. D., Werling, H., Meyer, J., and Dittler, A. "In Situ Tracking of Break-up, Resuspension, and Transport of Reactive Particle Structures in a Single Wall-Flow Filter Channel." In: *Emission Control Science and Technology* (2023). DOI: 10.1007/s40825-023-00228-x.

[110]   Hinds, W. C. *Aerosol technology : properties, behavior, and measurement of airborne particles*. 2. ed. LiteraturangabenIMD-Felder maschinell generiert (GBV). Wiley, 1999.

[111]   Opris, C. N. and Johnson, J. H. "A 2-D Computational Model Describing the Flow and Filtration Characteristics of a Ceramic Diesel Particulate Trap." In: *International Congress & Exposition*. 1998. DOI: 10.4271/980545.

[112]   Konstandopoulos, A. G., Skaperdas, E., Warren, J., and Allansson, R. "Optimized Filter Design and Selection Criteria for Continuously Regenerating Diesel Particulate Traps." In: *International Congress & Exposition*. 1999. DOI: 10.4271/1999-01-0468.

[113]   Yang, S., Deng, C., Gao, Y., and He, Y. "Diesel particulate filter design simulation: A review." In: *Advances in Mechanical Engineering* 8.3 (2016), p. 1687814016637328. DOI: 10.1177/1687814016637328.

[114]   Brinkman, H. C. "A calculation of the viscous force exerted by a flowing fluid on a dense swarm of particles." In: *Flow, Turbulence and Combustion* 1.1 (1949), p. 27. DOI: 10.1007/BF02120313.

[115]   Spaid, M. A. A. and Phelan, F. R. "Lattice Boltzmann methods for modeling microscale flow in fibrous porous media." In: *Physics of Fluids* 9.9 (1997), pp. 2468–2474. DOI: 10.1063/1.869392.

[116]   Shan, X. and Chen, H. "Lattice Boltzmann model for simulating flows with multiple phases and components." In: *Phys. Rev. E* 47 (3 1993), pp. 1815–1819. DOI: 10.1103/PhysRevE.47.1815.

[117]   Martys, N. S. "Improved approximation of the Brinkman equation using a lattice Boltzmann method." In: *Physics of Fluids* 13.6 (2001), pp. 1807–1810. DOI: 10.1063/1.1368846.

[118]   Martys, N. S., Shan, X., and Chen, H. "Evaluation of the external force term in the discrete Boltzmann equation." In: *Phys. Rev. E* 58 (5 1998), pp. 6855–6857. DOI: 10.1103/PhysRevE.58.6855.

[119]   Guo, Z., Zheng, C., and Shi, B. "Discrete lattice effects on the forcing term in the lattice Boltzmann method." In: *Phys. Rev. E* 65 (4 2002), p. 046308. DOI: 10.1103/PhysRevE.65.046308.

[120]   Noble, D. R. and Torczynski, J. R. "A Lattice-Boltzmann Method for Partially Saturated Computational Cells." In: *International Journal of Modern Physics C* 09.08 (1998), pp. 1189–1201. DOI: 10.1142/S0129183198001084.

[121]   Krause, M. J., Klemens, F., Henn, T., Trunk, R., and Nirschl, H. "Particle flow simulations with homogenised lattice Boltzmann methods." In: *Particuology* 34 (2017), pp. 1–13. DOI: 10.1016/j.partic.2016.11.001.

[122]   Bhatnagar, P. L., Gross, E. P., and Krook, M. "A Model for Collision Processes in Gases. I. Small Amplitude Processes in Charged and Neutral One-Component Systems." In: *Phys. Rev.* 94 (3 1954), pp. 511–525. DOI: 10.1103/PhysRev.94.511.

[123] He, X. and Luo, L.-S. "Theory of the lattice Boltzmann method: From the Boltzmann equation to the lattice Boltzmann equation." In: *Phys. Rev. E* 56 (6 1997), pp. 6811–6817. DOI: 10.1103/PhysRevE.56.6811.

[124] Ergun, S. "Fluid Flow through Packed Columns." In: *Journal of Chemical Engineering Progress* Vol. 48.No. 2 (1952), pp. 89–94.

[125] Kupershtokh, A., Medvedev, D., and Karpov, D. "On equations of state in a lattice Boltzmann method." In: *Computers & Mathematics with Applications* 58.5 (2009). Mesoscopic Methods in Engineering and Science, pp. 965–974. DOI: 10.1016/j.camwa.2009.02.024.

[126] Wen, B., Zhang, C., Tu, Y., Wang, C., and Fang, H. "Galilean invariant fluid–solid interfacial dynamics in lattice Boltzmann simulations." In: *Journal of Computational Physics* 266 (2014), pp. 161–170. DOI: 10.1016/j.jcp.2014.02.018.

[127] Verlet, L. "Computer "Experiments" on Classical Fluids. I. Thermodynamical Properties of Lennard-Jones Molecules." In: *Phys. Rev.* 159 (1 1967), pp. 98–103. DOI: 10.1103/PhysRev.159.98.

[128] Swope, W. C., Andersen, H. C., Berens, P. H., and Wilson, K. R. "A computer simulation method for the calculation of equilibrium constants for the formation of physical clusters of molecules: Application to small water clusters." In: *The Journal of Chemical Physics* 76.1 (1982), pp. 637–649. DOI: 10.1063/1.442716.

[129] Porter, S., Saul, J., Aleksandrova, S., Medina, H., and Benjamin, S. "Hybrid flow modelling approach applied to automotive catalysts." In: *Applied Mathematical Modelling* 40.19 (2016), pp. 8435–8445. DOI: 10.1016/j.apm.2016.04.024.

[130] Latt, J., Chopard, B., Malaspinas, O., Deville, M., and Michler, A. "Straight velocity boundaries in the lattice Boltzmann method." In: *Phys. Rev. E* 77 (5 2008), p. 056703. DOI: 10.1103/PhysRevE.77.056703.

[131] Ladd, A. J. C. "Numerical simulations of particulate suspensions via a discretized Boltzmann equation. Part 1. Theoretical foundation." In: *Journal of Fluid Mechanics* 271 (1994), pp. 285–309. DOI: 10.1017/S0022112094001771.

[132] Kamp, C. J., Zhang, S., Bagi, S., Wong, V., Monahan, G., Sappok, A., and Wang, Y. "Ash Permeability Determination in the Diesel Particulate Filter from Ultra-High Resolution 3D X-Ray Imaging and Image-Based

Direct Numerical Simulations." In: *SAE International Journal of Fuels and Lubricants* 10.2 (2017), pp. 608–618.

[133]   Bermúdez, V., Serrano, J. R., Piqueras, P., and Sanchis, E. J. "On the Impact of Particulate Matter Distribution on Pressure Drop of Wall-Flow Particulate Filters." In: *Applied Sciences* 7.3 (2017). DOI: 10.3390/app7030234.

[134]   Lohse, M., Wittig, S., and Hacker, J. *Clean air. Nitrogen oxides and particulate matter in ambient air: Basic principles and recommendations.* Tech. rep. 2019.

[135]   Aravelli, K. and Heibel, A. "Improved Lifetime Pressure Drop Management for Robust Cordierite (RC) Filters with Asymmetric Cell Technology (ACT)." In: *SAE World Congress & Exhibition.* 2007. DOI: 10.4271/2007-01-0920.

[136]   Segré, G. and Silberberg, A. "Radial Particle Displacements in Poiseuille Flow of Suspensions." In: *Nature* 189.4760 (1961), pp. 209–210. DOI: 10.1038/189209a0.

[137]   Segré, G. and Silberberg, A. "Behaviour of macroscopic rigid spheres in Poiseuille flow Part 2. Experimental results and interpretation." In: *Journal of Fluid Mechanics* 14.1 (1962), pp. 136–157. DOI: 10.1017/s0022112062001111.

[138]   Ginzburg, I. "Equilibrium-type and link-type lattice Boltzmann models for generic advection and anisotropic-dispersion equation." In: *Advances in Water Resources* 28.11 (2005), pp. 1171–1195. DOI: 10.1016/j.advwatres.2005.03.004.

[139]   Simonis, S., Haussmann, M., Kronberg, L., Dörfler, W., and Krause, M. "Linear and brute force stability of orthogonal moment multiple–relaxation–time lattice Boltzmann methods applied to homogeneous isotropic turbulence." In: *Philosophical Transactions of the Royal Society A: Mathematical, Physical and Engineering Sciences* 379.2208 (2021), p. 20200405. DOI: 10.1098/rsta.2020.0405.

[140]   Chapman, S., Cowling, T., Burnett, D., and Cercignani, C. *The Mathematical Theory of Non-uniform Gases: An Account of the Kinetic Theory of Viscosity, Thermal Conduction and Diffusion in Gases.* Cambridge University Press, 1990.

[141] Ferziger, J. H. and Perić, M. *Numerische Strömungsmechanik*. ger. Springer Berlin Heidelberg, 2008, Online–Ressource (XV, 509 S, online resource). DOI: 10.1007/978-3-540-68228-8.

[142] Liu, J., Huang, C., Chai, Z., and Shi, B. "A diffuse-interface lattice Boltzmann method for fluid–particle interaction problems." In: *Computers & Fluids* 233 (2022), p. 105240. DOI: 10.1016/j.compfluid.2021.105240.

[143] Skordos, P. A. "Initial and boundary conditions for the lattice Boltzmann method." In: *Phys. Rev. E* 48 (6 1993), pp. 4823–4842. DOI: 10.1103/PhysRevE.48.4823.

[144] Sappok, A., Kamp, C., and Wong, V. "Sensitivity Analysis of Ash Packing and Distribution in Diesel Particulate Filters to Transient Changes in Exhaust Conditions." In: *SAE International Journal of Fuels and Lubricants* 5.2 (2012), pp. 733–750. DOI: 10.4271/2012-01-1093.

[145] Ghia, U., Ghia, K., and Shin, C. "High-Re solutions for incompressible flow using the Navier-Stokes equations and a multigrid method." In: *Journal of Computational Physics* 48.3 (1982), pp. 387–411. DOI: 10.1016/0021-9991(82)90058-4.

[146] Nassauer, B. and Kuna, M. "Contact forces of polyhedral particles in discrete element method." In: *Granular Matter* 15.3 (2013), pp. 349–355. DOI: 10.1007/s10035-013-0417-9.

[147] Carvalho, A. S. and Martins, J. M. "Exact restitution and generalizations for the Hunt–Crossley contact model." In: *Mechanism and Machine Theory* 139 (2019), pp. 174–194. DOI: 10.1016/j.mechmachtheory.2019.03.028.

[148] Pandey, A., Shyam, A., Watkins, T. R., Lara-Curzio, E., Stafford, R. J., and Hemker, K. J. "The Uniaxial Tensile Response of Porous and Microcracked Ceramic Materials." In: *Journal of the American Ceramic Society* 97.3 (2014), pp. 899–906. DOI: 10.1111/jace.12720.

[149] Thota, S. K., Cao, T. D., and Vahedifard, F. "Poissons Ratio Characteristic Curve of Unsaturated Soils." In: *Journal of Geotechnical and Geoenvironmental Engineering* 147.1 (2021), p. 04020149. DOI: 10.1061/(ASCE)GT.1943-5606.0002424.

[150] Savitzky, A. and Golay, M. J. E. "Smoothing and differentiation of data by simplified least squares procedures." In: *Analytical Chemistry* 36 (1964), pp. 1627–1639. DOI: 10.1021/ac60214a047.

[151] Gaedtke, M., Wachter, S., Rädle, M., Nirschl, H., and Krause, M. J. "Application of a lattice Boltzmann method combined with a Smagorinsky turbulence model to spatially resolved heat flux inside a refrigerated vehicle." In: *Computers & Mathematics with Applications* 76.10 (2018), pp. 2315–2329. DOI: 10.1016/j.camwa.2018.08.018.

[152] Simonis, S., Oberle, D., Gaedtke, M., Jenny, P., and Krause, M. J. "Temporal large eddy simulation with lattice Boltzmann methods." In: *Journal of Computational Physics* 454 (2022), p. 110991. DOI: 10.1016/j.jcp.2022.110991.

[153] Di Sarli, V. and Di Benedetto, A. "Modeling and simulation of soot combustion dynamics in a catalytic diesel particulate filter." In: *Chemical Engineering Science* 137 (2015), pp. 69–78. DOI: 10.1016/j.ces.2015.06.011.

[154] Huang, T., Hu, G., Meng, Z., and Zeng, D. "Exhaust temperature control for safe and efficient thermal regeneration of diesel particulate filter." In: *Applied Thermal Engineering* 189 (2021), p. 116747. DOI: 10.1016/j.applthermaleng.2021.116747.

[155] Hettel, M., Daymo, E., Schmidt, T., and Deutschmann, O. "CFD-Modeling of fluid domains with embedded monoliths with emphasis on automotive converters." In: *Chemical Engineering and Processing - Process Intensification* 147 (2020), p. 107728. DOI: 10.1016/j.cep.2019.107728.

Appendix

A List of Application Cases

All application cases used in this work, have been combined into a single generic one, which provides a set of compile-time options to yield the specific case necessary for a particular study. It can be found on the master branch of OPENLBs repository hosted at gitlab.com/openlb/olb. In order to recreate the results presented, the different states of the application case at the time of conducting the respective studies are listed below. All states compile and run successfully with GCC 11.3.0 and OPEN MPI 4.0.7. For states requiring a previous build system, complete deletion of the build folder and recreation of the config file is mandatory. While compiling and running successfully, it should be noted that those older states throw a *caught-signal-11* segmentation fault after execution with the compiler version mentioned above.

1. Wall-Flow-Channel – Step 4: Plug formation investigation

   Description: see Chapter 5
   Commit hash: `3245f617376fceee1bd4`
   Case folder: `apps/nicolas/A_WallFlow/wallFlow`
   Date: 05/05/2023
   Released state: Version 1.6

2. Wall-Flow-Channel – Step 3: Model velocity scaling

   Description: see Chapter 4
   Commit hash: `2a67f4529d5c2f2a1e16`
   Case folder: `apps/nicolas/A_WallFlow/wallFlow`
   Date: 06/04/2023
   Released state: Version 1.5

3. Wall-Flow-Channel – Step 2: Single fragment investigation

   Description: see Chapter 3
   Commit hash: `f4b271a3c6c150b28067`
   Case folder: `apps/nicolas/A_WallFlow/wallFlow`
   Date: 27/08/2021
   Released state: Version 1.4
   Note: Previous build system

4. Wall-Flow-Channel – Step 1: Model development

   Description: see Chapter 2

Commit hash: `367d2c645d39158abb82`
Case folder: `apps/nicolas/A_WallFlow/wallFlow`
Date: 23/03/2021
Released state: Version 1.4
Note: Previous build system

B Acronyms

BGK Bhatnagar-Gross-Krook

CFD computational fluid dynamics

CNG compressed natural gas

DEM discrete element method

DPF diesel particulate filter

EOC experimental order of convergence

EPA United States Environmental Protection Agency

FPS frames per second

FVM finite volume method

GPF gasoline particulate filter

GPGPU general purpose computation on graphics processing unit

HCCI homogeneous charge compression ignition

HLBM homogenized lattice Boltzmann method

IBM immersed boundary method

ICE internal combustion engine

LBE lattice Boltzmann equation

LBM lattice Boltzmann method

LES large eddy simulation

LPG liquefied petroleum gas

MBM moving boundary method

NRMM non-road mobile machinery

NSE Navier-Stokes equation

PM particulate matter

PN particle number

PSM partially saturated method

RCCI reactivity controlled compression ignition

RDE real driving emissions

SEPA State Environmental Protection Administration

SP Spaid-Phelan

TBC thermal barrier coating

WHO World Health Organization